Contribution to the numerical reconstruction in inverse elasto-acoustic scattering

Izar Azpiroz

UNIVERSITÉ PAU - UPPA - UFR SCIENCES
École Sciences Exactes et leurs Applications de l'Université de Pau et des Pays de l'Adour- ED 211

THÈSE

Pour l'obtention du titre de

DOCTEUR EN SCIENCES
de L'UNIVERSITÉ DE PAU ET DES PAYS DE L'ADOUR

Spécialité : Mathématiques Appliquées

Présentée par

Izar AZPIROZ IRAGORRI

CONTRIBUTION TO THE NUMERICAL RECONSTRUCTION IN INVERSE ELASTO-ACOUSTIC SCATTERING

Thèse dirigée par : **Mme. Hélène BARUCQ**
M. Julien DIAZ
M. Rabia DJELLOULI

Après avis de :

M. Marc BONNET	Directeur de Recherche, Laboratoire POEMS-ENSTA Paris Tech	Rapporteur
M. Ignacio MUGA	Professeur, Universidad Católica de Valparaiso (PUCV), Chile	Rapporteur

Devant le jury :

Mme Hélène BARUCQ	Directrice de Recherche, INRIA	Directrice de thèse
M. Marc BONNET	Directeur de Recherche, POEMS-ENSTA Paris Tech	Rapporteur
M. Gilles CARBOU	Professor, UPPA	Président du Jury
M. Julien DIAZ	Chargé de recherche, INRIA	Directeur de thèse
M. Rabia DJELLOULI	Professor, IRIS-CSUN	Directeur de thèse
Mme. Elodie ESTÉCAHANDY	Ingénieure de Recherche, TOTAL	Examinatrice
M. Ignacio MUGA	Professeur, PUCV, Chile	Rapporteur
M. David PARDO	Directeur de Recherche, BCAM, Spain	Examinateur

Soutenu à Pau, le 28 février de 2018

Contents

Eskerrik asko!

I would like to thank my directors and advisers Hélène Barucq, Julien Diaz and Rabia Djellouli for guiding and supporting me over the three years. You have set an example of excellence as a researcher, mentor, instructor, and role model. I sincerely thank you your guidance through this process; your discussion, ideas, and feedback have been absolutely invaluable.

Je remercie tous les membres de l'équipe Magique 3D pour votre bonne humeur quotidienne! Un grand merci à ceux avec qui j'ai partagé mon bureau, mes voyage, mes repas, merci à ceux avec qui j'ai partagé beaucoup de discussions culturelles, culinaires, sentimentales et amicales. Je remercie surtout ceux qui ont supporté mon caractère pendant ces derniers mois de thèse et ceux qui m'ont aidé avec les petits inconvénients techniques et informatiques.

Os dedico mi mas sincero abrazo a toda mi familia de Pau. Mi paciencia, esperanza y el buen humor habrian desaparecido si no fuese por la calidez y el carino que he sentido entre vosotros. Muchas gracias por cada abrazo, consejo, taller de terapia inprovisada, cerveza y momentos magicos que hemos compartido.

Azkenik, besarka haundi ta goxo bat Oiartzunen, ain gertu ta ain urrun, zaudeten adiskide kuttun eta familia aldaezinari. Telefono zalea ez banaiz ere, beti presente zaituztet, eta gaur egun naizena zuen ondoan igarotako ainbeste momenturi esker bada. Miya esker zeatenangatik! Eta zuri Bitxito, *the last but not the least*, eskerrik goxuenak egunero, momentu gazi ta gozoetan, hor eon zealako ta zaudelako. Zure besarkadek ta hitz goxuek ekaitz askotatik babestu diate.

General Introduction

The characterization of hidden objects from scattered wave measurements is involved in many applications such as geophysical exploration, non destructive testing, medical imaging, etc. It can be achieved numerically by solving an Inverse Problem (IP) which is nonlinear and ill-posed. It is thus a difficult task and its successful accomplishment depends dramatically on the selection of very different parameters coming from the data but also from the numerical method itself.

There exist various computational methods for solving the IP and we refer the reader to [26] which reviews the current state of the art regarding inverse acoustic scattering problems. Among these, the regularized Newton-like methods (for example, see [81, 73]) have demonstrated a very good potential for solution accuracy. Nevertheless, they require solving, at each iteration, the solution of several direct acoustic scattering problems. For this reason, Newton-like methods have been applied mainly to the solution of two-dimensional IOPs even if successful reconstructions have been carried out in [41]. The linear sampling method is also widely used, firstly introduced in [27, 29]. It consists in solving the integral far field equation and to use the norm of its solution as indicator for the obstacle in the scattering. It has been successfully applied to a large number of scattering problems and we refer the reader to the overview [24]. Linear sampling methods are easy to implement and for some ranges of data, it turns out that the reconstruction of the obstacle is fast. Linear sampling methods have been followed by the factorization method proposed by Andreas Kirsch in [70, 71]. Both methods aim at characterizing the support of the scatterer by deciding whether a point z in space is inside or outside the scattering object. The fundamental difference between the factorization method and the linear sampling method is the equation that is actually solved and the factorization approach provides a rigorous characterization of the obstacle. These algorithms are very efficient compared to other techniques solving inverse scattering problems since their numerical implementation basically requires the computation of the singular value decomposition of a discretization of the far field operator. The linear sampling methods have also been coupled with topological sensitivity in [15]. Topological sensitivity has been applied to a wide variety of inverse scattering problems. It provides an indicator function of the hidden objects created by estimating the perturbation of a cost function thanks to the computation of its topological derivatives. It has been emphasized in [37] that in the time domain, the approach is similar to time reversal. Most of the time, the concept of topological derivative is heuristic but it is worth mentioning that [14] develops the concept for the L^2 norm of the misfit function between far-field measurements which is a considerable effort for justifying mathematically the topological derivative concept.

In some communities like geophysics, the nonlinear inverse problem is solved by applying an optimization approach based on the adjoint method. Following the pioneering works of Tarentola and Lailly [75, 99], who proposed to apply the adjoint method for imaging the subsurface, some tremendous progresses have been realized recently, thanks to the use of HPC architectures. The adjoint method provides a way for computing the gradient of the cost function to be minimized. It has long been considered too much computationally intensive but, here again, the recent progresses of scientific computing have now made it very efficient even in realistic situations [87, 88]. It is worth mentioning that the gradient is approximated and most of the time, the optimization algorithm involves its first order approximation. Some works have addressed the use of a second-order approximation [22, 42].

It has been observed that in some cases, the convergence is improved [22] but it turns out that a significant improvement is not obvious in all the cases [42].

In this thesis, the solution methodology for solving the IP is based on a regularized Newton-type method proposed in [101]. This approach does not require the computation of the gradient but it employs the Fréchet derivatives of the scattered field with respect to the parameters of interest. Then the success of the reconstruction depends also on the regularization parameter. In that context, several works have been devoted to the reconstruction of the shape parameters in the acoustic case [40, 62, 70, 74, 93]. In [35, 36, 41], the Fréchet derivative of the scattered field with respect to the shape is characterized as a solution to an exterior boundary value problem which differs from the direct problem in the right-hand sides. The study of the direct exterior problem deserves thus an important attention. Its well-posedness has been formally addressed for instance in [76] in the acoustic case and in [67, 86] in the elastic case. The extension to elasto-acoustic scattering problems coupling the Helmholtz equation set in the exterior of a solid with the Navier equation representing the displacement into a bounded solid has been less considered. To the best of our knowledge, the well-posedness character of the corresponding mixed problem has been investigated in [58, 78] requiring the shape of the solid is regular enough, that is C^2. More recently, in [10], the result has been extended to the case of Lipschitz continuous obstacles. The key idea consists in introducing the Dirichlet-to-Neumann operator which allows for constructing an equivalent problem which can be solved by applying the Fredholm theory [19, 94, 95].

To the best of our knowledge, there exist few numerical studies on the full reconstruction of a solid immersed into a fluid. In [20, 21], the geometry of the two-dimensional orthotropic elastic solid is supposed to be known. The authors show that the measurement of the surface velocity is sufficient for retrieving the orthotropic parameters but the acoustic pressure measurement only allows a partial reconstruction. In [103], the inverse problem solution is obtained through the minimization of a Modified Error Constitutive Equation (MECE) functional. The developed methodology leads to the reconstruction of the elastic parameters both in 2D and 3D from measurements carried out in the solid or in the fluid. Regarding the recovering of constitutive information of the obstacle in addition to its shape, there is a recent work in the acoustic case [17] where the problem is to reconstruct the shape of the scatterer and the two parameters defining the impedance boundary condition. The objective of the thesis are then threefold:

- Propose a solution methodology based on a regularized Newton-type method for solving the IP leading to the full reconstruction of an elastic obstacle illuminated by an acoustic wave.
- Assess the sensitivity of the IP data with respect to the parameters of interest.
- Assess the sensitivity of the method to the frequency of the data and to the regularization parameter.
- Achieve the full reconstruction in the case of noisy data.

The document is organized into 6 chapters. The first chapter deals with the direct problem. We introduce the functional framework adapted to the well-posedness of the corresponding boundary value problem (BVP). We then introduce a general BVP including different right-hand sides and we obtain existence and uniqueness results in the case of a Lipschitz continuous obstacle. It is worth mentioning that these results differ from the ones in [10] because they consider a larger class of right-hand sides and the Helmholtz-Navier system is coupled with a radiation boundary condition. Chapter 1 describes also the finite element method we use for solving the direct problem. As in [9], we use an Interior Penalty Discontinuous Galerkin approximation which is based on high-order discontinuous finite elements both in the fluid and the solid. It also includes the important feature of having curved finite elements at the fluid-solid interface. It has been demonstrated in [9] that it allows to ensure a very good convergence.

In Chapter 2, we study the sensitivity of the scattered field with respect to the different parameters describing the solid which is assumed to be an isotropic medium. The content of this chapter is very important since it leads to the characterization of the Fréchet derivatives of the scattered field with respect to the parameters of interest. We remind existing results associated to the shape parameters. In the case of a non penetrable obstacle illuminated by an acoustic wave, the literature is extensive (see for instance [56, 57, 69, 89, 91]). Some works have also been devoted to electromagnetic problems [31, 51, 77, 90]. There are relatively few papers on the elasto-acoustic problem and the sensitivity with respect the shape has been addressed in [36], where the corresponding Fréchet derivative has been characterized formally. It turns out that it is given as the solution to the direct problem with non homogeneous transmission conditions. In [11] the corresponding right-hand sides are defined in the case of regular polygonal solid but the well-posedness of the associated BVP remains an open question, due to the lack of regularity of the right-hand sides. In this chapter, we investigate the sensitivity of the scattered field with respect to the Lamé parameters and the density of the solid medium. As in [40], we end up with the characterization of the corresponding Fréchet derivatives as solutions to the direct problem with modified right-hand sides. Then we focus on the case of a disk-shaped obstacle for which we have the analytical expression of the Fréchet derivatives. By this way, we can validate the computation of the Fréchet derivatives with the IPDG solver. We conclude the chapter by addressing the well-posedness of the different BVPs that define the Fréchet derivatives. Unlike in the case of the shape reconstruction, we obtain existence and uniqueness results in the case of regular obstacles, that is at least C^2 which delivers a complete characterization of the Fréchet derivatives with respect to the Lamé parameters and the density.

In Chapter 3, we introduce two solution methodologies for solving the IP. They are based on an iterative regularized Newton-like method depending on a regularization parameter ensuring the stability of the reconstruction process. To assess the performance of the two algorithms, we limit our investigations to the reconstruction of the shape and the Lamé parameters in the isotropic case. One approach aims at retrieving all the parameters in the same time while the other updates the shape and material parameters independently.

Chapter 4 develops an extended study of the behavior of the reconstruction process regarding the choice of the initial guess. We observe that the Lamé parameters do not impact on the measurements in the same way. Indeed, λ seems to be easier to retrieve than μ, at least in the range of frequencies that we have used. This is an *a priori* important information indicating that the reconstruction of μ could be more unstable than the one of λ. We also assess the impact of the incident wave frequency on the convergence of the iterative method, which is illustrated by the depiction of the cost function in each case. In particular we underline the existence of possible Jones modes [40, 53, 78] which can hamper the reconstruction process.

In Chapter 5, we propose a collection of numerical experiments aiming at fully reconstructing the solid. We consider various shaped obstacles and we also address the retrieving of the density and the location of the solid. In the latter case, we use measurements of the Far Field Pattern (FFP) whereas the shape parameters and the constitutive parameters are recovered from the measurement of the intensity of the FFP. More importantly, we also consider the case of limited aperture data, noisy data. In particular, we have been able to reconstruct a solid with limited aperture data by employing a pool of incident waves. Regarding noisy data, we illustrate the potential of a multi-frequency solution methodology for improving the convergence of the iterative optimization process. This result confirms what was already observed in [42] for geophysical applications.

Chapter 6 is the last one of the manuscript. It delivers some preliminary results for anisotropic obstacles formerly described in [16, 100]. It turns out that by increasing the number of parameters, the reconstruction becomes more difficult. Indeed, we have been able to retrieve the five material

parameters assuming the shape is known. When we search for the shape of the obstacle too, we were not able to retrieve all the parameters. This study is still ongoing.

Summary of Considered Acronyms

The main goal of this list is to introduce the considered different concepts during different Chapters.

- **SRA:** Simultaneous Reconstruction Algorithm, name of the Algorithm that retrieves all parameters at the same time.
- **SWRA:** Stepwise Reconstruction Algorithm, name of the Algorithm that retrieves parameters of different nature independently.
- **RR:** Relative Residual at the n-th iteration:

$$RR(n) = \frac{\| \widetilde{\overline{p_\infty}} \widetilde{p_\infty} - \overline{F(\mathcal{P}^n)} F(\mathcal{P}^n) \|_2}{\| \widetilde{\overline{p_\infty}} \widetilde{p_\infty} \|_2} \times 100$$

  RR computes the relative error between the intensity of the synthetic data and the intensity of the computed FFP at the n-th iteration. We denote by n the number of iterations for all the definitions.

- **RR_2:** Relative Residual corresponding to the FFP field at the n-th iteration:

$$RR_2(n) = \frac{\| \widetilde{p_\infty} - F(\mathcal{P}^n) \|_2}{\| \widetilde{p_\infty} \|_2} \times 100$$

- **UVS:** Updated Variations on the Shape parameters at the n-th iteration:

$$UVS(n) = \frac{\left(\sum_{i=1}^{N_\Gamma} \mid s_i^{n-1} - s_i^n \mid^2 \right)^{\frac{1}{2}}}{\left(\sum_{i=1}^{N_\Gamma} \mid s_i^{n-1} \mid^2 \right)^{\frac{1}{2}}} \times 100$$

- **UVM:** Updated Variations on the Material parameters at the n-th iteration:

$$UVM(n) = \frac{\mid (\lambda^{n-1} - \lambda^n)^2 + (\mu^{n-1} - \mu^n)^2 \mid^{\frac{1}{2}}}{\mid (\lambda^{n-1})^2 + (\mu^{n-1})^2 \mid^{\frac{1}{2}}} \times 100$$

- **REM:** Relative Error on Material Parameters at the n-th iteration:

$$REM(n) = \frac{\mid (\lambda - \lambda^n)^2 + (\mu - \mu^n)^2 \mid^{\frac{1}{2}}}{\mid \lambda^2 + \mu^2 \mid^{\frac{1}{2}}} \times 100$$

- **RES:** Relative Error on Shape Parameters at the n-th iteration:

$$RES(n) = \frac{\left(\sum_{i=1}^{N_\Gamma} \mid s_i - s_i^n \mid^2 \right)^{\frac{1}{2}}}{\left(\sum_{i=1}^{N_\Gamma} \mid s_i \mid^2 \right)^{\frac{1}{2}}} \times 100$$

- **RED:** Relative Error on Density at the n-th iteration:

$$RED(n) = \frac{\mid \rho - \rho^{(n)} \mid}{\mid \rho \mid} \times 100$$

- **REL:** Relative Error on Location parameters at the n-th iteration:

$$REL(n) = \frac{\left| \left(x_c - x_c^{(n)} \right)^2 + \left(y_c - y_c^{(n)} \right)^2 \right|^{1/2}}{\mid x_c^2 + y_c^2 \mid^{1/2}} \times 100$$

- **REV$_p$:** Relative Error on V_p at the n-th iteration:

$$REV_p(n) = \frac{\mid V_p - V_p^{(n)} \mid}{\mid V_p \mid} \times 100$$

- **REV$_s$:** Relative Error on V_s at the n-th iteration:

$$REV_s(n) = \frac{\mid V_s - V_s^{(n)} \mid}{\mid V_s \mid} \times 100$$

- **REV$_\epsilon$:** Relative Error on Thomsen parameter ϵ (RE_ϵ) at the n-th iteration:

$$RE_\epsilon(n) = \frac{\mid \epsilon - \epsilon^{(n)} \mid}{\mid e \mid} \times 100$$

- **REV$_\delta$:** Relative Error on Thomsen parameter δ (RE_δ) at the n-th iteration:

$$RE_\delta(n) = \frac{\mid \delta - \delta^{(n)} \mid}{\mid \delta \mid} \times 100$$

Chapter 1

The Direct Elasto-Acoustic Scattering Problem

Contents

In this chapter, we present the considered elasto-acoustic scattering problem first in an unbounded domain, and then in a bounded domain surrounded by an artificial absorbing boundary. Then we remind that the solution to this problem can be analytically computed when the obstacle is a disk-shaped isotropic obstacle. We provide the analytic expression of the solution as a series of Hankel functions. Next, we analyze the well-posedness of the general problem. To this aim, we derive a variational formulation that we prove to be equivalent to the original problem, and we study the existence and uniqueness of the solution to this variational formulation. Finally, we describe Interior Penalty Discontinuous Galerkin method that we have used to compute a numerical approximation to the problem.

1.1 Problem Statement

Let Ω^s be a bounded domain of $\mathbb{R}^2$ representing an elastic solid immersed into a fluid, $\Omega^f = \mathbb{R}^2 \setminus \bar{\Omega}^s$. The boundary of the domain Ω^s denoted by Γ is assumed to be Lipschitz continuous.

The solid is illuminated by a time-harmonic acoustic wave p^{inc} as depicted in Figure 1.1.1. When p^{inc} impinges the solid, it generates a wave into the solid which is represented by its displacement u while it transforms into a scattered wave p into the fluid. The direct problem is to determine the scattered wave p in the fluid and the transmitted elastic wave u in the elastic obstacle. Considering that the time dependence $e^{-i\omega t}$ is harmonic, we propose the following system of equations as the coupling of the Navier equation with the Helmholtz equation, **BVP 0** (a) and (b) respectively:

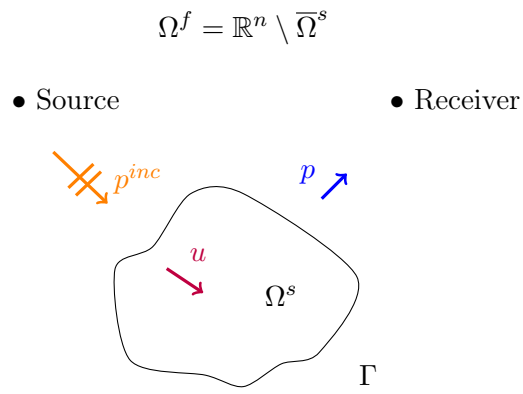

Fig. 1.1.1: Problem statement in infinite domain.

$$\textbf{(BVP 0)} \quad \begin{cases} \nabla \cdot \sigma(u) + \omega^2 \rho_s u = 0 & \text{in } \Omega^s \quad \text{(a)} \\ \Delta p + k^2 p = 0 & \text{in } \Omega^f \quad \text{(b)} \\ \tau(u) = -p\nu - p^{inc}\nu & \text{on } \Gamma \quad \text{(c)} \\ \omega^2 \rho_f u \cdot \nu = \frac{\partial p}{\partial \nu} + \frac{\partial p^{inc}}{\partial \nu} & \text{on } \Gamma \quad \text{(d)} \\ \lim\limits_{r \to +\infty} \sqrt{r} \left(\frac{\partial p}{\partial r} - ikp \right) = 0 & \text{(e)} \end{cases}$$

The elasto-acoustic scattered field is represented by the pair (p, u). The fluid pressure p is in Ω^f while u is the displacement field in Ω^s. The incident plane wave is defined by $g = p^{inc} = e^{i\omega/c_f x \cdot d}$ on Γ, where ω represents the circular frequency and c_f is the sound velocity in the fluid. The densities of the fluid Ω^f and of the scatterer Ω^s are denoted by the positive real numbers ρ_f and ρ_s respectively. The normal vector outwardly directed to Ω_s is denoted by ν. The wave number $k = \frac{\omega}{c_f}$ associates the frequency ω and the velocity c_f. The strain tensor ε is related to the displacement field as follows [67, 83]:

$$\varepsilon(u) = \frac{1}{2} \left[\nabla u + (\nabla u)^t \right],$$

while the stress tensor σ and the strain tensor ε are connected by Hooke's law:

$$\sigma(u) = C\varepsilon(u) \qquad \text{with} \qquad \sigma_{jl} = \sum_{mn} c_{jlmn} \varepsilon_{mn}.$$

The tensor c_{jlmn} is a fourth order elastic stiffness tensor, it is symmetric ($c_{jlmn} = c_{ljmn} = c_{mnjl}$) and bounded from above, that is

$$\sum_{jlmn} c_{jlmn} \varepsilon_{jl} \varepsilon_{mn} \geq \alpha_\sigma \sum_{jl} \varepsilon_{jl}^2 = \alpha_\sigma \parallel \varepsilon \parallel^2, \tag{1.1.1}$$

for some positive constant α_σ, for all symmetrical second order tensor ε. We remind that in the case of an isotropic medium [67], we have

$$c_{jlmn} = \lambda \delta_{jl} \delta_{mn} + \mu(\delta_{jm}\delta_{ln} + \delta_{jn}\delta_{lm}), \tag{1.1.2}$$

where λ and μ are the Lamé coefficients, and δ_{jl} is the Kronecker symbol. The matrix of coefficients corresponding to the isotropic medium tensor can be expressed as

$$C = \begin{pmatrix} \lambda + 2\mu & \lambda & 0 \\ \lambda & \lambda + 2\mu & 0 \\ 0 & 0 & \mu \end{pmatrix},$$

for Voigt notation (see [79]). We define the tensorial scalar product as follows:

$$\sigma : \xi = \sum_{ij} \sigma_{ij} \xi_{ij}. \tag{1.1.3}$$

The following properties of tensors are worth mentioning :

$$\begin{array}{lll} (a) & \xi : \nabla u = \xi : \varepsilon(u) & \forall \xi \text{ symmetric.} \\ (b) & C\nabla u = C\varepsilon(u) & \\ (c) & C\xi : \overline{\xi} \in \mathbb{R} & \forall \xi \text{ symmetric.} \\ (d) & C\xi : \overline{\xi} \geq \alpha_\sigma \parallel \xi \parallel^2 & \forall \xi \text{ hermitian.} \end{array} \tag{1.1.4}$$

In addition, τ represents the traction vector on the surface of the scatterer, defined as follows:

$$\tau(u) = \sigma(u)\nu. \tag{1.1.5}$$

The transmission conditions described by **BVP 0**(c)-(d) are respectively kinematic and dynamic coupling conditions [58, 78]. The first one represents the equilibrium of the forces while the second one expresses the equality of normal displacements of the solid and fluid.

The Sommerfield outgoing radiation condition **BVP 0**(e) indicates that there is no wave created at infinity [97, 98]. This condition, proposed by Sommerfield [98] in 1912, ensures the uniqueness of the solution.

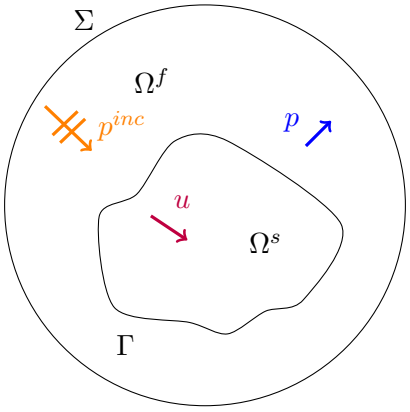

Fig. 1.1.2: Problem statement in finite domain.

Due to computational purposes, we introduce the following approximate problem which is set in a bounded domain. For that purpose, let Σ be an arbitrary shape surrounding the solid and including strictly a part of the fluid. Then, we can define a bounded domain denoted by Ω_b^f, having for

boundary $\Gamma \cup \Sigma$, and we now consider a new BVP which is now set in Ω_b^f. The resulting BVP requires introducing a surface operator B acting on Σ. To get an equivalent formulation of **BVP 0** restricted to the bounded domain Ω_b^f, it is usual to introduce the Dirichlet-to-Neumann (DtN) operator. It is a nonlocal mapping from $H^{1/2}(\Sigma)$ into $H^{-1/2}(\Sigma)$ in the regular case (i.e. for a pressure field given in $H^1(\Omega_b^f)$ at least). DtN operator relates the trace of the pressure on Σ to normal derivative on Σ. In the case of a circle with radius R, the DtN operator is given by [1, 24, 40]:

$$T_R p = \sum_{n=0}^{\infty} p_n \mu_n(k, R) e^{in\theta} \tag{1.1.6}$$

for $\theta \in [0, 2\pi]$, and

- $\mu_n(k, R) = k \dfrac{H_n'^{(1)}(kR)}{H_n^{(1)}(kR)}$,
- $p_n = \frac{1}{2\pi} \int_0^{2\pi} p(R, \theta) e^{-in\theta} d\theta$.

In this case, the Absorbing Boundary Condition is exact, and the original problem **BVP 0** is equivalent to **BVP 1** for $B = T_R p$ [40] (see Fig. 1.1.3(a)). It is clear that T_R defines a nonlocal operator given by a series expansion, which, in practice, is replaced by an approximation which corresponds to a truncation of the series.

$$\textbf{(BVP 1)} \quad \begin{cases} \nabla \cdot \sigma(u) + \omega^2 \rho_s u = 0 & \text{in } \Omega^s \quad \text{(a)} \\ \Delta p + k^2 p = 0 & \text{in } \Omega_b^f \quad \text{(b)} \\ \tau(u) = \sigma(u) \cdot \nu = -p\nu - g\nu & \text{on } \Gamma \quad \text{(c)} \\ \omega^2 \rho_f u \cdot \nu = \frac{\partial p}{\partial \nu} + \frac{\partial g}{\partial \nu} & \text{on } \Gamma \quad \text{(d)} \\ \frac{\partial p}{\partial \nu} = Bp & \text{on } \Sigma \quad \text{(e)} \end{cases} \tag{1.1.7}$$

However, the representation of T_R as a series is limited to canonical geometries like the circle [61]. Hence, it is common to use simpler boundary conditions which are known as approximations of the DtN operator and can be used for general regular surfaces. The simplest one is given by:

$$B_1 p = ikp \qquad \text{on } \Sigma. \tag{1.1.8}$$

Another condition which has demonstrated better accuracy is given by:

$$B_2 p = ikp - \frac{\kappa}{2} p \qquad \text{on } \Sigma \tag{1.1.9}$$

where κ denotes the curvature of Σ. For derivation of these conditions, see [4]. For the sake of simplicity, we will basically work with ABC B_2, that is, $B = B_2$.

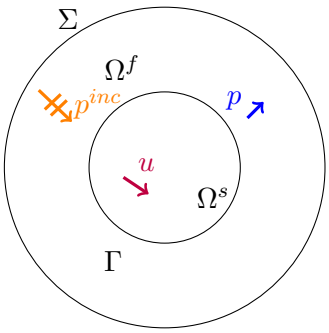

(a) Disk-shaped obstacle in a bounded domain.

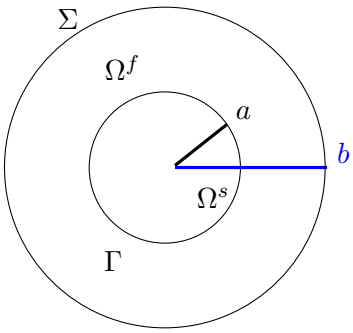

(b) Problem statement for a disk-shaped domain.

Fig. 1.1.3: Computational domain.

1.2 Analytical Solution

In order to obtain the analytical expression of the solution, we assume the same experimental setup as in [60, 9]. We consider a *steel* infinite cylinder immersed in water. The axis of the cylinder follows the z-axis direction, and the plane wave follows the positive x-axis direction. The symmetric geometry of the cylinder permit to reduce the problem to a 2D scattering problem in the (x, y)-plane. Then, the computational domain is an elastic circle Ω^s of radius a embedded in a water circular field of radius b (see Fig. 1.1.3(b)) that truncates the physical infinite domain. The spatial part of the time-harmonic plane wave of frequency $\omega/2\pi$ propagating in this medium is $p^{inc}(x) = e^{i\frac{\omega}{c_f}x\cdot d}$. Indeed, for the incident wave oriented for $d = (1, 0)$, the scattered pressure field can be expressed as follows [18]:

$$p = \sum_{n=0}^{+\infty} \Big[A_n\, H_n^{(1)}(kr) + B_n\, H_n^{(2)}(kr) \Big]\, cos(n\theta) \qquad a \le r \le b, \quad \theta \in [0, 2\pi), \tag{1.2.1}$$

where $H_n^{(1)}$ and $H_n^{(2)}$ denote the Hankel functions of the first and second kind, defined at (1.2.2)-(1.2.3). The first group of terms in the series represents the outgoing field, while the second one corresponds to the incoming wave due to the presence of the exterior boundary Σ.

We denote by J_n and Y_n the Bessel functions of the first and second kind [1]. Then, the definition of the corresponding Hankel function of the first kind reads:

$$H_n^{(1)}(z) = J_n(z) + iY_n(z), \tag{1.2.2}$$

while the Hankel function of the second kind is defined as follows:

$$H_n^{(2)}(z) = J_n(z) - iY_n(z). \tag{1.2.3}$$

The incident plane wave admits the following Jacobi-Anger expansion [18]:

$$g = p^{inc}(r, \theta) = e^{ikx\cdot d} = e^{ikrcos\theta} = \sum_{n=0}^{+\infty} \varepsilon_n i^n J_n(kr) cos(n\theta), \tag{1.2.4}$$

where

$$\varepsilon_0 = 1 \qquad \text{and} \qquad \varepsilon_n = 2 \quad \forall n > 0.$$

On the other hand, in the solid obstacle, the scattered displacement field u is expressed using two displacement potentials ϕ and ψ [83]:

$$u = \nabla\phi + (-e_z) \times \nabla\psi, \tag{1.2.5}$$

where the two potentials are given by:

$$\phi(r,\theta,\lambda,\mu) = \sum_{n=0}^{+\infty} C_n(r,\lambda,\mu) J_n(k_p r) cos(n\theta), \tag{1.2.6}$$

$$\psi(r,\theta,\lambda,\mu) = \sum_{n=0}^{+\infty} D_n(r,\lambda,\mu) J_n(k_s r) sin(n\theta); \quad 0 \le r < a, \theta \in [0, 2\pi)\,. \tag{1.2.7}$$

Moreover, we have

$$k_p = \omega\sqrt{\frac{\rho_s}{\lambda + 2\mu}}, \quad k_s = \omega\sqrt{\frac{\rho_s}{\mu}},$$

where k_p and k_s represent the wavenumbers of the pressure and shear waves in the solid.

We now develop the Fourier series representation of both components of the displacement field u. In polar coordinates, we have:

$$\begin{aligned} \nabla\phi &= \frac{\partial\phi}{\partial r}\vec{e}_r + \frac{1}{r}\frac{\partial\phi}{\partial\theta}\vec{e}_\theta, \\ (-e_z) \times \nabla\psi &= \frac{1}{r}\frac{\partial\psi}{\partial\theta}\vec{e}_\theta - \frac{\partial\psi}{\partial r}\vec{e}_r. \end{aligned} \tag{1.2.8}$$

We define:

$$\begin{aligned} u_r &= \frac{\partial\phi}{\partial r} + \frac{1}{r}\frac{\partial\psi}{\partial\theta}, \\ u_\theta &= \frac{1}{r}\frac{\partial\phi}{\partial\theta} - \frac{\partial\psi}{\partial r}. \end{aligned} \tag{1.2.9}$$

Consequently, we get:

$$u = u_r\vec{e}_r + u_\theta\vec{e}_\theta. \tag{1.2.10}$$

Due to the fact that the polar basis vectors are given by

$$\vec{e}_r = (cos\theta, \sin\theta)^t, \qquad \vec{e}_\theta = (-sin\theta, cos\theta)^t, \tag{1.2.11}$$

the displacement field is written in the canonical basis as follows:

$$\begin{cases} u_x = & u_r cos\theta - u_\theta sin\theta, \\ u_y = & u_r sin\theta + u_\theta cos\theta, \end{cases} \tag{1.2.12}$$

where

$$\begin{aligned} u_r = & \sum_{n=0}^{+\infty} \left[C_n k_p J_n^{'}(k_p r) + \frac{n}{r} D_n J_n(k_s r) \right] cos(n\theta), \\ u_\theta = & \sum_{n=0}^{+\infty} - \left[\frac{n}{r} C_n J_n(k_p r) + D_n k_s J_n^{'}(k_s r) \right] sin(n\theta). \end{aligned} \tag{1.2.13}$$

The relationships between the Fourier series displacement potentials and corresponding displacements and tractions are described in [83].

Let us introduce the vector $X_n = (A_n, B_n, C_n, D_n)^t$. The analytical solution is uniquely defined thanks to the boundary conditions of Γ ($r = a$) and Σ ($r = b$) as the solution to the linear system:

$$E_n(a, \lambda, \mu) X_n(a, \lambda, \mu) = e_n(a) \tag{1.2.14}$$

where the matrix E_n is represented by the following entries:

$$\begin{aligned} E_n^{11} &= k H_n^{\prime(1)}(ka), \\ E_n^{12} &= k H_n^{\prime(2)}(ka), \\ E_n^{13} &= -\omega^2 \rho_f k_p J_n^{\prime}(k_p a), \\ E_n^{14} &= -\omega^2 \rho_f \frac{n}{a} J_n(k_s a), \\ E_n^{21} &= H_n^{(1)}(ka), \\ E_n^{22} &= H_n^{(2)}(ka), \\ E_n^{23} &= \frac{2\mu}{a^2} \left[(n^2 + n - \frac{1}{2} k_s^2 a^2) J_n(k_p a) - k_p a J_{n-1}(k_p a) \right], \\ E_n^{24} &= \frac{2\mu}{a^2} \left[n(-(n-1) J_n(k_s a) + k_s a J_{n-1}(k_s a)) \right], \\ E_n^{31} &= E_n^{32} = E_n^{43} = E_n^{44} = 0, \\ E_n^{33} &= -\frac{2\mu}{a^2} \left[n(-(n-1) J_n(k_p a) + k_p a J_{n-1}(k_p a)) \right], \\ E_n^{34} &= -\frac{2\mu}{a^2} \left[(n^2 + n - \frac{1}{2} k_s^2 a^2) J_n(k_s a) - k_s a J_{n-1}(k_s a) \right], \\ E_n^{41} &= k\, H_n^{\prime(1)}(kb) \, + \, (\frac{\kappa}{2} - ik) H_n^{(1)}(kb), \\ E_n^{42} &= k\, H_n^{\prime(2)}(kb) \, + \, (\frac{\kappa}{2} - ik) H_n^{(2)}(kb) \end{aligned} \tag{1.2.15}$$

where κ is the curvature of Σ, that is, $\kappa = \frac{1}{b}$ as specified in [61]. We note that due the proposed ABC differs from the one used in [9, 60], and consequently, the corresponding entries in the matrix E_n^{41}, E_n^{42} differs from those defined in [9, 60].

The right-hand side $e_n(a) \in \mathbb{C}^4$ is given by

$$\begin{aligned} e_n^1 &= -\varepsilon_n i^n k J_n'(ka), \\ e_n^2 &= -\varepsilon_n i^n J_n(ka), \\ e_n^3 &= e_n^4 = 0, \end{aligned}$$

where $\varepsilon_0 = 1$ and $\varepsilon_n = 2$ for $n \geq 1$.

For the time being, we assume that E_n is invertible, we will address that question later on.

Remark: The exact solution to **BVP 0** can be derived similarly ignoring the effect of the exterior boundary. More specifically, the solution pair (p, u) is characterized by Eqs. 1.2.1-1.2.5 and coefficients obtained from the linear equation system $\hat{E_n}\hat{X_n} = \hat{e}_n$ for $\hat{E}_n = \left(E_n^{jl}\right)_{j=1,2,3;l=1,3,4}$, $\hat{X_n} = (A_n, C_n, D_n)$ and $\hat{e}_n = \left(e_n^j\right)_{j=1,2,3}$. Indeed, due to the computational limits of the problem, our main interest is focus on the problem set into the bounded domain **BVP 1** with the corresponding ABC. This is why the exact solution is derived for the truncated finite domain rather than the infinite domain.

1.3 Far-field Pattern

Since the fluid pressure solution to **BVP 0** is an outgoing solution of the Helmholtz equation in $\mathcal{R}^2 \setminus \Omega^s$, it has the asymptotic behavior of an outgoing spherical wave, characterized by (see [28])

$$p(x) = \frac{e^{ikr}}{\sqrt{r}}\left(p_\infty\left(\frac{1}{r}\right) + \mathcal{O}\left(\frac{x}{r}\right)\right) \qquad , \qquad r = \|x\|_2 \longrightarrow +\infty \tag{1.3.1}$$

where p_∞ is the so-called *far-field pattern* (FFP). It can be expressed using the representation on any closed curve $\hat{\Gamma}$ enclosing Ω^s, i.e. $\hat{\Gamma} \subset \overline{\mathcal{R}^2 \setminus \Omega^s}$,

$$p_\infty(\hat{x}) = \frac{e^{i\pi/4}}{\sqrt{8\pi k}} \int_{\hat{\Gamma}} \left(e^{-ik\hat{x}\cdot y}\frac{\partial p}{\partial \nu}(y) - \frac{\partial e^{-ik\hat{x}\cdot y}}{\partial \nu} p(y)\right) d\hat{\Gamma}, \quad \hat{x} \in C^1 \tag{1.3.2}$$

where C^1 denotes the unitary circle. The *true* 2D analytic far-field pattern p_∞ for p pressure field solution to **BVP 0** for the incident wave p^{inc} with $d = (1, 0)$ can be characterized as (see Appendix A derived from [28, 18, 40]):

$$p_\infty(\hat{x}) = \sum_n \sqrt{\frac{2}{k\pi}} \frac{e^{i\pi/4}}{i^{n+1}} A_n cos(n\theta) \quad \theta \in [0, 2\pi)\,, \tag{1.3.3}$$

for coefficients obtained from $\hat{E_n}\hat{X_n} = \hat{e}_n$. However, for **BVP 1**, we consider the definition given by Eq. 1.3.2 for the pressure field obtained from **BVP 1**, following the same criteria to compute the far field from the near field as in [40, 82]. In addition, the FFP can be defined on a smooth curve $\hat{\Gamma}$ outside of Ω^s or on the boundary of the obstacle Γ (that is, $\hat{\Gamma} = \Gamma$). Thus, using the transmission condition **BVP 1** (d), the corresponding FFP can be calculated as follows:

$$p_\infty(\hat{x}) = \frac{e^{i\pi/4}}{\sqrt{8\pi k}} \int_{\Gamma} \left(e^{-ik\hat{x}\cdot y}\left(\omega^2 \rho_f u \cdot \nu + \frac{\partial p^{inc}}{\partial \nu}\right) - \frac{\partial e^{-ik\hat{x}\cdot y}}{\partial \nu} p(y)\right) d\Gamma, \quad \hat{x} \in C^1. \tag{1.3.4}$$

Using Γ provides some computation facility, which involves zero-th order traces, and avoids having to calculate the conormal derivative of p on a new curve. Consequently, for the sake of simplicity, we generally compute the FFP from Γ (unless the boundary of the obstacle is particularly irregular).

1.4 Well Posedness Analysis

This paragraph aims at giving well-posedness results for a class of **BVP**s that will include the different problems considered in this manuscript. Hence, for convenience, we introduce the following generalized Boundary Value Problem **BVP** :

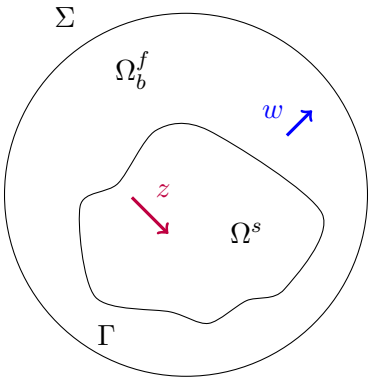

Fig. 1.4.1: Problem statement in finite domain

$$\textbf{(BVP)} \quad \begin{cases} \nabla \cdot \sigma(z) + \omega^2 \rho_s z = F & \text{in } \Omega^s \quad \text{(a)} \\ \Delta w + k^2 w = 0 & \text{in } \Omega_b^f \quad \text{(b)} \\ \sigma(z)\nu + w\nu = f & \text{on } \Gamma \quad \text{(c)} \\ \omega^2 \rho_f z \cdot \nu = \frac{\partial w}{\partial \nu} + g & \text{on } \Gamma \quad \text{(d)} \\ \frac{\partial w}{\partial \nu} = Bw & \text{on } \Sigma \quad \text{(e)} \end{cases} \tag{1.4.1}$$

where $Bw = (ik - \frac{\kappa}{2})w$, $F \in \left(L^2(\Omega^s)\right)^2$, $f \in (L^2(\Gamma))^2$ and $g \in L^2(\Gamma)$. It is worth mentioning that **BVP** includes the direct problem **BVP 1** with $F = 0$, $f = -p^{inc}\nu$ and $g = \frac{\partial p^{inc}}{\partial \nu}$. Besides we will see later on that it represents other **BVP**s that are involved in the solution of inverse problems under study.

In this section, following the guidelines of [10, 32], we address the question of the existence and uniqueness of **BVP**. Employing the Fredholm alternative [95] (we refer the reader to Appendix B to read the summarized Fredholm alternative), the existence of the solution is a consequence of the uniqueness, and therefore, it is sufficient to prove the uniqueness of the solution. The proof of the uniqueness requires the expression of a variational formulation that satisfies a Gårding's inequality.

We introduce the classical Hilbert space $W = H^1(\Omega_b^f)$. Hence, we define $\|\cdot\|_W$ as being the classical H^1-norm, that is, for $w \in H^1(\Omega_b^f)$, $\| w \|_W = (\| w \|_0^2 + \| \nabla w \|_0^2)^{1/2}$ where $\|\cdot\|_0^2 = (\int_{\Omega_b^f} |\cdot|^2 \, dx)^{1/2}$.

On the other hand, the displacement component z in the scatterer is sought in $Z = (H^1(\Omega^s))^2$. We then propose the functional space $\mathbf{H}$ for both fields which is the following product space:

$$\mathbf{H} = W \times Z = H^1(\Omega_b^f) \times (H^1(\Omega^s))^2. \tag{1.4.2}$$

The Hilbert space $\mathbf{H}$ is equipped with the standard graph norm,

$$\| (w, z) \|_{\mathbf{H}} = (\| w \|_W^2 + \| z \|_Z^2)^{1/2}. \tag{1.4.3}$$

1.4.1 Variational Formulation of BVP

We consider **BVP** set in the finite computational domain $\Omega_b^f \times \Omega^s$ and develops its associated variational formulation.

We assume that the interface Γ is regular, of class C^2. Let $F \in \left(L^2(\Omega^s)\right)^2$, $f \in (L^2(\Gamma))^2$ and $g \in L^2(\Gamma)$. The variational problem associated with **BVP** reads as follows:

$$\textbf{(VF)} \quad \begin{cases} \text{Find } (w, z) \in \mathbf{H}, \text{ such that} \\ \\ a((w, z), (q, v)) = l(q, v), \text{ for all } (q, v) \in \mathbf{H}, \end{cases} \tag{1.4.4}$$

where

$$\begin{cases} a((w, z), (q, v)) = \dfrac{1}{\omega^2 \rho_f} a^f(w, q) + a^s(z, v) + b((w, z), (q, v)) + b^*((w, z), (q, v)) + \dfrac{1}{\omega^2 \rho_f} c(w, q) & (1.4.5) \\ l(q, v) = l_1(q) + l_2(v) + l_3(v) & (1.4.6) \end{cases}$$

and

$$\begin{cases} a^f(w, q) = \displaystyle\int_{\Omega_b^f} \nabla w \cdot \nabla \bar{q} dx - \frac{\omega^2}{c_f^2} \int_{\Omega_b^f} w \bar{q} dx \\ a^s(z, v) = \displaystyle\int_{\Omega^s} \sigma(z) : \nabla \bar{v} dx - \omega^2 \rho_s \int_{\Omega^s} z \cdot \bar{v} dx \\ b((w, z), (q, v)) = \displaystyle\int_{\Gamma} z \cdot \nu \bar{q} d\gamma \\ b^*((w, z), (q, v)) = \overline{b((q, v), (w, z))} \qquad \text{adjoint of b} \\ c(w, q) = \displaystyle\int_{\Sigma} (\frac{\kappa}{2} - ik) w \bar{q} dx \\ l_1(v) = \displaystyle\int_{\Gamma} g \bar{q} d\gamma \\ l_2(v) = -\displaystyle\int_{\Omega^s} F \cdot \bar{v} dx \\ l_3(v) = \displaystyle\int_{\Gamma} f \cdot \bar{v} d\gamma \end{cases}$$

To get **VF**, we can formally apply the Green formula for test functions $(q, v) \in \mathcal{D}(\overline{\Omega}_b^f) \times (\mathcal{D}(\overline{\Omega}^s))^2$ assuming (w, z) satisfies **BVP** with suitable regularity. Then, 1.4.4 generalizes to $(q, v) \in \mathbf{H}$ by density and the following result establishes the correspondence between **BVP** and **VF**:

Theorem 1. *Let F, f, g be given respectively in $\left(L^2(\Omega^s)\right)^2$, $\left(L^2(\Gamma)\right)^2$, $L^2(\Gamma)$. $(w, z) \in \mathbf{H} = H^1(\Omega_b^f) \times (H^1(\Omega^s))^2$ is a solution of **BVP** if and only if (w, z) is a solution of **VF**.*

Proof.

(i) First we show that if (w, z) is a solution of the **BVP**, then $(w, z) \in \mathbf{H}$ is a solution to the variational problem **VF**.

Let us assume that **BVP** admits a solution (w, z) in **H**. Then, from **BVP** (a) and **BVP** (b) we have:

$$\int_{\Omega^s} \nabla \cdot \sigma(z) \cdot \bar{v} dx + \omega^2 \rho_s \int_{\Omega^s} z \cdot \bar{v} dx = \int_{\Omega^s} F \cdot \bar{v} dx, \tag{1.4.7}$$

$$\int_{\Omega_b^f} \Delta w \bar{q} dx + \frac{\omega^2}{c_f^2} \int_{\Omega_b^f} w \bar{q} dx = 0 \tag{1.4.8}$$

for any $(q, v) \in \mathbf{H}$. We have performed the integrations in L^2 because $z \in \left(H^1(\Omega^s)\right)^2 \subset \left(L^2(\Omega^s)\right)^2$, $F \in \left(L^2(\Omega^s)\right)^2$ together with **BVP** (a) implies that $\nabla \cdot \sigma(z) \in \left(L^2(\Omega^s)\right)^2$. In the same way, **BVP** (b) with $w \in H^1(\Omega_b^f) \subset L^2(\Omega_b^f)$ implies that $\Delta w \in L^2(\Omega_b^f)$. By this way, we are able to define $\sigma(z)\nu$ in $\left(H^{-1/2}(\Gamma)\right)^2$ and $\left.\frac{\partial w}{\partial \nu}\right|_\Gamma$ in $H^{-1/2}(\Gamma)$ thanks to standard trace regularity results in Lipschitz continuous domains (see [65] for instance). We can then apply the Green formula to both equations. For (1.4.7), we get:

$$\int_{\Omega^s} \sigma(z) : \nabla \bar{v} dx - \omega^2 \rho_s \int_{\Omega^s} z \bar{v} dx - \langle \sigma(z)\nu, v \rangle_{-\frac{1}{2}, \frac{1}{2}, \Gamma} = - \int_{\Omega^s} F \cdot \bar{v} dx \tag{1.4.9}$$

for any $v \in (\mathcal{D}(\overline{\Omega}^s))^2$.

Now, we want to use the transmission condition on Γ to remove the term $\sigma(z)\nu$. We have that $f \in \left(L^2(\Gamma)\right)^2$. Moreover, $w \in H^1(\Omega_b^f)$ implies that $w \mid_\Gamma \in H^{1/2}(\Gamma)$. When Γ is Lipschitz continuous, $\nu \in \left(L^\infty(\Gamma)\right)^2$ which implies that ν is a multiplier of $L^2(\Gamma)$. Hence $w\nu$ is defined in $\left(L^2(\Gamma)\right)^2$ and (1.4.9) gives:

$$\begin{aligned} \int_{\Omega^s} \sigma(z) : \nabla \bar{v} dx - \omega^2 \rho_s \int_{\Omega^s} z \bar{v} dx + \int_\Gamma w\nu \cdot \bar{v} d\gamma = \\ = - \int_{\Omega^s} F \cdot \bar{v} dx + \int_\Gamma f \cdot \bar{v} d\gamma. \end{aligned}$$

for any $v \in (\mathcal{D}(\overline{\Omega}^s))^2$. Next, applying the Green's Theorem to equation (1.4.8),

$$\int_{\Omega_b^f} \nabla w \cdot \nabla \bar{q} dx - \frac{\omega^2}{c_f^2} \int_{\Omega_b^f} w \bar{q} dx + \langle \frac{\partial w}{\partial \nu}, q \rangle_{-1/2,1/2,\Gamma} - \langle \frac{\partial w}{\partial \nu}, q \rangle_{-1/2,1/2,\Sigma} = 0 \qquad \forall q \in \mathcal{D}(\overline{\Omega}_b^f). \tag{1.4.10}$$

As previously, we use the transmission condition to remove $\left.\frac{\partial w}{\partial \nu}\right|_{\Gamma}$. We have $g \in L^2(\Gamma)$. Moreover, $z \in \left(H^1(\Omega^s)\right)^2$ implies that $z|_\Gamma \in \left(H^{1/2}(\Gamma)\right)^2$. When Γ is Lipschitz continuous, $\nu \in (L^\infty(\Gamma))^2$ which implies that ν is a multiplier of $\left(L^2(\Gamma)\right)^2$. Hence, $z \cdot \nu|_\Gamma \in L^2(\Gamma)$ and the transmission condition **BVP** (d) transforms the integral formulation (1.4.10) into

$$\int_{\Omega_b^f} \nabla w \cdot \nabla \bar{q} dx - \frac{\omega^2}{c_f^2} \int_{\Omega_b^f} w \bar{q} dx + \omega^2 \rho_s \int_\Gamma z \cdot \nu \bar{q} d\gamma - \langle \frac{\partial w}{\partial \nu}, q \rangle_{-1/2,1/2,\Sigma} = \int_\Gamma g \bar{q} d\gamma.$$

Moreover, the radiation boundary condition on Σ implies that $\left.\frac{\partial w}{\partial \nu}\right|_{\Sigma} \in L^2(\Sigma)$ at least since $w \in H^1(\Omega_b^f)$ and thus $\left(\frac{1}{2}\kappa - ik\right) w|_\Gamma \in L^2(\Sigma)$, κ being at least in $L^\infty(\Gamma)$. Hence we get:

$$\int_{\Omega_b^f} \nabla w \cdot \nabla \bar{q} dx - \frac{\omega^2}{c_f^2} \int_{\Omega_b^f} w \bar{q} dx + \omega^2 \rho_s \int_\Gamma z \cdot \nu \bar{q} d\gamma + \int_\Sigma (\frac{1}{2}\kappa w - ikw) \bar{q} d\Sigma = \int_\Gamma g \bar{q} d\gamma.$$

Since $\mathcal{D}(\overline{\Omega}_b^f) \times (\mathcal{D}(\overline{\Omega}^s))^2$ is dense into $H^1(\Omega_b^f) \times (H^1(\Omega^s))^2$, the problem can thus be rewritten as follows:

$$(\widetilde{VF}) \quad \begin{cases} \text{Find } (w,z) \in \mathbf{H}, \text{ such that} \\ a^f(w,q) + \omega^2 \rho_f b((w,z),(q,v)) + c(w,q) = l_1(q), & \forall q \in W, \\ a^s(z,v) + b^*((w,z),(q,v)) = l_2(v) + l_3(v) & \forall v \in Z, \end{cases}$$

Then, **VF** given by (1.4.4) is an immediate consequence of adding the equations of $(\widetilde{VF})$.

(ii) Conversely, we prove that if $(w,z) \in \mathbf{H}$ is a solution of the variational problem **VF**, then (w,z) is a solution of **BVP** . Indeed, let $(\varphi,\phi) \in \mathcal{D}(\Omega_b^f) \times (\mathcal{D}(\Omega^s))^2$. If $(\varphi,\phi) = (\varphi,0)$, then we have:

$$a^f(w,\varphi) = 0 \qquad \forall \varphi \in \mathcal{D}(\Omega_b^f). \tag{1.4.11}$$

Therefore, we obtain:

$$\int_{\Omega_b^f} \nabla w \cdot \nabla \bar{\varphi} dx - \frac{\omega^2}{c_f^2} \int_{\Omega_b^f} w \bar{\varphi} dx = 0 \qquad \forall \varphi \in \mathcal{D}(\Omega_b^f), \tag{1.4.12}$$

which can be rewritten as

$$\langle \Delta w + \frac{\omega^2}{c_f^2} w, \varphi \rangle = 0 \qquad \forall \varphi \in \mathcal{D}(\Omega_b^f). \tag{1.4.13}$$

Hence, we conclude that, in the distribution sense at least, w satisfies:

$$\Delta w + \frac{\omega^2}{c_f^2} w = 0 \qquad \text{in } \mathcal{D}'(\Omega_b^f). \tag{1.4.14}$$

Now, since $w \in L^2(\Omega_b^f)$, (1.4.14) is satisfied in $L^2(\Omega_b^f)$ which is a space of distributions. It implies that $\Delta w \in L^2(\Omega_b^f)$.

Equivalently, let $(\varphi, \phi) = (0, \phi)$. Since ϕ vanishes in the neighborhood of Γ, we have:

$$a^s(z, \phi) = l_1(\phi). \tag{1.4.15}$$

We thus have,

$$\int_{\Omega^s} \sigma(z) : \nabla\bar{\phi} dx - \omega^2 \rho_s \int_{\Omega^s} z\bar{\phi} dx = -\int_{\Omega^s} F\bar{\phi} dx \qquad \forall \phi \in (\mathcal{D}(\Omega^s))^2, \tag{1.4.16}$$

which can be rewritten as:

$$\langle \nabla \cdot \sigma(z) + \omega^2 \rho_s z, \phi \rangle = \langle F, \phi \rangle \qquad \forall \phi \in (\mathcal{D}(\Omega^s))^2. \tag{1.4.17}$$

We conclude that, z satisfies the following equation

$$\nabla \cdot \sigma(z) + \omega^2 \rho_s z = F \qquad \text{in } (\mathcal{D}'(\Omega^s))^2 \tag{1.4.18}$$

in the distribution sense. Moreover, since $F \in \left(L^2(\Omega^s)\right)^2$ and $z \in \left(L^2(\Omega^s)\right)^2$, (1.4.18) is satisfied in $\left(L^2(\Omega^s)\right)^2$ which implies that $\nabla \cdot \sigma(z) \left(L^2(\Omega^s)\right)^2$. As a consequence, we have obtained:

$$\Delta w + \frac{\omega^2}{c_f^2} w = 0 \qquad \text{in } \Omega_b^f, \tag{1.4.19}$$

$$\nabla \cdot \sigma(z) + \omega^2 \rho_s z = F \qquad \text{in } \Omega^s. \tag{1.4.20}$$

Now, we characterize w and z at the boundaries. Let $(\varphi, \phi) \in \mathcal{D}(\overline{\Omega}_b^f) \times (\mathcal{D}(\overline{\Omega}^s))^2$. We first select $\phi = 0$. Then,

$$a^f(w, \varphi) + \omega^2 \rho_f b((w, z), (\varphi, 0)) + c(p, \varphi) = l_3(\varphi), \tag{1.4.21}$$

that is:

$$\int_{\Omega_b^f} \nabla w \cdot \nabla\bar{\varphi} dx - \frac{\omega^2}{c_f^2} \int_{\Omega_b^f} w\bar{\varphi} dx + \omega^2 \rho_s \int_\Gamma z \cdot \nu\bar{\varphi} d\gamma + \int_\Sigma (\frac{1}{2}\kappa w - ikw)\bar{\varphi} dx = \int_\Gamma g\bar{\varphi} d\gamma. \tag{1.4.22}$$

We have that $w \in H^1(\Omega_b^f)$ and we have first established that $\Delta w \in L^2(\Omega_b^f)$. This allows us to give a sense to $\left.\frac{\partial w}{\partial \nu}\right|_\Gamma$ in $H^{-1/2}(\Gamma)$ and we can apply the Green formula:

$$\begin{aligned} &\int_{\Omega_b^f} \left(\Delta w + \frac{\omega^2}{c_f^2} w\right) \bar{\varphi} dx + \langle \frac{\partial w}{\partial \nu}, \varphi \rangle_{-\frac{1}{2},\frac{1}{2},\Gamma} - \langle \frac{\partial w}{\partial \nu}, \varphi \rangle_{-\frac{1}{2},\frac{1}{2},\Sigma} - \omega^2 \rho_s \int_\Gamma z \cdot \nu\bar{\varphi} d\gamma \\ &- \int_\Sigma (\frac{1}{2}\kappa w - ikw)\bar{q} dx = -\int_\Gamma g\bar{\varphi} d\gamma \qquad \forall \varphi \in \mathcal{D}(\overline{\Omega}_b^f). \end{aligned} \tag{1.4.23}$$

We then deduce from (1.4.19) that

$$\begin{aligned} &\langle \frac{\partial w}{\partial \nu}, \varphi \rangle_{-\frac{1}{2},\frac{1}{2},\Gamma} - \langle \frac{\partial w}{\partial \nu}, \varphi \rangle_{-\frac{1}{2},\frac{1}{2},\Sigma} - \omega^2 \rho_s \int_\Gamma z \cdot \nu\bar{\varphi} d\gamma - \int_\Sigma (\frac{1}{2}\kappa w - ikw)\bar{q} dx \\ &= -\int_\Gamma g\bar{\varphi} d\gamma \qquad \forall \varphi \in \mathcal{D}(\overline{\Omega}_b^f). \end{aligned} \tag{1.4.24}$$

Next, selecting φ that vanishes on Σ, we obtain the transmission conditions on the fluid-structure interface Γ:

$$\omega^2 \rho_f z \cdot \nu - \frac{\partial w}{\partial \nu} = g \qquad \text{in } \mathcal{D}'(\Gamma) \tag{1.4.25}$$

which makes sense in $L^2(\Gamma)$ since $g \in L^2(\Gamma)$ and $z \cdot \nu|_\Gamma \in L^2(\Gamma)$. On the other hand, for ϕ vanishing in a neighborhood of Γ, we obtain the boundary condition on Σ:

$$\frac{\partial w}{\partial \nu} + \frac{1}{2}\kappa w - ikw = 0 \qquad \text{in } \mathcal{D}'(\Sigma) \tag{1.4.26}$$

which makes sense in $L^2(\Gamma)$ since $(\frac{\kappa}{2} - ik)w|_\Gamma \in L^2(\Gamma)$. At the same time, for $\varphi = 0$, we have:

$$a^s(z, \phi) + b^*((w, z), (0, \phi)) = l_1(\phi) + l_2(\phi), \tag{1.4.27}$$

which equates: for any $\phi \in (\mathcal{D}(\overline{\Omega}^s))^2$

$$\int_{\Omega^s} \sigma(z) : \nabla \bar{\phi} dx - \omega^2 \rho_s \int_{\Omega^s} z \cdot \bar{\phi} dx + \int_\Gamma w\nu \cdot \bar{\phi} d\gamma = -\int_{\Omega^s} F \cdot \bar{\phi} dx + \int_\Gamma f \cdot \bar{\phi} d\gamma. \tag{1.4.28}$$

We have proven that $\nabla \cdot \sigma(z) \in (H(div, \Omega^s))^2$ where

$$H(div, \Omega^s) = \left\{ \Phi \in \left(L^2(\Omega^s)\right)^2, div\Phi \in L^2(\Omega^s) \right\}. \tag{1.4.29}$$

By this way, we are able to consider $\sigma(z)\nu|_\Gamma$ in $\left(H^{-1/2}(\Gamma)\right)^2$ (see [65]). We can thus integrate by parts (1.4.28), which gives:

$$\begin{aligned} &\int_{\Omega^s} \left(\nabla \cdot \sigma(z) + \omega^2 \rho_s z\right) \cdot \bar{\phi} dx - \langle \sigma(z)\nu, \phi \rangle_{-\frac{1}{2},\frac{1}{2},\Gamma} - \int_\Gamma w\nu \cdot \bar{\phi} d\gamma = \\ &= \int_{\Omega^s} F\bar{\phi} dx - \int_\Gamma f \cdot \bar{\phi} d\gamma \qquad \forall \phi \in (\mathcal{D}(\overline{\Omega}^s))^2. \end{aligned} \tag{1.4.30}$$

Using (1.4.20), we then deduce that:

$$-\langle \sigma(z)\nu, \phi \rangle_{-\frac{1}{2},\frac{1}{2},\Gamma} - \int_\Gamma w\nu \cdot \bar{\phi} d\gamma = -\int_\Gamma f \cdot \bar{\phi} d\gamma \qquad \forall \phi \in (\mathcal{D}(\overline{\Omega}^s))^2, \tag{1.4.31}$$

which implies the following expression:

$$\sigma(z)\nu + w\nu = f \qquad \text{in } (\mathcal{D}'(\Gamma))^2. \tag{1.4.32}$$

Then, since $f \in (L^2(\Gamma))^2$ and so does $w\nu_{|\Gamma}$, (1.4.32) is true in $(L^2(\Gamma))^2$ and we have that $\sigma(z)\nu_{|\Gamma} \in \left(L^2(\Gamma)\right)^2$.

Remark 1. *We have assumed that f belongs to $(L^2(\Gamma))^2$ and g belongs to $L^2(\Gamma)$ for convenience. Indeed, it allows us to write down the variational formulation from standard integrals set in L^2. Nevertheless, it is worth mentioning that Theorem 1 straightforwardly extends to data in $(H^{1/2}(\Gamma))^2$ and $H^{1/2}(\Gamma)$. In that case, the integrals involving f and g are replaced by duality brackets between $H^{-1/2}(\Gamma)$ and $H^{1/2}(\Gamma)$.*

1.4.2 Existence and Uniqueness

Now that we have established the equivalence between **BVP** and its variational formulation **VF**, the objective here is to use **VF** and the Fredholm alternative to establish existence and uniqueness results. The principle of Fredholm theory has been reminded in Apprendix B.

Let $\mathbf{U}$ be the following Hilbert space:

$$\mathbf{U} = L^2(\Omega_b^f) \times (L^2(\Omega^s))^3 \tag{1.4.33}$$

equipped with the standard graph norm. Then, from Rellich-Kondrachov theorem [2], we have: $\mathbf{H} \subset \mathbf{U} \subset \mathbf{H}'$, with dense and compact embedding $\mathbf{H} \subset\subset \mathbf{U}$.

According to Fredholm theory, we need to show that the sesquilinear form $a(\cdot,\cdot)$ given by (1.4.5) satisfies the Gårding's inequality and that it is continuous.

Proposition 1. *The sesquilinear form $a(\cdot,\cdot)$ defined by (1.4.5) satisfies a Gårding's inequality on $\mathbf{H}$, that is, there are two constants $C_{\mathbf{U}} \geq 0$ and $\alpha \geq 0$ such that:*

$$\Re[a((w,z),(w,z))] + C_{\mathbf{U}} \parallel (w,z) \parallel^2_{\mathbf{U}} \geq \alpha \parallel (w,z) \parallel^2_{\mathbf{H}}, \qquad \forall (w,z) \in \mathbf{H}. \tag{1.4.34}$$

Proof: Let $(w,z) \in \mathbf{H}$ be a solution to **VF**. The procedure continues for each form in $a(\cdot,\cdot)$ given by (1.4.5) separately as follows:
It follows from (1.4.1) that:

$$\begin{aligned} a^f(w,w) &= \int_{\Omega_b^f} \nabla w \cdot \nabla \bar{w} dx - \frac{\omega^2}{c_f^2} \int_{\Omega_b^f} w \bar{w} dx \\ &= \parallel \nabla w \parallel_0^2 - \frac{\omega^2}{c_f^2} \parallel w \parallel_0^2 . \end{aligned}$$

Then we have:

$$a^f(w,w) + \left(\frac{\omega^2}{c_f^2} + 1 \right) \parallel w \parallel_0^2 = \parallel w \parallel_W^2 \qquad \forall w \in W. \tag{1.4.35}$$

We see that $a^f(w,w)$ is real and that it satisfies a Gårding's inequality in W since we have (1.4.35).

We also have:

$$\begin{aligned} a^s(z,z) &= \int_{\Omega^s} \sigma(z) : \nabla \bar{z} dx - \omega^2 \rho_s \int_{\Omega^s} \mid z \mid^2 dx \\ &= \int_{\Omega^s} \sigma(z) : \varepsilon(\bar{z}) dx - \omega^2 \rho_s \int_{\Omega^s} \mid z \mid^2 dx \\ &= \int_{\Omega^s} \sum_{lm} \sum_{jn} C_{lmjn} \varepsilon_{jn}(z) \varepsilon_{lm}(\bar{z}) dx - \omega^2 \rho_s \int_{\Omega^s} \mid z \mid^2 dx. \end{aligned}$$

We remind that due to (1.1.4)(c) $a^s(z,z)$ is a real number. Then, according to 1.1.1,

$$\int_{\Omega^s} \sum_{lm} \sum_{jn} C_{lmjn} \varepsilon_{jn}(z) \varepsilon_{lm}(\bar{z}) dx - \omega^2 \rho_s \int_{\Omega^s} \mid z \mid^2 dx$$
$$\geq \alpha_\sigma \int_{\Omega^s} \varepsilon(z) : \varepsilon(\bar{z}) dx - \omega^2 \rho_s \int_{\Omega^s} \mid z \mid^2 dx.$$

We conclude that:

$$a^s(z,z) + \omega^2 \rho_s \parallel z \parallel_0^2 \geq \alpha_\sigma \parallel \varepsilon(z) \parallel_0^2 . \tag{1.4.36}$$

In addition, the second Korn's inequality [38] holds and ensures the existence of a constant $C_k > 0$ such that:

$$\parallel \varepsilon(z) \parallel_0^2 + \parallel z \parallel_0^2 \quad \geq \quad C_k \parallel z \parallel_Z^2 \qquad \forall z \in Z. \tag{1.4.37}$$

We thus have

$$a^s(z,z) + \omega^s \rho_s \parallel z \parallel_0^2 \quad \geq \alpha_\sigma \left(C_k \parallel z \parallel_Z^2 - \parallel z \parallel_0^2 \right).$$

Consequently, with $C_2 = \alpha_\sigma + \omega^s \rho_s$ and $\alpha_2 = \alpha_\sigma C_k$, we obtain:

$$a^s(z,z) + C_2 \parallel z \parallel_0^2 \geqslant \alpha_2 \parallel z \parallel_Z^2 \qquad \forall z \in Z, \tag{1.4.38}$$

which proves that $a^s(\cdot,\cdot)$ satisfies Gårding's inequality in Z.

Let us move on considering the terms $b\left((w,z),(w,z)\right) + b^*\left((w,z),(w,z)\right)$ that we will denote by $b + b^*$ for the sake of simplicity. By definition, we have

$$b + b^* = b + \bar{b} = 2\mathcal{R}[b]. \tag{1.4.39}$$

Hence,

$$b + b^* = 2\mathcal{R}\left[\int_\Gamma z \cdot \nu \bar{w} d\gamma \right]. \tag{1.4.40}$$

Now our purpose is to establish a Gårding inequality and since $b + b^*$ involves a term coupling z and w, there is no chance of giving a sign to that term. The only option that we have is to provide an estimate of $|b + b^*|$ that is depending on a parameter which can be adjusted to get a Gårding estimate. That is why we are going to use the fact that accroding to [38], for any $0 < \tau < 1$, for any $\delta > 0$, there exists a constant $C_\delta > 0$ such that for any $\varphi \in H^1(\Omega)$,

$$\parallel \varphi \parallel_{H^\tau(\Omega)}^2 \quad \leq \quad \delta |\varphi|_{H^1(\Omega)}^2 + C_\delta \parallel \varphi \parallel_0^2,$$

where $\Omega = \Omega^s$ or Ω_b^f and $|\varphi|_{H^1(\Omega)}^2 = \parallel \nabla \varphi \parallel_0^2$. In particular, for $\tau = 3/4$, we have

$$\parallel \varphi \parallel_{H^{3/4}(\Omega)}^2 \quad \leq \quad \delta |\varphi|_{H^1(\Omega)}^2 + C_\delta \parallel \varphi \parallel_0^2 . \tag{1.4.41}$$

Moreover, for Γ Lipschitz continuous, the trace mapping is linear continuous from $H^{3/4}(\Omega)$ into $H^{1/4}(\Gamma)$. This property allows us to develop the following estimates:

$$|b+b^*| = 2\left|\mathcal{R}\left[\int_\Gamma z\cdot\nu\bar{w}d\gamma\right]\right| \tag{1.4.42}$$

$$\leq 2 \parallel z \parallel_{(L^2(\Gamma))^2} \parallel w \parallel_{L^2(\Gamma)} \tag{1.4.43}$$

$$\leq 2C \parallel z \parallel_{(H^{1/4}(\Gamma))^2} \parallel w \parallel_{H^{1/4}(\Gamma)}, \tag{1.4.44}$$

where C denotes a constant representing the continuous embedding of $H^{1/4}(\Gamma)$ into $L^2(\Gamma)$. We thus have:

$$|b+b^*| \leq 2C^* \parallel z \parallel_{(H^{3/4}(\Omega^s))^2} \parallel w \parallel_{H^{3/4}(\Omega_b^f)}, \tag{1.4.45}$$

where C^* represents the continuity of the trace mapping in $H^{3/4}(\Omega)$. Now we use (1.4.41) combined with the standard inequality $2|ab| \leq a^2+b^2$ to finally get:

for any $\delta > 0$, there exists a constant C_δ^* such that

$$|b+b^*| \leq \delta \parallel (w,z) \parallel^2_{\mathbf{H}} + C_\delta^* \parallel (w,z) \parallel^2_{\mathbf{U}}, \tag{1.4.46}$$

where C_δ^* depends on C^* and C_δ.

As a conclusion, for any $\delta > 0$, there exists $C_\delta > 0$ such that

$$b+b^* \geq -\delta \parallel (w,z) \parallel^2_{\mathbf{H}} - C_\delta \parallel (w,z) \parallel^2_{\mathbf{U}} . \tag{1.4.47}$$

The last term that we have to consider is the one on the external boundary. It is defined as:

$$c(w,w) = \int_\Sigma \left(\frac{\kappa}{2} - ik\right)|w|^2 d\Sigma. \tag{1.4.48}$$

We thus observe that

$$\mathcal{R}\left[c(w,w)\right] = \int_\Sigma \frac{\kappa}{2}|w|^2 d\Sigma, \tag{1.4.49}$$

which shows that when Σ is a convex surface,

$$\mathcal{R}\left[c(w,w)\right] \geq 0. \tag{1.4.50}$$

In practice, we do use a convex external surface. So we have $\mathcal{R}\left[c(w,w)\right] \geq 0$ which means that we do not have to consider this term when dealing with the Gårding inequality.

As a conclusion, assuming that Σ is convex, we have:

$$\mathcal{R}\left[a\left((w,z),(w,z)\right)\right] = \mathcal{R}\left[\frac{1}{\omega^2\rho_f}a^f(w,w) + a^s(z,z) + b + b^* + \frac{1}{\omega^2 c_f^2}c(w,w)\right] \tag{1.4.51}$$

$$\geq \quad \frac{1}{\omega^2\rho_f}a^f(w,w) + a^s(z,z) + 2\mathcal{R}[b], \tag{1.4.52}$$

which implies, according to (1.4.35), (1.4.38) and (1.4.47),

$$\mathcal{R}\left[a\left((w,z),(w,z)\right)\right] \geq -\left(\frac{1}{\omega^2 c_f^2}+1\right) \parallel w \parallel_0^2 + \frac{1}{\omega^2\rho_f} \parallel w \parallel_W^2 - C_2 \parallel z \parallel_0^2 + \alpha_2 \parallel z \parallel_Z^2 - \delta \parallel (w,z) \parallel_{\mathbf{H}}^2 - C_\delta \parallel (w,z) \parallel_{\mathbf{U}}^2 .$$

To conclude, it remains to choose $\delta > 0$ such that

$$\frac{1}{\omega^2\rho_f} \parallel w \parallel_W^2 + \alpha_2 \parallel z \parallel_Z^2 - \delta \parallel (w,z) \parallel_{\mathbf{H}}^2 \geq C \parallel (w,z) \parallel_{\mathbf{H}}^2 . \tag{1.4.53}$$

For that purpose, $\delta = 2\max\left(\frac{1}{\omega^2\rho_f}, \alpha_2\right)$ works.

We have thus established that providing Σ is convex, the bilinear form a satisfies a Gårding inequality which complets the proof of Proposition 1. □

Let's see the continuity of the sesquilinear form $a(\cdot,\cdot)$ given by (1.4.5) and the linear form $l(\cdot,\cdot)$ given by (1.4.6) .

Proposition 2. *The sesquilinear form $a(\cdot,\cdot)$ given by (1.4.5) is continuous in $\mathbf{H}\times\mathbf{H}$, that is, there exists a positive constant C_a such that,*

$$\mid a\left((w,z),(q,v)\right) \mid \leq C_a \parallel (w,z) \parallel_{\mathbf{H}} \parallel (q,v) \parallel_{\mathbf{H}}, \qquad \forall (w,z) \in \forall (q,v) \in \mathbf{H}. \tag{1.4.54}$$

Moreover, the form $l(\cdot,\cdot)$ given by (1.4.6) is a linear form continuous on $\mathbf{H}$:

there exists a positive constant c_l such that for any $(q,v)\in\mathbf{H}$, $\mid l(q,v) \mid \leq c_l \parallel (q,v) \parallel_{\mathbf{H}}$

Proof:

Let $((w,z),(q,v)) \in \mathbf{H}$. Each term in $a(\cdot,\cdot)$ defined in (1.4.5) can be bounded separately as follows. On the one hand, we have:

$$\begin{aligned}
\mid a^f(w,q) \mid &= \mid \int_{\Omega_b^f} \nabla w \cdot \nabla \bar{q} dx - \frac{\omega^2}{c_f^2} \int_{\Omega_b^f} w \bar{q} dx \mid \\
&\leq \mid \int_{\Omega_b^f} \nabla w \cdot \nabla \bar{q} dx \mid + \frac{\omega^2}{c_f^2} \mid \int_{\Omega_b^f} w \bar{q} dx \mid \\
&\leq \parallel \nabla w \parallel_0 \parallel \nabla q \parallel_0 + \frac{\omega^2}{c_f^2} \parallel w \parallel_0 \parallel q \parallel_0 \\
&\leq \max\left(1, \frac{\omega^2}{c_f^2}\right)\left(\parallel \nabla w \parallel_0 + \parallel w \parallel_0\right)\left(\parallel \nabla q \parallel_0 + \parallel q \parallel_0\right) \\
&\leq 2\max\left(1, \frac{\omega^2}{c_f^2}\right) \parallel w \parallel_W \parallel q \parallel_W .
\end{aligned}$$

We select

$$C_1 = 2\max\left(1, \frac{\omega^2}{c_f^2}\right). \tag{1.4.55}$$

Then, we conclude that:

$$\mid a^f(p,q) \mid \leq C_1 \parallel w \parallel_W \parallel q \parallel_W \tag{1.4.56}$$

proving the continuity of $a^f(w,q)$ on $W \times W$.

On the other hand, we have:

$$\begin{aligned} \mid a^s(z,v) \mid &= \mid \int_{\Omega^s} \sigma(z) : \nabla \bar{v} dx - \omega^2 \rho_s \int_{\Omega^s} z \bar{v} dx \mid \\ &\leq \mid \int_{\Omega^s} \sigma(z) : \nabla \bar{v} dx \mid + \omega^2 \rho_s \mid \int_{\Omega^s} z \bar{v} dx \mid \\ &\leq \mid \int_{\Omega^s} \sigma(z) : \nabla \bar{v} dx \mid + \omega^2 \rho_s \parallel z \parallel_0 \parallel v \parallel_0 . \end{aligned} \tag{1.4.57}$$

At the same time, the Hooke's law relates the stress tensor σ to the strain tensor ε as follows:

$$\sigma_{jl} = C_{jlmn} \varepsilon_{mn}, \tag{1.4.58}$$

Supposing that $C_{lmjn} \in L^\infty(\Omega^s)$, we denote by $C_\sigma = sup_{jlmn} |C_{jlmn}|$. From (1.4.58) we have that:

$$\begin{aligned} \mid \int_{\Omega^s} \sigma(z) : \nabla \bar{v} dx \mid &= \mid \int_{\Omega^s} \sum_{lm} \left(\sum_{jn} C_{lmjn} \varepsilon_{jn}(z) \right) \nabla \bar{v} dx \mid \\ &\leq C_\sigma \mid \int_{\Omega^s} \sum_{lm} \left(\sum_{jn} \varepsilon_{jn}(z) \right) \nabla \bar{v} dx \mid \\ &\leq 9 C_\sigma \parallel \varepsilon(z) \parallel_0 \parallel \nabla \bar{v} \parallel_0 . \end{aligned} \tag{1.4.59}$$

Replacing (1.4.59) into (1.4.57), the property $\parallel \varepsilon(z) \parallel_0 \leq \parallel \nabla z \parallel_0$, leads to:

$$\begin{aligned} \mid a^s(z,v) \mid &\leq 9 C_\sigma \parallel \nabla z \parallel_0 \parallel \nabla v \parallel_0 + \omega^2 \rho_s \parallel z \parallel_0 \parallel v \parallel_0 \\ &\leq 2\text{max } (9C_\sigma, \omega \rho_s) \parallel z \parallel_Z \parallel v \parallel_Z . \end{aligned}$$

We select

$$C_2 = 2\text{max } (9C_\sigma, \omega \rho_s). \tag{1.4.60}$$

Consequently,

$$\mid a^s(z,v) \mid C_2 \parallel z \parallel_Z \parallel v \parallel_Z, \tag{1.4.61}$$

which proves the continuity of $a^s(z,v)$ on $Z \times Z$.

Moreover, using the continuity of the trace mappings from $H^1(\Omega_b^f)$ into $L^2(\Gamma)$, and from $(H^1(\Omega_b^f))^2$ into $(L^2(\Gamma))^2$ respectively, we get that:

$$\begin{aligned} \mid b((w,z),(q,v)) \mid &= \mid \int_\Gamma z \cdot \nu \bar{q} d\sigma \mid \\ &\leq \parallel z \cdot \nu \parallel_{L^2(\Gamma)} \parallel q \parallel_{L^2(\Gamma)} \\ &\leq \parallel z \parallel_{(L^2(\Gamma))^3} \parallel q \parallel_{L^2(\Gamma)} \\ &\leq C \parallel z \parallel_Z \parallel q \parallel_W \\ &\leq C (\parallel w \parallel_W^2 + \parallel z \parallel_Z^2)^{1/2} (\parallel q \parallel_W^2 + \parallel v \parallel_Z^2)^{1/2} \end{aligned}$$

for some positive constant C. Therefore, there exists $C_b > 0$ such that

$$| b((w,z),(q,v)) | \leq C_b \parallel (w,z) \parallel_{\mathbf{H}} \parallel (q,v) \parallel_{\mathbf{H}}, \qquad \forall (w,z),(q,v) \in \mathbf{H} \tag{1.4.62}$$

which proves the continuity of $b(\cdot,\cdot)$ on $\mathbf{H} \times \mathbf{H}$.

Finally, from the radiation condition we obtain:

$$\begin{aligned} | c(w,q) | &= | \int_{\Sigma} (\frac{\kappa}{2} - ik) w \bar{q} dx | \\ &\leq \parallel \frac{\kappa}{2} \parallel_{L^\infty} \parallel w \parallel_{L^2(\Sigma)} \parallel q \parallel_{L^2(\Sigma)} + k \parallel w \parallel_{L^2(\Sigma)} \parallel q \parallel_{L^2(\Sigma)} \\ &\leq C \left(\parallel \frac{\kappa}{2} \parallel_{L^\infty} + k \right) \parallel w \parallel_W \parallel q \parallel_W . \end{aligned}$$

If we choose

$$C_R = C \left(\max \left(\parallel \frac{\kappa}{2} \parallel_{L^\infty} : \kappa > 0 \right) + k \right), \tag{1.4.63}$$

we obtain,

$$| c(w,q) | \leq C_R \parallel w \parallel_W \parallel q \parallel_W, \tag{1.4.64}$$

proving the continuity of $c(\cdot,\cdot)$ on $\mathbf{H}$.

As a conclusion, from (1.4.56)-(1.4.61)-(1.4.62) and (1.4.64) we have that :

$$\begin{aligned} | a((w,z),(q,v)) | &\leq \frac{1}{\omega^2 \rho_f} C_1 \parallel w \parallel_W \parallel q \parallel_W + C_2 \parallel w \parallel_W \parallel q \parallel_W \\ &+ 2C_b \parallel (w,z) \parallel_{\mathbf{H}} \parallel (q,v) \parallel_{\mathbf{H}} + \frac{1}{\omega^2 \rho_f} C_R \parallel w \parallel_W \parallel q \parallel_W \\ &\leq \max \left(\frac{1}{\omega^2 \rho_f} (C_1 + C_R), C_2 \right) (\parallel w \parallel_W + \parallel z \parallel_Z)(\parallel q \parallel_W + \parallel v \parallel_W) \\ &+ 2C_b \parallel (w,z) \parallel_{\mathbf{H}} \parallel (q,v) \parallel_{\mathbf{H}} \\ &\leq 2\max \left(\frac{1}{\omega^2 \rho_f} (C_1 + C_R), C_2 \right) (\parallel w \parallel_W^2 + \parallel z \parallel_Z^2)^{1/2} (\parallel q \parallel_W^2 + \parallel v \parallel_W^2)^{1/2} \\ &+ 2C_b \parallel (w,z) \parallel_{\mathbf{H}} \parallel (q,v) \parallel_{\mathbf{H}} . \end{aligned}$$

Then we introduce

$$C_a = 2 \left(\max \left(\frac{1}{\omega^2 \rho_f} (C_1 + C_R), C_2 \right) + C_b \right) \tag{1.4.65}$$

and we get

$$| a((w,z),(q,v)) | \leq C_a \parallel (w,z) \parallel_{\mathbf{H}} \parallel (q,v) \parallel_{\mathbf{H}}, \tag{1.4.66}$$

proving the continuity of the sesquilinear form $a(\cdot,\cdot)$.

On the other hand, the continuity of the linear form $l(\cdot,\cdot)$ given by (1.4.6) is a consequence of employing the Cauchy-Schwarz inequality.

$$\begin{aligned}
\mid l(q,v) \mid &= \mid l_1(q) + l_2(v) \mid + l_3(v) \mid \leq \mid l_1(q) \mid + \mid l_2(v) \mid + \mid l_3(v) \mid \\
&= \mid \int_\Gamma g\bar{q} d\gamma \mid + \mid \int_{\Omega^s} F \cdot \bar{v} dx \mid + \mid \int_\Gamma f \cdot \bar{v} d\gamma \mid + \leq \\
&\leq \| g \|_{L^2(\Gamma)} \| q \|_{L^2(\Gamma)} + \| F \|_{(L^2(\Omega^s))^2} \| v \|_{(L^2(\Omega^s))^2} + \| f \|_{(L^2(\Gamma))^2} \| v \|_{(L^2(\Gamma))^2} \\
&\leq C \left(\| g \|_W \| q \|_W + \| F \|_Z \| v \|_Z + \| f \|_Z \| v \|_Z \right). \qquad (1.4.67)
\end{aligned}$$

If we note

$$c_l = C \left(\| g \|_W + \| F \|_Z + \| f \|_Z \right), \qquad (1.4.68)$$

then,

$$\mid l(q,v) \mid \leq c_l \| \left(\| q \|_W^2 + \| v \|_Z^2 \right)^{1/2} = \| (q,v) \|_{\mathbf{H}} \qquad \forall (q,v) \in \mathbf{H}, \qquad (1.4.69)$$

which proves the continuity of the linear form $l(.)$. □

Remark 2. *As stated by Luke and Martin in [78, 53], for certain geometries and certain frequencies, there exist some nontrivial solutions to the homogeneous transmission problem. Specifically, there is an infinite set of free vibrations ω_n of the solid, with corresponding displacement modes of vibration, u_n, that satisfy $\tau(u_n) = 0$ on the boundary Γ. If moreover some of these frequencies u_n are such that $u_n \cdot \nu = 0$ on Γ, such nontrivial solutions u_n are called Jones modes and the associated frequencies ω_n are the so-called Jones frequencies.*

We are now in a position to prove the well-posedness of **BVP**.

Theorem 2. *Let us assume that Γ is Lipschitz continuous and that Σ is convex. For any $F \in \left(L^2(\Omega^s)\right)^2$, $f \in (L^2(\Gamma))^2$ and $g \in L^2(\Gamma)$ **VF** admits a solution in the space $\mathbf{H} = H^1(\Omega_b^f) \times (H^1(\Omega^s))^2$. This solution is unique modulo Jones resonance frequencies defined in the elastic scatterer.*

Proof: Applying the Fredholm alternative allows to reduce the study to establish the uniqueness of the solution only.

We assume the existence of two solutions of the fluid-structure variational problem, **BVP** denoted by (p_1, u_1) and (p_2, u_2).

We introduce:

$$w = w_1 - w_2, \qquad z = z_1 - z_2. \qquad (1.4.70)$$

As a consequence, the pair (w, z) satisfies **BVP** with $f, g = 0$ and $F = 0$, and thus satisfies the homogeneous equation:

$$a((w,z),(w,z)) = 0, \qquad (1.4.71)$$

in other words,

$$\frac{1}{\omega^2 \rho_f} a^f(w,w) + a^s(z,z) + b((w,z),(w,z)) + b^*((w,z),(w,z)) + \frac{1}{\omega^2 \rho_f} c(w,w) = 0. \qquad (1.4.72)$$

The bilinear forms $a^s(z,z)$ and $a^f(w,w)$ are real, and we have

$$\Im \left[b((w,z),(w,z)) + b^*((w,z),(w,z)) \right] = 0. \qquad (1.4.73)$$

Consequently, we obtain

$$\Im\left[a((w,z),(w,z))\right] = \Im\left[c(w,w)\right] = -ik\int_{\Sigma} \mid w \mid^2 d\Sigma = 0. \tag{1.4.74}$$

Therefore,

$$w = 0 \qquad \text{on} \quad \Sigma. \tag{1.4.75}$$

On the other hand, we have

$$\frac{\partial w}{\partial \nu} - ikw + \frac{\kappa}{2}w = 0 \qquad \text{on} \quad \Sigma, \tag{1.4.76}$$

which implies that

$$\frac{\partial w}{\partial \nu} = 0 \qquad \text{on} \quad \Sigma. \tag{1.4.77}$$

Applying the analytic continuation principle [33], we have:

$$w = 0 \qquad \text{in} \quad \Omega_b^f, \tag{1.4.78}$$

which proves the uniqueness of the pressure velocity. □

Let (w,z) be the field given by (1.4.70). We know that:

$$\frac{\partial w}{\partial \nu} = 0 \qquad \text{on} \quad \Gamma. \tag{1.4.79}$$

Replacing (1.4.79) in the transmission conditions on the interface Γ (see (1.1.5) in Chapter 1), we have:

$$z\cdot\nu = 0 \qquad \text{and} \qquad \tau(z) = 0 \qquad \text{on} \quad \Gamma. \tag{1.4.80}$$

Consequently, the displacement field u is traction-free and tangent to the boundary. Then, these two homogeneous boundary equations, together with the homogeneous elastodynamic equation, do not necessarily imply that u vanishes in Ω^s.

As a conclusion, the solution (w,z) to **BVP** exists and it is unique modulo Jones frequencies. We will go back later on to this question. It turns out [53, 78] that Jones modes do exist for particular geometries including the disk and the ball. The good news is that in realistic situation, Jones modes do not exist and thus, there is no risk to have polluted numerical simulations.

Corollary 1. *Regarding the direct problem **BVP 1**, it corresponds to the case where $F = 0, f = -p^{inc}\nu$ and $g = \frac{\partial p^{inc}}{\partial \nu}$. Then, we have:*

*For any $p^{inc} \in H^1(\Gamma)$, **BVP 1** admits a solution (p,u) in $H^1(\Omega_b^f) \times H^1(\Omega^s)$. The solution is unique modulo Jones resonance frequencies.*

1.5 The IPDG-method

In order to compute the numerical solution of **BVP** , we have decided to use the Interior Penalty Discontinuous Galerkin Method (IPDG), as it is proposed in [9]. The use of Finite Element Method allows to model accurately the interface between the fluid and the solid, thanks to a triangular mesh with curved elements. Moreover, the use of discontinuous Galerkin techniques is very convenient to deal with *hp*-adaptivity and with parallel computing. Among all existing DG methods, we have chosen to consider the IPDG because it is one of the most accurate and stable [6, 7]. We refer to article [9] for a performance analysis of IPDG for elasto-acoustic problems.

Nomenclature and Assumptions

We adopt the following nomenclature and assumptions:

- $x = (x_1, x_2)$ is a point of $\mathbb{R}^2$ and $\| x \|_2$ is the distance from the origin point to x.
- $C^1 = \{x \in \mathbb{R}^2 \| x \|_2 = 1\}$ is the unitary circle in $\mathbb{R}^2$.
- d$\in C^1$ is a unit vector representing the direction of the incident planewave.
- M^* denotes the adjoint matrix of M, which is defined as the complex conjugate transpose of M.
- $\mathcal{K}_h^f$ and $\mathcal{K}_h^s$ are mesh partitions of the domains Ω^f and Ω^s respectively, composed of triangles K. $\mathcal{K}_h = \mathcal{K}_h^f \cup \mathcal{K}_h^s$ represents the total partition of the computational domain.
- For each element $K \in \mathcal{K}_h$, h_K represents the diameter of K, $h = \min_K h_K$, and d_K represents the diameter of the inscribed circle in K. We assume that there exists a constant $C \gg 1$ such that [25]
$$\frac{h_K}{d_K} \ll C, \qquad \forall h, \quad \forall K \in \mathcal{K}_h. \tag{1.5.1}$$
This condition prevents the presence of skinny triangles.
- $\mathbb{P}_m(K)$ designates the space of polynomial functions defined on K and of degree at most $m \gg 1$.
- The finite element approximation spaces for the pressure and the structural displacement solutions in the fluid and solid media are respectively given by
$$V_h^f = \{q \in L^2(\Omega^f) : q_{|K} \in \mathbb{P}_{m_K}(K), \forall K \in \mathcal{K}_h^f\}, \tag{1.5.2}$$
$$V_h^s = \{v \in \left(L^2(\Omega^s)\right)^2 : v_{|K} \in \left(\mathbb{P}_{m_K}(K)\right)^2, \forall K \in \mathcal{K}_h^s\}. \tag{1.5.3}$$
Hence, we consider functions that are piecewise polynomials in each element and whose degrees are less than or equal to m. However, unlike standard finite elements, such functions are not continuous over the all computational domain $\Omega^s \cup \Omega^f$. They are only L^2.
- $H^l(\mathcal{K}_h^f) = \{q \in L^2(\Omega^f) : q_{|K} \in H^l(K)\}$, $l \in \mathbb{N}$. Hence, $V_h^f \subseteq H^l(\mathcal{K}_h^f)$. Similarly, $\left(H^l(\mathcal{K}_h^s)\right)^2$ is the space for the vectorial displacement field in the solid.
- ε^f and ε^s denote the sets of all edges in $\mathcal{K}_h^f$ and $\mathcal{K}_h^s$. $\varepsilon_{h,R}^f$ is the set of edges on the exterior boundary Σ, and $\varepsilon_{h,tr}^{f,s}$ corresponds to the set of edges on the fluid-structure interface Γ. $\varepsilon_{h,int}^f$ and $\varepsilon_{h,int}^s$ represent the sets of internal edges in $\mathcal{K}_h^f$ and $\mathcal{K}_h^s$ such that $\varepsilon_{h,int}^f \cap \left(\varepsilon_{h,R}^f \cup \varepsilon_{h,tr}^{f,s}\right) = \emptyset$ and $\varepsilon_{h,int}^s \cup \varepsilon_{h,tr}^{f,s} = \emptyset$. It is worth mentioning that the boundary edges on the fluid-solid interface Γ and the exterior fluid surface $\varepsilon_{h,R}^f$ are curved and not straight boundary edges.
- Note that an edge e in $\varepsilon_{h,int}^f, \varepsilon_{h,int}^s$, or $\varepsilon_{h,tr}^{f,s}$ is shared by two elements denoted arbitrarily by K^+ and K^-, that is, $e = \partial K^+ \cap \partial K^-$.
- The unit normal vectors to K^+ and K^-, outwardly directed to their respective exterior, are denoted ν^+ and ν^-.
- For $e \in \varepsilon_{h,int}^f \cup \varepsilon_{h,int}^s$, we set $d_e = \frac{1}{2} min\{d_{K^+}, d_{K^-}\}$.
- For any $q \in H^1(K_h^f)$ and $K \in K_h^f$, we can define $q_{|\partial K}$. Then considering K^+ and K^- sharing a common edge, we can define $q^+ = q_{|\partial K^+}$, $q^- = q_{|\partial K^-}$ and $q\pm \in L^2(\partial K^\pm)$.

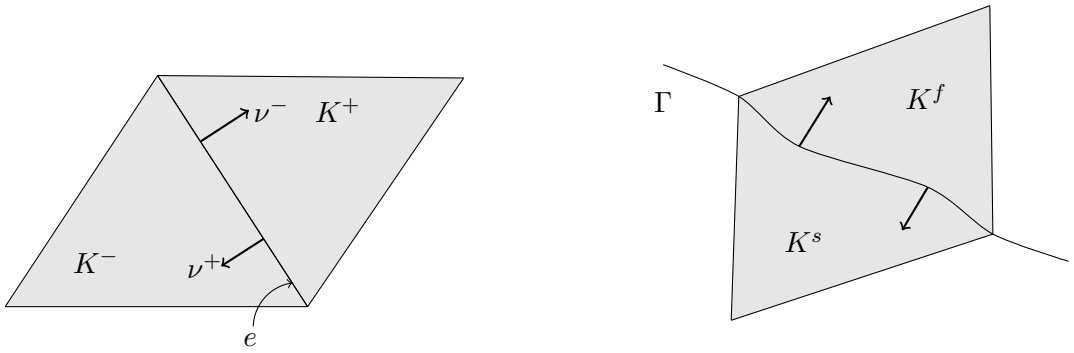

(a) Straight boundary edge for interior triangles

(b) Curved boundary edge for triangles at the fluid-structure interface

Fig. 1.5.1: Unit normal vectors for straight and curved boundary edges.

- The jump and average of $\phi \in V_h^f$ through an edge are defined by

$$[\phi] = \phi^+\nu^+ + \phi^-\nu^- \qquad \text{and} \qquad \{\phi\} = \frac{\phi^+ + \phi^-}{2} \qquad \text{on} \qquad \partial K^+ \cap \partial K^-, \tag{1.5.4}$$

while for $\phi \in (V_h^f)^2 \cup V_h^s$, we define

$$[\phi] = \phi^+ \cdot \nu^+ + \phi^- \cdot \nu^- \qquad \text{and} \qquad \{\phi\} = \frac{\phi^+ + \phi^-}{2} \qquad \text{on} \qquad \partial K^+ \cap \partial K^-. \tag{1.5.5}$$

At the same time, the jump and average of $\psi \in V_h^s$ through an edge are determined by

$$[[\psi]] = \psi^+ \otimes \nu^+ + \psi^- \otimes \nu^- \qquad \text{and} \qquad \{\psi\} = \frac{\psi^+ + \psi^-}{2} \qquad \text{on} \qquad \partial K^+ \cap \partial K^-, \tag{1.5.6}$$

where $\otimes$ denotes the tensor product defined as:

$$v \otimes w = v^T w = \begin{bmatrix} v_x w_x & v_x w_y \\ v_y w_x & v_y w_y \end{bmatrix}.$$

While for $\psi \in (V_h^s)^2$,

$$[\psi] = \psi^+\nu^+ + \psi^-\nu^- \qquad \text{and} \qquad \{\psi\} = \frac{\psi^+ + \psi^-}{2} \qquad \text{on} \qquad \partial K^+ \cap \partial K^-. \tag{1.5.7}$$

Note that for an edge on the exterior boundary $\phi \in V_h^f$, they are reduced to

$$[\phi] = \phi^+\nu^+ \qquad \text{and} \qquad \{\phi\} = \phi \qquad \text{on} \qquad \partial K^+ \cap \Sigma, \tag{1.5.8}$$

or for similarly, for $\phi \in (V_h^f)^2$,

$$[\phi] = \phi^+ \cdot \nu^+ \qquad \text{and} \qquad \{\phi\} = \phi \qquad \text{on} \qquad \partial K^+ \cap \Sigma. \tag{1.5.9}$$

1.5.1 Discrete Variational Formulation

Next, we formulate variational formulation corresponding to **BVP**. First of all, we derive the variational forms of the Navier and Helmholtz (a)-(b) in **BVP** multiplying by the corresponding pair of test functions $v_h \in V_h^s, q_h \in V_h^f$, integrating over the corresponding elements K and summing as follows:

$$\sum_{K\in K_h^s}\left(\int_K \nabla\cdot\sigma(z)\cdot\bar{v_h}dx+\omega^2\rho_s\int_K z\cdot\bar{v_h}dx\right)=\sum_{K\in K_h^s}\left(\int_K F\cdot\bar{v_h}dx\right) \tag{1.5.10}$$

$$\sum_{K\in K_h^f}\left(\int_K \Delta w\bar{q_h}dx+\frac{\omega^2}{c_f^2}\int_K w\bar{q_h}dx\right)=0. \tag{1.5.11}$$

The use of Green formula on each triangle K in the elastic domain Ω^s leads to:

$$\begin{aligned}&\sum_{K\in K_h^s}\left(\int_K \sigma(z):\nabla\bar{v_h}dx-\omega^2\rho_s\int_K z\cdot\bar{v_h}dx\right)\\&-\sum_{e\in\varepsilon_{h,int}^s}\left(\int_e(\sigma(z)^+\nu^+)\cdot\bar{v_h}^+ +(\sigma(z)^-\nu^-)\cdot\bar{v_h}^- ds\right)\\&-\sum_{e\in\varepsilon_{h,tr}^{f,s}}\left(\int_e(\sigma(z)\nu^+)\cdot\bar{v_h}ds\right)=-\sum_{K\in K_h^s}\left(\int_K F\cdot\bar{v_h}dx\right).\end{aligned} \tag{1.5.12}$$

On each internal edge, we have:

$$(\sigma(z)^+\nu^+)\cdot\bar{v_h}^+ +(\sigma(z)^-\nu^-)\cdot\bar{v_h}^- =(\sigma(z)^+\bar{v_h}^+)\cdot\nu^+ +(\sigma(z)^-\bar{v_h}^-)\cdot\nu^- =[\sigma(z)\bar{v_h}] \tag{1.5.13}$$

Then, substituting 1.5.13 and the transmission condition of the **BVP** (c) into (1.5.12), we obtain:

$$\begin{aligned}&\sum_{K\in K_h^s}\left(\int_K \sigma(z):\nabla\bar{v_h}dx-\omega^2\rho_s\int_K z\cdot\bar{v_h}dx\right)\\&-\sum_{e\in\varepsilon_{h,int}^s}\left(\int_e[\sigma(z)\bar{v_h}]\,ds\right)\\&+\sum_{e\in\varepsilon_{h,tr}^{f,s}}\left(\int_e w\nu^+\cdot\bar{v_h}ds\right)=-\sum_{K\in K_h^s}\left(\int_K F\cdot\bar{v_h}dx\right)-\sum_{e\in\varepsilon_{h,tr}^{f,s}}\left(\int_e f\cdot\bar{v_h}ds\right).\end{aligned} \tag{1.5.14}$$

Furthermore, using the definition of the mean and the jump, we obtain

$$[\sigma(z)\bar{v_h}]=[\sigma(z)]\cdot\{\bar{v_h}\}+\{\sigma(z)\}:[[\bar{v_h}]]. \tag{1.5.15}$$

As z is a solution to **BVP**, the stress tensor $\sigma(z)$ satisfies on each internal edge:

$$[\sigma(z)]=0. \tag{1.5.16}$$

Straightaway, we rewrite the expression given by (1.5.15):

$$[\sigma(z)\bar{v_h}]=\{\sigma(z)\}:[[\bar{v_h}]]. \tag{1.5.17}$$

This term is not hermitian. However, due to the fact that z is solution to **BVP**, we have:

$$[[z]] = 0, \tag{1.5.18}$$

on each internal edge. Then, we can write:

$$[\sigma(z)\bar{v_h}] = \{\sigma(z)\} : [[\bar{v_h}]] + \{\sigma(\bar{v_h})\} : [[z]]. \tag{1.5.19}$$

Consequently, substituting (1.5.19) in (1.5.14), we obtain:

$$\begin{aligned}
&\sum_{K\in K_h^s}\left(\int_K \sigma(z) : \nabla\bar{v_h}dx - \omega^2\rho_s\int_K z\cdot\bar{v_h}dx\right)\\
&-\sum_{e\in\varepsilon_{h,int}^s}\left(\int_e \{\sigma(z)\} : [[\bar{v_h}]] + \{\sigma(\bar{v_h})\} : [[z]]ds\right)\\
&+\sum_{e\in\varepsilon_{h,tr}^{f,s}}\left(\int_e (w\nu^+)\cdot\bar{v_h}ds\right) = -\sum_{K\in K_h^s}\left(\int_K F\cdot\bar{v_h}dx\right) - \sum_{e\in\varepsilon_{h,tr}^{f,s}}\left(\int_e f\cdot\bar{v_h}ds\right).
\end{aligned} \tag{1.5.20}$$

Similarly, employing the Green's theorem on the fluid domain and using (d)(e) of **BVP** corresponding to the transmission and absorbing boundary conditions respectively, we get:

$$\begin{aligned}
&\sum_{K\in K_h^f}\left(\int_K \frac{1}{\rho_f}\nabla w\cdot\nabla\bar{q_h}dx - \frac{1}{\rho_f}\frac{\omega^2}{c_f^2}\int_K w\bar{q_h}dx\right)\\
&-\sum_{e\in\varepsilon_{h,int}^f}\left(\int_e\left[\frac{1}{\rho_f}\nabla w\bar{q_h}\right]ds\right)\\
&+\sum_{e\in\varepsilon_{h,tr}^{f,s}}\left(\int_e \omega^2 z\cdot\nu^+\bar{q_h}ds\right) - \sum_{e\in\varepsilon_{h,R}^f}\left(\int_e \frac{1}{\rho_f}(ik-\frac{\kappa}{2})w\bar{q_h}ds\right) =\\
&\sum_{e\in\varepsilon_{h,int}^f}\int_e \frac{1}{\rho_f}g\bar{q_h}^+ds.
\end{aligned} \tag{1.5.21}$$

Moreover, using the definition of the mean and the jump, we obtain:

$$\left[\frac{1}{\rho_f}\nabla w\bar{q_h}\right] = \left[\frac{1}{\rho_f}\nabla w\right]\{\bar{q_h}\} + \left\{\frac{1}{\rho_f}\nabla w\right\}\cdot[\bar{q_h}]. \tag{1.5.22}$$

As w is solution to **BVP** , it satisfies in each internal edge:

$$\left[\frac{1}{\rho_f}\nabla w\right] = 0, \tag{1.5.23}$$

so that we can write:

$$\left[\frac{1}{\rho_f}\nabla w\bar{q_h}\right] = \left\{\frac{1}{\rho_f}\nabla w\right\}\cdot[\bar{q_h}]. \tag{1.5.24}$$

Once again, this term is not hermitian, but since w is solution to **BVP** , we have in all internal edges:

$$[w] = 0, \tag{1.5.25}$$

and (1.5.24) can be written as

$$\left[\frac{1}{\rho_f}\nabla w\bar{q_h}\right] = \left\{\frac{1}{\rho_f}\nabla w\right\}\cdot[\bar{q_h}] + \left\{\frac{1}{\rho_f}\nabla\bar{q_h}\right\}\cdot[w]. \tag{1.5.26}$$

Replacing (1.5.26) in (1.5.21), we obtain:

$$\begin{aligned}
&\sum_{K\in K_h^f}\left(\int_K\frac{1}{\rho_f}\nabla w\cdot\nabla\bar{q_h}dx - \frac{1}{\rho_f}\frac{\omega^2}{c_f^2}\int_K w\bar{q_h}dx\right)\\
&-\sum_{e\in\varepsilon_{h,int}^f}\left(\int_e\left(\left\{\frac{1}{\rho_f}\nabla w\right\}\cdot[\bar{q_h}] + \left\{\frac{1}{\rho_f}\nabla\bar{q_h}\right\}\cdot[w]\right)ds\right)\\
&+\sum_{e\in\varepsilon_{h,tr}^{f,s}}\left(\int_e\omega^2 z\cdot\nu^+\bar{q_h}ds\right) - \sum_{e\in\varepsilon_{h,R}^f}\left(\int_e\frac{1}{\rho_f}(ik-\frac{\kappa}{2})w\bar{q_h}ds\right) =\\
&\sum_{e\in\varepsilon_{h,int}^f}\int_e\frac{1}{\rho_f}g\bar{q_h}^+ds.
\end{aligned} \tag{1.5.27}$$

Finally, to ensure the coercivity and therefore the stability of the bilinear form of the IPDG, we add the following positive penalty terms, one in each domain:

$$\frac{\gamma_f c_{max}^f}{d_e}[w]\cdot[\bar{q_h}] \qquad \text{and} \qquad \frac{\gamma_s c_{max}^s}{d_e}[[z]] : [[\bar{v_h}]], \tag{1.5.28}$$

where

- For $e\in\varepsilon_{h,int}^f\cup\varepsilon_{h,int}^s$, we set $d_e = \frac{1}{2}min\{d_{K^+}, d_{K^-}\}$,
- γ_f and γ_s are two penalty terms that depend on the polynomial order, and have been exhaustively studied in [40],
- $c_{max}^f = \max(\frac{1}{\rho_f^+}, \frac{1}{\rho_f^-})$,
- $c_{max}^s = \max(c_{K^+}, c_{K^-})$, where $c_{K^+} = \max\limits_{ijkl} \mid c_{ijkl} \mid$.

Given all these rearrangements, we introduce the IPDG as the following variational formulation derived from the **BVP** :

$$\begin{cases}
\text{Find } (w_h, z_h)\in V_h^f\times V_h^s \text{ such that}\\
\\
a_h^f(w_h,q_h) + b_h((w_h,z_h),(q_h,v_h)) + c_h(w_h,q_h) = f_1(q_h), \qquad \forall(q_h,v_h)\in V_h^f\times V_h^s\\
\\
a_h^s(z_h,v_h) + b_h^*((w_h,z_h),(q_h,v_h)) = f_2(v_h) + f_3(v_h),
\end{cases} \tag{1.5.29}$$

where a_h^f and a_h^s are two sesquilinear hermitian forms described by:

$$\begin{aligned} a_h^s(z_h, v_h) = & \sum_{K \in K_h^s} \left(\int_K \sigma(z_h) : \nabla \bar{v_h} dx - \omega^2 \rho_s \int_K z_h \cdot \bar{v_h} dx \right) \\ & - \sum_{e \in \varepsilon_{h,int}^s} \left(\int_e \{\sigma(z_h)\} : [[\bar{v_h}]] + \{\sigma(\bar{v_h})\} : [[z_h]] ds \right) \\ & + \sum_{e \in \varepsilon_{h,int}^f} \frac{\gamma_s c_{max}^s}{d_e} \int_e [[z_h]] : [[\bar{v_h}]] ds, \end{aligned} \tag{1.5.30}$$

$$\begin{aligned} a_h^f(w_h, q_h) = & \sum_{K \in K_h^f} \frac{1}{\omega^2} \left(\int_K \frac{1}{\rho_f} \nabla w_h \cdot \nabla \bar{q_h} dx - \frac{1}{\rho_f} \frac{\omega^2}{c_f^2} \int_K w_h \bar{q_h} dx \right) \\ & - \sum_{e \in \varepsilon_{h,int}^f} \frac{1}{\omega^2} \left(\int_e \left\{ \frac{1}{\rho_f} \nabla w_h \right\} \cdot [\bar{q_h}] + \left\{ \frac{1}{\rho_f} \nabla \bar{q_h} \right\} \cdot [w_h] ds \right) \\ & + \sum_{e \in \varepsilon_{h,int}^s} \frac{\gamma_f c_{max}^f}{\omega^2 d_e} \int_e [w_h] \cdot [\bar{q_h}] \, ds, \end{aligned} \tag{1.5.31}$$

and, b_h and c_h are two sesquilinear forms defined as follows:

$$b_h((w_h, z_h), (q_h, v_h)) = \sum_{e \in \varepsilon_{h,tr}^{f,s}} \int_e z_h \cdot \nu \bar{q_h} ds, \tag{1.5.32}$$

$$c_h(w_h, q_h) = - \sum_{e \in \varepsilon_{h,R}^f} \frac{1}{\omega^2} \int_e \frac{1}{\rho_f} (ik - \frac{\kappa}{2}) w_h \bar{q_h} ds. \tag{1.5.33}$$

Finally, we describe the linear forms given by:

$$f_1(q_h) = \sum_{e \in \varepsilon_{h,tr}^{f,s}} \int_e \frac{1}{\omega^2 \rho_f} g \bar{q_h} ds, \tag{1.5.34}$$

$$f_2(v_h) = - \sum_{K \in K_h^s} \int_K F \cdot \bar{v_h} dx. \tag{1.5.35}$$

$$f_3(v_h) = - \sum_{e \in \varepsilon_{h,tr}^{f,s}} \int_e f \cdot \bar{v_h} ds, \tag{1.5.36}$$

In summary, the three first integrals in a_h^s and in a_h^f result from the application of the Green formula while taking into account the jump across the interior element edges. Observe that the sesquilinear forms a_h^f and a_h^s are hermitian, a property that does not change when adding a continuity constraint on the jumps. Moreover, the stability of both local variational forms is enforced by adding interior penalty terms giving rise to the two penalty parameters γ_f and γ_s in the fluid and solid parts respectively. Consequently, as the resulting bilinear system is coercive and consistent, we have for any (p, u) solution to **BVP 1** and for all $(q_h, v_h) \in V_h^f \times V_h^s$ that

$$\begin{cases} a_h^f(p, q_h) = a^f(p, q_h) \\ a_h^s(u, v_h) = a^s(u, v_h). \end{cases} \tag{1.5.37}$$

1.5.2 Basis of the Discrete Spaces

In this section, we introduce a basis of the spaces V_h^f and V_h^s defined in (1.5.2) and (1.5.3). They are constructed element by element from the definition of the basis on the reference element $\hat{K}$ that is the triangle $\{(0,0),(0,1),(1,0)\}$. We denote by N_{tri}^f and N_{tri}^s the number of elements in the fluid and in the solid media respectively, and by N_{tri} the local number of elements in the mesh ($N_{tri} = N_{tri}^f + N_{tri}^s$).

Let $\mathbb{P}_m(\hat{K})$ denote the space of polynomial functions of degree at most m on the reference element $\hat{K}$. The dimension of this space is $\dim(\mathbb{P}_m(\hat{K})) = \frac{1}{2}(m+2)(m+1)$ which we denote by n_m. We consider here the classical Lagrange basis functions

$$(\hat{\varphi}_i^m)_{i=1,\dots,n_m}\,. \tag{1.5.38}$$

The associated degrees of freedom $\left(\hat{P}_i^m\right)_{i=1,\dots,n_m}$ are equireparted on the reference element $\hat{K}$. They are represented in Figure (1.5.2) for $m = 1,2,3,4$, and quantified in Table (1.5.1). The Lagrange basis functions are such that $\hat{\varphi}_i^m\left(\hat{P}_j^m\right) = \delta_{ij} \qquad \forall i,j = 1,\dots,n_m$.

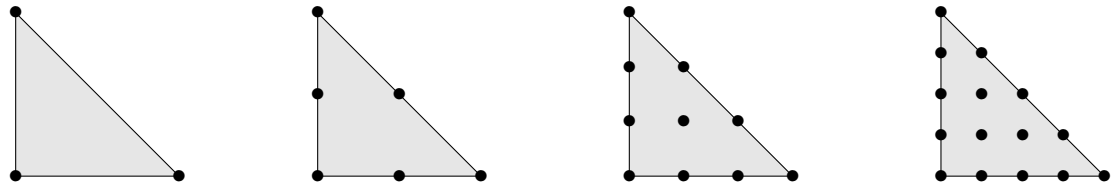

(a) $\mathbb{P}_1$ (b) $\mathbb{P}_2$ (c) $\mathbb{P}_3$ (d) $\mathbb{P}_4$

Fig. 1.5.2: Location of the degrees of freedom in 2D for four interpolation orders.

Interpolation order	$\mathbb{P}_1$	$\mathbb{P}_2$	$\mathbb{P}_3$	$\mathbb{P}_4$	$\mathbb{P}_5$
Ndof by Triangle	3	6	10	15	21
Ndof by Edge	2	3	4	5	6

Tab. 1.5.1: Number of degrees of freedom per element as a function of the interpolation degree.

Now, let m_K be the polynomial degree of the approximation on the element K. For a given triangle $K_l \in \mathcal{K}_h^f$, we consider the linear function

$$\begin{aligned} F_{K_l}:\quad & \mathbb{R}^2 \longmapsto \mathbb{R}^2 \\ & \hat{K} \hookrightarrow F_{K_l}(\hat{K}) = K_l. \end{aligned} \tag{1.5.39}$$

The basis functions of $\mathbb{P}_{m_{K_l}}(K_l)$ are defined by

$$\varphi_i^{K_l}(x) = \begin{cases} \hat{\varphi}_i{}^{m_{K_l}} \circ F_{K_l}^{-1}(x) & x \in K_l \\ 0 & x \notin K_l \end{cases} \tag{1.5.40}$$

and the degrees of freedom are defined by $P_j^{K_l} = F_{K_l}(\hat{P}_j{}^m)$.

Consequently, any function $q_h \in V_h^f$ can be expressed as follows:

$$q_h(x) = \sum_{l=1}^{N_{tri}^f} \sum_{i=1}^{m_{K_l}} q_i^{K_l^f} \varphi_i^{K_l^f}(x), \tag{1.5.41}$$

and the dimension of V_h^f is

$$N_{dof}^f = \dim(V_h^f) = \sum_{l=1}^{N_{tri}^f} n_{m_{K_l}} = \sum_{l=1}^{N_{tri}^f} \frac{1}{2}(m_{K_l}+2)(m_{K_l}+1). \tag{1.5.42}$$

We define a basis of V_h^s similarly. We denote by (e_x, e_y) the canonical basis in $\mathbb{R}^2$ and we set for any K_l in $\mathcal{K}_l^s$:

$$\psi_i^{K_l}(x) = \begin{cases} \left(\hat{\varphi}_i^{m_{K_l}} \circ F_{K_l}^{-1}\right) e_x & x \in K_l \\ 0 & x \notin K_l \end{cases} \qquad \text{for } i = 1, ..., m_{K_l}. \tag{1.5.43}$$

$$\psi_i^{K_l}(x) = \begin{cases} \left(\hat{\varphi}_{i-m_{K_l}}^{m_{K_l}} \circ F_{K_l}^{-1}\right) e_y & x \in K_l \\ 0 & x \notin K_l \end{cases} \qquad \text{for } i = m_{K_l}+1, ..., 2m_{K_l}. \tag{1.5.44}$$

and any function $v_h \in V_h^s$ can be expanded under the following expression:

$$v_h(x) = \sum_{l=1}^{N_{tri}^s} \sum_{j=1}^{2m_{K_l}} v_j^{K_l} \psi_j^{K_l}(x) \tag{1.5.45}$$

and the total number of degrees of freedom is

$$N_{dof}^s = \dim(V_h^s) = \sum_{l=1}^{N_{tri}^s} 2n_{m_{K_l}} = \sum_{l=1}^{N_{tri}^s} (m_{K_l}+2)(m_{K_l}+1). \tag{1.5.46}$$

We conclude that the discretization of the basis spaces V_h^f and V_h^s consist of $\sum_{l=1}^{N_{tri}^f} \frac{1}{2}(m_{K_l}+2)(m_{K_l}+1)$ and $\sum_{l=1}^{N_{tri}^s} (m_{K_l}+2)(m_{K_l}+1)$ degrees of freedom respectively.

1.5.3 Algebraic Formulation

Since the basis of discrete spaces have been introduced, we are now in a position to develop the algebraic expression of the variational formulation (1.5.29). Then, the IPDG formulation of **BVP** can be writen as:

$$\begin{pmatrix} A^f & B \\ B^* & A^s \end{pmatrix} \begin{pmatrix} W \\ Z \end{pmatrix} = \begin{pmatrix} F_1 \\ F_2 \end{pmatrix}$$

where the unknown vector W and Z are given by:

$$\begin{cases} W &= \left(\left(w_i^{K_l^f} \right)_{i=1...m_{K_l^f}} \right)_{K_l^f=1,...,N_{tri}^f} \\ Z &= \left(\left(z_i^{K_l^s} \right)_{i=1...m_{K_l^s}} \right)_{K_l^s=1,...,N_{tri}^s} \end{cases}$$

and

$$A^f = \left(\left(A_{ij}^{f,K_l K_l'} \right)_{1\le i,j\le m_{K_l^f}} \right)_{1\le K_l,K_l'\le N_{tri}^f}, \tag{1.5.47}$$

$$A^s = \left(\left(A_{ij}^{s,K_l K_l'} \right)_{1\le i,j\le m_{K_l^s}} \right)_{1\le K_l,K_l'\le 2N_{tri}^s}, \tag{1.5.48}$$

$$B = \left(\left(B_{ij}^{f,s,K_l K_l'} \right)_{1\le i\le m_{K_l^s},1\le j\le m_{K_l^s}} \right)_{1\le K_l\le 2N_{tri}^s,1\le K_l'\le N_{tri}^f} \tag{1.5.49}$$

$$F_1 = \left(\left(F_{1,j}^{f,K_l} \right)_{1\le j\le m_{K_l^f}} \right)_{1\le K_l\le N_{tri}^f} \tag{1.5.50}$$

$$F_2 = \left(\left(F_{2,j}^{s,K_l} \right)_{1\le j\le m_{K_l^s}} \right)_{1\le K_l\le 2N_{tri}^s} \tag{1.5.51}$$

where

$$\begin{aligned} A_{ij}^{f,K_l K_l'} = & \sum_{K\in K_h^f} \frac{1}{\omega^2} \int_K \frac{1}{\rho_f} \nabla\varphi_i^{K_l} \cdot \nabla\varphi_j^{K_l'} dx - \frac{1}{\rho_f}\frac{\omega^2}{c_f^2} \int_K \varphi_i^{K_l}\varphi_j^{K_l'} dx \\ & - \sum_{e\in\varepsilon_{h,int}^f} \frac{1}{\omega^2} \int_e \left(\left\{ \frac{1}{\rho_f} \nabla\varphi_i^{K_l} \right\} [\varphi_j^{K_l'}] + \left\{ \frac{1}{\rho_f} \nabla\varphi_j^{K_l'} \right\} \cdot [\varphi_i^{K_l}] \right) ds \\ & - \sum_{e\in\varepsilon_{h,R}^f} \frac{1}{\omega^2} \int_e \frac{1}{\rho_f} (ik - \frac{\kappa}{2}) \varphi_i^{K_l}\varphi_j^{K_l'} ds \end{aligned} \tag{1.5.52}$$

$$\begin{aligned} A_{ij}^{s,K_l K_l'} = & \sum_{K\in K_h^s} \int_K \sigma\left(\psi_i^{K_l}\right) : \nabla\psi_j^{K_l'} dx - \omega^2\rho_s \int_K \psi_i^{K_l} \cdot \psi_j^{K_l'} dx \\ & - \sum_{e\in\varepsilon_{h,int}^s} \int_e \left(\{\sigma(\psi_i^{K_l})\} \cdot [\psi_j^{K_l'}] + \left\{ \sigma(\psi_j^{K_l'}) \right\} \left[\psi_i^{K_l} \right] \right) ds \end{aligned} \tag{1.5.53}$$

$$B_{ij}^{K_l K_l'} = \sum_{e\in\varepsilon_{h,tr}^{f,s}} \int_e \psi_i^{K_l} \cdot \nu\varphi_j^{K_l'} ds \tag{1.5.54}$$

$$F_{1,j}^{K_l} = \sum_{e\in\varepsilon_{h,tr}^{f,s}} \int_e \frac{1}{\omega^2\rho_f} g\varphi_j^{K_l} ds \tag{1.5.55}$$

$$F_{2,j}^{K_l} = -\sum_{K\in K_h^s} \int_e F\cdot\psi_j^{K_l} ds - \sum_{e\in\varepsilon_{h,tr}^{f,s}} \int_e f\cdot\psi_j^{K_l} ds \tag{1.5.56}$$

Remark 3. *In order to have control of the accuracy of the solution, it is necessary to prove that the proposed IPDG method is stable (hence well-posed) without any mesh constraint. In [43] a rigorous stability and error analysis of the IPDG has been carried out for the Helmholtz equation, while a posteriori error estimates of IPDG method for Navier equations have been developed in [54, 55]. Unfortunately, we have not found any error analysis that studies the stability of the coupled systems Navier and Helmholts equations. An a priori error of DG approximation of coupled Navier-Stokes and Darcy Equations have been studied in [44], which can be a good reference with the other papers to study the stability of the IPDG for the proposed transmission problem.*

1.5.4 The Computational Complexity

Finally, in order to express the computational complexity corresponding to the algebraic formulation, we assume that the polynomial order is constant on each triangle, that is, $m_K = m$, and we remind that the total number of unknowns is equal to $n_m \times (N_{tri}^f + 2N_{tri}^s)$, where n_m is the dimension of the space of polynomial functions as we have seen in subsection 1.5.2.

Let K_l and K_l' be two elements in the fluid domain. Then, $A^{f,K_l,K_l'}$ is non zero only if $K_l = K_l'$ or K_l' is a neighbor of K_l. The size of the corresponding sub-matrix is m^2. Similarly, let K_l and K_l' be two elements in the solid domain. Then, $A^{s,K_l,K_l'}$ is non zero only if $K_l = K_l'$ or K_l' is a neighbor of K_l, and the size of the corresponding sub-matrix is $4m^2$. Now, let K_l be in the fluid domain and K_l' in the solid domain. $B^{f,s,K_l,K_l'}$ is non zero if K_l' is a neighbor of K_l, and in this case, the size of the block is $2m^2$.

This means that due to the fact that each triangle K_l has at most three neighbors, it is enough to store four blocks of size $m \times m$ for the elements that are in the fluid, four blocks of size $4 \times m \times m$ for the elements in the solid and four blocks of size $2m^2$ for elements of the interface. Consequently, in the global matrix there are at most $4 \times m^2 \times (N_{tri}^f + 4N_{tri}^s + 2)$ nonzero entries. This global matrix is factorized by the open source program MUMPS [3]. The upper-part of the corresponding sparse matrix with symmetric structure is illustrated in Figure 1.5.3. The corresponding mesh is composed of 48 triangles in the fluid part and 18 triangles in the solid part. This Figure 1.5.3 and more detailed explanations can be found in [40].

e (m)	# points		# elements		Total # dof	# nonzero terms
	Γ	Σ	N_h^s in Ω^s	N_h^f in Ω^f		
$h = \dfrac{\lambda}{N}$	$\dfrac{2\pi a}{h}$	$\dfrac{2\pi b}{h}$	$\dfrac{2\pi a^2}{h^2}$	$\dfrac{2\pi(b^2-a^2)}{h^2}$	$m\left(\dfrac{2\pi(b^2+a^2)}{h^2}\right)$	$2m^2\left(\dfrac{2\pi(b^2+a^2)}{h^2}\right)$

Tab. 1.5.2: Computational Complexity of IPDG for the disk-shaped domain, for N the number of elements per wavelength λ.

1.5.5 Illustrative Numerical Results

The main goal of this section is to asses the accuracy of the numerical solution pair (p, u) to the transmission problem **BVP 1**. To this end we perform some comparisons between the analytical and numerical values of pressure and displacement field expressions. We first illustrate -for validation purpose- similar results to [9] (they differ slightly as the ABC is different), and then, the comparison between analytical FFPs corresponding to **BVP 0** and **BVP 1** respectively.

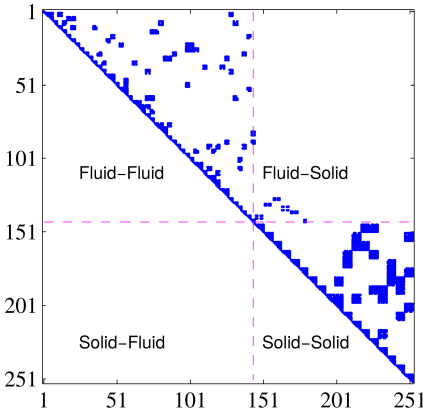

Fig. 1.5.3: Sparse global matrix.

Numerical settings We consider a *steel* infinite cylinder immersed in water. The axis of the cylinder follows the z-axis direction, and the plane wave follows the positive x-axis direction. The symmetric geometry of the cylinder permit to reduce the problem to a 2D scattering problem in the (x, y)-plane. Then, the computational domain is an elastic circle Ω^s of radius $a = 1$cm embedded in a water circular field of radius $b = 7.5$cm that truncates the physical infinite domain [60, 9]. The spatial part of the time-harmonic planewave of frequency $\omega/2\pi$ propagating in this medium is $p^{inc}(x) = e^{i\frac{\omega}{c_f}x\cdot d}$. The density of the water is $\rho_f = 1000$ kg m^{-3}, and the Lamé coefficients of the *steel* $\lambda = 115.40$ GPa and $\mu = 76.9$ GPa with the density $\rho_s = 7900$ kg m^{-3}. The speed of sound on water is $c_f = 1500\ m\ s^{-1}$, and the range of the frequency $4 \leq ka \leq 15$, where $k = \frac{\omega}{c_f}$, for $\omega = 2\pi f$.

Numerical quantities The numerical quantities (p^{num}, u^{num}) are computed by the IPDG solver associated to the variational formulation previously described, with interior penalty terms γ_f, γ_s detailed in [40]. The mesh discretization is determined by the number of discretization points of $\lceil\frac{2\pi a}{h}\rceil$ and $\lceil\frac{2\pi b}{h}\rceil$ on the interface Γ and the boundary Σ respectively. The latter quantity h is controlled by the angular frequency ω and by the number of points per wavelength N_λ as $h = \frac{2\pi c_f}{\omega N_f}$. The numeric FFP p_∞^{num} is computed applying the FFP characterization defined in Eq. 1.3.4 to p^{num}.

Analytical quantities For comparison purpose, we recall that the truncated version of the true analytic series described with Eqs. 1.2.1-1.2.5. The truncated analytical pressure field is computed as follows

$$p^{ana} = \sum_{n=0}^{N} \Big[A_n\, H_n^{(1)}(kr) + B_n\, H_n^{(2)}(kr)\Big]\, cos(n\theta), \qquad a \leq r \leq b \tag{1.5.57}$$

for $\theta \in [0, 2\pi)$ together with the displacement field

$$u^{ana} = \nabla\phi + (-e_z) \times \nabla\psi, \quad \phi = \sum_{n=0}^{N} [C_n\, J_n(k_p r)]\, cos(n\theta), \quad \psi = \sum_{n=0}^{N} [D_n J_n(k_s r)]\, sin(n\theta),$$

with the sum of $N = 2\lceil kb\rceil + 1$ modes [9]. The computation of the coefficients $X_n = (A_n, B_n, C_n, D_n)$ require the resolution of the linear system $E_n\, X_n = e_n$ for each mode n (see Eq. 1.2.14). The corresponding analytic FFP is computed applying the FFP characterization defined in Eq. 1.3.4 to p^{ana}.

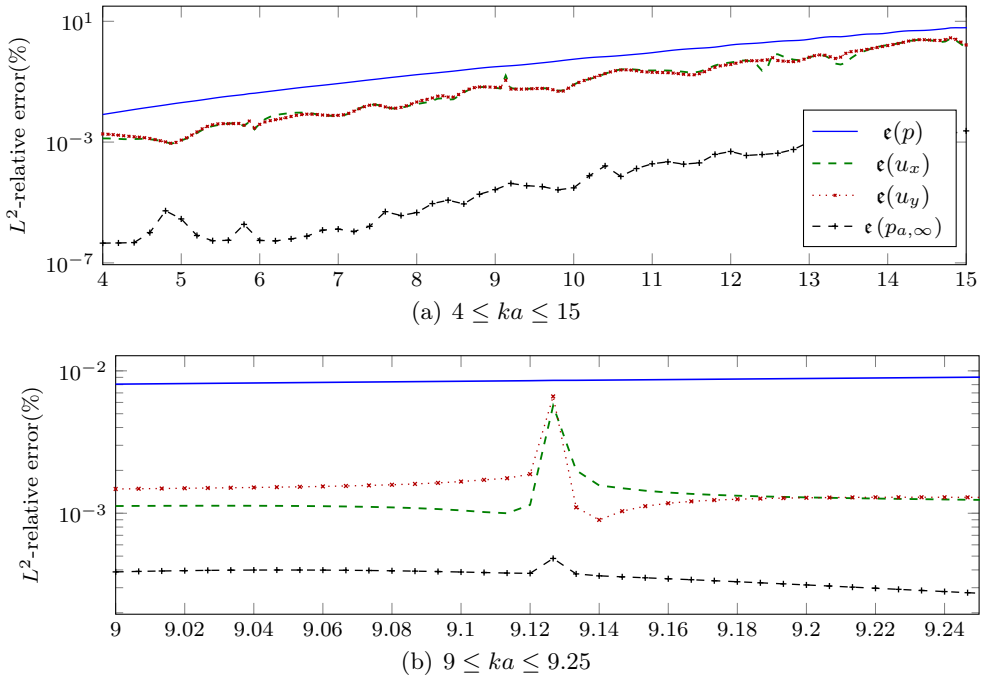

Fig. 1.5.4: Comparison between the analytical and numerical values for fluid pressure, solid displacement and FFP. Numerical experiments are performed with IPDG method with $\mathbb{P}_3$ order elements, curved-boundary elements, fixed mesh discretized with $\lambda_f = 0,015807$ and $N_\lambda = 7$.

In order to quantify our results, we define the following generalized L^2-relative error operator:

$$\mathfrak{e}(g) = \frac{\| g^{ana} - g^{num} \|_2}{\| g^{ana} \|_2} \times 100$$

for $g = p,\ u_x,\ u_y]$ and $|\ p_\infty\ |$. The following outcomes are worthwhile mentioning:

In Figure 1.5.4 we have tried to reproduce similar results illustrated in [9] for the frequency range $4 \leq ka \leq 15$. An unique mesh has been employed for this experiments, determined by the mesh discretization parameter h corresponding to the lower angular frequency (that is, $\omega = 0.6$ rad s^{-1}). The selection of a fixed mesh, $\mathbb{P}_3$ order elements and curved boundary elements lead to reproduce the relative errors around 10^{-3} observed in [9], despite the different ABC. Indeed, the step-size selected for 1.5.4(a) is $\delta_{ka} = 0.067$, which is not sufficient to reproduce the same accuracy illustrated in [9]. However, this accuracy is obtained refining the step-size of the frequency with $\delta_{ka} = 0.0067$, as illustrated in Fig. 1.5.4(b).

On the contrary, updating the mesh for each frequency with the corresponding control parameter h, employing $\mathbb{P}_5$ order elements and curved boundary elements lead to more stable error as illustrated in in Fig. 1.5.5. In this case, we observe that the errors $\mathfrak{e}(p), \mathfrak{e}(u_x), \mathfrak{e}(u_y)$ and $\mathfrak{e}(p_\infty)$ take values around 10^{-5}, and do not decrease for bigger frequencies as in Fig. 1.5.4. Indeed, updating the mesh but using $\mathbb{P}_3$ order elements, keeps the error values around 10^{-3} without increasing for higher frequencies.

Finally, in Fig. 1.5.6 we illustrate the error $\mathfrak{e}(p_\infty)$ and $\mathfrak{e}_2 = \dfrac{\| p_\infty - p_\infty^{ana} \|}{\| p_\infty \|} \times 100$ being p_∞ the analytical FFP solution to **BVP 0** described in Eq. 1.3.3 and p_∞^{ana} the FFP obtained from the characterization defined in Eq. 1.3.2 applied to the analytic solution p^{ana}. We observe that the error is around 10^{-1} for all frequencies, while the error between analytic and numeric FFP values is around 10^{-5}. Thus we conclude that the proposed truncated problem **BVP 1** leads to quite good approximate solutions to **BVP 0**.

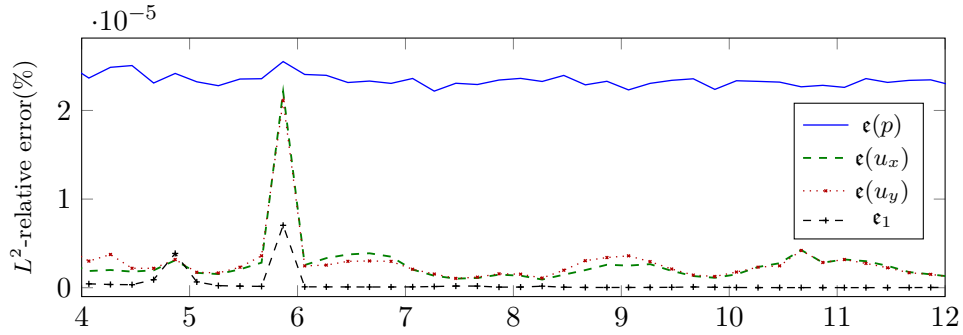

Fig. 1.5.5: Comparison between the analytical and numerical values for fluid pressure, solid displacement and FFP. Numerical experiments are performed with IPDG method with $\mathbb{P}_5$ order elements, curved-boundary elements, updated mesh for $h = \frac{2\pi c_f}{\omega N_\lambda}$ and $N_\lambda = 7$.

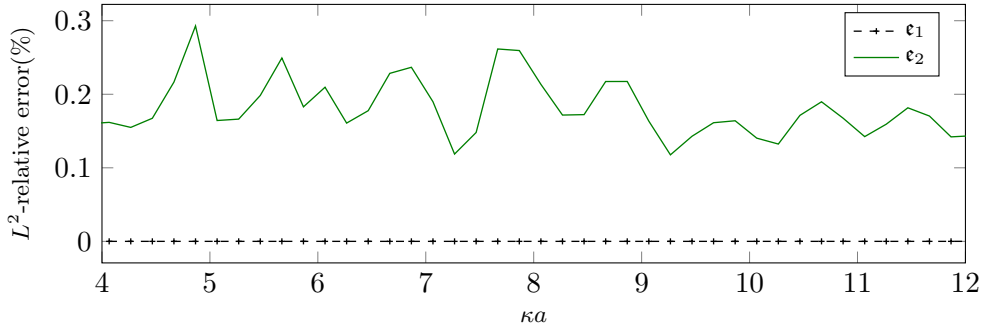

Fig. 1.5.6: Comparison of the error between analytic and numeric FFP values vs. analytic and *true* FFP for $4 \leq ka \leq 12$.

Chapter 2

Sensitivity of the Scattered Field to the Domain's Parameters

Contents

Chapter 2 investigates the dependency of the scattered field with respect to the different parameters characterizing the solid obstacle to be retrieved. It reveals that the Fréchet derivative of the scattered field can be represented as the solution to a BVP that is obtained from the formal derivation of the solution to **BVP 1**. The sensitivity analysis consists then in establishing that the corresponding problem is well-posed. Next, we construct an analytical representation of the Fréchet derivative which is compared with the IPDG solution of the problem. We end up with some illustrative numerical examples in order to validate the numerical computation of the Fréchet derivatives in our code.

2.1 Sensitivity to the Shape of the Scatterer

Almost two centuries after of the foundation of differential calculus by Newton and Leibniz in the seventeenth century, the modern mathematical analysis emerged at the hand of Cauchy with the introduction of the mathematical limit. Indeed, he proposed a precise definition of the existence of the derivative of a function at a point. [39].

Nearly one century ago, the French mathematicians Fréchet and Gâteaux stretched the concept of derivative in two different ways to functions of infinite dimensional Banach spaces. Nowadays these notions are widely used in physical sciences such as quantum field theory, even if they may not exist or despite existing, they may not lead to continuous functions. An important remark about the Fréchet differentibiliaty is that, as it is the basic notion of the differential calculus in normed spaces, any good definition of differentibiliaty in topological linear spaces must coincide with it when the spaces are normed [39, 106].

Before introducing the interest of the Fréchet derivative in the elasto-acoustic problematic, we remind its basic definition. We consider that f is a function defined from an open subset U of a Banach space X into the Banach space Y, we say that f is Fréchet differentiable at $x \in U$ if and only

if there is a bounded and linear operator $F_x : X \longmapsto Y$ such that

$$\lim_{t\to 0} \frac{f(x+th)-f(x)}{t} = F_x(h) \tag{2.1.1}$$

is uniform for every h in some neighborhood $\mathcal{N}_x$ of $0 \in X$ (see [13]). Then, the operator F_x is called the Fréchet derivative of f at x. According to [40], if (p,u) denotes the scattered field solution to **BVP 1**, its Fréchet derivatives with respect to the shape Γ satisfies:

$$\textbf{(BVP 2)} \quad \begin{cases} \nabla \cdot \sigma(u') + \omega^2 \rho_s u' = 0 & \text{in } \Omega^s \\ \Delta p' + k^2 p' = 0 & \text{in } \Omega_b^f \\ \tau(u') = -p'\nu + F_j(p,u,h_j) & \text{on } \Gamma \\ \omega^2 \rho_f u' \cdot \nu = \frac{\partial p'}{\partial \nu} + G_j(p,u,h_j) & \text{on } \Gamma \\ \frac{\partial p'}{\partial \nu} = Bp' & \text{on } \quad \Sigma \end{cases}$$

where the functions F_j and G_j are given by

$$F_j(p,u,h_j) = -h_j^t \nabla\sigma(u)\nu - \nabla p^T \cdot h_j \nu + \sigma(u)[h_j']^t\nu + p^T[h_j']^t\nu, \tag{2.1.2}$$

$$G_j(p,u,h_j) = -(\omega^2\rho_f \nabla u - \nabla(\nabla p^T))h_j \cdot \nu + (\omega^2\rho_f u - \nabla p^T)\cdot [h_j']^t\nu, \tag{2.1.3}$$

for $p^T = p + p^{inc}$. We have $h_j = \frac{\partial \Gamma}{\partial s_j}(s), \quad j = 1, ..., N_\Gamma$ when Γ is parametrized by the set $(s_1, ..., s_{N_\Gamma})$ of parameters (different parametrizations are described in Appendix C).

For instance, if we consider a disk-shaped scatter, the shape of the obstacle is parametrized as

$$\Gamma = \{r(\cos\theta, \sin\theta) \quad \theta \in [0, 2\pi]\}.$$

In that way, being the radius of the circle the unique shape parameter $s_1 = r$, $h = \frac{\partial \Gamma}{\partial r} = (\cos\theta, \sin\theta)$ and $h' = \frac{1}{r}\begin{pmatrix} sin^2\theta & -cos\theta\sin\theta \\ -cos\theta\sin\theta & cos^2\theta \end{pmatrix}$ (see [34] for the definitions of h and $[h']$).

We thus see that the formal pair (p', u') of derivatives is solution to **BVP 2** which belongs to **BVP**-class for particular right-hand sides. It is then important to check that **BVP 2** is well-posed.

2.1.1 Well-posedness of the Fréchet Derivative with Respect to Shape Parameters

As previously observed, as far as the shape parameters are concerned, the corresponding derivatives are solutions to **BVP 2** which falls into **BVP** category with:

$$F = 0,$$

$$f = -h_j^t \nabla\sigma(u)\nu - \nabla p^T \cdot h_j\nu + \sigma(u)[h_j']^t\nu + p^T[h_j']^t\nu,$$

$$g = -(\omega^2\rho_f\nabla u - \nabla(\nabla p^T))h_j \cdot \nu + (\omega^2\rho_f u - \nabla p^T)\cdot[h_j']^t\nu,$$

where $h_j = \frac{\partial \Gamma}{\partial s_j}(s), \quad j = 1, ..., N_\Gamma$ when Γ is parametrized by the set $(s_1, ..., s_{N_\Gamma})$ of parameters.

In [40], it has been proved that when Ω^s is of class C^2, then $f \in \left(H^{-1/2}(\Gamma)\right)$ and $g \in H^{-1/2}(\Gamma)$. We thus see that f and g are less regular than required than in **Theorem 1** to get the well-posedness of the corresponding system. Indeed, in **Theorem 1**, we have assumed that $f \in \left(L^2(\Gamma)\right)^2$ and $g \in L^2(\Gamma)$. Nevertheless, according to **Remark 1**, the result of **Theorem 1** can be extended to right-hand sides f and g which are in $H^{-1/2}$. Hence, we are able to define the shape derivative of the scattered field in the case of a regular obstacle Ω^s of class C^2 from the application of **Theorem 1**. We then have:

Proposition 3. *Let us assume that Ω^s is of class C^2 and that $p^{inc} \in H^1(\Gamma)$. Then the shape derivative of the scattered field exists as a solution to **BVP 1** and is unique modulo possibly existing Jones modes.*

It is worth mentioning that if Ω^s is less regular, the question of well-posedness remains open.

2.1.2 Analytical Study

Once we have obtained the well-posedness of **BVP 2**, we can perform computations by applying the IPDG method introduced in Chapter 1. To validate these computations, we provide here an analytical solution of **BVP 2** in the case of a circle with radius a. In this case, we can compute the scattered field derivative analytically. We take this chance for providing a way of validating the characterization of the numerical derivatives as a solution to **BVP 2**. The analytical expression of the Fréchet derivative with respect to the shape can be computed from **BVP 2**, following the same methodology as in Chapter 1 for **BVP 1**, but for practical interest, we obtain it deriving the series term by term corresponding to the analytical solution to **BVP 1**. As we consider a disk shaped obstacle, the parameter of interest is the variable a representing the radius of the obstacle. The construction of analytical Fréchet derivatives is based upon a formal derivation of the series defined by Eqs. 1.2.1, 1.2.6 and 1.2.7. For the sake of simplicity, we adopt the general notations p', ϕ' and ψ' standing for the derivatives of p, ϕ and ψ.

The main step for calculating the Fréchet derivatives consists in defining the derivative of the coefficients X_n. As for the wavefield, we denote it X_n' for now. According to Eq. 1.2.14, we have:

$$X_n'(a) = \left(E_n(a)^{-1} e_n(a)\right)' = \left(E_n(a)^{-1}\right)' e_n(a) + E_n(a)^{-1} \left(e_n(a)\right)' \tag{2.1.4}$$

presuming that E_n is invertible. Then, since $E_n(a)E_n(a)^{-1} = \mathbb{1}_d$, $\mathbb{1}_d$ denoting the identity, we have that

$$E'(a)E_n^{-1}(a) + E_n(a)\left(E_n^{-1}(a)\right)' = 0, \tag{2.1.5}$$

which implies that

$$\left(E_n^{-1}(a)\right)' = -E_n^{-1}(a)E'(a)E_n^{-1}(a). \tag{2.1.6}$$

Now, from Eqs. 2.1.4 and 2.1.6, we deduce that

$$X_n'(a) = -E_n^{-1}(a)E'(a)X_n(a) + E_n(a)^{-1}\left(e_n(a)\right)', \tag{2.1.7}$$

with $X_n(a) = E_n^{-1}(a)e_n$.

By this way, we get a formula for computing the derivatives of A_n, B_n, C_n and D_n. Indeed, the following expressions of $E'(a)$ and $\left(e_n(a)\right)'$ are necessary to complete the calculus of Eq. 2.1.7:

$$
\begin{aligned}
&\frac{\partial E_n^{11}}{\partial a} = k^2 H_n''^{(1)}(ka),\\
&\frac{\partial E_n^{12}}{\partial a} = k^2 H_n''^{(2)}(ka),\\
&\frac{\partial E_n^{13}}{\partial a} = -\omega^2 \rho_f k_p^2 J_n''(k_p a),\\
&\frac{\partial E_n^{14}}{\partial a} = -\omega^2 \rho_f \frac{n}{a} J_n'(k_s a) k_s + \omega^2 \rho_f \frac{n}{a^2} J_n(k_s a),\\
&\frac{\partial E_n^{21}}{\partial a} = k^2 H_n''^{(1)}(kb) - ik^2 H_n'^{(1)}(kb),\\
&\frac{\partial E_n^{22}}{\partial a} = k^2 H_n''^{(2)}(kb) - ik^2 H_n'^{(2)}(kb),\\
&\frac{\partial E_n^{23}}{\partial a} = 0 = \frac{\partial E_n^{24}}{\partial a},\\
&\frac{\partial E_n^{31}}{\partial a} = H_n'^{(1)}(ka) k,\\
&\frac{\partial E_n^{32}}{\partial a} = H_n'^{(2)}(ka) k,\\
&\frac{\partial E_n^{33}}{\partial a} = -\frac{4\mu}{a^3}\left[(n^2+n-\frac{1}{2}k_s^2 a^2) J_n(k_p a) - k_p a J_{n-1}(k_p a)\right] +\\
&+ \frac{2\mu}{a^2}\left[-k_s^2 a J_n(k_p a) + (n^2+n-\frac{1}{2}k_s^2 a^2) J_n'(k_p a) k_p - k_p^2 a J_{n-1}'(k_p a) - k_p J_{n-1}(k_p a))\right],\\
&\frac{\partial E_n^{34}}{\partial a} = -\frac{4\mu}{a^3}\left[n(-(n-1) J_n(k_s a) + k_s a J_{n-1}(k_s a))\right] +\\
&+ \frac{2\mu}{a^2}\left[n(-(n-1) J_n'(k_s a) k_s + k_s a J_{n-1}'(k_s a) k_s + k_s J_{n-1}(k_s a)\right],\\
&\frac{\partial E_n^{41}}{\partial a} = \frac{\partial E_n^{42}}{\partial a} = 0,\\
&\frac{\partial E_n^{43}}{\partial a} = \frac{4\mu}{a^3}\left[n(-(n-1) J_n(k_p a) + k_p a J_{n-1}(k_p a))\right],\\
&- \frac{2\mu}{a^2}\left[n(-(n-1) J_n'(k_p a) k_p + k_p^2 a J_{n-1}'(k_p a) + k_p J_{n-1}(k_p a)\right],\\
&\frac{\partial E_n^{44}}{\partial a} = \frac{4\mu}{a^3}\left[(n^2+n-\frac{1}{2}k_s^2 a^2) J_n(k_s a) - k_s a J_{n-1}(k_s a)\right],\\
&- \frac{2\mu}{a^2}\left[-k_s^2 a J_n(k_s a) + (n^2+n-\frac{1}{2}k_s^2 a^2) J_n'(k_s a) k_s - k_s^2 a J_{n-1}'(k_s a) - k_s J_{n-1}(k_s a)\right].
\end{aligned}
$$

The right-hand side $(e_n(a))' \in \mathbb{C}^4$ is given by

$$
\begin{aligned}
\left(e_n^1\right)' &= -\varepsilon_n i^n k J_n''(ka) k,\\
\left(e_n^2\right)' &= -\varepsilon_n i^n k J_n'(ka) k,\\
\left(e_n^3\right)' &= \left(e_n^4\right)' = 0,
\end{aligned}
$$

where $\varepsilon_0 = 1$ and $\varepsilon_n = 2$ for $n \geq 1$.

2.1.3 Illustrative Numerical Results

The computation of the derivative with respect to the radius using the DG method for solving **BVP 2** has been validated in [40]. Nevertheless, we provide one example in Figure 2.1.1 to make that chapter self-content. The considered computational domain is a disk shaped scatterer Ω^s of radius $a = 1$cm surrounded by an acoustic domain Ω_b^f, whose external boundary is a circle of radius $b = 7.5$cm. The density of the fluid is $\rho_f = 1000$ kg m^{-3} (water), while the scatterer Ω^s is made of *steel* whose material parameters are the Lamé coefficients $\lambda = 115.40$ (GPa) and $\mu = 76.9$ (GPa), and the density $\rho_s = 7900$ kg m^{-3}. The normalized frequency is $ka = 5.33$. In order to compute the numerical expression of the derivative, we employ the IPDG solver with fourth-order elements (with 15 dof per element) with a mesh discretization of five elements per wavelength. For the analytical expression, the number of modes is set to be $N = 2\lceil ka \rceil + 1$. The relative error between the analytic and numeric solution is around 0.98%.

The exact solution corresponds to the analytical derivative while the approximate one is obtained by solving **BVP 2** following the procedure described in Chapter 1 for **BVP**.

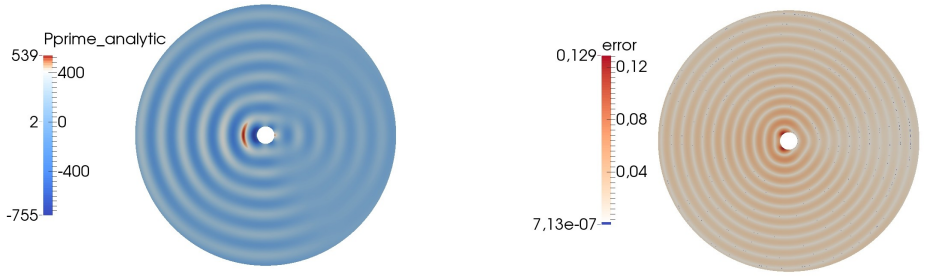

(a) Analytical solution (b) Absolute error between both solutions

Fig. 2.1.1: Figure (a): Real part of the analytic derivative of the pressure field p' with respect to shape parameter a for the exact and approximate solutions for $ka = 5.33$. Figure (b): Absolute error between analytic and numeric solutions.

2.2 Sensitivity to the Material Parameters

Here we consider the pair of Lamé parameters λ and μ and the mass density ρ_s. Once again, we end up with boundary value problems which belong with **BVP** class.

Let (p', u') be the derivatives of the wavefield with respect to one of these three parameters. It is formally defined as the solution to the **BVP**:

$$\textbf{(BVP 3-4)} \quad \begin{cases} \nabla \cdot \sigma(u') + \omega^2 \rho_s u' = -\nabla \cdot \partial C\varepsilon(u) & \text{in } \Omega^s \quad \text{(a)} \\ \Delta p' + k^2 p' = 0 & \text{in } \Omega_b^f \quad \text{(b)} \\ \sigma(u') \cdot \nu + p'\nu = -\partial C\varepsilon(u) \cdot \nu & \text{on } \Gamma \quad \text{(c)} \\ \omega^2 \rho_f u' \cdot \nu = \frac{\partial p'}{\partial \nu} & \text{on } \Gamma \quad \text{(d)} \\ \frac{\partial p'}{\partial \nu} = Bp' & \text{on } \Sigma \quad \text{(e)} \end{cases}$$

where ∂C takes the form:

$$\partial C = \partial_\lambda C = \begin{pmatrix} 1 & 1 & 0 \\ 1 & 1 & 0 \\ 0 & 0 & 0 \end{pmatrix}, \tag{2.2.1}$$

when deriving with respect to λ, that is **BVP 3**.

$$\partial C = \partial_\mu C = \begin{pmatrix} 2 & 0 & 0 \\ 0 & 2 & 0 \\ 0 & 0 & 1 \end{pmatrix}, \tag{2.2.2}$$

when deriving with respect to μ, represented by **BVP 4**.

In the case of the density ρ_s, we get a simpler problem of the form

$$\textbf{(BVP 5)} \quad \begin{cases} \nabla \cdot \sigma(u') + \omega^2 \rho_s u' = -\omega^2 u & \text{in } \Omega^s \quad \text{(a)} \\ \Delta p' + k^2 p' = 0 & \text{in } \Omega_b^f \quad \text{(b)} \\ \tau(u') = \sigma(u') \cdot \nu = -p'\nu & \text{on } \Gamma \quad \text{(c)} \\ \omega^2 \rho_f u' \cdot \nu = \frac{\partial p'}{\partial \nu} & \text{on } \Gamma \quad \text{(d)} \\ \frac{\partial p'}{\partial \nu} = Bp' & \text{on } \Sigma \quad \text{(e)} \end{cases}$$

2.2.1 Well-posedness of the Fréchet Derivative with Respect to Material Parameters

In this subsection, we propose to give a sense to the formal Fréchet derivatives with respect to the material parameters.

Let us now consider **BVP 3**. It corresponds to **BVP** with

$$F = \nabla \cdot \partial_\lambda C \varepsilon(u), \qquad f = \partial_\lambda C \varepsilon(u)\nu \quad \text{and} \qquad g = 0, \tag{2.2.3}$$

where u is the displacement field into Ω^s defined by **BVP 1**, and

$$\partial_\lambda C = \begin{pmatrix} 1 & 1 & 0 \\ 1 & 1 & 0 \\ 0 & 0 & 0 \end{pmatrix}. \tag{2.2.4}$$

Regarding the solution to the direct problem denoted by (p, u), we know that $u \in \left(H^1(\Omega^s)\right)^2$ and the corresponding $p \in H^1(\Omega_b^f)$ if Γ is Lipschitz and $p^{inc} \in H^1(\Gamma)$. It turns out that his regularity is not sufficient to fall into the context of Theorem 1. In fact, when the boundary of Ω^s is regular enough, that is at least C^2, (p, u) is more regular. Indeed, we have, according to [32] and [65], $u \in \left(H^2(\Omega^s)\right)^2$ and $p \in \left(H^2(\Omega_b^f)\right)^2$. We thus deduce that $\nabla u \in \left(H^1(\Omega^s)\right)^4$ which implies that $F \in \left(L^2(\Omega^s)\right)^2$ and $f \in \left(H^{1/2}(\Gamma)\right)^2$.

We thus have, according to Chapter 1:

Proposition 4. *Assume that Ω^s is a C^2 bounded domain of $\mathbb{R}^2$. Then for any incident wave $p^{inc} \in H^1(\Gamma)$, **BVP 3** admits a solution $(w, z) \in H^1(\Omega_b^f) \times \left(H^1(\Omega^s)\right)^2$ which is unique modulo the possibly existing Jones modes.*

This proposition establishes then the existence of the Fréchet derivative of the scattered field with respect to λ.

As far as **BVP 4** is concerned, it is defined for:

$$F = \nabla \cdot \partial_\mu C\varepsilon(u), \qquad f = \partial_\mu C\varepsilon(u)\nu \quad \text{and} \qquad g = 0. \tag{2.2.5}$$

where (p, u) is solution to **BVP 1**. We have:

$$\partial_\mu C = \begin{pmatrix} 2 & 0 & 0 \\ 0 & 2 & 0 \\ 0 & 0 & 1 \end{pmatrix}. \tag{2.2.6}$$

We see that we can use exactly the same arguments than before to get:

Proposition 5. *Assume that Ω^s is a C^2 bounded domain of $\mathbb{R}^2$. Then for any incident wave $p^{inc} \in H^1(\Gamma)$, **BVP 4** admits a solution $(w, z) \in H^1(\Omega_b^f) \times \left(H^1(\Omega^s)\right)^2$ which is unique modulo the possibly existing Jones modes.*

We get thus a justification of the derivative of the scattered field with respect to μ.

The derivative with respect to the density ρ_s has been defined as the solution to **BVP 5**. It corresponds **BVP** with

$$F = -\omega^2 u, \qquad f = 0 \quad \text{and} \qquad g = 0. \tag{2.2.7}$$

We can thus apply **Theorem 1** without any difficulty since even in the case where Ω^s is Lipschitz continuous, we have $u \in (L^2(\Omega^s))^2$. Hence, we have:

Proposition 6. *Let Ω^s be a solid with a boundary Γ that is Lipschitz continuous. Let $p^{inc} \in H^1(\Gamma)$. Then, the derivative of the scattered field is the solution to **BVP 5** and is unique modulo Jones modes that may exist.*

It would be interesting to extend the **Proposition 4** and **5** to the case of a Lipschitz boundary surface or at least a $C^{1,1}$ polygonal boundary. Some regularity results are at our disposal (see page 23 in [23]) that could be used to handle this case. For instance, when $u \in \left(H^{3/2}(\Omega^s)\right)^2$, we have $\nabla u \in \left(H^{1/2}(\Omega^s)\right)^4$ and so does $\partial C\varepsilon(u)$. Hence we have $F = \nabla \cdot \partial C\varepsilon(u) \in \left(H^{-1/2}(\Omega^s)\right)^4$ and according to [23], we can give a sense to $\partial C\varepsilon(u)\nu$ on Γ. Nevertheless, once the right-hand sides are defined for a Lipschitz solid, it is necessary to reconsider the problem of existence based on a Gårding estimate. This will be the subject of further investigations.

2.2.2 Analytical Study

In this subsection, our goal is to get an explicit formulation of the derivatives with respect to the material parameters λ and μ. By this way, we will dispose of reference solutions which will provide data to validate the computational derivatives obtained as numerical solutions to **BVP 3** and **BVP 4** following Chapter 1. We adopt the general notations p', ϕ' and ψ' standing for the derivatives of p, ϕ and ψ, without specifying if we consider λ or μ as long as we describe the method of calculation.

For the sake of simplicity, the analytical expression of the Fréchet derivative with respect to Lamé coefficients have been obtained deriving the series representing the analytical solution to **BVP 1**. According to Eq. 1.2.14, we obtain the derivatives of the coefficients X_n, denoted by X_n':

$$X_n'(\lambda,\mu) = \left(E_n(\lambda,\mu)^{-1}e_n\right)' = \left(E_n(\lambda,\mu)^{-1}\right)' e_n \tag{2.2.8}$$

presuming that E_n is invertible. Then, from $E_n(\lambda,\mu)E_n(\lambda,\mu)^{-1} = \mathbb{1}_d$ we get:

$$E'(\lambda,\mu)E_n^{-1}(\lambda,\mu) + E_n(\lambda,\mu)\left(E_n^{-1}(\lambda,\mu)\right)' = 0, \tag{2.2.9}$$

and therefore,

$$\left(E_n^{-1}(\lambda,\mu)\right)' = -E_n^{-1}(\lambda,\mu)E'(\lambda,\mu)E_n^{-1}(\lambda,\mu). \tag{2.2.10}$$

Straightaway, from Eqs. 2.2.8 and 2.2.10, we obtain that

$$X_n'(\lambda,\mu) = -E_n^{-1}(\lambda,\mu)E'(\lambda,\mu)X_n(\lambda,\mu), \tag{2.2.11}$$

with $X_n(\lambda,\mu) = E_n^{-1}(\lambda,\mu)e_n$.

Finally, we deduce the following formula for computing the derivatives of A_n, B_n, C_n and D_n:

(a) Regarding the parameter λ, we have:

$$\frac{\partial X_n}{\partial\lambda}(\lambda,\mu) = -E_n^{-1}(\lambda,\mu)\frac{\partial E_n}{\partial\lambda}(\lambda,\mu)X_n(\lambda,\mu) \tag{2.2.12}$$

with $\dfrac{\partial E_n}{\partial\lambda}(\lambda,\mu)$ given by:

$$\begin{aligned}
&\frac{\partial\left(E_n^{11}\right)}{\partial\lambda} = \frac{\partial\left(E_n^{12}\right)}{\partial\lambda} = \frac{\partial\left(E_n^{14}\right)}{\partial\lambda} = 0,\\
&\frac{\partial\left(E_n^{13}\right)}{\partial\lambda} = -\omega^2\rho_f\frac{\partial k_p}{\partial\lambda}J_n'(k_pa) - \omega^2\rho_f k_p J_n''(k_pa)\frac{\partial k_p}{\partial\lambda}a,\\
&\frac{\partial\left(E_n^{21}\right)}{\partial\lambda} = \frac{\partial\left(E_n^{22}\right)}{\partial\lambda} = \frac{\partial\left(E_n^{23}\right)}{\partial\lambda} = \frac{\partial\left(E_n^{24}\right)}{\partial\lambda} = 0,\\
&\frac{\partial\left(E_n^{31}\right)}{\partial\lambda} = \frac{\partial\left(E_n^{32}\right)}{\partial\lambda} = \frac{\partial\left(E_n^{34}\right)}{\partial\lambda} = 0,\\
&\frac{\partial\left(E_n^{33}\right)}{\partial\lambda} = \frac{2\mu}{a^2}\left[(n^2+n-\frac{1}{2}k_s^2a^2)J_n'(k_pa)\frac{\partial k_p}{\partial\lambda}a - \frac{\partial k_p}{\partial\lambda}aJ_{n-1}(k_pa)\right]\\
&\qquad\qquad - \frac{2\mu}{a^2}\left[k_paJ_{n-1}'(k_pa)\frac{\partial k_p}{\partial\lambda}a\right],\\
&\frac{\partial\left(E_n^{41}\right)}{\partial\lambda} = \frac{\partial\left(E_n^{42}\right)}{\partial\lambda} = \frac{\partial\left(E_n^{44}\right)}{\partial\lambda} = 0,\\
&\frac{\partial\left(E_n^{43}\right)}{\partial\lambda} = -\frac{2\mu}{a^2}n\left[-(n+1)J_n'(k_pa)\frac{\partial k_p}{\partial\lambda}a + \frac{\partial k_p}{\partial\lambda}aJ_{n-1}(k_pa)\right],\\
&\qquad\qquad - \frac{2\mu}{a^2}n\left[k_paJ_{n-1}'(k_pa)a\frac{\partial k_p}{\partial\lambda}\right].
\end{aligned}$$

From these expressions, we can define the formal derivative $\frac{\partial p}{\partial \lambda}$ as follows:

$$\frac{\partial p}{\partial \lambda}(r,\theta,\lambda,\mu) = \sum_{n=0}^{+\infty} \left[\frac{\partial A_n}{\partial \lambda}(\lambda,\mu) H_n^{(1)}(kr) + \frac{\partial B_n}{\partial \lambda}(\lambda,\mu) H_n^{(2)}(kr) \right] cos(n\theta) \qquad a \leq r \leq b, \quad \theta \in [0, 2\pi). \tag{2.2.13}$$

The formal derivative of ϕ and ψ are given by:

$$\phi' = \frac{\partial \phi}{\partial \lambda}(r,\theta,\lambda,\mu) = \sum_{n=0}^{+\infty} \left[\frac{\partial C_n}{\partial \lambda}(\lambda,\mu) J_n(k_p r) + C_n(\lambda,\mu) J_n^{'}(k_p r) \frac{\partial k_p}{\partial \lambda} r \right] cos(n\theta), \tag{2.2.14}$$

$$\psi' = \frac{\partial \psi}{\partial \lambda}(r,\theta,\lambda,\mu) = \sum_{n=0}^{+\infty} \left[\frac{\partial D_n}{\partial \lambda}(\lambda,\mu) J_n(k_s r) + D_n(\lambda,\mu) J_n^{'}(k_s r) \frac{\partial k_s}{\partial \lambda} r \right] sin(n\theta). \tag{2.2.15}$$

(b) As far as μ is concerned, we have:

$$\frac{\partial X_n}{\partial \mu}(\lambda,\mu) = -E_n^{-1}(\lambda,\mu) \frac{\partial E_n}{\partial \mu}(\lambda,\mu) X_n(\lambda,\mu) \tag{2.2.16}$$

with $\frac{\partial E_n}{\partial \mu}(\lambda,\mu)$ is defined as:

$$
\begin{aligned}
&\frac{\partial\left(E_n^{11}\right)}{\partial\mu} = \frac{\partial\left(E_n^{12}\right)}{\partial\mu} = 0,\\
&\frac{\partial\left(E_n^{13}\right)}{\partial\mu} = -\omega^2\rho_f\frac{\partial k_p}{\partial\mu}J_n'(k_pa) - \omega^2\rho_f k_p J_n''(k_pa)\frac{\partial k_p}{\partial\mu}a,\\
&\frac{\partial\left(E_n^{14}\right)}{\partial\mu} = -\omega^2\rho_f\frac{n}{a}J'(k_sa)\frac{\partial k_s}{\partial\mu}a,\\
&\frac{\partial\left(E_n^{21}\right)}{\partial\mu} = \frac{\partial\left(E_n^{22}\right)}{\partial\mu} = \frac{\partial\left(E_n^{23}\right)}{\partial\mu} = \frac{\partial\left(E_n^{24}\right)}{\partial\mu} = 0,\\
&\frac{\partial\left(E_n^{31}\right)}{\partial\mu} = \frac{\partial\left(E_n^{32}\right)}{\partial\mu} = 0,\\
&\frac{\partial\left(E_n^{33}\right)}{\partial\mu} = \frac{2}{a^2}\left[(n^2+n-\frac{1}{2}k_s^2a^2)J_n(k_pa) - k_paJ_{n-1}(k_pa)\right]\\
&\qquad + \frac{2\mu}{a^2}\left[-k_s\frac{\partial k_s}{\partial\mu}a^2J_n(k_pa) + (n^2+n-\frac{1}{2}k_s^2a^2)J_n'(k_pa)\frac{\partial k_p}{\partial\mu}a - \frac{\partial k_p}{\partial\mu}aJ_{n-1}(k_pa)\right]\\
&\qquad - \frac{2\mu}{a^2}\left[k_paJ_{n-1}'(k_pa)\frac{\partial k_p}{\partial\mu}a\right],\\
&\frac{\partial\left(E_n^{34}\right)}{\partial\mu} = \frac{2}{a^2}\left[n(-(n+1)J_n(k_sa) + k_saJ_{n-1}(k_sa))\right],\\
&\qquad + \frac{2\mu}{a^2}\left[n(-(n+1)J_n'(k_sa)\frac{\partial k_s}{\mu}a + \frac{\partial k_s}{\partial\mu}aJ_{n-1}(k_sa) + k_saJ_{n-1}'(k_sa)\frac{\partial k_s}{\partial\mu}a\right],\\
&\frac{\partial\left(E_n^{41}\right)}{\partial\mu} = \frac{\partial\left(E_n^{42}\right)}{\partial\mu} = 0,\\
&\frac{\partial\left(E_n^{43}\right)}{\partial\mu} = -\frac{2n}{a^2}\left[-(n+1)J_n(k_pa) + k_paJ_{n-1}(k_pa)\right],\\
&\qquad - \frac{2\mu}{a^2}n\left[-(n+1)J_n'(k_pa)\frac{\partial k_p}{\partial\mu}a + \frac{\partial k_p}{\partial\mu}aJ_{n-1}(k_pa)\right],\\
&\qquad - \frac{2\mu}{a^2}n\left[k_paJ_{n-1}'(k_pa)a\frac{\partial k_p}{\partial\mu}\right],\\
&\frac{\partial\left(E_n^{44}\right)}{\partial\mu} = -\frac{2}{a^2}\left[(n^2+n-\frac{1}{2}k_s^2a^2)J_n(k_sa) - k_saJ_{n-1}(k_sa)\right]\\
&\qquad - \frac{2\mu}{a^2}\left[-k_s\frac{\partial k_s}{\partial\mu}a^2J_n(k_sa) + (n^2+n-\frac{1}{2}k_s^2a^2)J_n'(k_sa)\frac{\partial k_s}{\partial\mu}a - \frac{\partial k_s}{\partial\mu}aJ_{n-1}(k_sa)\right]\\
&\qquad - \frac{2\mu}{a^2}\left[-k_saJ_{n-1}'(k_sa)\frac{\partial k_s}{\partial\mu}a\right].
\end{aligned}
$$

Then, we formally have:

$$
\frac{\partial p}{\partial\mu}(r,\theta,\lambda,\mu) = \sum_{n=0}^{+\infty}\left[\frac{\partial A_n}{\partial\mu}(\lambda,\mu)H_n^{(1)}(kr) + \frac{\partial B_n}{\partial\mu}(\lambda,\mu)H_n^{(2)}(kr)\right]cos(n\theta) \qquad a\le r\le b, \quad \theta\in[0,2\pi), \tag{2.2.17}
$$

$$\phi' = \frac{\partial \phi}{\partial \mu}(r,\theta,\lambda,\mu) = \sum_{n=0}^{+\infty} \left[\frac{\partial C_n}{\partial \lambda}(\lambda,\mu) J_n(k_p r) + C_n(\lambda,\mu) J_n^{'}(k_p r) \frac{\partial k_p}{\partial \mu} r \right] cos(n\theta), \tag{2.2.18}$$

$$\psi' = \frac{\partial \psi}{\partial \mu}(r,\theta,\lambda,\mu) = \sum_{n=0}^{+\infty} \left[\frac{\partial D_n}{\partial \mu}(\lambda,\mu) J_n(k_s r) + D_n(\lambda,\mu) J_n^{'}(k_s r) \frac{\partial k_s}{\partial \lambda} r \right] sin(n\theta). \tag{2.2.19}$$

Remark: The construction of the analytical Fréchet derivatives has been carried out in a formal way by deriving term by term the formal series representing the wavefields. The computations have been performed by assuming the matrix E_n is invertible. We will address this issue later on which may raise some difficulties. Obviously the derivation term by term should be justified. One way to do this could be to construct the analytical solution to **BVP 2** straight-forwardly. This is an ongoing work.

2.2.3 Illustrative Numerical Results

Here the main goal is to assess the accuracy of the Fréchet derivative with respect to material parameters. To this end we perform some comparisons between the analytical and numerical expressions. In the following simulations, the computational domain is an elastic circle Ω^s of radius $a = 1$cm surrounded by an acoustic domain Ω_b^f, whose external boundary is a circle of radius $b = 7.5$cm. The density of the fluid is $\rho_f = 1000$ kg m^{-3} (water), while the sought-after scatterer Ω^s is made of *steel* whose material parameters are the Lamé coefficients $\lambda = 115.40$ GPa and $\mu = 76.9$ GPa with the density $\rho_s = 7900$ kg m^{-3}. Different experiments are performed with six circular frequencies. These normalized frequency values are **k a=2.67,3.33,4,5.33,6.67,8**. The mesh update criteria that is employed for all experiments is adapted to the normalized frequency ω: the mesh is updated/created by software `triangle`[1] taking three variables: the number of discretization points on interface Γ and boundary Σ, denoted by N_Γ and N_Σ respectively, and elemental area $\mathfrak{a}_h$. These are defined by

$$N_\Gamma = \left[\tfrac{2\pi a}{h}\right] \quad , \quad N_\Sigma = \left[\tfrac{2\pi b}{h}\right] \quad , \quad \mathfrak{a}_h = \tfrac{h^2}{2},$$

in terms of 'mesh size' h. The quantity 'mesh size' h defined as

$$h = \tfrac{\lambda_f}{N_\lambda} = \tfrac{2\,\pi\, c_f}{\omega\, N_\lambda},$$

is controlled by normalized frequency ω, and '♯ points per wavelength, denoted by N_λ.

Initially we employ the IPDG solver with three-order elements (with 10 dof per element) with a mesh discretization of five elements per wavelength, that is, $N_\lambda = 5$. The number of modes is set to be $N = 2\lceil ka \rceil + 1$ for the analytical expression.

In order to quantify our results, we will use L^2-relative error (%). First we compare the Fréchet derivative with respect to the Lamé coefficient λ for normalized frequencies $ka = 2.67, 3.33, 4$. The results pertaining to this comparison are depicted in Figures 2.2.1-2.2.2 -2.2.3, where we can observe the real analytical part of the Fréchet derivative, together with the absolute error between numeric and analytic values. The L^2-relative error results pertaining to this comparison are summarized in Table 2.2.1.

[1] `https://www.cs.cmu.edu/~quake/triangle.html`

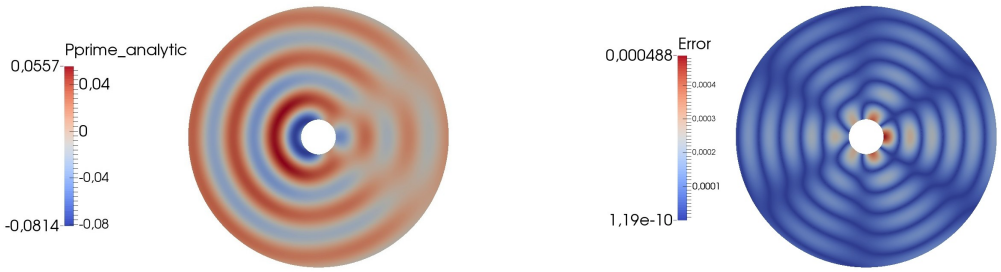

(a) Analytical solution (b) Absolute error between both solutions

Fig. 2.2.1: Figure (a): Real part of the analytic derivative of the pressure field p' with respect to λ for $ka = 2.67$. Figure (b): Absolute error between analytic and numeric solutions.

Normalized frequency ka	p'	u'_x	u'_y
2.67	0.32	0.11	0.12
3.33	0.28	$8.42 \cdot 10^{-2}$	$9.982 \cdot 10^{-3}$
4	0.25	$6.35 \cdot 10^{-2}$	$8.69 \cdot 10^{-3}$

Tab. 2.2.1: L^2-relative error(%) results for normalized frequency values $ka = 2.67, 3.33, 4$ corresponding to the Fréchet derivative with respect to λ.

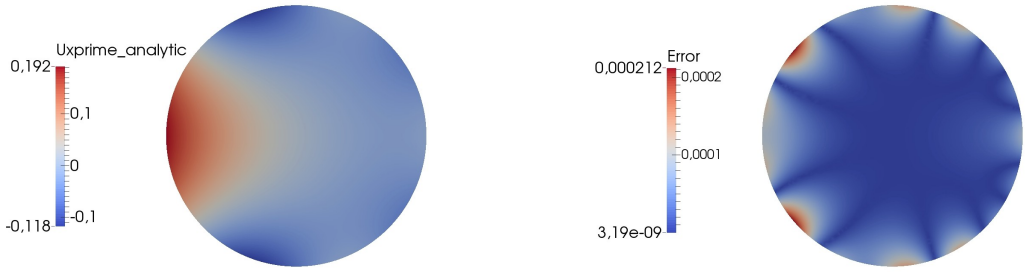

(a) Analytical solution (b) Absolute error between both solutions

Fig. 2.2.2: Figures (a): Real part of the analytic derivative of the displacement component u'_x with respect to λ for $ka = 3.33$. Figure (b): Absolute error between analytic and numeric solutions.

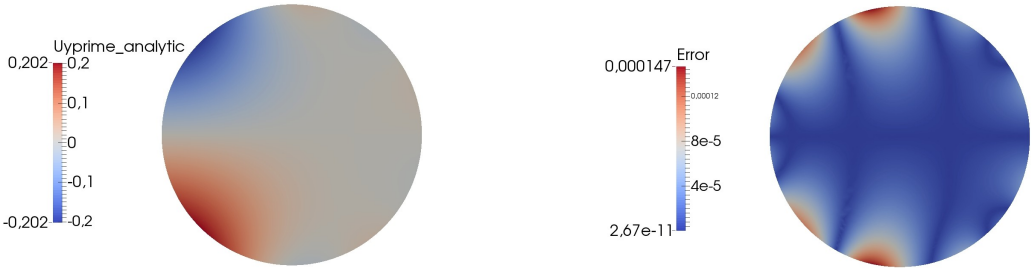

(a) Analytical solution (b) Absolute error between both solutions

Fig. 2.2.3: Figure (a): Real part of the derivative of the displacement component u_y' with respect to λ for $ka = 4$. Figure (b): Absolute error between analytic and numeric solutions.

We also provide some comparisons corresponding to the Fréchet derivative with respect to the material parameter μ, illustrating the real analytical part of the Fréchet derivative, together with the absolute error between analytic and numeric values of the Fréchet derivative in Figures 2.2.4-2.2.5-2.2.6. The respective relative errors for normalized frequency values $ka = 5.33, 6.67, 8$ are depicted in Table 2.2.2:

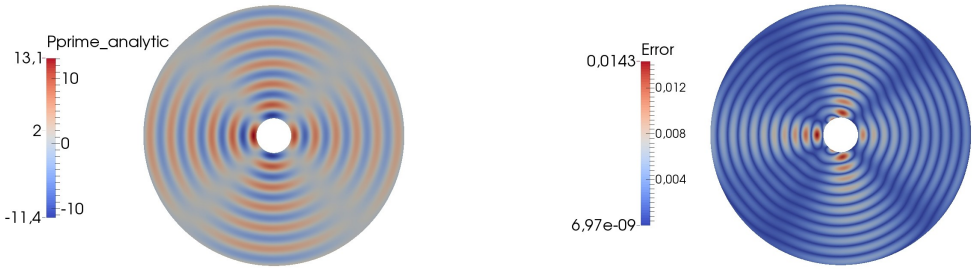

(a) Analytical solution (b) Absolute error between both solutions

Fig. 2.2.4: Figure (a): Real part of the derivative of the pressure field p' with respect to μ for $ka = 5.33$. Figure (c): Absolute error between analytic and numeric solutions.

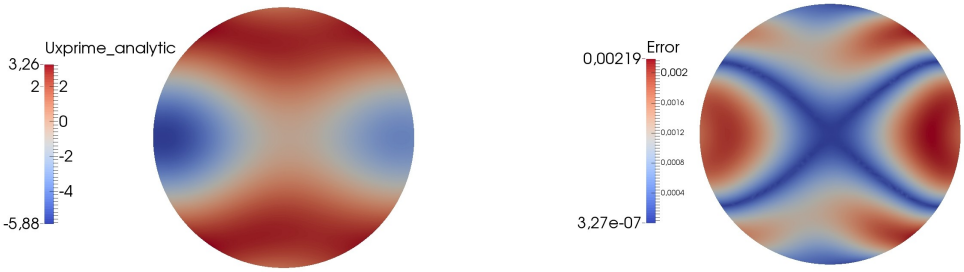

(a) Analytical solution (b) Absolute error between both solutions

Fig. 2.2.5: Figure (a): Real parts of the derivative of the displacement component u_x' with respect to μ for $ka = 6.67$. Figure (b): Absolute error between analytic and numeric solutions.

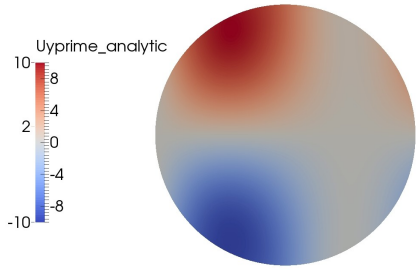

(a) Analytical solution

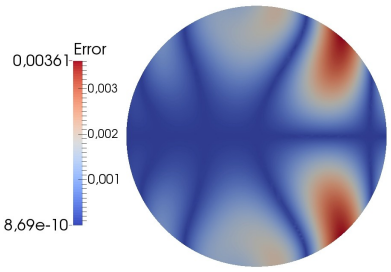

(b) Absolute error between both solutions

Fig. 2.2.6: Figure (a): Real parts of the derivative of the displacement component u'_y with respect to μ for $ka = 8$. Figure (b): Absolute error between both solutions.

Normalized frequency ka	p'	u'_x	u'_y
5.33	0.17	$9.07 \cdot 10^{-2}$	$9.62 \cdot 10^{-3}$
6.67	0.27	0.16	0.22
8	$8.65 \cdot 10^{-2}$	$6.07 \cdot 10^{-2}$	$5.86 \cdot 10^{-2}$

Tab. 2.2.2: L^2-relative error(%) results for normalized frequency values $ka = 5.33, 6.67, 8$ corresponding to the Fréchet derivative with respect to μ.

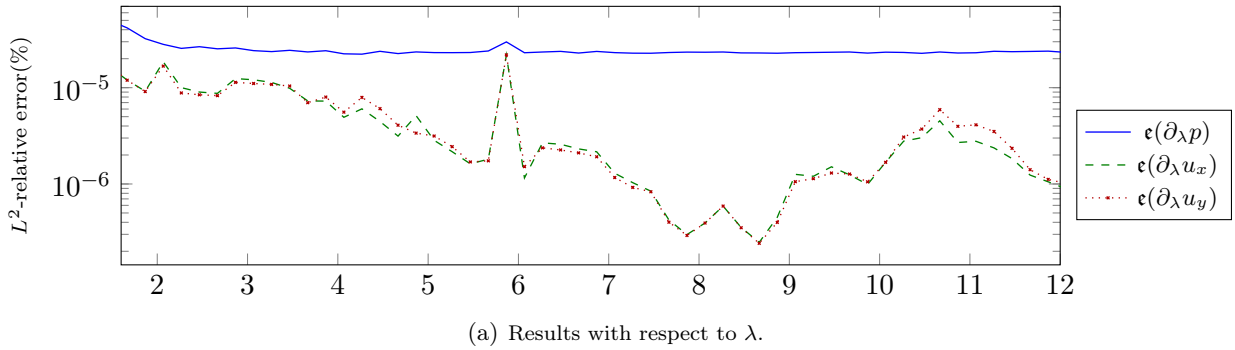

(a) Results with respect to λ.

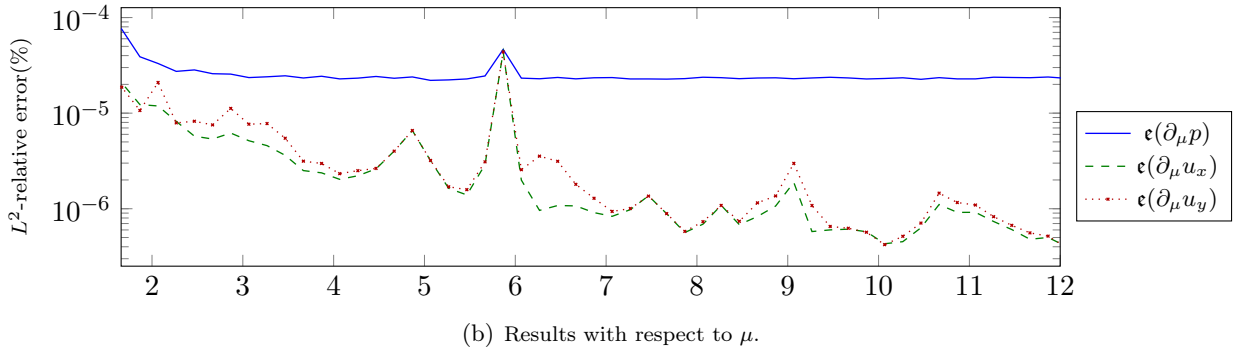

(b) Results with respect to μ.

Fig. 2.2.7: Comparison between the analytical and numerical value of the Fréchet derivative of fluid pressure $\mathfrak{e}(\partial p)$ and solid displacement $\mathfrak{e}(\partial u_x)$, $\mathfrak{e}(\partial u_y)$ with respect to Lamé parameters λ and μ.

The results obtained in Tables 2.2.1 and 2.2.2 have been extended in Figure 2.2.7 by calculating

the L^2-relative error for the frequency interval $2 \leq ka \leq 12$ with the following quantity,

$$\mathfrak{e}(g) \;=\; \frac{\|g_{ana} - g_{num}\|_2}{\|g_{ana}\|_2} \times 100\,.$$

where g represents the functions ∂p, ∂u_x, ∂u_y, $\mathfrak{R}\,(\partial p_{a,\infty})$, $\mathfrak{I}\,(\partial p_{a,\infty})$, $|\partial p_{a,\infty}|$.

The mesh discretization parameters that we employ for this experiment are five-order elements (with 21 dof per element) with a mesh discretization of seven elements per wavelength, that is, $N_\lambda = 7$. We observe that the corresponding relative errors are all below than 10^{-4} for $\mathfrak{e}(\partial p)$ and $\mathfrak{e}(\partial u)$ for all frequencies, c.f. Figure 2.7(a)–2.7(b). Hence, the main conclusion on the relative error results depicted in Tables 2.2.1-2.2.2 and Figure 2.2.7 is that the numerical Fréchet derivative has been successfully validated in both cases, in the case where the derivative is defined with respect to the Lamé parameter λ as well as μ. Moreover, the accuracy level can be improved increasing the order of elements or/and the number of elements per wavelength.

The main goal of the following experiments is to validate the numerical FFP derivative with respect to the material parameters. For the sake of simplicity, we consider the computational domain previously introduced for the numerical validation of the derivatives of pressure and displacement fields. The normalized frequency takes the values $ka = 1.5, 3, 4.5, 7$.

In Figure 2.2.8 we plot (a) the modulus, (b) the real part and (c) the imaginary part of the analytical (blue dashed curve) and numerical (green plain curve) FFP derivatives with respect to λ. We can see that these curves are quite similiar, meaning that the error between them is small (see L^2-relative errors detailed in Table 2.2.3). This reveals that the numerical computation is validated successfully.

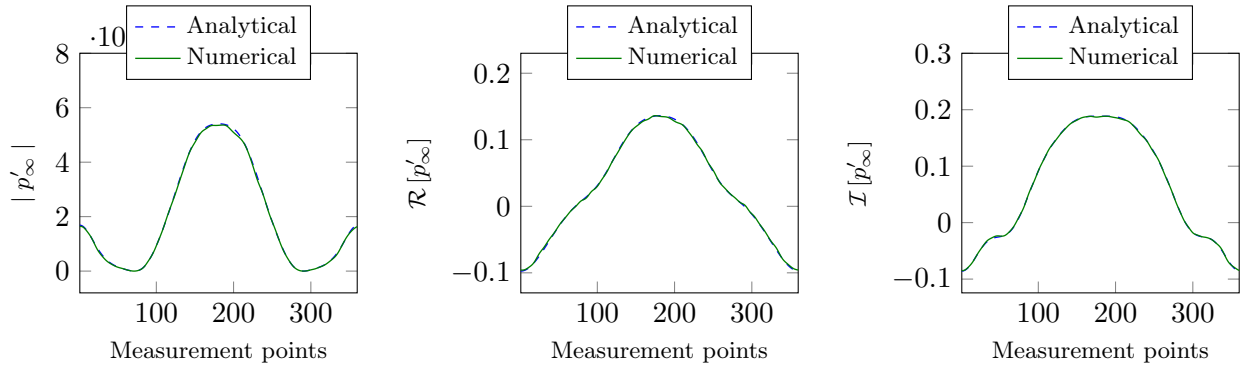

(a) Intensity (b) Real part (c) Imaginary part

Fig. 2.2.8: The analytic FFP derivative vs numeric with respect to Lamé parameter λ, for $ka = 1.5$, and corresponding to the *steel* material.

On the other hand, in Figures 2.2.9(a)-(b) and (c) we have plotted the modulus, the real part and the imaginary part respectively for the analytical (blue dashed curve) and numerical (green plain curve) FFP derivatives with respect to μ. The small difference of these curves has been computed with L^2-relative norms, and the corresponding relative errors are depicted in Table 2.2.4.

For completeness purpose, we compute the relative error of the FFP Fréchet derivative with respect to both Lamé parameters for the frequency range $2 \leq ka \leq 12$. The mesh is discretizated for each frequency using five-order elements and seven points per wavelength.

L^2-relative error(%)	$\mathcal{R}(p'_\infty)$	$\mathcal{I}(p'_\infty)$	$\lvert p'_\infty \rvert$
$ka = 1.5$	0.14	0.19	0.05
$ka = 3$	0.14	0.19	0.05
$ka = 4.5$	0.03	0.02	0.09
$ka = 7$	0.34	0.12	1.25

Tab. 2.2.3: L^2-relative error(%) results for different normalized frequency valued corresponding to the Fréchet derivative with respect to λ.

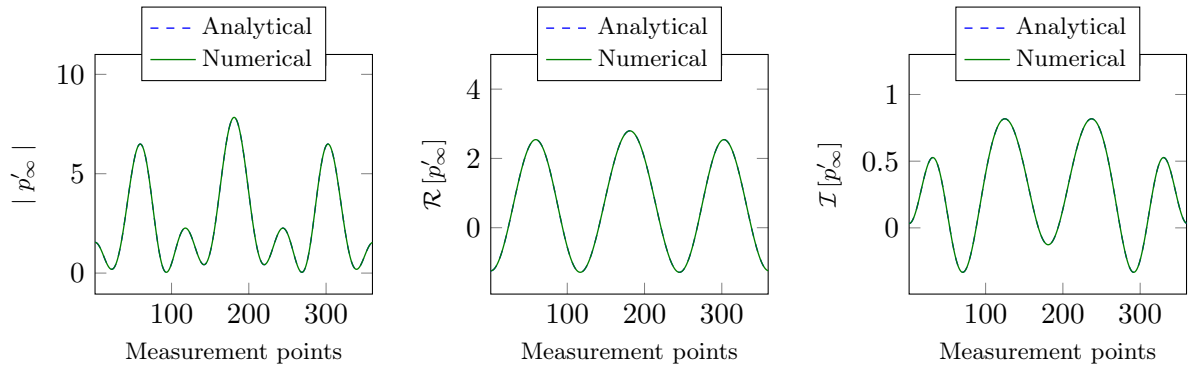

(a) Intensity (b) Real part (c) Imaginary part

Fig. 2.2.9: The analytic FFP derivative vs numeric with respect to Lamé parameter μ, for $ka = 4.3$, and corresponding to the *steel* material.

L^2-relative error(%)	$\mathcal{R}(p'_\infty)$	$\mathcal{I}(p'_\infty)$	$\lvert p'_\infty \rvert$
$ka = 1.5$	0.21	0.09	0.11
$ka = 3$	0.09	0.12	0.09
$ka = 4.5$	0.10	0.01	0.01
$ka = 7$	0.26	0.21	1.31

Tab. 2.2.4: L^2-relative error(%) results for different normalized frequencies corresponding to the Fréchet derivative with respect to μ.

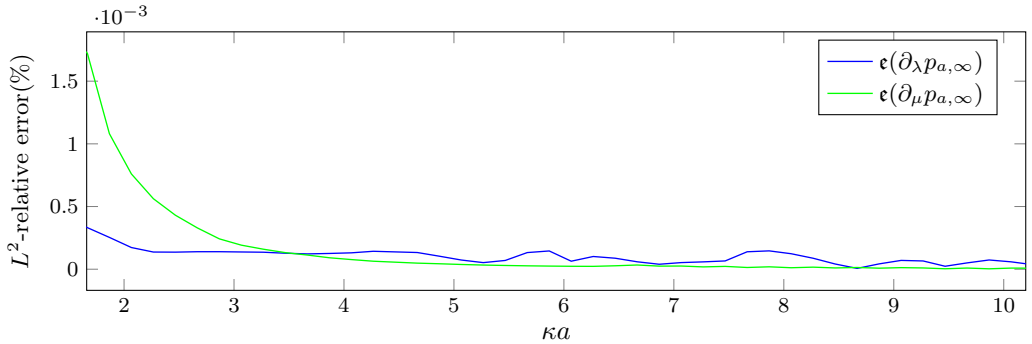

Fig. 2.2.10: Comparison between the analytical and numerical values of the Fréchet derivative of FFP, $\mathfrak{e}(\partial_\lambda p_\infty)$, $\mathfrak{e}(\partial_\mu p_\infty)$.

In comparing between λ and μ, we see that Figure 2.2.10 show that $\mathfrak{e}(\partial_\mu p_\infty)$ is always below $\mathfrak{e}(\partial_\lambda p_\infty)$, while in Figure 2.7(a)–2.7(b), the peak just before $\kappa a = 6$ is more pronounced in $\mathfrak{e}(\partial_\mu p)$ than in $\mathfrak{e}(\partial_\lambda p)$. However, apart from these minute distinctions, the error with respect to λ behaves in the same way as with respect to μ. Moreover, we observe that the error depicted in Tables 2.2.3 and 2.2.4 have been improved two times the order of magnitude in Figure 2.2.10. We conclude that the numerical computation of the FFP Fréchet derivative is validated successfully for both material parameters λ and μ, and that the accuracy level can be improve selecting higher values of elements' order or/and elements per wavelength.

Chapter 3

Solution Methodologies for the Inverse Problems

Contents

In this chapter, we consider the reconstruction of a solid immersed in a fluid from the knowledge of the far field pattern. We aim at recovering both shape and physical parameters. We introduce two solution methodologies that we call Simultaneous Reconstruction Algorithm (**SRA**) and Stepwise Reconstruction Algorithm (**SWRA**) respectively. Both are iterative algorithms based on the Newton method which are regularized thanks to the Tikhonov regularization in order to deal with the ill-posed nature of the problem. The main difference between the two algorithms is that the first one retrieves all the parameters at the same time whereas the other retrieves shape and material parameters independently. Finally, we assess the performance of the algorithms for two different configurations including the circle for which we dispose of analytical solution. We compare in particular the number of required iterations to reach a given accuracy.

3.1 The Inverse Elasto-Acoustic Scattering Problems

The inverse problems we consider aim at providing quantitative information from measurements of physical phenomena. The pressure field and displacement field have been introduced as the quantities

that we obtain as a solution to the direct problem **BVP 1**, but in practice, we do not measure none of these data. Indeed, we rather dispose of the far-field pattern p_∞ of the solution p characterizing the asymptotic behavior of the acoustic scattered field [28], as it has been previously defined in Chapter two in (1.3.2):

$$p(x) = \frac{e^{ikr}}{\sqrt{r}}\left(p_\infty\left(\frac{1}{r}\right) + \mathcal{O}\left(\frac{x}{r}\right)\right) \qquad , \qquad r = \|x\|_2 \longrightarrow +\infty \tag{3.1.1}$$

p_∞ is defined for each point $\hat{x}$ of the unitary circle C^1, and admits the following representation:

$$p_\infty(\hat{x}) = \frac{e^{i\pi/4}}{\sqrt{8\pi k}}\int_\Gamma \left(e^{-ik\hat{x}\cdot y}\frac{\partial p}{\partial \nu}(y) - \frac{\partial e^{-ik\hat{x}\cdot y}}{\partial \nu}p(y)\right) d\Gamma \tag{3.1.2}$$

where Γ still denotes the surface of the solid.

This idea of reconstructing scatterers from the far-field pattern is quite popular for physical parameters such as the boundary and the location of the obstacle [40, 62, 70, 74, 93]. In this work, we focus on the characterization of a solid Ω^s from far field patterns. The direct problem is represented by a map which associates Ω^s to p_∞ and the inverse problem consists in retrieving Ω^s from p_∞, the reconstruction of Ω^s being clarified from a set of parameters of interest.

They are many ways for defining Ω^s. In [40], the objective was to retrieve the shape of Ω^s by reconstructing its boundary Γ as a set of parameters $s_1, ..., s_{N_\Gamma}$, being N_Γ the number of shape parameters (see Appendix C for details). In this work, we propose to enrich the characterization of Ω^s by addressing the question of getting information on the constitutive parameters of the interior of Ω^s in addition to its shape.

The direct elasto-acoustic scattering problem (**BPV 1**) defines an operator F defined as

$$\begin{aligned} F: \quad \mathbb{R}^3 \times \mathbb{R}^{N_\Gamma+2} &\longrightarrow \quad \mathbb{C} \\ (\lambda, \mu, \rho, \Gamma, x_c, y_c) &\hookrightarrow \quad p_\infty(\lambda, \mu, \rho, \Gamma, x_c, x_y) \end{aligned}$$

which maps the material, shape and location parameters of the scatterer Ω^s onto the far field pattern p_∞. This map is defined first computing the pressure and displacement fields as a solution pair to **BVP 1**, and straightaway, computing the corresponding FFP from the pressure field (see Eq.3.1.2). The derivatives of the FFP are computed with the same methodology, but the derivatives of the pressure and displacement fields are solutions to **BVP 2-4** depending on the nature of the derivative. For the delicate case of the Fréchet derivative of the FFP with respect to the shape parameters the previous characterization has been proved in [34].

The measured far-field pattern usually have some errors, hence they are denoted by $\widetilde{p_\infty}$. Here, the boundary is assumed to be smooth enough so that we can parametrize it without problems of regularity. In the following, we will consider four types of inverse problems:

- **IP(1):** Given a set of measured $\widetilde{p_\infty}$ corresponding to one or multiple incident waves and assuming that density ρ, shape Γ and location parameters x_c, y_c are known, find the Lamé parameters λ and μ such that
$$F(\lambda, \mu, \rho, \Gamma, x_c, y_c) = \widetilde{p_\infty} \tag{3.1.3}$$
- **IP(2):** Given a set of measured $\widetilde{p_\infty}$ corresponding to one or multiple incident waves and assuming that density ρ and location parameters x_c, y_c are known, find the Lamé coefficients λ and μ and the shape parameters of Γ such that
$$F(\lambda, \mu, \rho, \Gamma, x_c, y_c) = \widetilde{p_\infty} \tag{3.1.4}$$

- **IP(3):** Given a set of measured $\widetilde{p_\infty}$ corresponding to one or multiple incident waves and assuming that the Lamé parameters λ and μ are known, find the density ρ, the shape Γ and the location parameters x_c, y_c such that
$$F(\lambda, \mu, \rho, \Gamma, x_c, y_c) = \widetilde{p_\infty} \tag{3.1.5}$$
The last reconstruction requires to adapt the definition of F as follows:
$$\begin{array}{rccl} F: & \mathbb{R}^5 \times \mathbb{R}^{N_\Gamma} & \longrightarrow & \mathbb{C} \\ & (\rho, V_p, V_s, \epsilon, \delta, \Gamma) & \hookrightarrow & p_\infty(\rho, V_p, V_s, \epsilon, \delta, \Gamma) \end{array} \tag{3.1.6}$$
which maps the material parameters and shape parameters of an anisotropic media onto the far field pattern p_∞ (see Appendix C for technicalities). Then, we consider

- **IP(4):** Given a set of measured $\widetilde{p_\infty}$ corresponding to one or multiple incident waves, find the density ρ, the velocities V_p, V_s, the Thomsen parameters ϵ, δ [100] and the shape Γ parameters of Γ such that
$$F(\rho, V_p, V_s, \epsilon, \delta, \Gamma) = \widetilde{p_\infty} \tag{3.1.7}$$

For the sake of simplicity, we denote by $\mathcal{P}$ the set of parameters to be retrieved from p_∞ and by F the considered different operators derived from **BVP 1**. Then, depending on the definition of $\mathcal{P}$, all these problems can be formulated in a compact way as:
$$F(\mathcal{P}) = \widetilde{p_\infty} \tag{3.1.8}$$
where p_∞ is the far field pattern of a given incident plane wave and $\widetilde{p_\infty}$ the corresponding quantity including some noise arising from measurements.

In practice, the measurements are obtained from a given set of incident plane waves. The success of the reconstruction strongly depends on the incident waves along with the frequency that are used both for the survey and the simulations. In the simplest case of acoustic scattering problems, there exist many works addressing the important question of uniqueness. The problem is to establish sufficient conditions to uniquely determine the scatterer from the far field pattern p_∞. In the case of a sound-soft obstacle, the uniqueness has been established for an infinite number of incident plane waves with distinct directions and one fixed frequency. Uniqueness has also been proven for a finite number of incident waves and one fixed wavenumber but *a priori* information is required on the size of the scatterer. In particular, if the scatterer is contained in a ball of radius R such that $kR < \pi$, the obstacle is uniquely defined by the far field pattern of one incident plane wave with wavenumber k. We refer reader to the book of Colton and Kress [28] where detailed proofs are provided including extended works to acoustic sound-hard obtacles. In [64], the case of retrieving the impedance coefficients of an acoustic obstacle is also considered.

In this manuscript, we address the case of a solid object immersed into a fluid. We propose to explore the reconstruction of the object from a numerical point of view. Some theoretical questions should be addressed to make this study complete. They will be discussed by the end of the manuscript.

In particular, we will perform generally the numerical experiments with full-aperture data (see Figure 3.1.1(a)) and some other with limited-aperture data (see Figure 3.1.1(b)) to figure out the sensitivity of the reconstruction with respect to the data.

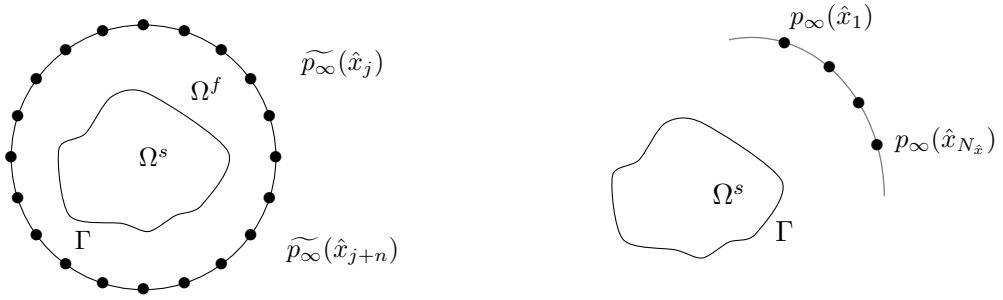

(a) Full-aperture data.

(b) Limited-aperture data.

Fig. 3.1.1: Distribution of measurements.

3.2 Regularized Iterative Methods

In this section we detail the mathematical tools that we use in order to deal with the ill-posed nature of the inverse problems. We first present the Newton algorithm we use in order to find the minimum of a nonlinear function. Then we describe the Tikhonov regularization method that is used to deal with the ill-posedness of the problem. Finally we define stopping criteria that avoid infinite loops in the iterative procedures.

3.2.1 The Newton Equation and Least-squares Formulation

In what follows, for the sake of simplicity, we consider a finite number of measurements

$$\{\widetilde{p_\infty}(\hat{x}_j) \quad : \quad 1 \leq j \leq N_M\} \tag{3.2.1}$$

with full-aperture distribution (Fig. 3.1.1(a)) corresponding to one incident wave characterized by a direction d and a fixed wavenumber k. Under these considerations, the Inverse Problem can be formulated as follows:

(IP) Given far field pattern measurements, reconstruct the set of parameters $\mathcal{P}$ corresponding to the physical properties of the obstacle Ω^s, such that

$$F(\mathcal{P})(\hat{x}_j) = \widetilde{p_\infty}(\hat{x}_j), \qquad j = 1, ..., N_M \tag{3.2.2}$$

$\{\hat{x}_j, 1 \leq j \leq N_M\}$ is a set of points of the unitary circle on which the far field pattern is evaluated and N_M stands for the number of measurements. We are thus searching for the minimum value of a nonlinear function and for that purpose, we propose to apply the Newton method.

The first step of the solution methodology consists in linearizing the problem by considering a small perturbation of $\mathcal{P}$ denoted by $\delta\mathcal{P}$. If $\overline{\mathcal{P}} = \mathcal{P} + \delta\mathcal{P}$ denotes the set of perturbed parameters, we then have, by applying a Taylor expansion around $\mathcal{P}$:

$$F\left(\overline{\mathcal{P}}\right)(\hat{x}_j) - \widetilde{p_\infty}(\hat{x}_j) = F(\mathcal{P})(\hat{x}_j) - \widetilde{p_\infty}(\hat{x}_j) + \nabla_{\mathcal{P}} F(\mathcal{P})(\hat{x}_j)\delta\mathcal{P} + \mathcal{O}(\| \delta\mathcal{P} \|) \tag{3.2.3}$$

Hence, searching for $\overline{\mathcal{P}}$ solution to $F\left(\overline{\mathcal{P}}\right)(\hat{x}_j) = \widetilde{p_\infty}(\hat{x}_j)$, we propose to compute $\delta\mathcal{P}$ as the solution to the linear system:

$$\nabla_{\mathcal{P}} F(\mathcal{P})(\hat{x}_j)\delta\mathcal{P} = \widetilde{p_\infty}(\hat{x}_j) - F(\mathcal{P})(\hat{x}_j) \qquad \text{for } 1 \leq j \leq N_M. \tag{3.2.4}$$

It is worth mentioning that in general, the number of measurements differs from the number of parameters to be retrieved. System (3.2.4) is thus not square. This is why in practice, it is replaced by a square one where the matrix of coefficients

$$\left(\nabla_{\mathcal{P}} F\left(\mathcal{P}\right)\right)_l \left(\hat{x}_j\right) \tag{3.2.5}$$

is multiplied by its transposed one.

Let J be the so-called jacobian matrix with coefficients:

$$J_{lj} = \left(\nabla_{\mathcal{P}} F\right)_l \left(\hat{x}_j\right) \qquad 1 \leq l \leq N_{\mathcal{P}}, \quad 1 \leq j \leq N_M, \tag{3.2.6}$$

where $N_{\mathcal{P}}$ denotes the number of parameters. Then, $\delta\mathcal{P}$ is computed as the solution to the square linear system:

$$\left(J^T J\right)\left(\delta\mathcal{P}\right) = J^T \left(\widetilde{p_\infty}(\hat{x}) - F\left(\mathcal{P}\right)\left(\hat{x}\right)\right), \tag{3.2.7}$$

As a conclusion, the inverse problem consists of an iterative process and at each iteration, we compute $\left(\delta\mathcal{P}\right)^n$ as a solution to

$$\left(\left(J^n\right)^T J^n\right)\left(\delta\mathcal{P}^n\right) = \left(J^n\right)^T \left(\widetilde{p_\infty}(\hat{x}) - F\left(\mathcal{P}^n\right)\left(\hat{x}\right)\right), \tag{3.2.8}$$

and the set of parameters is updated until convergence as follows:

$$\mathcal{P}^{n+1} = \mathcal{P}^n + \left(\delta\mathcal{P}\right)^n. \tag{3.2.9}$$

3.2.2 The Tikhonov Regularization Procedure

We have set the Newton method without addressing the question of ill-posedness. Following [72] and [101]), we apply the Tikhonov regularization method which consists in including a perturbation by a diagonal matrix to make the system invertible. Let α_s^n and α_m^n be the regularization parameter for shape and material parameters respectively updated at the n-th iteration. Then at each iteration, the system to be solved is given by:

$$\left(d_\alpha^n + \left(J^n\right)^T J^n\right)\left(\delta\mathcal{P}^n\right) = \left(J^n\right)^T \left(\widetilde{p_\infty}(\hat{x}) - F\left(\mathcal{P}^n\right)\left(\hat{x}\right)\right) \tag{3.2.10}$$

where d_α^n is a regularization diagonal matrix whose entries are positive and correspond to shape and material parameters (α_s^n and α_m^n resp). The convergence of the method strongly depends on the choice of d_α^n. Some theoretical strategies have been devised for choosing these regularization parameters. Among them, the Morozov's discrepancy principle [96] is often cited but limited to cases of noisy data.

We can also mention the L-curve method [52] but it is not really efficient for nonlinear problems. For instance, [68] provides nice illustrative examples of under-regularized solutions which explains why the regularization parameter is frequently chosen heuristically. In addition, different regularization parameters are used for different parameters. This why we denote them for instance by α_m for material parameters, α_s shape parameters and α_{ρ_s} for the density.

Instead of using $\widetilde{p_\infty}$, it is also current to exploit the intensity of the far field pattern as depicted in [40, 41, 62, 74]. It is defined by:

$$\overline{\widetilde{p_\infty}}\widetilde{p_\infty} \tag{3.2.11}$$

and we are then searching for the minimum value of the functional

$$\mathfrak{F}(\mathcal{P}) = A(\mathcal{P}) - \overline{\widetilde{p_\infty}}\widetilde{p_\infty}. \tag{3.2.12}$$

where $A(\mathcal{P}) = \overline{F}(\mathcal{P})F(\mathcal{P})$. The same solution methodology applies also to this formulation of the inverse problem. It is worth mentioning that the intensity is invariant with respect to the location (see D in Appendix). Hence by using this formulation, the set of parameters that we can retrieve does not include the location of the solid Ω^s. In this case, the algebraic system to be solved (instead of Eq. 3.2.10) is given by:

$$\left(d_\alpha^n + (J_A^n)^T\ J_A^n\right)(\delta\mathcal{P}^n) = (J_A^n)^T\left(\overline{\widetilde{p_\infty}(\hat{x})}\widetilde{p_\infty}(\hat{x}) - A(\mathcal{P}^n)(\hat{x})\right) \tag{3.2.13}$$

where d_α^n is a regularization diagonal matrix whose entries are positive and correspond, usually, to position parameters.

As a conclusion, the solution of the inverse problems requires to characterize the Fréchet derivatives $\nabla_{\mathcal{P}}F$ regarding the definition of $\mathcal{P}$. In the previous chapter, we have characterized a set of Fréchet derivatives that we will actually use in the following for solving a class of inverse problems.

3.2.3 Stopping Criteria

The stopping criteria and the accuracy assessment of the reconstruction process should be based on the error between the numerical solution (numerical parameters) and the exact one (actual parameters). In practice, we do not have access to the values of the real parameters since we are actually searching for them. Hence, we introduce auxiliary quantities which involve the FFP. By this way, on the one hand we introduce a stopping criteria that avoids unnecessary iterations. On the other hand, we are able to estimate the accuracy of the numerical FFP which should provide a reliable measure of accuracy, assuming that the parameters of Ω^s are uniquely defined from the FFP of one incident wave.

We denote by $\widetilde{p_\infty}$ the synthetic data, while $F(\mathcal{P}^n)$ represents the FFP computed at the n-th iteration, and $A(\mathcal{P}^n)$ the corresponding intensity. We thus introduce:

- Relative Residual (RR):

$$RR(n) = \frac{\| \overline{\widetilde{p_\infty}}\widetilde{p_\infty} - A(\mathcal{P}^n) \|_2}{\| \overline{\widetilde{p_\infty}}\widetilde{p_\infty} \|_2} \times 100 \tag{3.2.14}$$

  RR computes the relative error between the intensity of the synthetic data and the intensity of the computed FFP. This is the most widely used measurement of accuracy as demonstrated in the literature [62, 70, 74, 93]. One criteria to stop the iterations of the procedure is when this RR stops decreasing, as we interpret that we are going away from the good parameters, either stagnation. An indicator of the stagnation is the quantity:

$$\frac{\|A(\mathcal{P}^n) - A(\mathcal{P}^{n+1})\|_2}{\|A(\mathcal{P}^n)\|_2}. \tag{3.2.15}$$

  If this quantity is smaller than 0.1, as we consider that the decrease of RR is too slow, we stop the algorithm. In addition, a criterion of success reconstruction for noise-free data is considered when RR takes values below 0.1%. This quantity is explained with an illustrative example during the first experiment. On the contrary, this criteria is adapted for noisy data (see chapter 5.1 for details): a successful reconstruction is considered when the RR achieves the noise level corresponding to the experiment.

Similar quantities are defined for the reconstruction procedure that employs the FFP field (see Chapter 5.1). The corresponding Relative Residual (RR_2) is defined as follows

$$RR_2(n) = \frac{\| \widetilde{p_\infty} - F(\mathcal{P}^n) \|_2}{\| \widetilde{p_\infty} \|_2} \times 100, \tag{3.2.16}$$

and the corresponding stagnation quantity:

$$\frac{\|F(\mathcal{P}^n) - F(\mathcal{P}^{n+1})\|_2}{\|F(\mathcal{P}^n)\|_2}. \tag{3.2.17}$$

The convergence (and stagnation) criteria corresponding to this inversion procedure differs only in the Relative Residual, we compute RR_2 instead of RR in order to observe the convergence history of the reconstruction (and the corresponding stagnation quantity).

Since, in practice, we do not have any information on the set $\{s_j, 1 \leq j \leq N_\Gamma\}$, we consider the following relative error which evaluates the evolution of the parameters at each iteration. It is called :

- Updated Variations on the Shape parameters at the n-th iteration UVS:

$$UVS(n) = \frac{\left(\sum_{i=1}^{N_\Gamma} \mid s_i^{n-1} - s_i^n \mid^2\right)^{\frac{1}{2}}}{\left(\sum_{i=1}^{N_\Gamma} \mid s_i^{n-1} \mid^2\right)^{\frac{1}{2}}} \times 100 \tag{3.2.18}$$

We introduce a similar indicator for the material parameters:

- Updated Variations on the Material parameters at the n-th iteration UVM:

$$UVM(n) = \frac{\mid (\lambda^{n-1} - \lambda^n)^2 + (\mu^{n-1} - \mu^n)^2 \mid^{\frac{1}{2}}}{\mid (\lambda^{n-1})^2 + (\mu^{n-1})^2 \mid^{\frac{1}{2}}} \times 100 \tag{3.2.19}$$

It is worth mentioning that both $UVS$and $UVM$are good indicators for predicting the convergence in the sense that if they do not converge to zero, we are able to claim that the reconstruction is failing. In particular, their computation is a determining factor in whether or not the regularization parameter must be changed. Moreover even in the case of blind tests, we always have access to these quantities. Of course, the convergence of $UVS$and UVMdoes not implies the convergence to the targeted values.

Remark: Even if we know that in practice, the exact values of material and shape parameters are unknown, in order to asses the accuracy of the performance of the reconstruction, we also consider the direct error on the material parameters. For instance, for isotropic material parameters, we introduce:

- Relative Error on Material Parameters (REM):

$$REM(n) = \frac{\mid (\lambda - \lambda^n)^2 + (\mu - \mu^n)^2 \mid^{\frac{1}{2}}}{\mid \lambda^2 + \mu^2 \mid^{\frac{1}{2}}} \times 100 \tag{3.2.20}$$

- Relative Error on Shape Parameters (RES):

$$RES(n) = \frac{\left(\sum_{i=1}^{N_\Gamma} \mid s_i - s_i^n \mid^2\right)^{\frac{1}{2}}}{\left(\sum_{i=1}^{N_\Gamma} \mid s_i \mid^2\right)^{\frac{1}{2}}} \times 100 \tag{3.2.21}$$

where n stands for the number of iterations.

3.3 Setting of the Algorithms

For the sake of completeness, we describe here the algorithm corresponding to, the **IP(3)**. In order to solve the inverse problem of interest, we consider one or several measured far-field patterns $\tilde{p}_\infty(\hat{x})$, corresponding to a unique given incident wave characterized by its direction d and a wavenumber k. Under these considerations, one can formulate the Inverse Problem **IP(3)** defined in section 3.1 as follows:

IP(3) Find the Lamé coefficients λ, μ, density ρ_s, shape $s_1, ..., s_{N_\Gamma}$ and position parameters x_c, y_c such that

$$F\left(\lambda, \mu, \rho_s, \Gamma\left(s_1, ..., s_{N_\Gamma}\right), x_c, y_c\right)\left(\hat{x_j}\right) = \widetilde{p_\infty}\left(\hat{x}\right) \quad \hat{x_j} \in C^1 \qquad : \quad j = 1, ..., N_{\hat{x}} \tag{3.3.1}$$

In addition, in the literature instead of using $\widetilde{p_\infty}$, it is also current to exploit the intensity of the far field pattern as depicted in [40, 41, 62, 74], that is, $\|\widetilde{p_\infty}\|^2$. This quantity is invariant with respect to the position of the obstacle (see Appendix D), and consequently, we employ a multi-stage solution methodology to the complete reconstruction of the scatterer [63].

We first employ the intensity of the FFP to find the material parameters λ, μ, ρ_s, and the shape Γ of the scatterer, and straightaway, the FFP field to reconstruct the position parameters $\boldsymbol{x_c}$ of the scatterer. That is, the Inverse problem is divided in the following two sub-problems:

IP(3)-Stage 1 Given a set of measured FFP for one or several incident plane waves, that differ from the incident direction and/or the frequency regime, find the parameters λ, μ, ρ_s, and the shape Γ such that

$$A\left(\lambda, \mu, \rho_s, \Gamma\right)\left(\hat{x}\right) = \overline{\widetilde{p_\infty}(\hat{x})}\widetilde{p_\infty}(\hat{x}); \quad \hat{x} \in S \subseteq S^1$$

where $A\left(\lambda, \mu, \rho_s, \Gamma\right) = F\left(\lambda, \mu, \rho_s, \Gamma, \right)^2$ represents the intensity or *modulus* of the numeric FFP. Straightaway,

IP(3)-Stage 2 Given a set of measured FFP for one or several incident plane waves, that differ from the incident direction and/or the frequency regime, find the parameters $\boldsymbol{x_c}$ for the updated parameters $\lambda, \mu, \rho_s, \Gamma$ such that

$$F\left(\lambda, \mu, \rho_s, \Gamma, \boldsymbol{x_c}\right)\left(\hat{x}\right) = p_\infty(\hat{x}); \quad \hat{x} \in S \subseteq S^1 \tag{3.3.2}$$

In addition, we set two strategies for retrieving the physical properties of the solid Ω^s during the Stage 1. First of all, it is worth mentioning that the following procedures are adimensionalized algorithms, so we do not consider any order of magnitude for the parameters. The main difference of the algorithms is the strategy to retrieve the parameters. In the first algorithm, we retrieve all the parameters together while in the second one we retrieve shape and material parameters independently.

3.3.1 Algorithm 1: Simultaneous Reconstruction Algorithm (SRA)

The first procedure that we propose consists in tackling simultaneously the shape and the material parameters. This goal is achieved by the following multistage solution procedure:

Initialization of parameters $\mathcal{P}^0 = (\lambda^0, \mu^0, \rho_s^0, \Gamma^0)$, and x_c^0, y_c^0

- Stage 1, Reconstruction of material and shape parameters with $\|\widetilde{p_\infty}(\hat{x})\|^2$

  Apply regularized Newton algorithm for multiple values of shape and material regularization parameters, $(\alpha_m, \alpha_s, \alpha_{\rho_s})$ to update the shape and material parameters until **convergence** or **stagnation**

If **stagnation**, **Switch** to a lower regularization parameters $(\alpha_m, \alpha_s, \alpha_{\rho_s})$ or a higher frequency and repeat Stage 1.

- Stage 2, Reconstruction of position parameters $\mathcal{P}^0 = (x_c^0,\, y_c^0)$ with $\widetilde{p_\infty}(\hat{x})$

  Apply regularized Newton algorithm for updated position regularization parameter α_p to update the position parameters until **convergence** or **stagnation**

  If **stagnation**, **Switch** to a lower regularization parameter α_p or a higher frequency and repeat Stage 2.

The algorithm corresponding to the simultaneous reconstruction is detailed as follows:

Algorithm 1 Simultaneous Reconstruction Algorithm (**SRA**)

1: Selection of initial frequency and regularization parameter, ω^0, α
2: Initialization of parameters, $\mathcal{P}^0 = (\lambda^0, \mu^0, \rho_s^0, \Gamma^0)$ and x_c^0, y_c^0
3: $RR = 10$, $n = 0$
4: **STAGE 1**
5: **while** Relative Residual RR >Noise Level && n <MaxNumberIter **do**
6: Stagnation=100
7: **while** Stagnation> 10^{-1} && n <MaxNumberIter **do**
8: Compute Far Field Pattern Intensity $A(\mathcal{P}^n)$
9: Compute Fréchet Derivative of material and shape parameters, $\frac{\partial A}{\partial \lambda}, \frac{\partial A}{\partial \mu}, \frac{\partial A}{\partial \rho_s}, \frac{\partial A}{\partial s_i}$ $i = 1, ..., N_\Gamma$
10: Update the material and shape parameters, $\mathcal{P}^{n+1} = \mathcal{P}^n + \delta\mathcal{P}^n$
11: Stagnation= $\frac{\|A(\mathcal{P}^n) - A(\mathcal{P}^{n+1})\|_2}{\|A(\mathcal{P}^n)\|_2}$
12: Compute RR
13: n=n+1
14: **end while**
15: Decrease α_s and (or) α_m and (or) α_{ρ_s}
16: **end while**
17: Increase the frequency and go to line 2
18:
19: $RR_2 = 10$, $n = 0$, $\mathcal{P}^0 = (x_c^0, y_c^0)$
20: **STAGE 2**
21: **while** Relative Residual RR_2 >Noise Level && n <MaxNumberIter **do**
22: Stagnation=100
23: **while** Stagnation> 10^{-1} && n <MaxNumberIter **do**
24: Compute Far Field Pattern $F(\mathcal{P}^n)$
25: Compute Fréchet Derivative of position parameters, $\frac{\partial F}{\partial x_c}, \frac{\partial F}{\partial y_c}$
26: Update the position parameters, $\mathcal{P}^{n+1} = \mathcal{P}^n + \delta\mathcal{P}^n$
27: Stagnation= $\frac{\|F(\mathcal{P}^n) - F(\mathcal{P}^{n+1})\|_2}{\|F(\mathcal{P}^n)\|_2}$
28: Compute RR_2
29: n=n+1
30: **end while**
31: Decrease α_c
32: **end while**
33: If we do not converge → increase the frequency and go to line 3

MaxNumberIter is an integer number that controls the number of iterations and thus ensures that the code does not run during an infinite number of iterations. As a matter of fact, by fixing

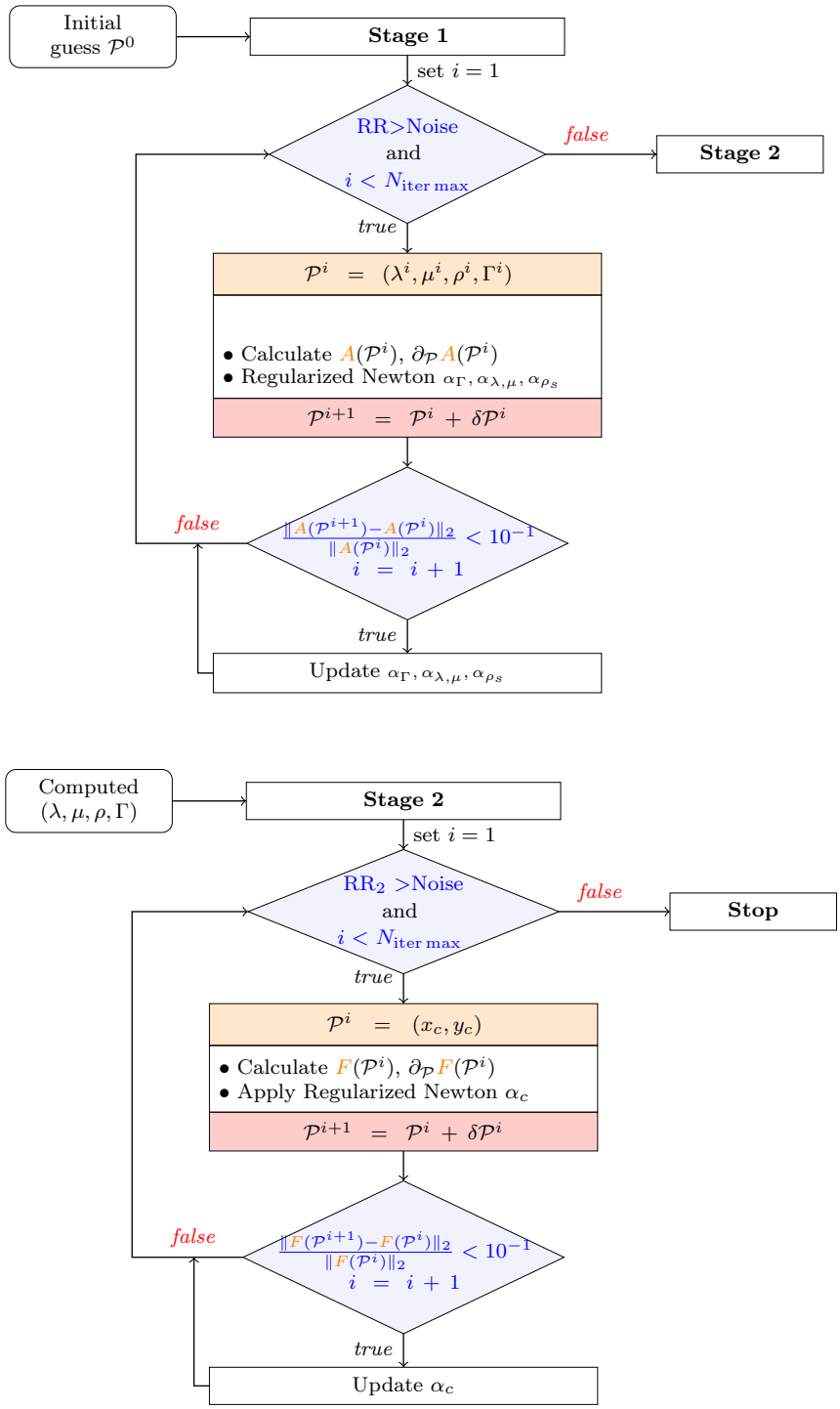

Fig. 3.3.1: Flow-illustration of the Simultaneous Reconstruction Algorithm

MaxNumberIter, the algorithm will stop even when the reconstruction fails. We do not increase the frequency systematically, we usually increase the frequency when the algorithm stagnates. It is a way for escaping from the possible local minima that might hamper the convergence of the algorithm. In our code, when it is necessary, the frequency is modified automatically thanks to a frequency step that is defined at the beginning of the simulation. This algorithm provides then a Simultaneous Reconstruction of the solid parameters and we refer to the process as Simultaneous Reconstruction Algorithm.

3.3.2 Algorithm 2: Stepwise Reconstruction Algorithm (SWRA)

The second algorithm is based on the observation that material and shape parameters are of two different nature and hence have very different impact on the far field pattern (as we will illustrate in Chapter 4 thanks to numerical results). Hence we propose to consider the reconstruction of shape and material parameters independently. The multistage solution of this procedure can be summarized as follows:

Initialization of parameters $\mathcal{P}^0 = (\lambda^0, \mu^0, \rho_s^0, \Gamma^0)$, and x_c^0, y_c^0

- Stage 1, Reconstruction of material and shape parameters with $\|\widetilde{p_\infty}(\hat{x})\|^2$

* Reconstruction of shape parameters with $\|\widetilde{p_\infty}(\hat{x})\|^2$

  - Apply regularized Newton algorithm for multiple values of shape regularization parameters, α_s to update the shape parameters until **convergence** or **stagnation**
  - If **stagnation**, **Switch** to a lower regularization parameters α_s.

* Reconstruction of material parameters with $\|\widetilde{p_\infty}(\hat{x})\|^2$

  - Apply regularized Newton algorithm for multiple values of material regularization parameters, $(\alpha_m, \alpha_{\rho_s})$ to update the material parameters until **convergence** or **stagnation**
  - If **stagnation**, **Switch** to a lower regularization parameters $(\alpha_m, \alpha_{\rho_s})$ and repeat Stage 1.

* If **convergence**, go to Stage 2

- Stage 2, Reconstruction of position parameters $\mathcal{P}^0 = (x_c^0, y_c^0)$ with $\widetilde{p_\infty}(\hat{x})$

  Apply regularized Newton algorithm for updated position regularization parameter α_p to update the position parameters until **convergence** or **stagnation**

  If **stagnation**, **Switch** to a lower regularization parameter α_p or a higher frequency and repeat Stage 2.

The second algorithm corresponding to the stepwise reconstruction is depicted as follows:

Algorithm 2 Stepwise Reconstruction Algorithm (**SWRA**)

1: Selection of initial frequency and regularization parameter, ω^0
2: Initialization of parameters, $\lambda^0, \mu^0, \rho_s^0, \Gamma^0, x_c^0, y_c^0$
3: $RR = 10$, $n = 0$, $m = 0$
4: **while** Relative Residual $RR > 10^{-2}$ && $n + m <$MaxNumberIter **do**
5: Stagnation=100
6: **while** Stagnation$> 10^{-1}$ && $n <$MaxNumberIter **do**
7: Select shape regularization parameter α_s
8: Compute Far Field Pattern intensity $A(\lambda^m, \mu^m, \rho_s^m, \Gamma^n)$
9: Compute Fréchet Derivative of shape parameters, $\frac{\partial A}{\partial s_i}$ $i = 1, ..., N_\Gamma$
10: Update the shape parameters $s_1^{n+1}, ..., s_{N_\Gamma}^{n+1}$
11: Compute RR
12: n=n+1
13: Stagnation= $\frac{\|A(\lambda^m,\mu^m,\rho_s^m,\Gamma^n)-A(\lambda^m,\mu^m,\rho_s^m,\Gamma^{n+1})\|_2}{\|A(\lambda^m,\mu^m,\rho_s^m,\Gamma^n)\|_2}$
14: **end while**
15: Decrease α_s
16: Stagnation=100, $RR = 10$
17: **while** Stagnation$> 10^{-1}$ && $m <$MaxNumberIter **do**
18: Select material regularization parameter α_m
19: Compute Far Field Pattern intensity $A(\lambda^m, \mu^m, \rho_s^m, \Gamma^n)$
20: Compute Fréchet Derivative of material parameters $\frac{\partial A}{\partial \lambda}, \frac{\partial A}{\partial \mu}, \frac{\partial A}{\partial \rho_s}$
21: Update the material parameters, $\lambda^{m+1}, \mu^{m+1}, \rho_s^{m+1}$
22: Compute RR
23: m=m+1
24: Stagnation= $\frac{\|A(\lambda^m,\mu^m,\rho_s^m,\Gamma^n)-A(\lambda^{m+1},\mu^{m+1},\rho_s^{m+1},\Gamma^n)\|_2}{\|A(\lambda^m,\mu^m,\rho_s^m,\Gamma^n)\|_2}$
25: **end while**
26: Decrease α_m
27: **end while**
28:
29: $RR_2 = 10$, $n = 0$, $\mathcal{P}^0 = (x_c^0, y_c^0)$
30: **STAGE 2**
31: **while** Relative Residual $RR_2 >$Noise Level && $n <$MaxNumberIter **do**
32: Stagnation=100
33: **while** Stagnation$> 10^{-1}$ && $n <$MaxNumberIter **do**
34: Compute Far Field Pattern $F(\mathcal{P}^n)$
35: Compute Fréchet Derivative of position parameters, $\frac{\partial F}{\partial x_c}, \frac{\partial F}{\partial y_c}$
36: Update the position parameters, $\mathcal{P}^{n+1} = \mathcal{P}^n + \delta\mathcal{P}^n$
37: Stagnation= $\frac{\|F(\mathcal{P}^n)-F(\mathcal{P}^{n+1})\|_2}{\|F(\mathcal{P}^n)\|_2}$
38: Compute RR_2
39: n=n+1
40: **end while**
41: Decrease α_c
42: **end while**
43: If we do not converge → increase the frequency and go to line 3

The Stage 2 is exactly the same in both reconstruction procedures. This is why we illustrate only the flux corresponding to Stage 1:

As in Algorithm 1, we may have to escape from local minima and for that purpose, we will change

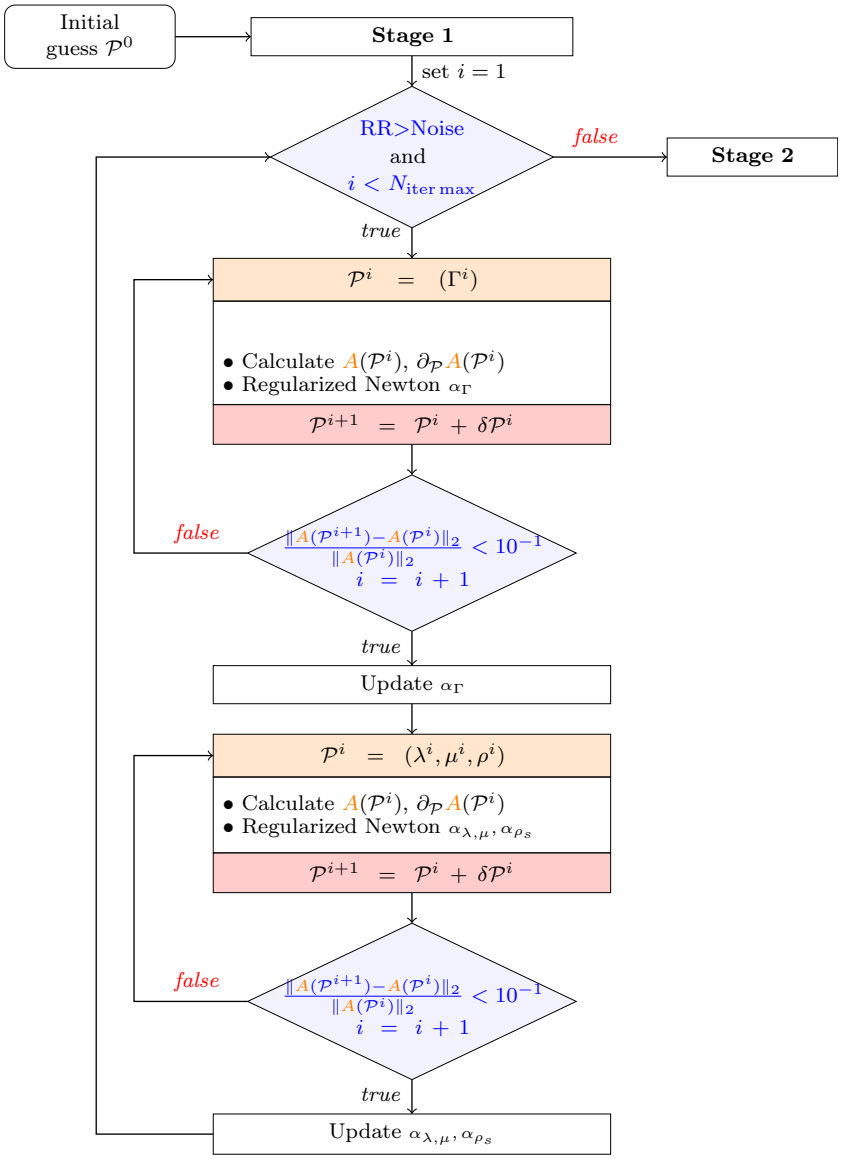

Fig. 3.3.2: Flow-illustration of the Stepwise Reconstruction Algorithm

the frequency and proceed to repeat Stage 1 and Stage 2. The difference with Algorithm 1 lies in the way of retrieving the solid features. We first address the reconstruction of the shape of the scatterer and next the material parameters.

3.3.3 Computational Complexity

The computational complexity associated to these two solution methodologies is due to the mainly solution of linear systems. For the sake of simplicity, we are going to focus only on the different computation complexity corresponding to Stage 1.

SRA consists of three different linear system solutions. The computation of the far field pattern (line 8) requires to solve one **BVP**. This procedure is carried out by a LU factorization and the solution of the associated linear system using MUMPS. The computation of the Fréchet derivatives (line 9) requires the solution of a linear system with $N_{RHS} = N_\Gamma + 2$ right-hand sides. Since the matrix to be inverted is the same matrix involved in the computation of the far field pattern, the same LU factorization can be used. Finally, the update of the material and shape parameters obtained by solving the regularized Newton equation (line 10) requires the inversion of a small $N_{RHS} \times N_{RHS}$ dense linear system, thanks to LAPACK.

The computational complexity of **SWRA** requires the solution to six linear systems. First, there are two computations of the far field pattern (lines 9 and 20) which are achieved thanks to a LU factorization using MUMPS. Then, there is the computation of the Fréchet derivatives (lines 10 and 21) that requires the solution of two linear system with $N_{RHS} = N_\Gamma$ and $N_{RHS} = 2$ right-hand sides. In both cases, the same LU factorization used in the far field pattern computation is employed. Finally, the update of shape and material parameters (lines 11 and 22) requires to invert two small dense matrices of size $N_\Gamma \times N_\Gamma$ (for the shape parameters) and 2×2 (for material parameters).

Hence, **SWRA** provides a smaller dense linear systems but requires more solutions to sparse linear systems. It is thus not possible to determine the most efficient algorithm which strongly depends on the configuration of the experiment.

3.3.4 Dimension Analysis

When expressed in the international system of units, the parameters we are looking for may have very different magnitudes. For instance, in the numerical experiments we present in the next chapters, λ and μ are about 10^{12} GPa, ρ is around 8000 kg m^{-3} and the size of the obstacle is of the order of 10^{-2}m. Hence, it is necessary to adimensionalize the problem, in particular for **SRA**, where we want to recover all parameters simultaneously. This will present from the ill conditioning of the matrix involved in the Newton equation. It will also improve the condition number of the matrix associated to the direct problem.

We start by adimensionalizing all the variables involving **BVP 1** by defining:

$$\tilde{\omega} = \frac{\omega}{\omega_0}, \qquad \tilde{c_f} = \frac{c_f}{c_0}, \qquad \tilde{\rho_s} = \frac{\rho_s}{\rho_{s,0}}, \qquad \tilde{x} = \frac{x}{x_0},$$
$$\tilde{u} = \frac{u}{u_0}, \qquad \tilde{p} = \frac{p}{p_0}, \qquad \tilde{C} = \frac{C}{C_0}, \qquad \tilde{g} = \frac{g}{p_0}.$$

Then **BVP 1** reads as:

$$\begin{aligned}
\frac{u_0 C_0}{x_0^2}\nabla\cdot\sigma(\tilde{u}) + u_0\omega_0^2\rho_0\tilde{\omega}^2\rho_s\tilde{u} &= 0,\\
\frac{p_0}{x_0^2}\Delta\tilde{p} + \frac{p_0\omega_0^2}{c_0^2}\frac{\tilde{\omega}^2}{\tilde{c_f}^2}\tilde{p} &= 0,\\
\omega_0^2 u_0\rho_{s,0}\omega^2\rho_s\tilde{u}\cdot\nu - \frac{p_0}{x_0}\frac{\partial\tilde{p}}{\partial\nu} &= \frac{p_0}{x_0}\frac{\partial\tilde{g}}{\partial\nu},\\
\frac{u_0 C_0}{x_0}\sigma(\tilde{u})\nu + p_0\tilde{p}\nu &= -p_0\tilde{g}\nu,\\
\frac{p_0}{x_0}\frac{\partial\tilde{p}}{\partial\nu} &= \frac{p_0\omega_0}{c_0}\frac{\tilde{\omega}}{\tilde{c_f}}(i-\frac{\kappa}{2})\tilde{p}.
\end{aligned}$$

which becomes:

$$\begin{aligned}
\nabla\cdot\sigma(\tilde{u}) + \tilde{\omega}^2\rho_s\tilde{u} &= 0,\\
\Delta\tilde{p} + \frac{\tilde{\omega}^2}{\tilde{c_f}^2}\tilde{p} &= 0,\\
\omega^2\rho_s\tilde{u}\cdot\nu - \frac{\partial\tilde{p}}{\partial\nu} &= \frac{\partial\tilde{g}}{\partial\nu},\\
\sigma(\tilde{u})\nu + \tilde{p}\nu &= -\tilde{g}\nu,\\
\frac{\partial\tilde{p}}{\partial\nu} &= \frac{\tilde{\omega}}{\tilde{c_f}}(i-\frac{\kappa}{2})\tilde{p}.
\end{aligned}$$

if

$$\frac{C_0}{x_0^2\omega_0^2\rho_{s,0}} = 1, \quad \frac{c_0^2}{x_0^2\omega_0^2} = 1, \quad \frac{\omega_0^2 u_0\rho_{s,0}x_0}{p_0} = 1, \quad \frac{C_0 u_0}{x_0 p_0} = 1, \quad \frac{\omega_0 x_0}{c_0} = 1.$$

Once C_0, x_0 and ω_0 are fixed, one can deduce $\rho_{s,0}$ and c_0 using

$$\rho_{s,0} = \frac{C_0}{x_0^2\omega_0^2} \text{ and } c_0 = x_0\omega_0 \tag{3.3.3}$$

Then, once p_0 is fixed, we deduced u_0 using $\dfrac{x_0 p_0}{C_0}$.

In the following, we propose to set ω_0 to the value of the considered frequency, to set $C_0 = \lambda + 2\mu$ where λ and μ are the Lamé parameters of the initial guess and to set x_0 to the characteristic length of the initial guessed obstacle. We set $p_0 = 1$Pa.

3.4 Performance Assessment: a comparison study

The main interest of this section, is to see the different effect of applying **SRA** or **SWRA**. For the sake of simplicity, we consider that the density and position parameters are known, that is, IP(2). Therefore, in order to assess the performance of the two algorithms, we employ them on IP(2) using noise-free FFP, full aperture data and only one frequency. To this end, we consider two different scatterers and two distinct materials: (a) a disk shaped obstacle made by *steel* and (b) an elliptic scatterer made by *aluminium* (see Figure 3.4.1).

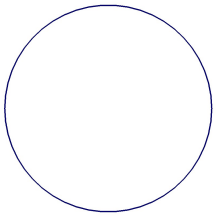

(a) Disk shaped scatterer.

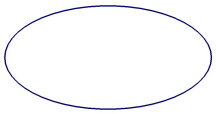

(b) Ellipse shaped scatterer.

Fig. 3.4.1: Considered obstacles

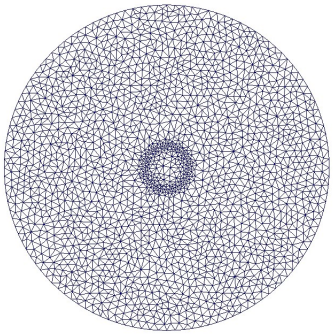

(a) Mesh corresponding to the Circle case

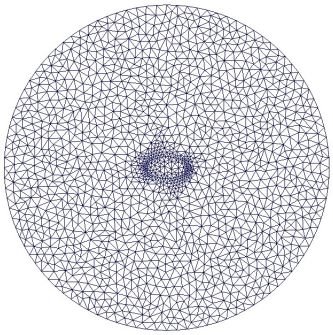

(b) Mesh corresponding to the Ellipse case

Fig. 3.4.2: Mesh illustration

3.4.1 The Case of a Circular Shaped Domain

Due to the high accuracy level between the analytical and numerical solutions to **BVPs** for the disk shaped scatterer, we use the IPDG method for the following experiments, and this is why we consider as the external boundary a circle with radius $b = 7.5$cm. The target of circle made of *steel* is a radius $a = 1$cm with the Lamé coefficients $\lambda = 115.4$GPa, $\mu = 76.9$GPa depicted in Table 3.4.1. The densities are $\rho_f = 1000$ kg m^{-3} and $\rho_s = 7900$ kg m^{-3} for the fluid and solid mediums respectively. The initial guesses for shape and material parameters detailed in Table 3.4.1 corresponds to the relative errors of 50% on the shape parameter, and 56.68% and 34.98% respectively on λ and μ. It is thus set far enough to be outside the resonance region. It means that the size of the computational domain allows to compute the FFP correctly. The mesh corresponding to this case is illustrated in Figure 3.4.2(a).

The pressure and displacement fields are created numerically by employing the IPDG code introduced in Chapter 2 and then the FFP measurements are calculated following 3.1.2. The most computationally intensive part is the first step, and in the following we will detail the parameters used for the IPDG computation. For the present experiment, synthetic measurements are computed with a fifth order finite element method applied on a mesh sized in such a way there are five points per wavelength. We then produce full-aperture data by storing the values of the FFP at 360 points of the unitary circle. It is worth mentioning that during the reconstruction process, we compute the numerical FFP by using the same finite element method but with only three points per wavelength. We then avoid making an inverse crime [28] and in the same time, we limit the computational costs by

applying a less accurate numerical method.

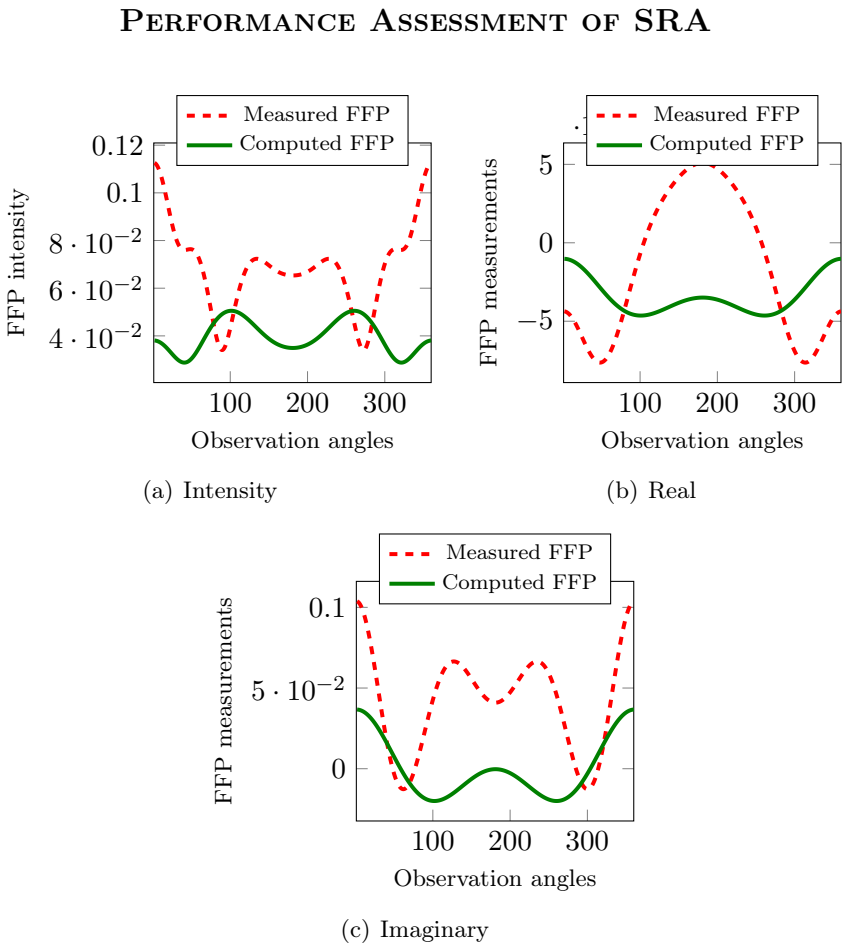

Fig. 3.4.3: The measured and computed FFPs for the target and initial guess respectively, for the disk shaped scatter made of *steel*, and $ka = 2.67$.

Our objective is now to study the impact of the regularization parameters on the reconstruction of the solid. We present some of the results corresponding to two experiments. The same regularization parameter is kept during the first experiment (see the corresponding convergence history in Figure 3.4.4 to observe the evolution of the relative residual), while during the second one the regularization parameters are updated.

Despite the convergence observable at Figure 3.4.4 and the decay on UVSdepicted in Figure 3.4.5, the reality is that the relative residual of 4.95 10^{-1}% at the 15th iteration is in fact composed of 3.63 10^{-2}% of RES and 39.44% of REM. We are thus observing that the FFP is quite insensitive to the material parameters. Performing other experiments, we have seen that it is necessary to make RR decrease below 0.1% to recover both shape and material parameters. Therefore, we decide to define this level of 0.1% as stopping criterion or criterion of success. In the case of the circle, this quantity has been reached decreasing the material regularization parameter α_m, as we will appreciate in the following experiment. Moreover, several regularization parameters have been tested but only the best results have been selected.

The selected blind-guess (see Table 3.4.3) leads to start outside the pre-asymptotic convergence region. Being in the pre-asymptotic convergence region means that RR is large but is decreasing.

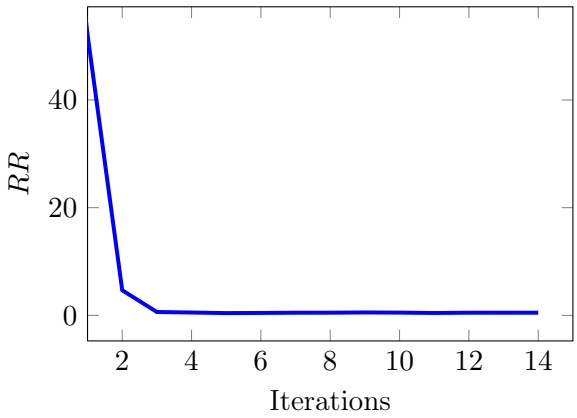

Fig. 3.4.4: Convergence history of **SRA** for a *steel* disk shaped scatterer with $a = 1cm$, $ka = 2.67$. Regularization parameters $\alpha_m = 10^{-2}$, $\alpha_s = 1$. Noise level= 0%.

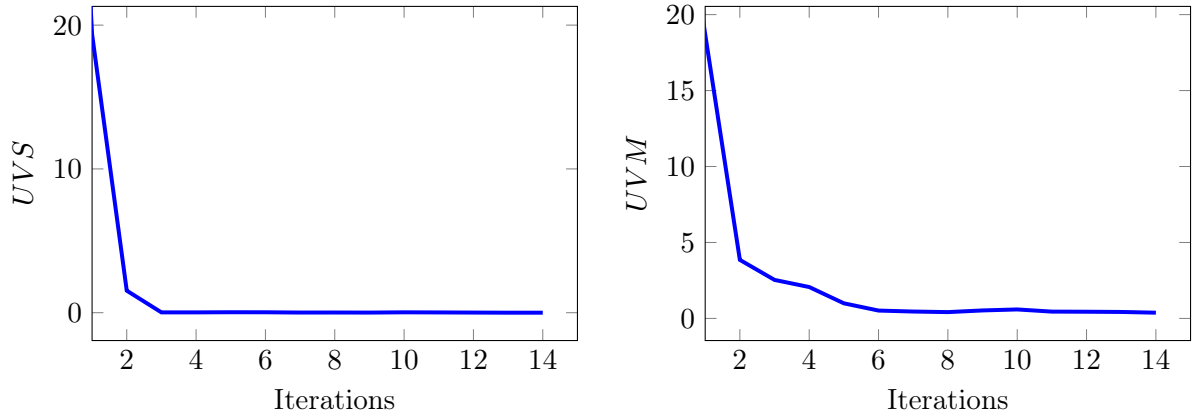

(a) Shape parameters

(b) Material parameters

Fig. 3.4.5: $UVS$and $UVM$of **SRA** for a *steel* disk shaped scatterer with $a = 1cm$, $ka = 2.67$. Regularization parameters $\alpha_m = 10^{-2}$, $\alpha_s = 1$. Noise level= 0%.

Parameter	**Target**	**Initial Guess**	**Computed**	**Relative error at convergence (%)**	
a	1	0.5	1.0004	$3.63\ 10^{-2}$	
λ	115.4	50	60.8	47.32	**REM**
μ	76.9	50	79.9	3.99	39.4

Tab. 3.4.1: Target, initial guess and computed parameters corresponding to the disk shaped scatterer case, after 15 iterations of **SRA**, constant regularization parameters $\alpha_m = 10^{-2}$, $\alpha_s = 1$, $ka = 2.67$, Noise level= 0%

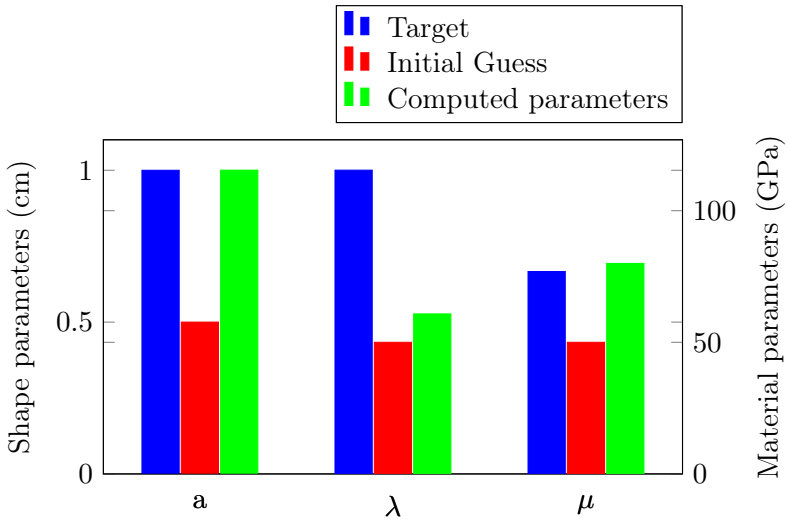

Fig. 3.4.6: Target, initial guess and computed parameters corresponding to the disk shaped scatterer case, after 15 iterations of **SRA**, constant regularization parameters $\alpha_m = 10^{-2}$, $\alpha_s = 1$, $ka = 2.67$, Noise level= 0%.

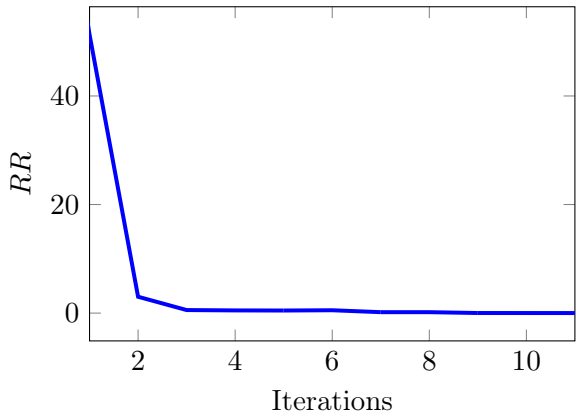

Fig. 3.4.7: Convergence history of **SRA** for a *steel* disk shaped scatterer with $a = 1cm$, $ka = 2.67$. Updated regularization parameters $\alpha_m = 10^{-2}, 10^{-4}, 10^{-5}, 0$, $\alpha_s = 1, 0.1$. Noise level= 0%.

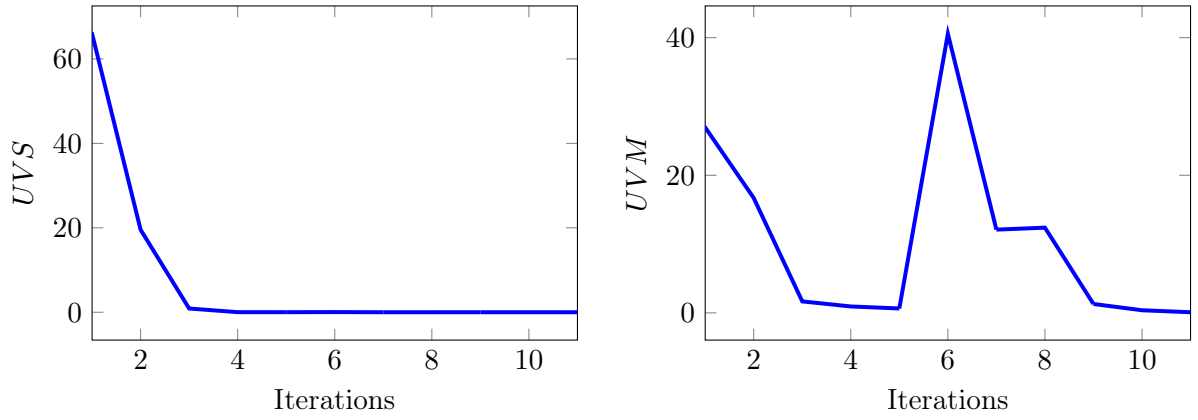

(a) Shape parameters

(b) Material parameters

Fig. 3.4.8: *UVS*and *UVM*of **SRA** for a *steel* disk shaped scatterer with $a = 1cm$, $ka = 2.67$. Updated regularization parameters $\alpha_m = 10^{-2}, 10^{-5}, 0$, $\alpha_s = 1, 0.1$. Noise level= 0%.

♯ iter(n)	RR	REM	RES
0	106.92	50.99	50
1	51.3	44.26	17.02
2	3.01	42.15	0.81
3	0.56	41.78	$6.6 \cdot 10^{-2}$
4	0.49	41.44	$4.7 \cdot 10^{-2}$

(a) $\alpha_m = 10^{-2}$, $\alpha_s = 1$.

♯ iter(n)	RR	REM	RES
5	0.52	40.77	$2.74 \cdot 10^{-2}$
6	0.17	12.15	$1.13 \cdot 10^{-3}$

(b) $\alpha_m = 10^{-5}$, $\alpha_s = 1$.

♯ iter(n)	RR	REM	RES
7	0.17	1.25	$4.84 \cdot 10^{-4}$
8	$1.6 \cdot 10^{-2}$	0.99	$1.28 \cdot 10^{-4}$

(c) $\alpha_m = 10^{-5}$, $\alpha_s = 0.1$.

♯ iter(n)	RR	REM	RES
9	$1.23 \cdot 10^{-2}$	$9.55 \cdot 10^{-2}$	$2.77 \cdot 10^{-4}$
10	$8.87 \cdot 10^{-3}$	$3.25 \cdot 10^{-3}$	$1.95 \cdot 10^{-4}$

(d) $\alpha_m = 0$, $\alpha_s = 0.1$.

Tab. 3.4.2: **SRA** for a *steel* disk shaped scatterer with $a = 1cm$, $ka = 2.67$. Noise level= 0%.

Parameter	**Target**	**Initial Guess**	**Computed**	**Relative error at convergence (%)**	
a	1	0.5	1.00	$1.95\ 10^{-4}$	
λ	115.4	50	115.3969	$2.7\ 10^{-3}$	**REM**
μ	76.9	50	76.8967	$4.3\ 10^{-3}$	$3.25\ 10^{-3}$

Tab. 3.4.3: Initial guess and target corresponding to the disk shaped scatterer case, after 10 iterations of **SRA**, updated regularization parameters $\alpha_m = 10^{-2}, 10^{-4}, 10^{-5}, 0$, $\alpha_s = 1, 0.1$, Noise level= 0%.

The experiment is summarized in Table 3.4.3. We can see in Figure 3.4.3 the considerable difference between the FFP corresponding to the target and the initial guess, meaning that we have done a blind choice of initial guess. The convergence history of that experiment is depicted in Tables 3.4.2 (a)-(b)-(c) and (d) and illustrated in Figure 3.4.7. During the first 4 iterations (Table 3.4.2(a)), RR decays but is still beyond the success criterion of 0.1%. Then we modify the value of α_m and use $\alpha_m = 10^{-5}$. We do not change the value of α_s since RES has reached a good value even after the first four iterations. For $\alpha_m = 10^{-5}$ (Table 3.4.2(b)), we see that RR almost reaches 0.1% and to ensure the success of the reconstruction we use next $\alpha_m = 10^{-5}$ and change α_s into $\alpha_s = 10^{-1}$ (Table 3.4.2(c)). Then, RR achieves 0.016% and the convergence of the iterative method is confirmed by changing α_m into $\alpha_m = 0$ and $\alpha_s = 10^{-1}$(Table 3.4.2(d)). The relative residual is largely below 0.1% and so do both REM and RES at the 10-th iteration.

Next, it is interesting to confront the behavior of UVMduring the two experiments. When the regularization parameter is constant, in Figure 3.4.5(b) we have a curve that depicts a phenomenon that might be considered as a successful reconstruction of the solid. Indeed, the curve is decaying, and stabilizes itself on a value that is close to zero. Unfortunately, the reconstruction has not happened since the material parameters are far from being retrieved after 14 iterations (see Table 3.4.1). When we adopt the regularization parameter, Figure 3.4.8(b) displays a discontinuous curve which could be interpreted as an unsuccessful story. In fact, the discontinuity events correspond to each updating of the regularization parameters and the figure displays a successful reconstruction.

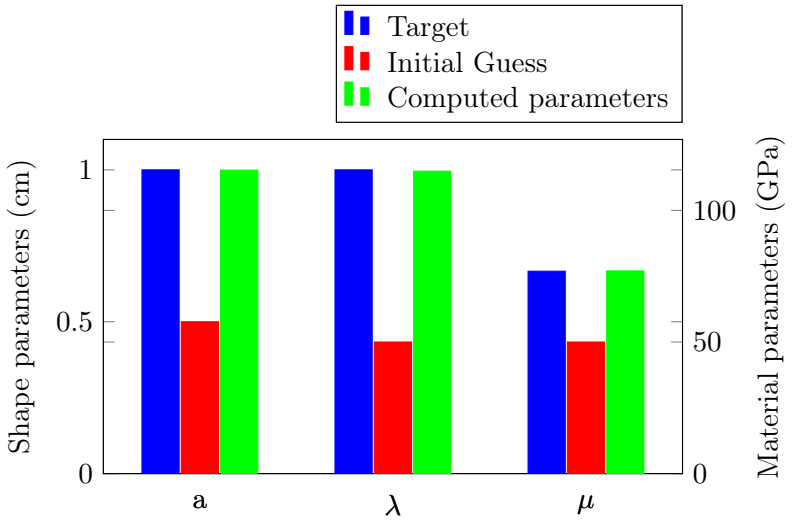

Fig. 3.4.9: Initial guess and target corresponding to the disk shaped scatterer case, after 15 iterations of **SRA**, updated regularization parameters $\alpha_m = 10^{-2}, 10^{-4}, 10^{-5}, 0$, $\alpha_s = 1, 0.1$, $ka = 2.67$, Noise level= 0%.

Parameter	**Target**	**Initial Guess**	**Computed**	**Relative error at convergence (%)**	
a	1	0.5	0.99	$3.3\ 10^{-3}$	
λ	115.4	50	115.39	$1.9\ 10^{-3}$	**REM**
μ	76.9	50	76.9	$6.8\ 10^{-5}$	$1.59\ 10^{-3}$

Tab. 3.4.4: Target, initial guess and computed parameters corresponding to the disk shaped scatterer case, 21 iterations of **SWRA**, updated regularization parameters $\alpha_m = 10^{-4}, 10^{-6}$, $\alpha_s = 10^{-2}$, $ka = 2.67$, Noise level= 0%

Performance Assessment of SWRA

We reproduce the same experiment than before but now we use the the stepwise method **SWRA**. The objective is to obtain the same level of accuracy as with **SRA**. We start with retrieving the shape (see Table 3.4.5(a)). We see that in 4 iterations, the relative residual reaches 5%. Then we move on reconstructing the material parameters and perform 11 iterations with $\alpha_m = 10^{-4}$ (Table 3.4.5(b)). Then the relative residual reaches 0.01% but the error on the material parameters is still 1.35%. So we go back to the recovering of the shape by using $\alpha_s = 10^{-2}$ (see Table 3.4.5(c)) and in 4 iterations, we have $RR = 1.78\%\ 10^{-2}$ which is still beyond the targeted value of $4.84\ 10^{-2}\%$. Then, we perform two iterations focusing on the material parameters with $\alpha_m = 10^{-6}$ and we finally have $RR = 4.09\ 10^{-4}\%$.

Conclusion

The conclusion is that we can obtain the same equality of reconstruction with the two different algorithms. Nevertheless, at least in the case of a very simple shape, we observe that the simultaneous reconstruction requires less iterations (10 vs 21) than the step-wise approach. To confirm this conclusion, we propose to conduct the same experiments but this time, we consider an obstacle of *aluminium* with an elliptic boundary parametrized with a_1 and a_2.

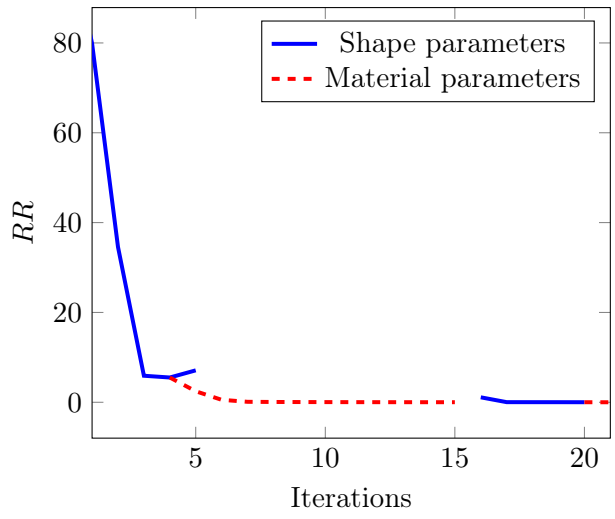

(a) Convergence history

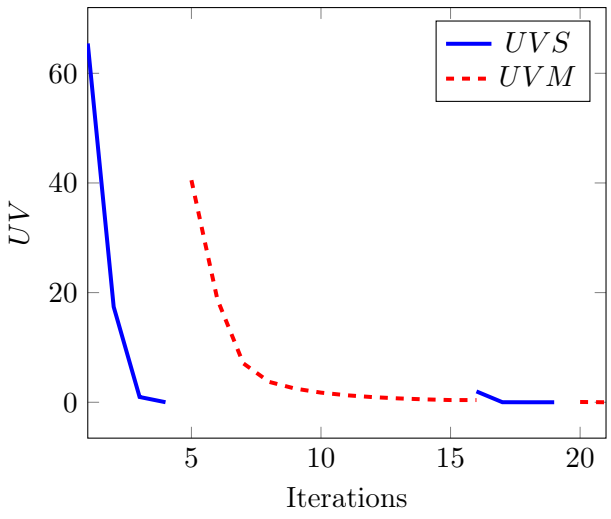

(b) Shape and material parameters

Fig. 3.4.10: Convergence history and $UVS$and $UVM$of the case of a disk shaped satterer with $a = 1cm$, $\lambda = 115.4$GPa, $\mu = 76.9$GPa, $\rho_s = 7900kgm^{-3}$, $ka = 2.67$ **SWRA**, updated regularization parameters $\alpha_m = 10^{-4}, 10^{-6}$, $\alpha_s = 10^{-2}$, Noise level= 0%.

♯ iter(n)	RR	RES
0	106.92	50
1	79.88	23.18
2	34.58	17.28
3	5.9	2.88
4	5.51	1.94
5	7.11	1.95

(a) $\alpha_s = 1$.

♯ iter(n)	RR	REM
5	2.45	37.55
6	0.55	17.96
7	0.1	12.39
8	$6.61 \cdot 10^{-2}$	9.05
9	$4.83 \cdot 10^{-2}$	6.73
10	$3.59 \cdot 10^{-2}$	5.07
11	$2.7 \cdot 10^{-2}$	3.85
12	$2.05 \cdot 10^{-2}$	2.94
13	$1.57 \cdot 10^{-2}$	2.26
14	$1.2 \cdot 10^{-2}$	1.74
15	$1.1 \cdot 10^{-2}$	1.34

(b) $\alpha_m = 10^{-4}$.

♯ iter(n)	RR	RES
16	1.1	$1.01 \cdot 10^{-2}$
17	$2.46 \cdot 10^{-2}$	$1.06 \cdot 10^{-4}$
18	$2.05 \cdot 10^{-2}$	$8.59 \cdot 10^{-4}$
19	$1.78 \cdot 10^{-2}$	$3.3 \cdot 10^{-3}$

(c) $\alpha_s = 10^{-2}$.

♯ iter(n)	RR	REM
20	$9.23 \cdot 10^{-3}$	$5.32 \cdot 10^{-2}$
21	$4.09 \cdot 10^{-4}$	$1.59 \cdot 10^{-3}$

(d) $\alpha_m = 10^{-6}$.

Tab. 3.4.5: Four steps of **SWRA** for a *steel* disk shaped scatterer with $a = 1cm$, $ka = 2.67$. Noise level= 0%.

3.4.2 The Case of an Elliptic Shaped Domain

Elastic medium *Aluminium*	λ	μ
Target (GPa)	51.09	26.32
Initial Guess (GPa)	30	50
Relative Errors (%)	41.28	89.99

Tab. 3.4.6: Lamé coefficients corresponding to the *aluminium*.

	s_1	s_2
Target (cm)	1.00	0.50
Initial Guess (cm)	0.75	0.75
Relative Error (%)	25	50

Tab. 3.4.7: Shape parameters: target vs. initial guess for the elliptic shape scatterer.

We reproduce the same experiments as before but now the solid is an elliptic shape obstacle made of *aluminium*, whose target and initial guess are depicted in Tables 3.4.6-3.4.7 for material and shape parameters respectively. The selected normalized frequency is $ka = 1.33$ (for $a = min\{a_1, a_2\}$), and the corresponding impact on the FFP for the target and initial guess is illustrated in Figure 3.4.11. The relative errors corresponding to the initial guess described at Tables 3.4.6-3.4.7 are 55.17% on material parameters and 31.62% on shape parameters respectively.

Performance Assessment of SRA

The convergence history depicted in Figure 3.4.12 indicates that the proposed computational procedure is applied outside the pre-asymptotic convergence region (the relative residual is over 127.34%) and converges after 12 iterations to a relative residual of about 1.57 10^{-3}%. At convergence, the relative error on the reconstructed Lamé parameters is 7.15 10^{-3}% whereas the exact values of the shape parameters are delivered as summarized in Table 3.4.8. The selected regularization parameters have been the following: $\alpha_m = 1, 10^{-3}, 10^{-5}, 0$ and $\alpha_s = 1, 10^{-1}, 10^{-2}$.

The reconstruction is divided in four steps detailed in Tables 3.4.9 (a)-(b)-(c) and (d) respectively. The first selected pair of regularization parameters $\alpha_m = 1$ - $\alpha_s = 1$ leads a considerable decrease on the relative residual as we can observe in Fig. 3.4.12 until stagnation in iteration 5 (as specified in Table 3.4.9(a)). This decrease is accompanied with the drop of the *UVS*, illustrated in Fig. 3.4.13(a), corresponding to the big influence of the shape parameters. The shape parameters are remarkably updated if we examine the *RES* in Table 3.4.9(a), while the material parameters are almost frozen. Then, the selected pair of regularization parameters has been $\alpha_m = 10^{-3}$ - $\alpha_s = 10^{-1}$, which leads to update the material parameters slightly. We do not observe remarkable changes in the *UVS* and *UVM* corresponding to this step in Figure 3.4.13(a) and (b) respectively, but the parameters are slightly updated as we observe the evolution of *RES* and *REM* in Table 3.4.9(b). At step 3, we decrease a bit more the pair of regularization parameters until $\alpha_m = 10^{-5}$ - $\alpha_s = 10^{-2}$, which has an immediate effect on the relative residual as depicted in Table 3.4.9(c). Observing the *UVM* from iteration 8 to 11 in Figure 3.4.13(a), we deduce that the material parameters have been successfully updated, which is true regarding *REM* in Table 3.4.9(c). We have already reached the relative residual of 9.61 10^{-1}%, that is, the criterion of a successful experiment. Even though, in order to obtain the best accuracy

possible, we carry out the last step with regularization parameters $\alpha_m = 0$ and $\alpha_s = 10^{-2}$, attaining the final errors of 7.15 10^{-3}% and 6.53 10^{-5}% on material and shape parameters respectively.

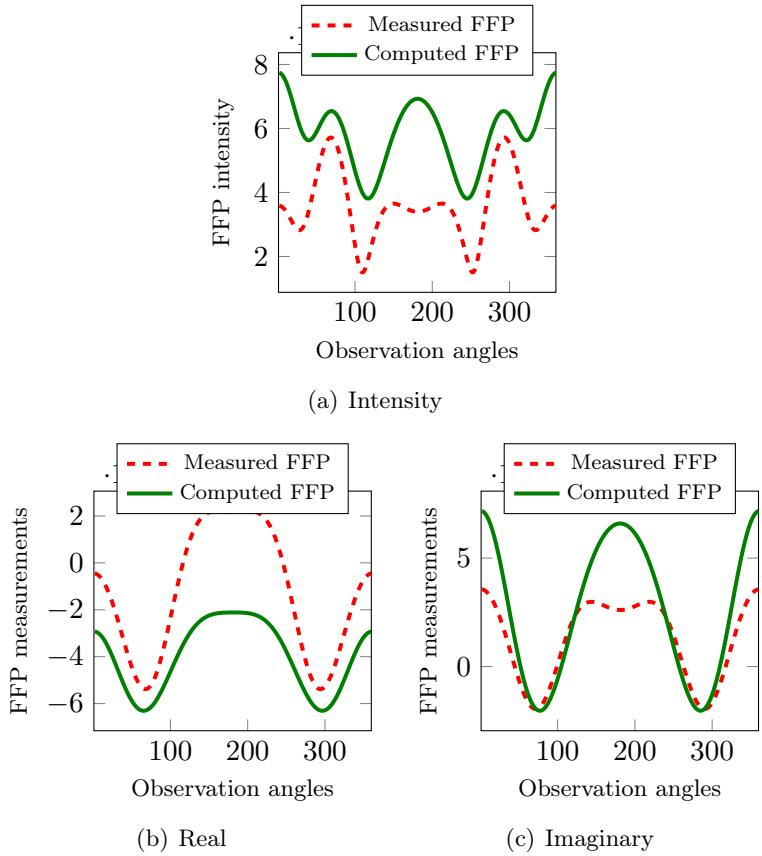

(a) Intensity

(b) Real

(c) Imaginary

Fig. 3.4.11: The measured and computed FFPs for the target and initial guess respectively, for $k = 1.33$, ellipse case.

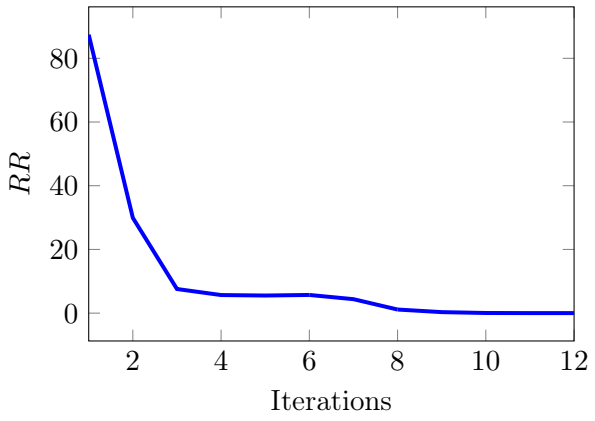

Fig. 3.4.12: Convergence history of **SRA** for an *aluminium* elliptic shaped scatterer with radius $a_1 = 10mm$, $a_2 = 5mm$, $ka = 1.33$, updated regularization parameters $\alpha_m = 1, 10^{-3}, 10^{-5}, 0$, $\alpha_s = 1, 10^{-1}, 10^{-2}$. Noise level= 0%.

Parameter	Target	Initial Guess	Computed	Relative error at convergence (%)	
a_1	1	0.75	0.999996	$2.28\ 10^{-5}$	**RES**
a_2	0.5	0.75	0.500006	$1.39\ 10^{-4}$	$6.53\ 10^{-5}$
λ	51.09	30	51.091	$9.8\ 10^{-3}$	**REM**
μ	26.32	50	26.316	$2\ 10^{-3}$	$7.15\ 10^{-3}$

Tab. 3.4.8: Target and initial guess corresponding to the ellipse shaped scatterer case, 12 iterations of **SRA**, updated regularization parameters $\alpha_m = 1, 10^{-3}, 10^{-5}, 0$, $\alpha_s = 1, 10^{-1}, 10^{-2}$, noise level= 0%.

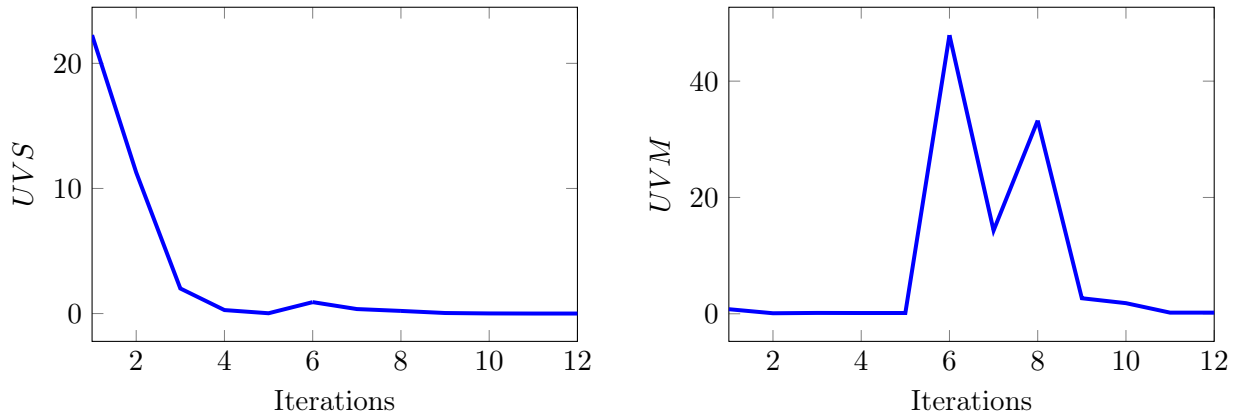

(a) Shape parameters

(b) Material parameters

Fig. 3.4.13: $UVS$and $UVM$of an elliptical-shaped scatterer with radius $a_1 = 10mm$, $a_2 = 5mm$, $ka = 1.33$ **SRA**, updated regularization parameters $\alpha_m = 1, 10^{-3}, 10^{-5}, 0$, $\alpha_s = 1, 10^{-1}, 10^{-2}$, noise level= 0%.

♯ iter(n)	RR	REM	RES
0	127.34	55.18	31.36
1	87.42	55.24	16.43
2	29.92	55.55	11.67
3	7.57	55.63	1.99
4	5.68	55.51	1.09
5	5.53	55.41	1.09

(a) $\alpha_m = 1$, $\alpha_s = 1$.

♯ iter(n)	RR	REM	RES
6	5.71	36.8	0.18
7	4.38	28.98	0.18

(b) $\alpha_m = 10^{-3}$, $\alpha_s = 10^{-1}$.

♯ iter(n)	RR	REM	RES
8	1.13	4.16	$3.5 \cdot 10^{-2}$
9	0.32	1.64	$9.16 \cdot 10^{-3}$
10	$4.33 \cdot 10^{-2}$	0.17	$1.45 \cdot 10^{-3}$
11	$9.61 \cdot 10^{-3}$	$3.43 \cdot 10^{-2}$	$2.34 \cdot 10^{-4}$

(c) $\alpha_m = 10^{-5}$, $\alpha_s = 10^{-2}$.

♯ iter(n)	RR	REM	RES
12	$1.57 \cdot 10^{-3}$	$7.15 \cdot 10^{-3}$	$6.53 \cdot 10^{-5}$

(d) $\alpha_m = 0$, $\alpha_s = 10^{-2}$.

Tab. 3.4.9: **SRA** for a *aluminium* ellipse shaped scatterer, $ka = 1.33$, noise level= 0%.

Performance Assessment of SWRA

We see that the final reconstruction of physical properties of the ellipse shaped obstacle using the **SWRA** (see the final reconstruction in Table 3.4.10) is almost the same than the one obtained with **SRA** (see summary in Table 3.4.8). In this case too, the number of iterations has been larger than the number of iterations corresponding to **SRA**, (23 *vs* 12). We can observe in Figure 3.4.14(a) that the relative residual decreases considerably during the first step corresponding to the shape reconstruction with $\alpha_s = 1$. The fast decay of both RR together with UVSillustrated in Figures 3.4.14(a) and (b) respectively, makes consider that the shape has been successfully approximated. This idea can be validated in Table 3.4.11(a). In addition, during the step 2 with $\alpha_m = 10^{-2}$, the material parameters seems to have a considerably good reconstruction regarding the evolution of UVM3.4.14(b) together with the decrease of the relative residual 3.4.14(a). We observe that, indeed, the REM has decreased as depicted in Table 3.4.11(b). The next steps cause a little increase on the RR from the last iteration 10 of step 2 (from $RR = 1.06\%$ to $RR = 4.09\%$). We notice this sometimes happens when updating the regularization parameters or, as it happens in this case, when we change the direction of the reconstruction from one parameter to other. We observe that the relative residual decays as the UVS(see Figures 3.4.14(a) and (b) respectively) for $\alpha_s = 10^{-1}$. Straightaway, the selection of $\alpha_m = 10^{-4}$ has a considerable impact on the UVM(see Figure 3.4.14(b)), as a signal that the material parameters have been successively updated. We confirm this idea regarding REM in Table 3.4.11(d). We see that in the end of step 4, the criteria of a successful experiment has been reached, but we add two step, one per different parameters, in order to obtain the most accurate results as possible. The final reconstruction, in Table 3.4.10, is similar than the one obtained by **SRA**.

Parameter	**Target**	**Initial Guess**	**Computed**	**Relative error at convergence (%)**	
a_1	1	0.75	0.999996	$3.21\ 10^{-4}$	**RES**
a_2	0.5	0.75	0.499990	$1.9\ 10^{-3}$	$9.01\ 10^{-4}$
λ	51.09	30	51.088	$8.29\ 10^{-5}$	**REM**
μ	26.32	50	26.317	$3.78\ 10^{-3}$	$1.73\ 10^{-3}$

Tab. 3.4.10: Target, initial guess and computed parameters corresponding to the ellipse shaped scatterer case, iterations of **SWRA**, updated regularization parameters $\alpha_m = 10^{-2}, 10^{-4}, 10^{-6}$, $\alpha_s = 1, 10^{-1}, 10^{-2}$, $ka = 1.33$, Noise level= 0%.

Conclusion

As a conclusion, the two different methodologies deliver results with the same accuracy, even if the **SWRA** requires more iterations. Consequently, for the remainder of the document, we use only the **SRA**. In addition, we remind that in practice we do not have access to the RES and REM values, so in order to create a predictive algorithm, we should focus mainly on RR, $UVS$and UVMmeasurements. However, in this chapter, the selection of the right regularization parameters has been carried out depending on the evolution of RES and REM as it was not sufficient to check RR, $UVS$and $UVM$to get a successful reconstruction. All these difficulties motivate the following Chapter.

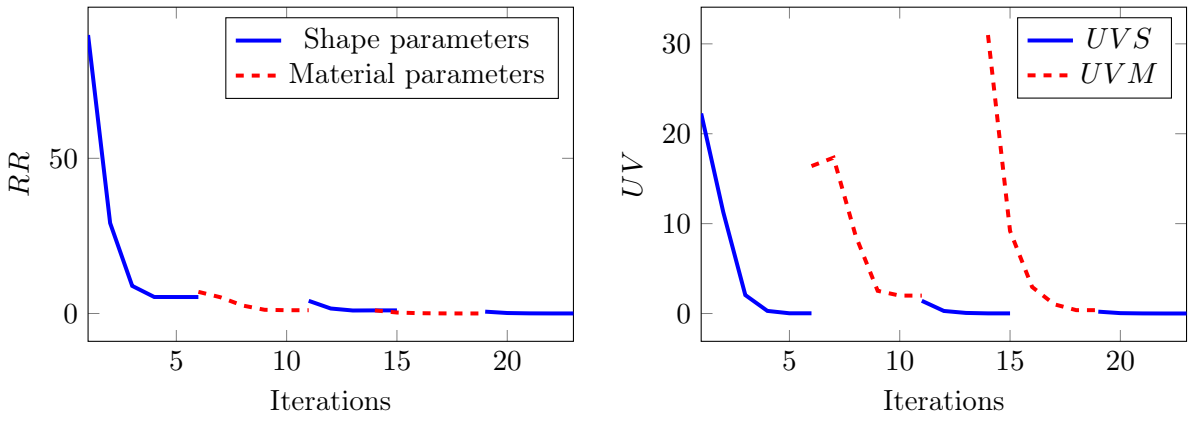

(a) Convergence history

(b) Shape and material parameters

Fig. 3.4.14: Convergence history, and $UVS$and $UVM$of **SWRA** for an *aluminium* elliptic shaped scatterer with radius $a_1 = 10mm$, $a_2 = 5mm$, updated regularization parameters $\alpha_m = 10^{-2}, 10^{-4}, 10^{-6}$, $\alpha_s = 1, 10^{-1}, 10^{-2}$, Noise level= 0%.

♯ iter(n)	RR	RES
0	127.34	31.36
1	89.72	17.43
2	29.13	11.67
3	8.9	2.02
4	5.32	1.07
5	5.31	1.08

(a) $\alpha_s = 1$.

♯ iter(n)	RR	REM
6	6.98	51.72
7	5.23	45.21
8	2.58	39.62
9	1.19	37.76
10	1.06	36.29

(b) $\alpha_m = 10^{-2}$.

♯ iter(n)	RR	RES
11	4.09	0.36
12	1.61	0.16
13	0.97	0.19
14	1	0.18

(c) $\alpha_s = 10^{-1}$.

♯ iter(n)	RR	REM
14	1	12.61
15	0.31	4.43
16	$9.95 \cdot 10^{-2}$	1.59
17	$3.53 \cdot 10^{-2}$	0.58
18	$1.29 \cdot 10^{-2}$	0.22

(d) $\alpha_m = 10^{-4}$.

♯ iter(n)	RR	RES
19	0.6	$3.35 \cdot 10^{-2}$
20	0.15	$8.62 \cdot 10^{-3}$
21	$4.58 \cdot 10^{-2}$	$2.75 \cdot 10^{-3}$
22	$1.84 \cdot 10^{-2}$	$9.01 \cdot 10^{-4}$

(e) $\alpha_s = 10^{-2}$.

♯ iter(n)	RR	REM
23	$4.68 \cdot 10^{-3}$	$1.66 \cdot 10^{-3}$

(f) $\alpha_m = 10^{-6}$.

Tab. 3.4.11: Four steps of **SWRA** for a *aluminium* ellipse shaped scatterer, $ka = 1.33$. Noise level= 0%.

Chapter 4

Sensitivity of the Reconstruction with Respect to the Data

Contents

The goal of this chapter is to investigate the impact of data (parameters of interest and frequencies) and of regularization parameters on the quality of the reconstruction. We start with the case of a disk-shaped solid for which we have analytical solutions, and we search for the Lamé parameters λ and μ assuming the radius of the obstacle to be known. Considering three different frequencies, the corresponding experiments illustrate that λ and μ have actually very different impact on the quality of the reconstruction. In order to go further in the analysis, we study the cost function associated to the problem for different frequency values. This enables us to show that λ and μ play a similar role for low frequencies while the impact of μ on the FFP is bigger than the one of λ when the frequency increases.

4.1 Sensitivity to Initial Guess

For the sake of simplicity, in this chapter we consider only **IP(1)**, that is, the reconstruction of material parameters. We present numerical results to illustrate how the reconstruction of the Lamé parameters depends on the wavenumber, the initial guess (IG) and the regularization parameter. Here we aim at recovering the material parameters λ and μ for three different frequencies, given by

$$ka = 1.33 \qquad ka = 4 \qquad ka = 5.33 \tag{4.1.1}$$

The computational domain is a disk-shaped obstacle made of *steel* and surrounded by water (as proposed in the previous numerical validations). Its characteristics are: radius of the scatterrer $a = 1cm$, $\lambda = 115.4$GPa, $\mu = 76.9$GPa, $\rho_s = 7900$kg m^{-3}, $\rho_f = 1000$kg m^{-3}.

We consider different IGs which distinguish themselves from the target in different ways. We propose to use two groups of initial guesses: in the first one, the initial value $\lambda^{(0)}$ of λ is fixed and far enough from the targeted λ while μ varies, being closer and closer to the targeted μ. The second one corresponds to the same arrangement switching $\lambda^{(0)}$ and $\mu^{(0)}$. The description of the different initial guesses is depicted in Table (4.1.1) and Figure (4.1.1).

Our first study addresses the influence of the regularization parameters on the accuracy of the reconstruction. We develop our analysis by considering the same approach for the three different values of frequency.

IG =	$(\lambda^{(0)}, \mu^{(0)})$	$\frac{\lvert\lambda-\lambda^{(0)}\rvert}{\lvert\lambda\rvert}100$	$\frac{\lvert\mu-\mu^{(0)}\rvert}{\lvert\mu\rvert}100$	$\frac{\lvert(\lambda,\mu)-(\lambda^{(0)},\mu^{(0)})\rvert}{\lvert(\lambda,\mu))\rvert}100$
IG-I	$(50, 50)$ (GPa)	56.67	34.98	50.99
IG-II	$(50, 60)$ (GPa)	56.67	22.98	48.7
IG-III	$(50, 80)$ (GPa)	56.67	4.03	47.21
IG-I	$(50, 50)$ (GPa)	56.67	34.98	50.99
IG-IV	$(80, 50)$ (GPa)	30.67	34.98	32.06
IG-V	$(100, 50)$ (GPa)	13.34	34.98	22.35

Tab. 4.1.1: Table of the relative errors corresponding to the different Initial Guesses with respect to the target $(\lambda, \mu) = (115.4, 76.9)$ (GPa) , *steel* material.

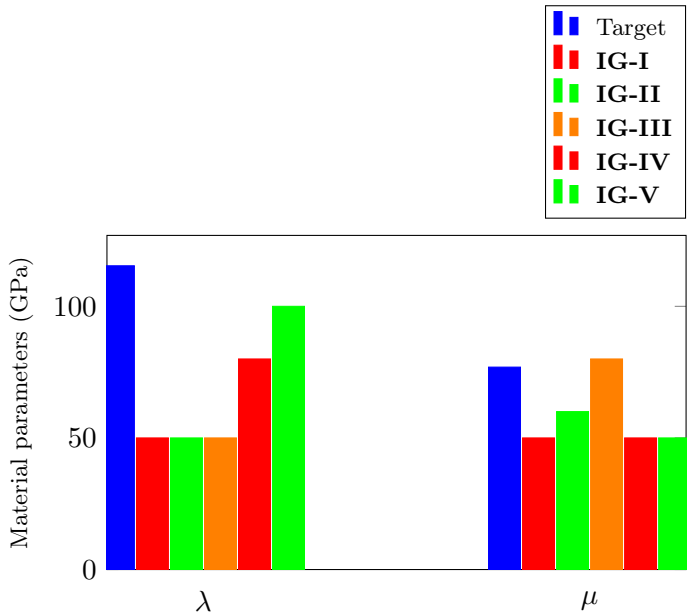

Fig. 4.1.1: Histogram corresponding to the Target vs different Initial Guesses described at Table 4.1.1.

4.1.1 Variation of μ, initial $\lambda = \lambda^{(0)}$ frozen

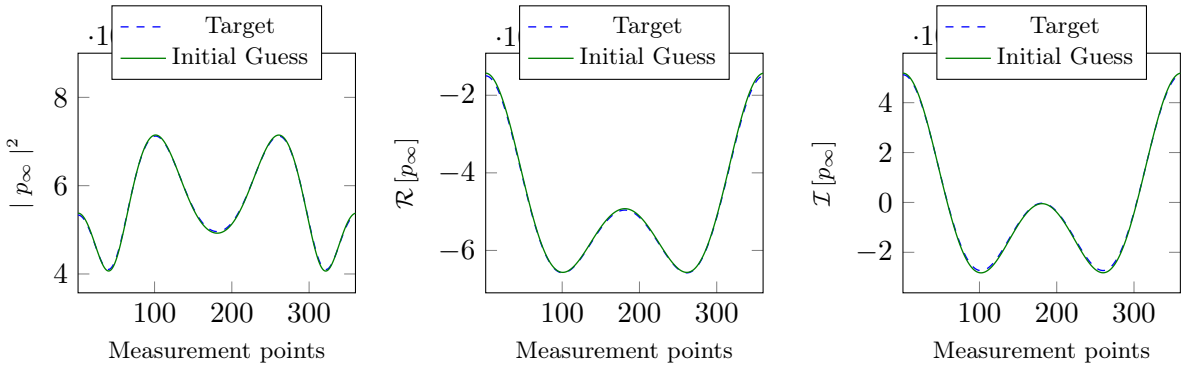

(a) Intensity (b) Real part (c) Imaginary part

Fig. 4.1.2: Intensity, real and imaginary parts of the FFPs corresponding to **IG-I** and the Target for $k = 1.33$, with relative differences of 0.78%, 0.73% and 2.33% respectively.

♯ iter(n)	RR	REM
0	0.78	50.99
1	0.24	26.61
2	$4.6 \cdot 10^{-2}$	8.38
3	$7.86 \cdot 10^{-3}$	1.87
4	$1.47 \cdot 10^{-3}$	0.46
5	$1.17 \cdot 10^{-3}$	0.2

(a) Evolution of RR and REM

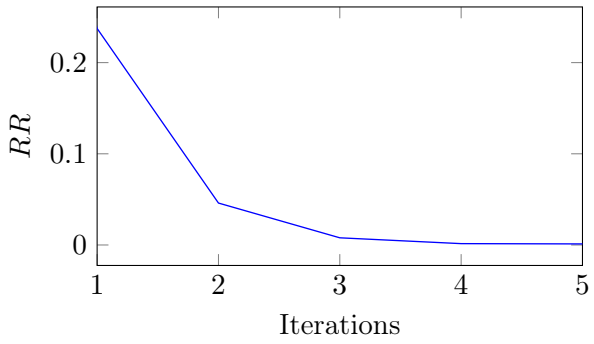

(b) Convergence history

Fig. 4.1.3: (a) Evolution of the relative error on material parameters (REM) and the relative residual of the FFP intensity (RR), together with (b) the convergence history, for $ka = 1.33$, **IG-I**, $\alpha_m = 10^{-6}$.

We begin with analyzing the error at the level of the FFP. We can see in Figure 4.1.2 that the FFP difference for the **IG-I** and target is very small. In Figure 4.1.3(a), we see that the convergence is fast, the relative residual reaches 2 10^{-3}% of error while the relative error on the materials is 0.2%. In Table 4.1.2, we have gathered all the experimental results that we have obtained: the sign ✓ indicates a success while × stands for a failure. We have that as far as $ka = 1.33$, we are able to retrieve the parameters with the three IGs. This is not surprising since **IG-II** and **IG-III** are closer to the target than **IG-I** and **IG-I** has demonstrated to be a successful initial guess.

Table 4.1.2 shows that the reconstruction becomes more difficult when increasing the frequency. For instance, for $ka = 4$, **IG-I** is no longer good candidate. We have tested a good variety of regularizing parameters ranging from 10^{-6} to 10^2 and we have never retrieved the targeted parameters with **IG-I**. Figure 4.1.4 represents the difference between the targeted FFP and the numerical one. For **IG-I** we can see that the error is very high, up to almost 130% for the intensity. For $ka = 4$, **IG-I** is thus too far from the target.

Normalized frequency (ka)	Initial Guess	Reconstruction
1.33	**IG-I**	✓
1.33	**IG-II**	✓
1.33	**IG-III**	✓
4	**IG-I**	×
4	**IG-II**	✓
4	**IG-III**	✓
5.33	**IG-I**	×
5.33	**IG-II**	×
5.33	**IG-III**	✓

Tab. 4.1.2: Summary of different reconstructions of Lamé parameters.

Concerning to $ka = 4$, the evolution of each measure of accuracy with **IG-I** is given in Table 4.1.3 for the case $\alpha_m = 1$. We can observe that the residual is oscillating and so does the error on materials. Regarding **IG-II**, we refer to Table 4.1.4 which shows the results for one experiment using updated regularization parameters $\alpha_m = 10^{-2}$ and 10^{-5}. In Table 4.1.4(a) and in Figure 4.1.5 we observe that the relative residual is decreasing during the first step, while the error on materials increases a little and then decreases very slowly. On the contrary, as detailed in Table 4.1.4(b), once the regularization parameter is updated, the decrease of the error on materials accelerates until the satisfactory value of 2.65 10^{-2}%.

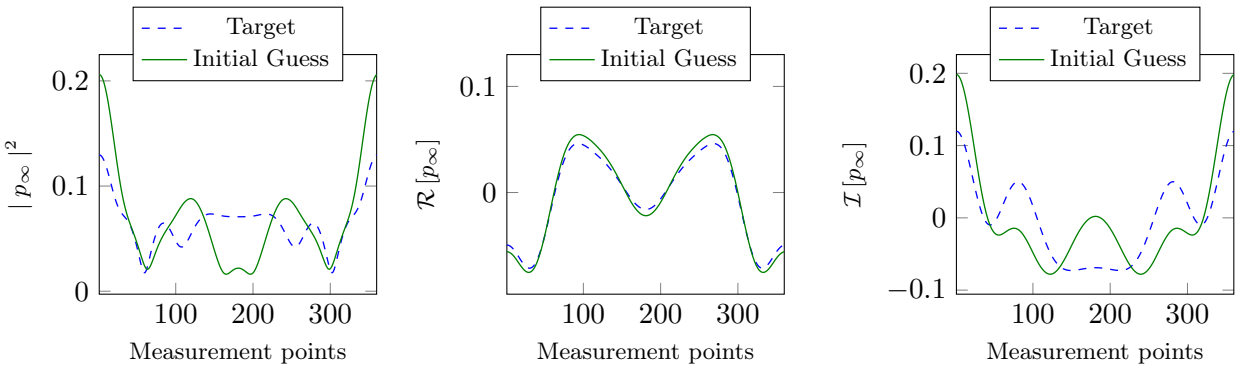

(a) Intensity (b) Real part (c) Imaginary part

Fig. 4.1.4: (a) Intensity, (b) real and (c) imaginary parts of the FFPs corresponding to **IG-I** and the Target for $k = 4$, with relative differences of 128.53%, 13.88% and 90.35% respectively.

Observing the convergence history illustrated in Figure 4.1.5(b) and detailed on Table 4.1.6, we see that for $\alpha_m = 10^{-5}$, **IG-III** allows to retrieve the parameters fastly. Here again, this result is predictable since **IG-III** is closer to the target than **IG-II** and **IG-II** is admissible for getting the parameters.

The impact on the FFP corresponding to the last selected normalized frequency $ka = 5$ is illustrated in Figure 4.1.6, where the intensity, real and imaginary parts of the FFP are illustrated for the **IG-I** and the Target with the corresponding relative errors. In this case, the tests corresponding to **IG-I** and **IG-II** have been unfruitful. It means that despite an extensive number of experiments, we have

♯ iter(n)	RR	REM
0	128.54	50.99
1	66.48	47.44
2	97.72	54.39
3	56.9	50.62
4	66.4	43.53
5	82.96	50.74
6	51.57	46.64

Tab. 4.1.3: Evolution of RR of the FFP intensity, **IG-I**, $\alpha_m = 1$ and normalized frequency $k = 4$.

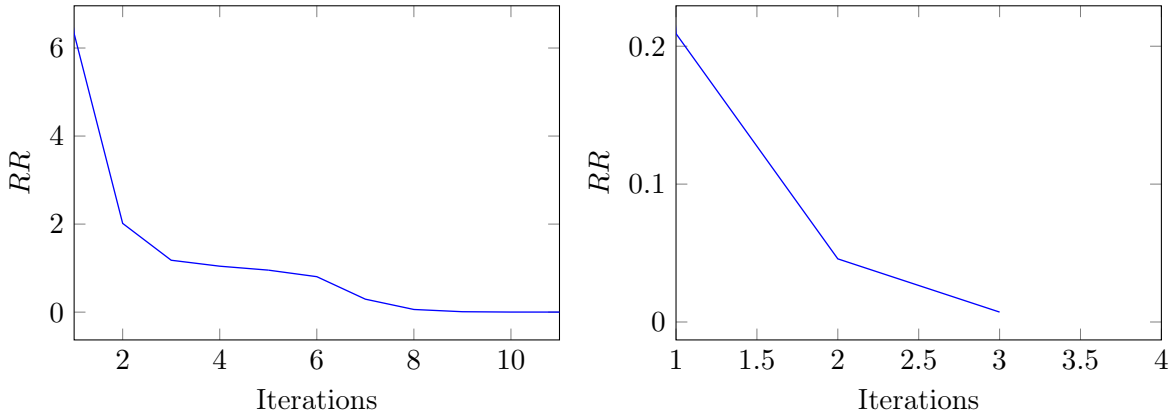

(a) **IG-II**, $\alpha_m = 10^{-2}, 10^{-5}$.

(b) **IG-III**, $\alpha_m = 10^{-5}$.

Fig. 4.1.5: Convergence histories corresponding to the normalized frequency $ka = 4$, for different initial guesses: (a) **IG-II** and (b) **IG-III**.

♯ iter(n)	RR	REM
0	15.87	48.7
1	6.33	69.58
2	2.02	63.25
3	1.18	59.06
4	1.04	56.07
5	0.95	53.67

(a) $\alpha_m = 10^{-2}$.

♯ iter(n)	RR	REM
5	0.95	53.67
6	0.81	51.63
7	0.29	22.77
8	$6.04 \cdot 10^{-2}$	5.89
9	$9.5 \cdot 10^{-3}$	1.04
10	$1.66 \cdot 10^{-3}$	0.17
11	$1.12 \cdot 10^{-3}$	$2.65 \cdot 10^{-2}$

(b) $\alpha_m = 10^{-5}$

Tab. 4.1.4: Evolution of the relative error on material parameters and the relative residual of the FFP intensity for $ka = 4$, **IG-II**, for updated regularization parameters (a) $\alpha_m = 10^{-2}$ and (b) $\alpha_m = 10^{-5}$.

Initial Guess		Normalized frequency	Computed	Individual Relative Errors	
				$\frac{\parallel \lambda - \lambda^{(0)} \parallel_{L^2}}{\parallel \lambda \parallel_{L^2}} 100$	$\frac{\parallel \mu - \mu^{(0)} \parallel_{L^2}}{\parallel \mu \parallel_{L^2}} 100$
IG-I	$(50, 50)$	$ka = 1.33$	(114.61,76.94)	0.68	0.05
IG-II	$(50, 60)$	$ka = 4$	(115.36,76.89)	0.03	0.01
IG-III	$(50, 80)$	$ka = 4$	(115.37,76.89)	0.03	0.01
IG-III	$(50, 80)$	$ka = 5.33$	(115.40,76.90)	$4.01\ 10^{-4}$	$1.43\ 10^{-5}$

Tab. 4.1.5: Relative errors at convergence corresponding to **IG-I**, **IG-II**, and **IG-III**, for normalized frequency values $ka = 1.33, 4, 5.33$, *steel* material.

$\sharp$ iter(n)	RR	REM
0	1.73	47.21
1	0.21	19.04
2	$4.58 \cdot 10^{-2}$	4.56
3	$7.19 \cdot 10^{-3}$	0.78

Tab. 4.1.6: Evolution of the relative error on material parameters and the relative residual of the FFP intensity for $ka = 4$, **IG-III** and $\alpha_m = 10^{-5}$.

not found the parameters to stabilize the reconstruction of the material parameters. On the contrary, the selection of **IG-III** has been successful as depicted in Table 4.1.7(a) (we observe how we achieve a final error of $3.33\ 10^{-4}\%$ after the relative residual of the intensity drops from 7.34% to $2.93\ 10^{-5}\%$).

To see what happens in the transition zone between **IG-II** (failure) and **IG-III** (success) we have considered the intermediate initial state $(\lambda^{(0)}, \mu^{(0)}) = (50, 70)$GPa. Using the regularization parameter $\alpha_m = 10^{-5}$ has then been successful. In this case, the RR starts around 32% and it is reduced until $1.37\ 10^{-2}\%$, while the final relative error on material parameters is 0.46%, as detailed in Table 4.1.7(b). Here we observe that even the decay of the evolution of the relative residual is smooth (see the corresponding history convergence in Figure 4.1.7(b)), the error on the material parameters seems to be unstable (see evolution of REM in Table 4.1.7(b)). We are clearly in a situation where the problem is strongly unstable and the regularization parameters play a crucial role in the reconstruction.

What deserves to be remarked is the form of the different initial guesses. They belong to the first groups: they share the value of $\lambda^{(0)}$ and $\mu^{(0)}$ varies. In the following, we present what we have obtained when $\lambda^{(0)}$ varies and $\mu^{(0)}$ is constant all along each experiment.

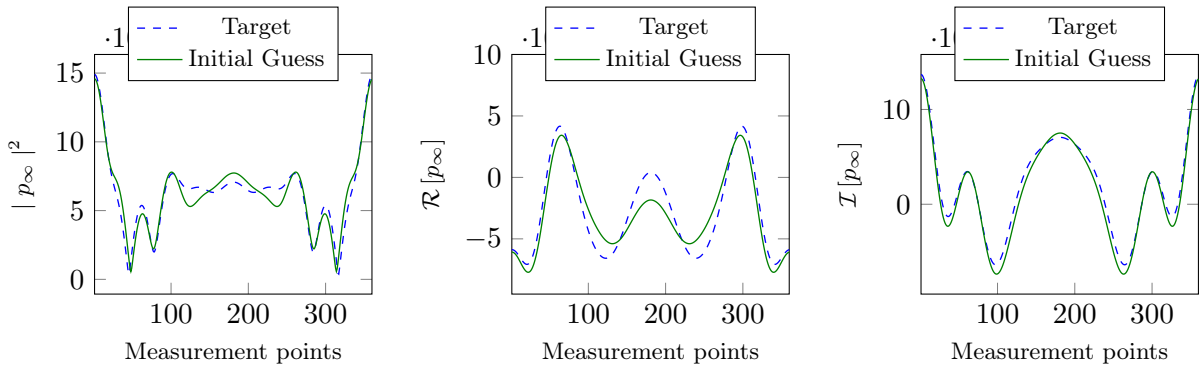

(a) Intensity (b) Real part (c) Imaginary part

Fig. 4.1.6: (a) Intensity, (b) real and (c) imaginary parts of the FFPs corresponding to **IG-I** and the Target for $k = 5.33$, with relative differences of 12.53%, 27.38% and 15.28% respectively.

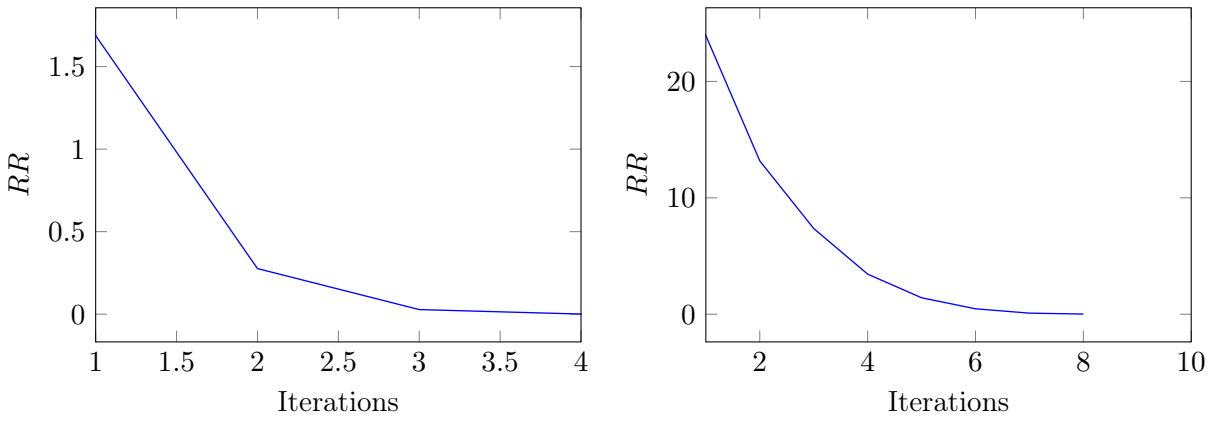

(a) **IG-III**, $\alpha_m = 10^{-5}$. (b) $(\lambda^{(0)}, \mu^{(0)}) = (50, 70)$, $\alpha_m = 10^{-5}$.

Fig. 4.1.7: Convergence histories corresponding to the normalized frequency $ka = 5.33$, for **IG-III** and $(\lambda^{(0)}, \mu^{(0)}) = (50, 70)$.

♯ iter(n)	RR	REM
0	7.34	47.21
1	1.69	24.26
2	0.28	7.44
3	$2.79 \cdot 10^{-2}$	0.82
4	$7.16 \cdot 10^{-4}$	$2.16 \cdot 10^{-2}$
5	$2.93 \cdot 10^{-5}$	$3.33 \cdot 10^{-4}$

(a) **IG-III**, $\alpha_m = 10^{-5}$.

♯ iter(n)	RR	REM
0	32.04	48.1
1	23.94	32.26
2	13.17	37.05
3	7.36	45.1
4	3.45	41.22
5	1.42	29.26
6	0.47	12.72
7	$9.2 \cdot 10^{-2}$	2.96
8	$1.37 \cdot 10^{-2}$	0.46

(b) $(\lambda^{(0)}, \mu^{(0)}) = (50, 70)$, $\alpha_m = 10^{-5}$

Tab. 4.1.7: Evolution of the relative error on material parameters and the relative residual of the FFP intensity for $ka = 5.33$, with the same regularization parameter $\alpha_m = 10^{-5}$ in both cases but different initial guesses: (a) **IG-III** and (b) $(\lambda^{(0)}, \mu^{(0)}) = (50, 70)$.

4.1.2 Variation of λ, initial $\mu = \mu^{(0)}$ frozen

In what follows we introduce the tests corresponding to the second set of initial guesses described in Table 4.1.1. We remind, that as illustrated in the histogram of Figure 4.1.1, $\mu^{(0)}$ is the same for each test and the initial guesses differ for the value of $\lambda^{(0)}$.

The reconstructions corresponding to **IG-IV** and **IG-V** employing the normalized frequency $ka = 1.33$ have been successful, as we can observe in the columns REM of Tables 4.1.8(a) and 4.1.8(b) respectively. In both cases the same regularization parameter $\alpha_m = 10^{-5}$ has been employed. These results are not surprising due to the fact that these IGs are closer to the target than **IG-I**, which is an appropriate initial guess to reconstruct the material parameters.

♯ iter(n)	RR	REM
0	0.68	32.06
1	0.19	10.62
2	$2.46 \cdot 10^{-2}$	1.33
3	$6.49 \cdot 10^{-4}$	0.14
4	$7.65 \cdot 10^{-5}$	0.14

(a) **IG-IV**.

♯ iter(n)	RR	REM
0	0.67	22.35
1	0.19	7.52
2	$2.54 \cdot 10^{-2}$	1.21
3	$9.85 \cdot 10^{-4}$	$1.42 \cdot 10^{-2}$
4	$1.32 \cdot 10^{-4}$	0.11

(b) **IG-V**.

Tab. 4.1.8: Evolution of the relative error on material parameters and the relative residual of the FFP intensity, for a common regularization parameter $\alpha_m = 10^{-6}$, $ka = 1.33$, and different initial guesses: (a) **IG-IV** and (b) **IG-V**.

The experiments corresponding to these initial guesses for the normalized frequency $ka = 4$ have failed. We have tried a considerable quantity of different regularization parameters ranging from 10^{-1} to 10^{-6} without obtaining suitable ones to stabilize the reconstruction of the Lamé coefficients. The summary of accuracy quantities for **IG-IV** and $\alpha_m = 10^{-1}$ are described in Figure 4.1.9(a), where we observe that the relative residual starts decreasing while the error on material parameters is completely unstable. In the test corresponding to **IG-V** and $\alpha_m = 10^{-1}$ the instability results are quite similar observing the evolution of the relative residual and the error on materials parameters in Figure 4.1.9(b). In this case, the fact that the initial guesses **IG-IV** and **IG-V** are closer to the target does not seem to have any influence on the reconstruction of Lamé parameters. Here we must remind that this proximity is focused on assigning to $\lambda^{(0)}$ closer values of λ while $\mu^{(0)}$ is frozen.

The last selected normalized frequency for **IG-IV** and **IG-V** is $ka = 5.33$. Here again, even if a lot of regularization parameters have been tested, we have not carried out stabilized reconstructions. We have selected **IG-IV** and $\alpha_m = 10^{-1}$ to illustrate the situation in Table 4.1.10(a): we see the unstable evolution of the error of materials while the relative residual seems to have a smooth decay. Similar results are observable in Table 4.1.10(b) for **IG-V** and $\alpha_m = 10^{-1}$. The evolution of the error on material parameters seems to be less unstable than for **IG-IV**, but in this case too, the fact that we have selected the initial guess value $\lambda^{(0)}$ closer to the target value λ does not help to stabilize the reconstruction of the material parameters.

We conclude that for higher frequencies the proximity of the initial parameter $\mu^{(0)}$ to the good parameter μ seems to be crucial in the success of the reconstruction. On the contrary, we have observe that we have more flexibility to select the initial parameter $\lambda^{(0)}$.

♯ iter(n)	RR	REM
0	126.97	32.06
1	64.59	25.85
2	65.25	36.22
3	50.9	32
4	62.35	44.6

(a) **IG-IV**.

♯ iter(n)	RR	REM
0	126.36	22.35
1	65.27	27.62
2	61.01	37.17
3	51.88	32.85
4	50.93	51.52
5	51.28	50.88

(b) **IG-V**.

Tab. 4.1.9: Evolution of the relative error on material parameters and the relative residual of the FFP intensity, for a common regularization parameter $\alpha_m = 10^{-1}$, $ka = 4$, and different initial guesses: (a) **IG-IV** and (b) **IG-V**.

♯ iter(n)	RR	REM
0	13.04	32.06
1	10.54	34.13
2	10.32	36.81
3	14.53	44.93
4	9.78	48.67

(a) **IG-IV**.

♯ iter(n)	RR	REM
0	13.41	22.35
1	11.21	20.26
2	12.06	20.61
3	13.86	25.6

(b) **IG-V**.

Tab. 4.1.10: Evolution of the relative error on material parameters and the relative residual of the FFP intensity, for a common regularization parameter $\alpha_m = 10^{-1}$, $ka = 5.33$, and different initial guesses: (a) **IG-IV** and (b) **IG-V**.

4.2 Cost Function and Convergence Region

In this section, we investigate the behavior of the cost function as a function of λ and μ, defined as:

$$\| \widetilde{p}_\infty - p_\infty \|_2^2 \tag{4.2.1}$$

where $\widetilde{p}_\infty$ is the FFP computed from the Target of the *steel* material parameters, while p_∞ is the FFP computed from different values of λ and μ. The goal of the numerical study is to share some highlights of the convergence region for various values of the frequency. For instance, we will see that when the Initial Guess $(\lambda^{(0)}, \mu^{(0)})$ is not in the neighborhood of the convex-zone of the cost function, the reconstruction fails.

We print the cost function for $(\lambda, \mu) \in [50, 150] \times [20, 150]$. In Figure 4.2.1, we consider the case where $ka = 1.33$ with the initial guess **IG-I**. On both Figures, we have represented the target by a white point while **IG-I** is a red square. We can observe that the cost function is smooth and most of its range consists of the convergence domain. We have not drawn **IG-II** and **IG-III** because they are closer to the target. **IG-I** being indeed in the convergence region yet, they cannot bring more information.

In order to clarify that the convergence region is bigger than the blue zone, we have selected the initial guess $(\lambda^{(0)}, \mu^{(0)}) = (10, 10)$GPa (outside of the blue zone) and the regularization parameter $\alpha_m = 10^{-8}$. The relative residual starts over 25% and drops until the value of 7.65 10^{-5}%, while the relative error decreases from 123.06% until 0.14%, as detailed in Table 4.2.1.

When increasing the frequency to $ka = 4$, the profile of the cost function changes (see Figures 4.2.2(a) and (b)). The total region is composed of two blue zones which are separated by a red zone, and we see that **IG-I** (black point) is located in the red zone. The two other points lie in the same blue zone as the target. They both correspond to convergent cases. We are observing the existence of local minimum that may attract the initial guess to a wrong solution. This last observation is even more apparent in Figures 4.2.3(a) and 4.2.3(b).

The convergence region seems to be quite well defined if we observe Figure 4.2.2(b). We introduce here the last numerical experiment of this chapter corresponding to the initial state $(\lambda^{(0)}, \mu^{(0)}) = (50, 53)$GPa, which is denoted by the symbol + and located on the red zone in Figure 4.2.3(b), but we observe that it is on the right side of the peak of the cost function (which means that it belongs to the convergence region even if it is in the red zone). It is clearly in the transition zone between **IG-I** (failure) and **IG-II** (success). Using the initial regularization parameter $\alpha_m = 1$ we observe that the relative residual decreases from 80% until 1.77% as described in Table 4.2.2(a), while the error on material parameters does not seem to change. While during the second step, we reduce the regularization parameter until $\alpha_m = 10^{-8}$, and as detailed in Table 4.2.2(b), the reconstruction is successful with a final error of 1.18 10^{-3}% on materials. Here, it is important to point out that the result of the inverse problem using the first initial guess is really sensitive to the frequency. Other regularization parameters have been tested, for instance $\alpha_m = 10^{-1}$, leading to an unstable and unsatisfactory experiments.

The last selected frequency is $ka = 5.33$, and the corresponding cost function is illustrated in Figures 4.2.4 and 4.2.5(a). Here also there are two blue zones and an intermediate section. The blue region where there are located the **IG-III** and Target depicted by the white symbol + and a white point belongs to the convergence region, while the other blue zone collects unsuccessful results as **IG-II**, denoted by a white square. If we select the Initial Guess $(\lambda^{(0)}, \mu^{(0)}) = (50, 70)$ which is located on the transition green zone in Figure 4.2.5(a), we converge, but it is really sensitive to the regularization parameters. In Figure 4.2.5(b) we clearly observe that this transition zone is not convex at all.

As a conclusion, we would like to make a remark about the different impacts of the material parameters λ and μ on the reconstruction of the material parameters. For the low normalized frequency value $ka = 1.33$ we could conclude from Figure 4.2.1 that the two parameters play a symmetric role. The situation is completely different for $ka = 4$. In Figure 4.2.3(a) the cost function seems to be constant for λ, while it varies with respect to μ. This behavior is even better illustrated in Figure 4.2.3(b), where we observe the dependence of the cost function on the material parameter μ. In other words, the convergence region has a considerably smaller aperture for valid values of $\mu^{(0)}$. It may reflect the dependency of the propagation velocities on λ and μ: reminding that in an elastic isotropic medium, we have:

$$v_p = \sqrt{\frac{\lambda + 2\mu}{\rho_s}}, \qquad v_s = \sqrt{\frac{\mu}{\rho_s}}. \tag{4.2.2}$$

we see that λ does not impact on the velocity v_s while μ impacts on both propagation velocities.

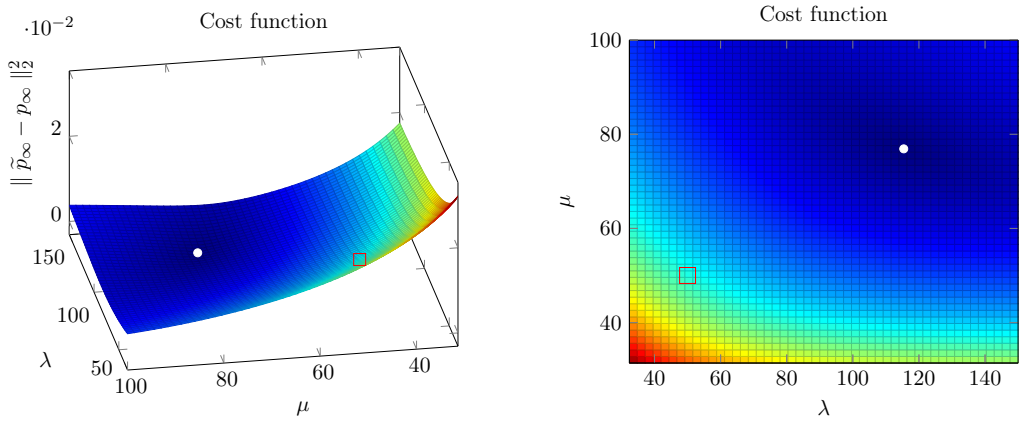

Fig. 4.2.1: The cost function for $ka = 1.33$, **IG-I** and Target illustrated by a red square, and a white point respectively.

$\sharp$ iter(n)	RR	REM
0	25.95	123.03
1	12.89	81.91
2	6.23	67.66
3	2.88	47.06
4	1.22	27.26
5	0.43	15.97
6	$9.6 \cdot 10^{-2}$	5.42
7	$7.18 \cdot 10^{-3}$	0.35
8	$7.65 \cdot 10^{-5}$	0.13
9	$7.65 \cdot 10^{-5}$	0.14

Tab. 4.2.1: Evolution of the relative error on material parameters and the relative residual of the FFP intensity for $ka = 4$, $(\lambda^{(0)}, \mu^{(0)}) = (50, 10)$ GPa and $\alpha_m = 10^{-8}$.

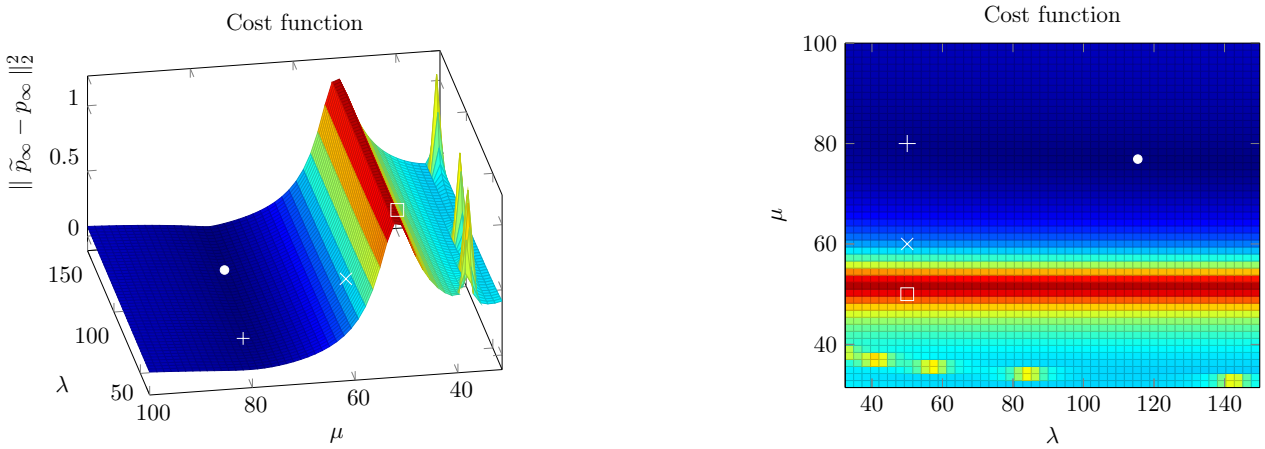

Fig. 4.2.2: The cost function for $ka = 4$, **IG-I**, **IG-II**, **IG-III** and Target illustrated by a square, symbols '×', '+' and a point respectively (all in white).

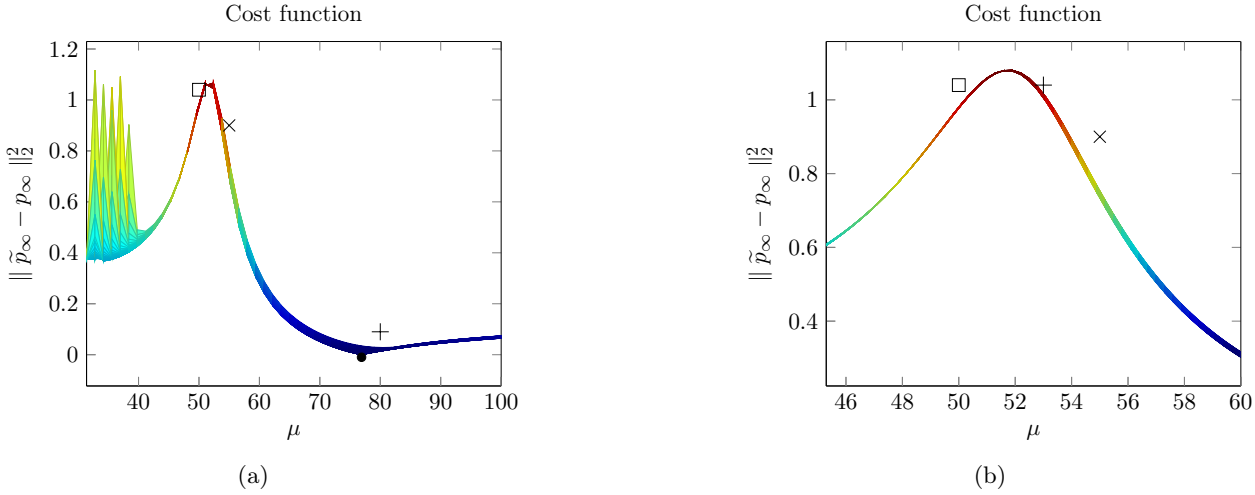

Fig. 4.2.3: (a) The cost function for $ka = 4$ with **IG-I**, **IG-II**, **IG-III** and Target illustrated by a square, symbols '×', '+' and a point respectively. (b) The cost function for $ka = 4$ with **IG-I**, $(\lambda^{(0)}, \mu^{(0)}) = (50, 53)$GPa and **IG-II** illustrated by a square, symbols '+' and'×' respectively (all in black).

♯ iter(n)	RR	REM
0	80.04	50.22
1	33.24	49.12
2	24.19	48.96
3	21.36	49.08
4	19.47	49.31
5	16.04	49.46
6	8.24	48.93
7	4.01	48.51
9	2.49	48.37
10	1.77	48.31

(a) $\alpha_m = 1$.

♯ iter(n)	RR	REM
10	1.77	48.31
11	1.37	22.64
12	0.26	4.67
13	$5.06 \cdot 10^{-2}$	0.2
14	$2.02 \cdot 10^{-3}$	$1.18 \cdot 10^{-3}$

(b) $\alpha_m = 10^{-8}$

Tab. 4.2.2: Evolution of the relative error on material parameters and the relative residual of the FFP intensity for $ka = 4$, $(\lambda^{(0)}, \mu^{(0)}) = (50, 53)$ GPa and $\alpha_m = 1, 10^{-8}$.

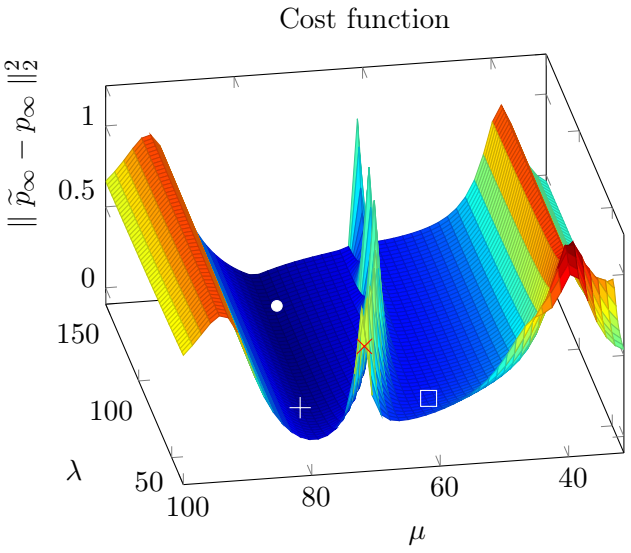

Fig. 4.2.4: The cost function for $ka = 5.33$, **IG-II**, **IG-III** and Target illustrated by a square, symbol '+' and a point respectively (all in white) together with the Initial Guess $(\lambda^{(0)}, \mu^{(0)}) = (50, 70)$, illustrated by the red symbol $\times$.

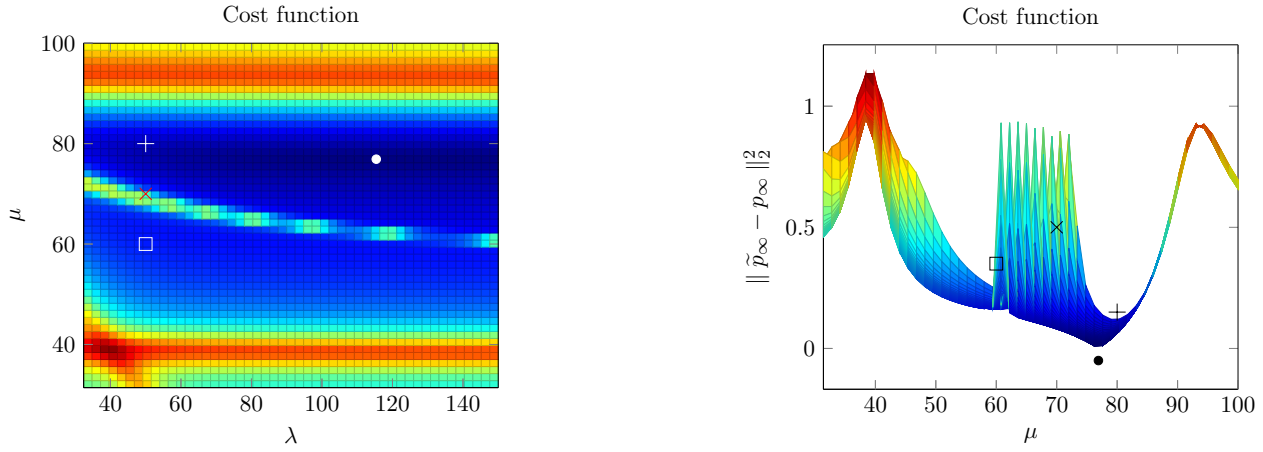

(a) (b)

Fig. 4.2.5: (a) The cost function for $ka = 5.33$, **IG-II**, **IG-III** and Target illustrated by a square, symbol '+' and a point respectively (all in white) together with the Initial Guess $(\lambda^{(0)}, \mu^{(0)}) = (50, 70)$, illustrated by the red symbol $\times$, (b) **IG-II**, **IG-III**, Target and Initial Guess $(\lambda^{(0)}, \mu^{(0)}) = (50, 70)$ by a square, symbol '+', a point and symbol '$\times$' respectively (all in black).

4.3 Sensitivity to the Frequency Values

Elastic medium *Steel*	λ (GPa)	μ (GPa)	a (cm)
Target	115.4	76.9	1.00

Tab. 4.3.1: Lamé coefficients corresponding to the *steel* disk shaped obstacle.

We have observed in the previous chapter that it is always much more difficult to retrieve the material parameters than the shape ones. When addressing the Lamé parameters alone (see previous Section 4.1), we have seen that using low frequency data ensures a stable reconstruction of the material features. Nevertheless, Section 3.4 shows that using low frequencies may be insufficient when targeting both the shape and the interior characteristics of the obstacle. The conjecture is then that the information contained in the FFP is very different whether you consider the shape parameters or the constitutive parameters of the obstacle. Moreover, the frequency regime used for the reconstruction plays a role too. Hence to figure out this problem, we have printed Fig. 4.3.1 which has been elaborated in the case of a disk-shaped obstacle filled with steel as follows. We denote by (λ_0, μ_0, a_0) the parameters given in Table 4.3.1. We then have computed the corresponding FFP for different values of the frequency ka ranging from 1 to 4. We denote the corresponding function of ka by FFP_0. Then, we propose to perturb the initial material parameters first and the shape parameters next by considering $(2\lambda_0, 2\mu_0, a_0)$ and then $(\lambda_0, \mu_0, 2a_0)$. As previously, we compute the corresponding FFPs for frequencies ka ranging from 1 to 4 and we get two functions of ka respectively denoted by FFP_m and FFP_s. The index indicates which parameters have been perturbed. Then we introduce the functions f_m and f_s defined by:

$$f_m(ka) = \frac{\| FFP_m(ka) - FFP_0(ka) \|_2}{\| FFP_0(ka) \|_2} \times 100 \tag{4.3.1}$$

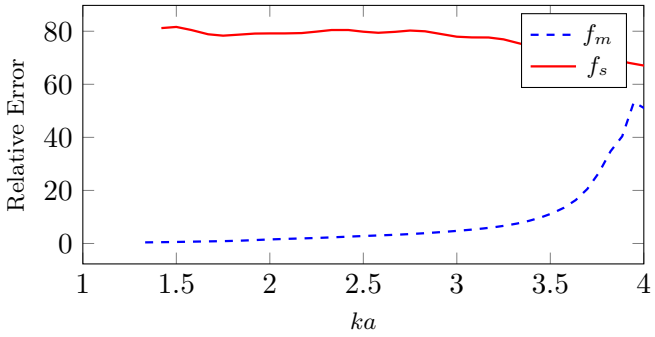

Fig. 4.3.1: The relative difference of the far field pattern intensity corresponding to material vs. shape parameter for $ka \in [1, 4]$.

$$f_s(ka) = \frac{\parallel FFP_s(ka) - FFP_0(ka) \parallel_2}{\parallel FFP_0(ka) \parallel_2} \times 100 \tag{4.3.2}$$

Figure 4.3.1 represents the evolution of f_m and f_s as functions of ka. The behavior of f_m shows that at low frequencies, the perturbation of Lamé parameters has a little impact on the FFP since f_m increases very slowly staying close to zero. Then we see that f_m begins increasing significantly for frequencies beyond 3.5. Regarding f_s, the perturbation of the shape parameters affects the FFP significantly for any value of ka. However, we can observe that f_s decreases, which should indicate that at high frequency the impact on FFP could be weaker. Hence, to see if the previous observations are still valid for a large range of frequencies, we have decided to reproduce the Figure 4.3.1 for ka ranging from 1 to 20. Figure 4.3.2 displays what we have obtained for f_m and we can observe a very unpredictable curve including peaks and describing a chaotic behavior while we expected the curve to increase with the frequency. However, we can see that for frequencies larger than $ka = 7$, f_m oscillates around the equilibrium state that could be 50%. We have also represented in Figure 4.3.2 the curve of f_m^* which is defined as f_m but the FFP is replaced by its intensity. We observe the same profile and the curve envelop seems to stabilize around an equilibrium state of approximately 30%. To understand this unexpected behavior, we have reconsidered the problem and the question of having Jones frequencies that polluted the curves has been raised. To locate the possible Jones frequencies, we have computed the determinant Δ_n of the linear system previously introduced in Chapter 1 (see Eq. 1.2.14, page 17) for determining analytical solutions. Similarly, we also illustrate the determinant of the modal matrix ignoring the effect of the ABC $\Delta_n^r = \left(\Delta_n^{jl}\right)_{j=1,2,3;1,3,4}$ and the determinant of $\Delta_n^s = \left(\Delta_n^{jl}\right)_{j=2,3;3,4}$, representing the solid Fourier modes as in [9]. We know that Δ_n (as Δ_n^r and Δ_n^s) tends to 0 in the vicinity of a Jones mode. On the top of the Figure 4.3.3, we have displayed Δ_0 (together with Δ_n^r and Δ_n^s) computed with steel Lamé parameters and represented in base-10 logarithm. The curve shows some local minima, each of them being different from zero. Nevertheless, we must have in mind that the curve has been drawn on the basis of a grid which could be too coarse to reproduce correctly the behavior of Δ_0 (together with Δ_n^r and Δ_n^s). To resolve that doubt, we have focused on the peak corresponding to $ka = 17.508$ which could correspond to a Jones frequency. We have then zoomed on the peak around $ka = 17.508$. The zoom is depicted at the bottom of the Figure 4.3.3. It provides a curve of Δ_0 in base-10 logarithm in the vicinity of $ka = 17.508$ where each point of evaluation of Δ_0 (together with Δ_n^r and Δ_n^s) is given as $17.508 \pm 7l10^{-8}$, l being an integer. On the abscissa, we have put the values of $\pm 7l10^{-8}$, $\quad l \in 0, ..., 100$ so that $ka = 17.508$ corresponds to 0. Then we see on the picture that the logarithm to the base 10 of Δ_0 (together with Δ_n^r and Δ_n^s) is negative around 0 which confirms that $ka = 17.508$ is a Jones frequency. We supplement the Figure 4.3.3 by Figure 4.3.4 where we have displayed the base-10 logarithm of Δ_1 (together with Δ_1^r and Δ_1^s) and Δ_2 with

Δ_2^r and Δ_2^s) computed again for steel Lamé parameters. The same zooms could be applied around the local minima of each curve to end up with the location of Jones frequencies. In Figure 4.3.5, we reproduce the same computations but this time for $(2\lambda_0, 2\mu_0, a_0)$. Here again we observe local minima which correspond to Jones frequencies. Then, in order to illustrate the link between Jones and the peaks of f_m, in Figure 4.3.6 we have superimposed the curves of f_m (illustrated in Figure 4.3.2) with $\log(\Delta_0)$, $\log(\Delta_1)$ and $\log(\Delta_2)$ (together with the corresponding minors, see Figure 4.3.4) to figure out the behavior of f_m while in Figure 4.3.7, we superimpose the curve of Figure 4.3.2 and the one of 4.3.5. We can see that Jones frequencies actually correspond to some of the peaks of f_m and are thus causing the chaotic behavior of f_m. We have done the same experiments considering shape parameters. The same conclusions hold regarding the existence of Jones frequencies that explain the profiles of the curves. On the contrary, Figure 4.3.8 shows that the FFP contains more information on the shape parameters at low frequencies than on the material parameters. Repeating the procedure doubling the target value of the shape parameters, in Figures 4.3.9 and 4.3.10 we observe the Jones modes corresponding to the target and $(\lambda_0, \mu_0, 2a_0)$ respectively. Finally, the relation between the Jones modes and the curve f_s is illustrated in Figure 4.3.11.

As a conclusion, we have illustrated how the reconstruction is sensitive to Jones frequencies what is not surprising since we know that the uniqueness of the direct problem is ensured modulo Jones modes. More importantly, we have shown that the FFP contains more or less information on the different parameters regarding the frequency regime. At low frequency, the reconstruction of the shape is more effective while the material parameters retrieval seems to be more stable at higher frequencies. This could suggest changing the values of the frequency inside the iterative process of inversion.

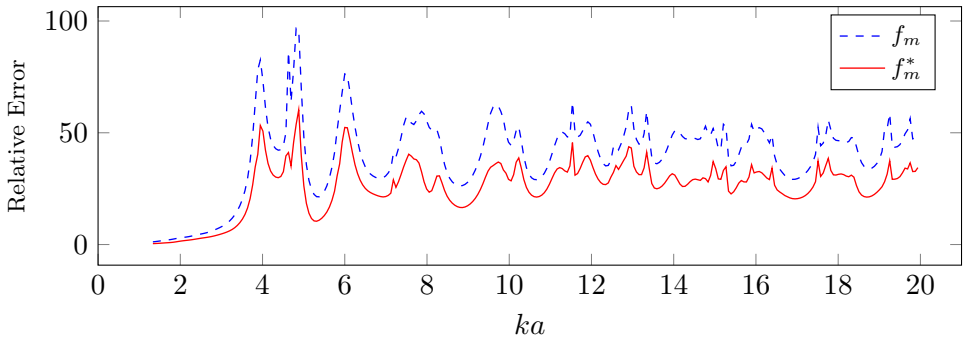

Fig. 4.3.2: The relative difference of the far field pattern and its intensity corresponding to material parameters' 50.99% error as a function of ka.

4.4 Conclusions

Chapter 4 content is a consequence of the difficulties we have faced to when tackling the reconstruction of the material parameters together with the shape ones. Chapter 3 proved that material parameters can be surely retrieved if the shape parameter reconstruction process converges. Nevertheless, the numerical analysis of Chapter 3 was not sufficient to assess the impact of each parameter on the FFP. In [40], there is an extended study on the reconstruction of the shape parameters that we have completed by analyzing the role of material parameters. It is worth noting that even if the FFP is much more sensitive to the shape parameters, it is sensitive to the material ones also and that the sensitivity depends on the frequency regime that is considered. When considering low frequencies and only material features, these parameters are easy to retrieve. Then we have illustrated the interest of using low frequencies as a way of enlarging the region of convergence (attraction basin for optimization problems) and thus increasing the probability of the initial guess to be in the good place for having

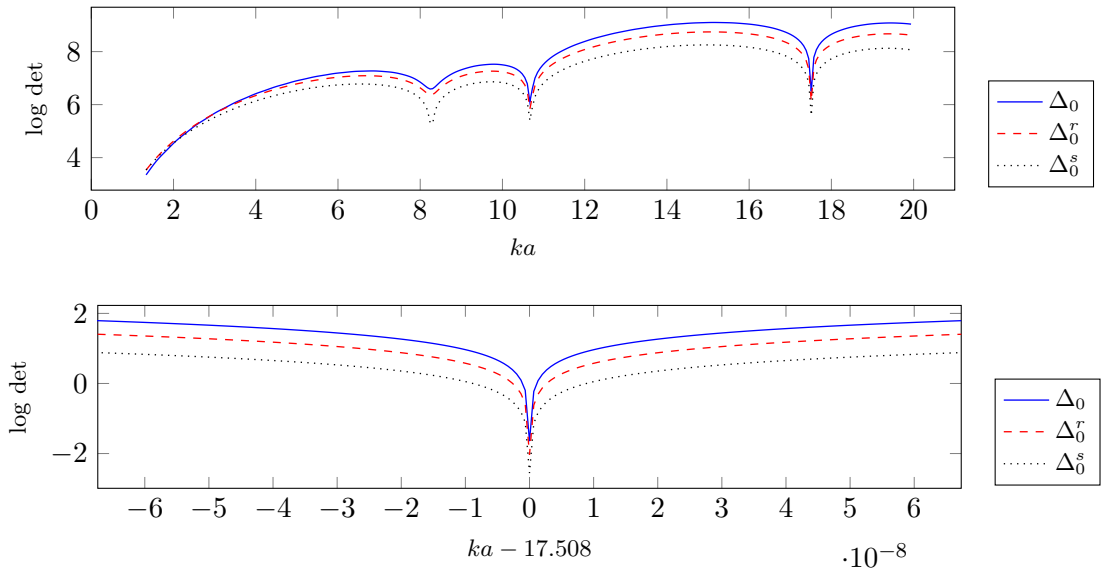

Fig. 4.3.3: Sensitivity of the determinant of the modal matrices ($n = 0$) for target Lamé parameters to the normalized frequency ka.

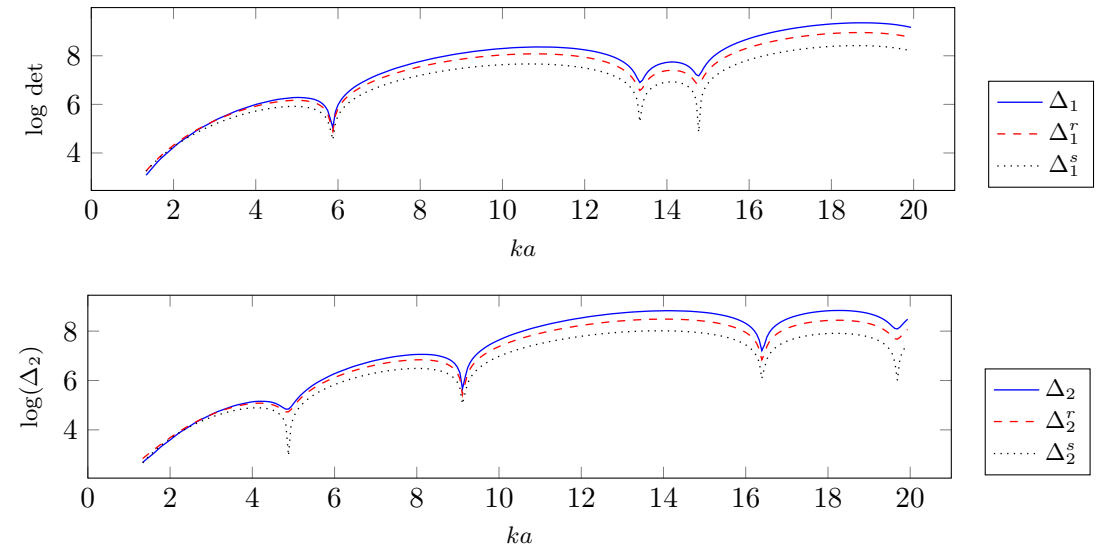

Fig. 4.3.4: Sensitivity of the determinant of the modal matrices ($n = 1, 2$) for target Lamé parameters to the normalized frequency ka.

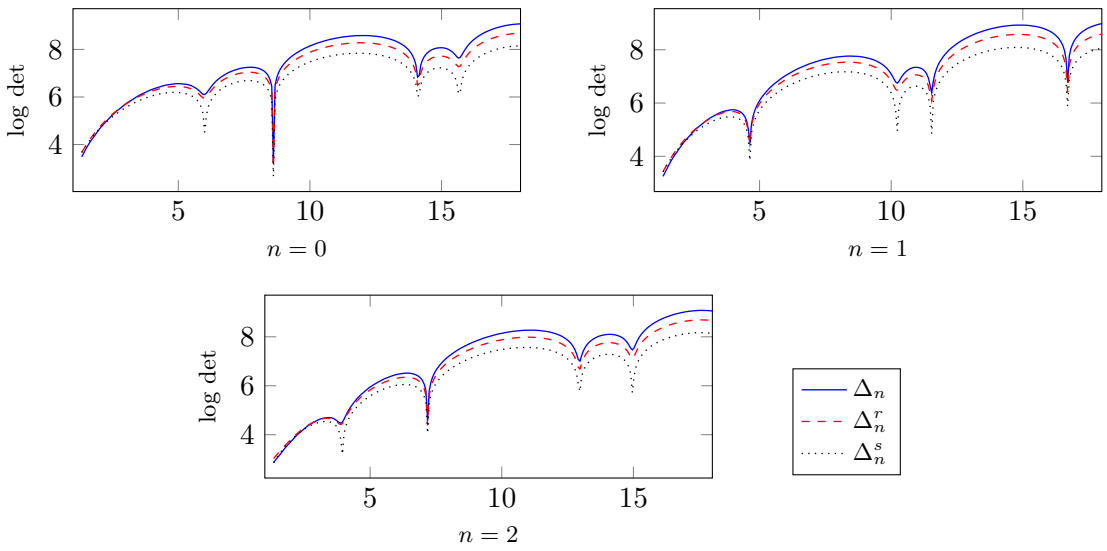

Fig. 4.3.5: Sensitivity of the determinant of the modal matrices for initial guess Lamé parameters to the normalized frequency ka.

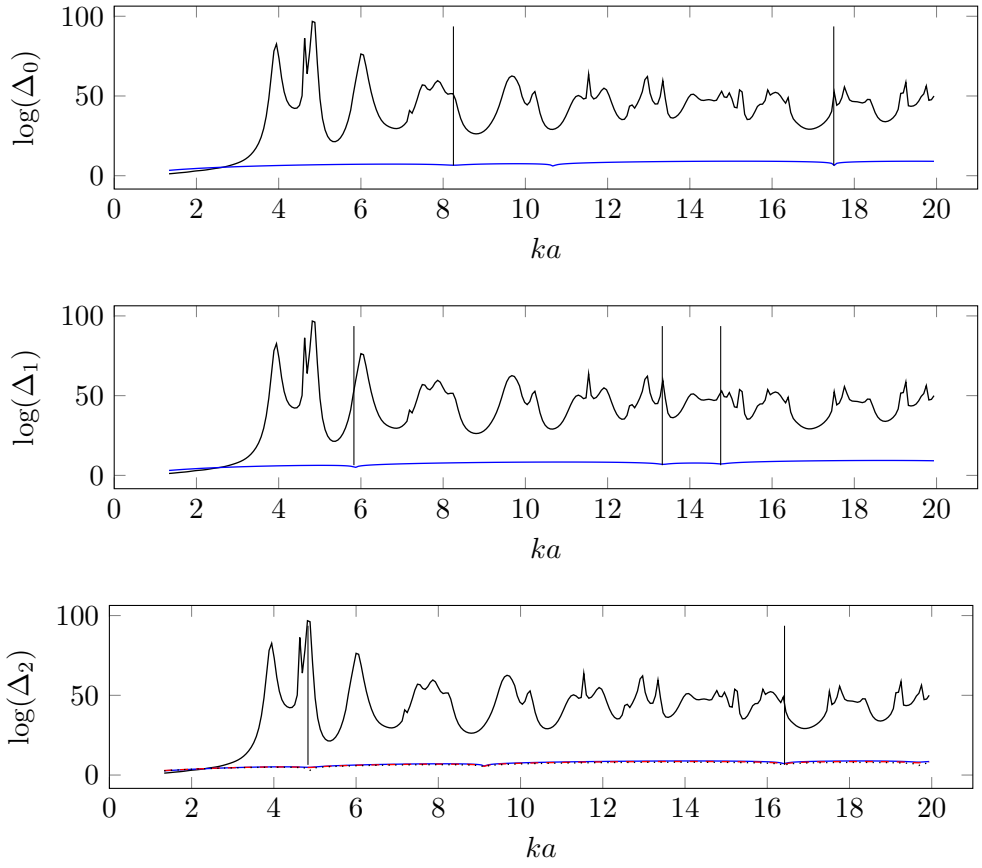

Fig. 4.3.6: Sensitivity of the determinant of the modal matrices for target Lamé parameters together with FFP difference to the normalized frequency ka.

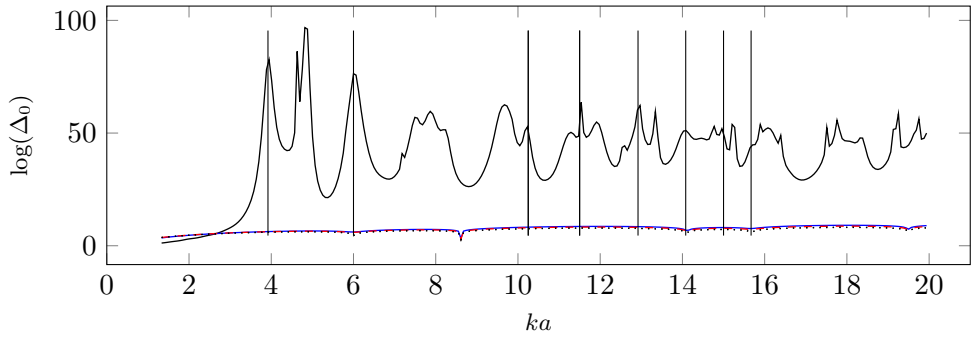

Fig. 4.3.7: Sensitivity of the determinant of the modal matrices for Lamé parameters $2\lambda_0$ and $2\mu_0$ together with FFP difference f_m for normalized frequency ka.

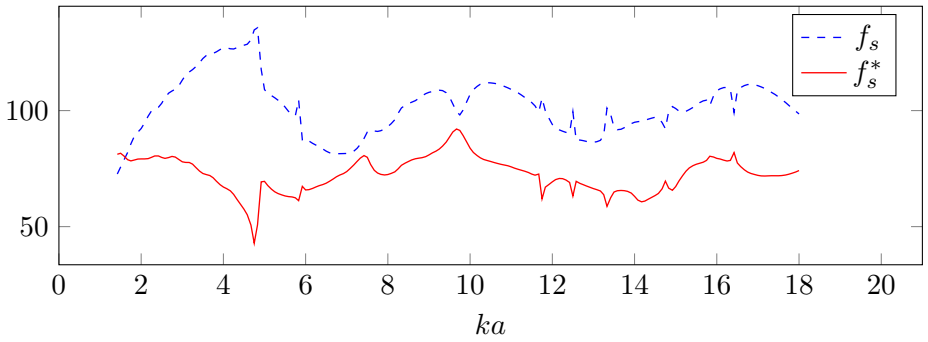

Fig. 4.3.8: The relative residual of the far field pattern and its intensity in L_2-norm corresponding to shape parameters' error of 50%.

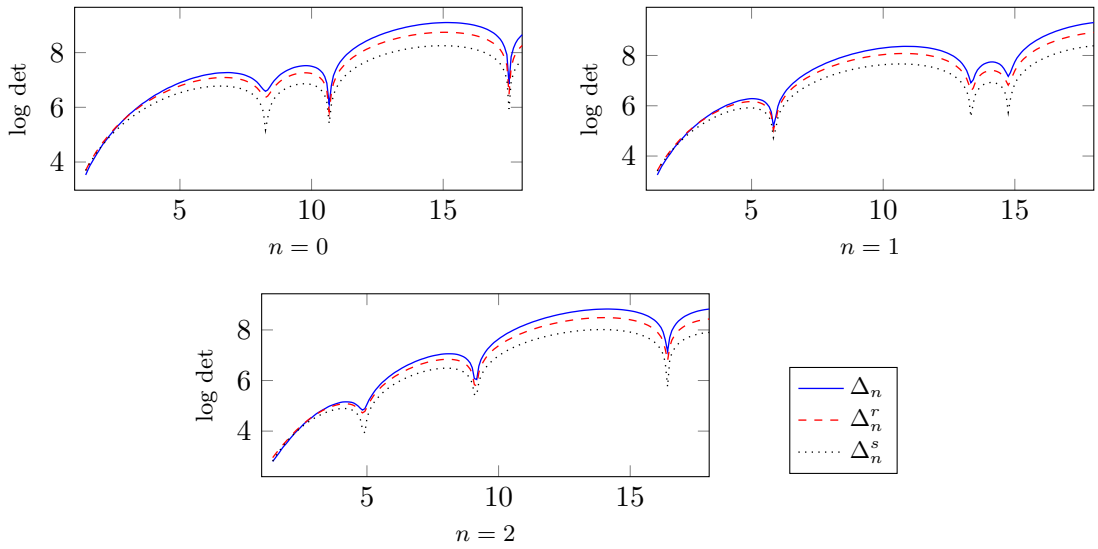

Fig. 4.3.9: Sensitivity of the determinant of the modal matrices for target shape parameter to the normalized frequency ka.

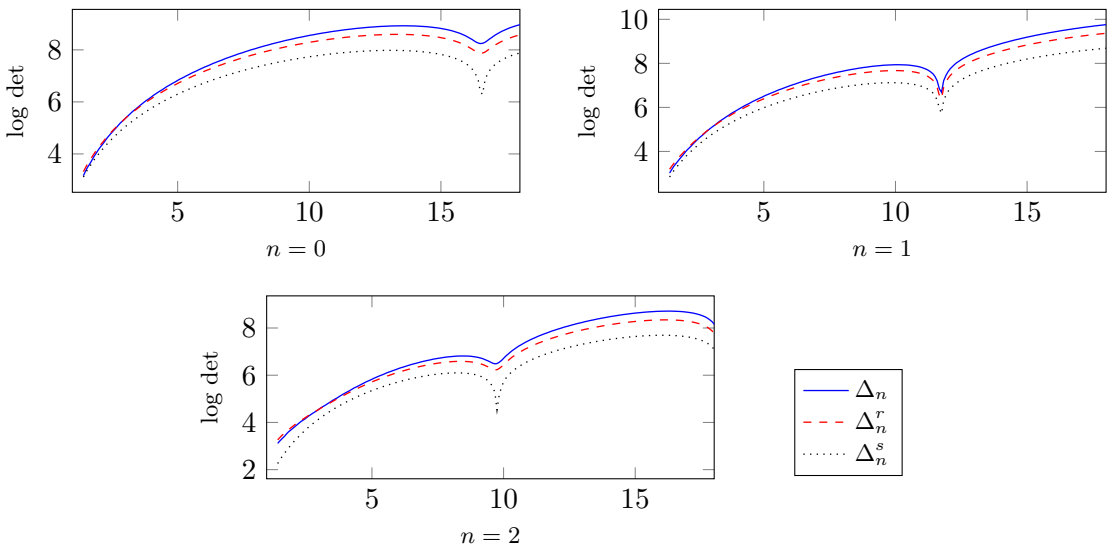

Fig. 4.3.10: Sensitivity of the determinant of the modal matrices for initial guess shape parameters to the normalized frequency ka.

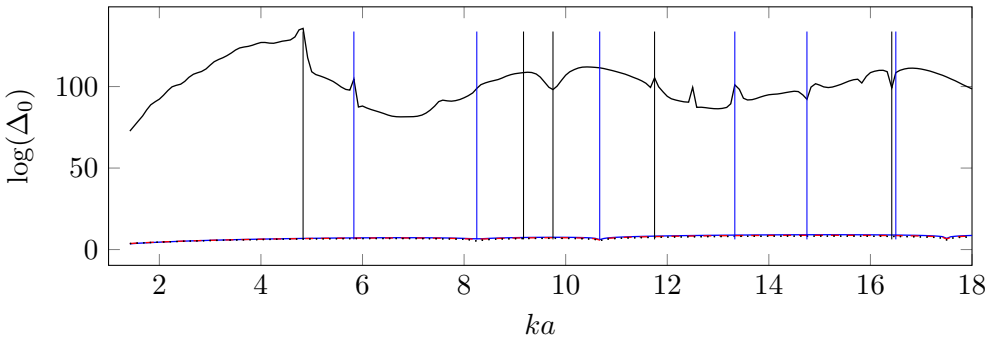

Fig. 4.3.11: Sensitivity of the determinant of the modal matrices for target and doubled value shape paraters (black and blue vertical lines respectively) together with FFP difference f_s the normalized frequency ka.

convergence. To perform that analysis, we have studied the cost function and shown that for high frequencies, initial guesses may be out of the region of convergence. We have also addressed the issue of initial guesses that should be chosen carefully. In particular, we have illustrated the fact that when the initial guess is out of the region of convergence, it turns out to be difficult and even impossible to reconstruct the material parameters. We do not have a rigorous proof of that result but we have tested a huge quantity of regularization parameters and none of them have succeeded in stabilizing the reconstruction.

Chapter 5

Two Dimensional Numerical Results

Contents

This chapter gathers numerical experiments covering different aspects related to the accuracy of the inverse problem delivered by **SRA**. We first address the issue of managing noisy data and we analyze the accuracy of the reconstruction for different noise levels (2%, 10%, 20%). Then we show that it is possible to recover the location of the obstacle together with its characteristics by using a two step algorithm. First we recover the shape and the physical parameters (we restrict ourselves to the density here), using the intensity of the FFP, and then we recover the location employing directly the FFP. In Section 5.3 we tackle a problem with limited aperture data and back-scattering measurements. We mimic here a physical setup composed of one source surrounded by receivers, which rotates around the obstacle. The restriction on the aperture is thus compensated by various incident waves. Finally, we consider the full reconstruction problem and we show that we can recover Lamé parameters, density, shape and location by using multiple frequency data.

5.1 Analysis of the Noise Effect in the Case of a Disk

In real-world situations, the data include noise generated during the measurement campain. Then, to have any chance of retrieving the material parameters from noisy data, we must ensure that material parameters have a stronger impact on the measurements than the level of noise. Regarding the reconstruction of the shape, the situation is quite clear at least for the range of frequencies $ka \in [1, 4]$ since we have seen that the shape parameters have a strong impact on the FFP exceeding in general 50%. Hence, the reconstruction is not very sensitive to noisy data as long as the noise is under 50% which corresponds to a very high level of noise which is expected not to be reached even in the case of realistic applications. Indeed, it corresponds to bad quality data that should be rejected or post-processed before any use. On the contrary, at low frequencies, the FFP is very little sensitive to the material parameters which indicates that the reconstruction may be affected largely by noisy data at low frequencies. This suggests the use of a multi-frequency strategy going to higher and higher frequencies to increase the impact of material parameters. Then the level of noise is used as a shutoff parameter hence defining the lowest error done when computing the FFP.

The computational domain is still a disk-shaped obstacle made of *steel* and surrounded by water. Its characteristics are: radius of the scatterrer $a = 1cm$, $\lambda = 115.4$GPa, $\mu = 76.9$GPa, $\rho_s = 7900\text{kg}\cdot\text{m}^{-3}$, $\rho_f = 1000\text{kg}\cdot\text{m}^{-3}$. The initial guesses that we consider for the following experiments are $(\lambda^{(0)}, \mu^{(0)}) = (50, 50)$GPa and $a^{(0)} = 0.5$cm, as depicted in Table 5.1.1. In addition, we compute the FFP measurements with a fourth order finite element method applied on a mesh sized in such a way there are five points per wavelength. On the other hand, in order to avoid the inverse crime [28], we reduce to three the number of points per wavelength for other FFP computations.

To perform our numerical investigations under control, we have to construct noisy FFPs from a given level of noise. Let the level of noise be quantified from a fixed number $\times$ of percent. Let $p_\infty(\hat{x}_i), \quad 1 \leq i \leq 360$ be the set of the measured FFPs produced synthetically before any perturbation with noise. Then let us introduce a vector *rand* composed of 360 pseudo-random points uniformly distributed between $-\frac{1}{2}$ and $\frac{1}{2}$. Then we normalize *rand* by dividing each of its components by its L^2-norm and we define the vector v with components v_i as

$$v_i = \frac{rand_i}{\| rand \|_2}.$$

The noisy FFP reads as

$$p_{\infty,noise}(\hat{x}_i) = (1 + \times v_i) p_\infty(\hat{x}_i) \qquad 1 \leq i \leq 360 \tag{5.1.1}$$

Elastic medium *Steel*		λ	μ
Target (GPa)		115.4	76.9
Initial Guess (GPa)	$(\lambda^{(0)}, \mu^{(0)})$	50	50
Relative Errors (%)		56.67	34.98

Tab. 5.1.1: Lamé coefficients corresponding to the *steel*.

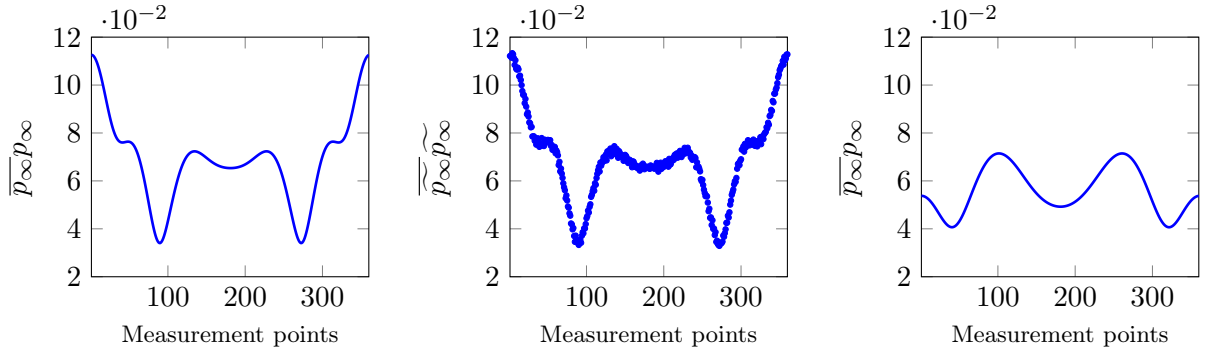

(a) FFP Target (b) FFP measured (c) FFP initial guess

Fig. 5.1.1: (a) FFP intensity corresponding to the target of a disk-shaped scatterer made of *steel*, (b) FFP intensity measured with 2% of noise level and (c) FFP intensity computed from the initial guess for normalized frequency $ka = 2.67$.

♯ iter(n)	RR	REM	RES
0	106.93	50.99	50
1	52.13	44.22	17.38
2	5.29	44.05	1.49
3	2.96	43.52	$9.21 \cdot 10^{-3}$
4	2.58	43.13	$4.47 \cdot 10^{-2}$
5	2.16	42.81	$9.72 \cdot 10^{-3}$

(a) $\alpha_m = 10^{-2}$, $\alpha_s = 1$.

♯ iter(n)	RR	REM	RES
6	2.15	29.68	$6.81 \cdot 10^{-2}$
7	2.12	24.31	$7.42 \cdot 10^{-2}$
8	2.1	20.27	$8.43 \cdot 10^{-2}$
9	2.07	18.12	$8.51 \cdot 10^{-2}$
10	2.05	15.89	$9.27 \cdot 10^{-2}$
11	2.04	15.17	$8.37 \cdot 10^{-2}$

(b) $\alpha_m = 10^{-4}$, $\alpha_s = 1$.

Tab. 5.1.2: RR, REM and RES of a disk-shaped scatterer made of *steel*, $ka = 2.67$, noise level= 2%.

5.1.1 2% Noise Level

Before describing the experiments, let us insist on the fact that with 2% of noise, we cannot expect a residual error RR better than 2%. The selected normalized frequencies are $ka = 2.67$ and 5.33. In Figure 5.1.1 we have plotted the FFP corresponding to the target, the FFP measured and the FFP computed for the initial guesses and a frequency of $ka = 2.67$. During the first stage of 11 iterations corresponding to $ka = 2.67$, the relative residual starts from 106.93% and ends around 2.04% as illustrated in Figure 5.1.3. The selected regularization parameters are $\alpha_m = 10^{-2}, 10^{-4}$, $\alpha_s = 1$, and the evolution of RR together with the errors REM and RES are depicted in Tables 5.1.2(a)-(b), for $\alpha_m = 10^{-2}$ and $\alpha_m = 10^{-4}$ respectively. We deduce from the fast decay of RR and UVSthat the shape parameter is retrieved in 3-4 iterations (see Table 5.1.2(a) and Figure 5.1.3(b) respectively), and this interpretation is validated regarding the column RES in Table 5.1.2(a). Other regularization parameters such as $\alpha_m = 10^{-5}, 10^{-6}$ have been tested after the stagnation at the 11th iteration, even if we have almost achieved 2% of error with RR. Indeed, at Table 5.1.2(b) we observe that the reconstruction error of shape parameters reaches 8.37 10^{-2}%, which is really good, while on material parameters the error is still around 15%.

Once having observed that decreasing the regularization parameter does not cause any improvement, we have decided to assess the impact of the frequency on the reconstruction. Figure 5.1.2 illustrates the dependency of the intensity with respect to the material parameters. We can observe that it increases with the frequency. Indeed, at $ka = 2.67$, the FFPs for the Target and for the IG $(\lambda^*, \mu^*) = (50, 50)$GPa

♯ iter(n)	RR	REM	RES
12	2.61	0.25	$7.59 \cdot 10^{-2}$
13	2.13	4.17	$6.42 \cdot 10^{-2}$
14	2.14	5.21	$6.3 \cdot 10^{-2}$

(a) $\alpha_m = 10^{-4}$, $\alpha_s = 1$.

♯ iter(n)	RR	REM	RES
14	2.14	2.84	$8.33 \cdot 10^{-2}$
15	2.12	3.02	$6.98 \cdot 10^{-2}$
16	2.15	4.05	$7.86 \cdot 10^{-2}$

(b) $\alpha_m = 10^{-5}$, $\alpha_s = 1$.

Tab. 5.1.3: RR, REM and RES of a disk-shaped scatterer made of *steel*, $ka = 5.33$, noise level= 2%.

only differ from 3.27% while their difference is about 10.5% at $ka = 5.33$. This suggests the possibly interest of increasing the frequency during the reconstruction process.

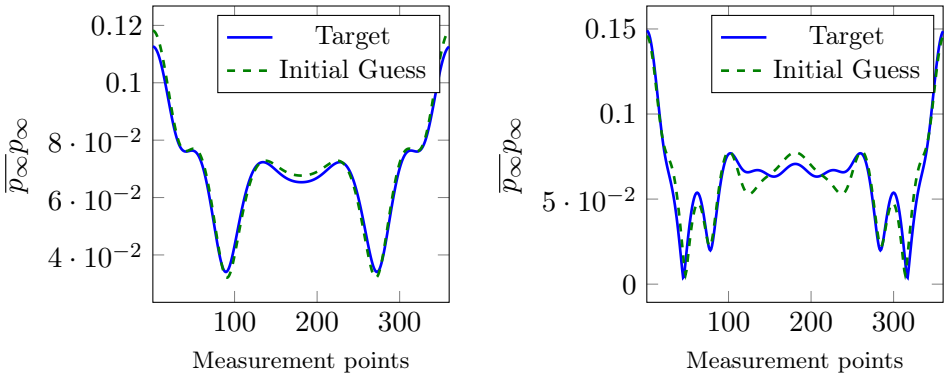

(a) $ka = 2.67$ (b) $ka = 5.33$

Fig. 5.1.2: The FFP intensity corresponding to the Target and material parameters $(\lambda^*, \mu^*) = (50, 50)$GPa for $k = 2.67$ and 5.33 respectively.

During the second stage we use $ka = 5.33$. Several regularization parameters have been tested for material parameters, such as $\alpha_m = 10^{-2}, 10^{-3}, 10^{-4}, 10^{-5}$ and $\alpha_m = 10^{-6}$. The best reconstruction corresponds to $\alpha_m = 10^{-4}$, and the corresponding evolutions of RR, REM and RES are detailed in Table 5.1.3(a). We stop at iteration 13, with 4.17% of error on material parameters and 6.42 10^{-1}% on shape parameters, where the relative residual takes the lowest value of 2.13%. We observe that with this quantity the RR attains the noise level of 2%, illustrated with a straight red line in Figure 5.1.3. In addition, we have tested more regularization parameters as $\alpha_m = 10^{-5}$ (depicted in Table 5.1.3(b)), and even if there is a little improvement, we have not achieved error values closer to 2%. In the last experiment corresponding to $\alpha_m = 10^{-5}$, the relative residual takes the lowest value at iteration 15, where the error on material parameters is about 3.02%.

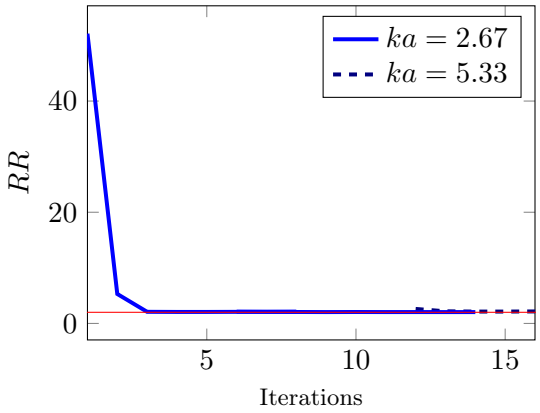

Fig. 5.1.3: Convergence history of a disk shaped scatterer made of *steel*, ka=2.67 then 5.33, noise level= 2%.

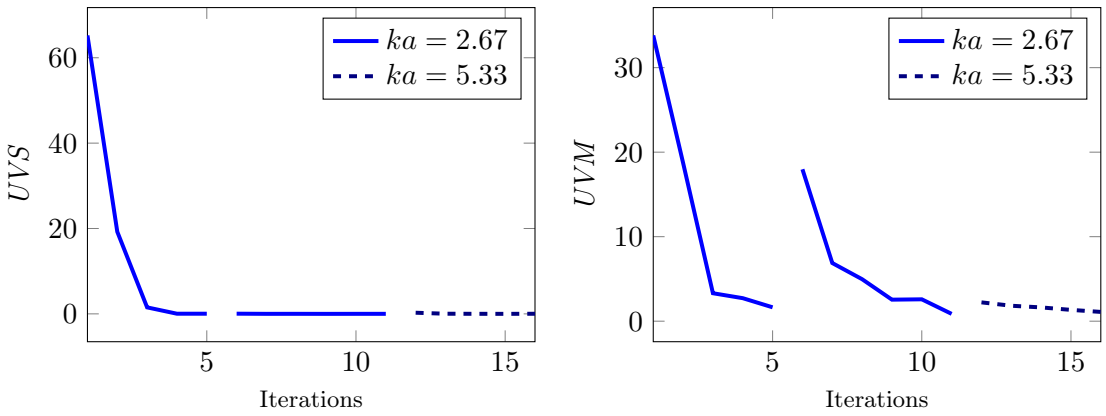

(a) Shape parameters

(b) Material parameters

Fig. 5.1.4: $UVS$and $UVM$of a disk shaped scatterer made of *steel*, ka=2.67 then 5.33, noise level= 2%.

♯ iter(n)	RR	REM	RES
0	106.88	50.99	50
1	51.59	44.2	16.95
2	11.45	44.15	1.76
3	10.28	44.11	0.32
4	10.19	44.25	0.27
5	10.07	44.41	0.3
6	10.05	44.4	0.28

(a) $\alpha_m = 10^{-2}$, $\alpha_s = 1$.

♯ iter(n)	RR	REM	RES
7	10.07	53.84	0.32
8	10.1	57.11	0.31

(b) $\alpha_m = 10^{-4}$, $\alpha_s = 1$

Tab. 5.1.4: RR, REM and RES of a disk-shaped scatterer made of *steel*, $ka = 2.67$, noise level= 10%.

5.1.2 10% Noise Level

As previously, we remind that with 10% of noise level, we cannot expect a RR lower than 10%. The selected normalized frequency at first step is $ka = 2.67$, and the regularization parameters are $\alpha_m = 10^{-2}$, $\alpha_s = 1$. We can observe the noisy data in Figure 5.1.5(b). The evolution of REM and RES for $\alpha_m = 10^{-2}$ and $\alpha_s = 1$ is depicted at Table 5.1.4(a), and we observe that the shape parameters have been remarkably well reconstructed while material parameters do not evolve. The relative residual is reduced from 106.88% to 10.5% after 6 iterations (see its evolution in Figure 5.1.6), while the relative errors at stagnation are around 44.4% and 0.28% for material and shape parameters respectively. Figure 5.1.7(a) depicts how the reconstruction of the material parameters behaves opposite to the one of the shape. This suggests to move on with $ka = 5.33$. But before, we have tested a lower value for $\alpha_m = 10^{-4}$. Table 5.1.4(b) shows that it creates some instabilities and incites us to change the frequency.

For a higher frequency, the influence of the material parameters may be bigger than the noise level. To this end, we have selected the normalized frequency $ka = 5.33$, which provides a physical context in which the material parameters have influence enough.

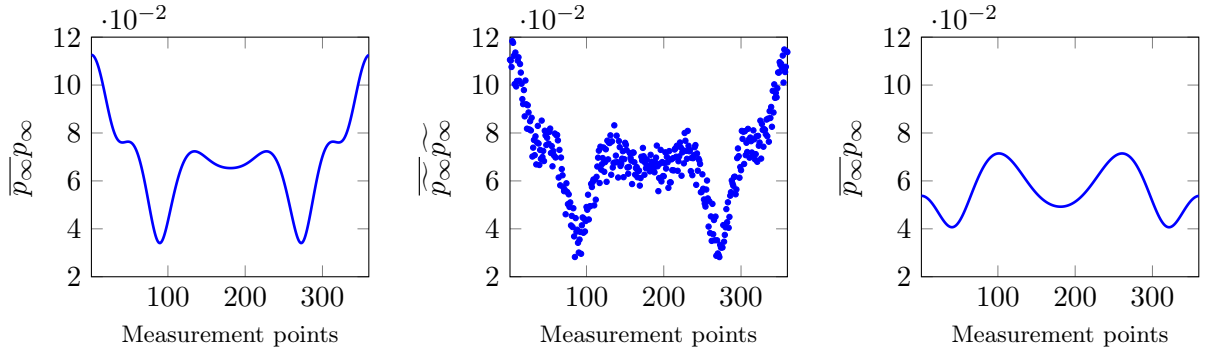

(a) FFP Target (b) FFP measured (c) FFP initial guess

Fig. 5.1.5: FFP intensity corresponding to the target of a disk-shaped scatterer made of *steel*, (b) FFP intensity measured with 10% of noise level and (c) FFP intensity computed from the initial guess for the normalized frequency $ka = 2.67$.

Table 5.1.5(a) confirms that increasing ka contributes to cause the convergence. The selected regularization parameters for step 2 are $\alpha_m = 10^{-2}$, $\alpha_s = 1$, and the errors at stagnation are 11.74%

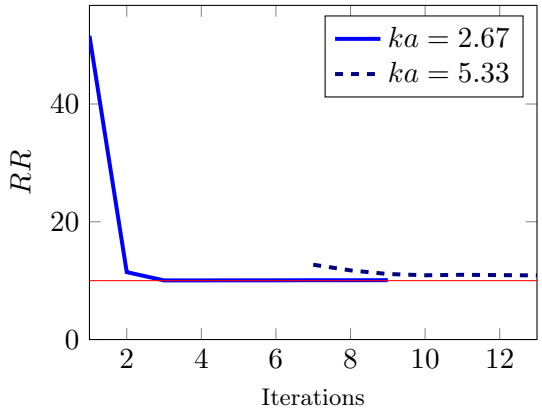

Fig. 5.1.6: Convergence history of a disk shaped scatterer made of *steel*, $ka = 2.67$ then 5.33, noise level= 10%.

and 0.65% on material and shape parameters respectively. We see that the reconstruction of shape parameters is a little bit less accurate, which is a side effect of increasing the frequency. In addition, the reconstruction of material parameters is illustrated in Figure 5.1.7(b), with the fast decay of UVM. A third step has been tested with $\alpha_m = 10^{-3}$, $\alpha_s = 1$ and we observe that the final reconstruction is better both for material and shape parameters, with final errors of 5.37% and 0.54% on material and shape parameters respectively. Let us specify that even if a considerable quantity of regularization parameters has been tested, we do not achieve lower values for RR.

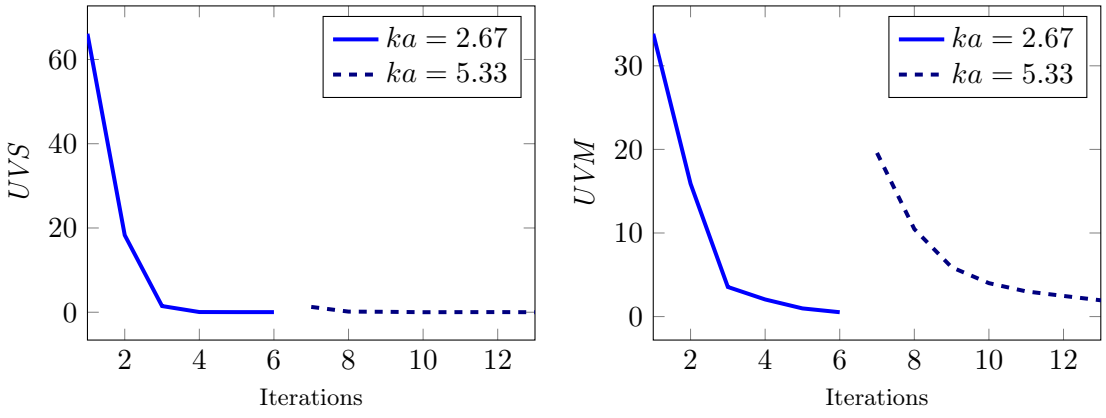

(a) Shape parameters

(b) Material parameters

Fig. 5.1.7: $UVS$and $UVM$of a disk shaped scatterer made of *steel*, $ka = 2.67$ then 5.33, noise level= 10%.

♯ iter(n)	RR	REM	RES
7	12.71	30.88	0.94
8	11.74	22.75	0.79
9	11.13	17.86	0.68
10	10.92	14.42	0.68
11	10.99	11.74	0.65

(a) $\alpha_m = 10^{-2}$, $\alpha_s = 1$.

♯ iter(n)	RR	REM	RES
11	10.98	1.77	0.57
12	10.94	5.37	0.54
13	10.96	9.67	0.52

(b) $\alpha_m = 10^{-3}$, $\alpha_s = 1$.

Tab. 5.1.5: RR, REM and RES of a disk-shaped scatterer made of *steel*, $ka = 5.33$, noise level= 10%.

5.1.3 20% Noise Level

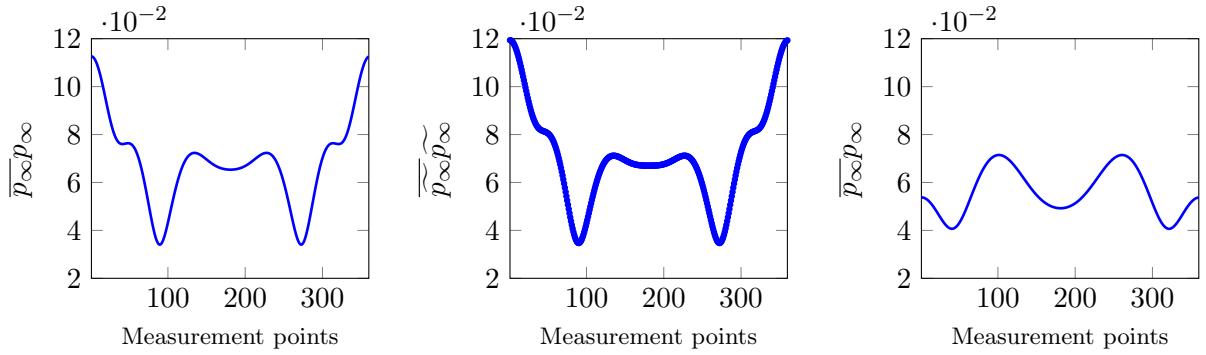

(a) FFP Target (b) FFP measured (c) FFP initial guess

Fig. 5.1.8: FFP intensity corresponding to the target of a disk-shaped scatterer made of *steel*, (b) FFP intensity measured with 20% of noise level and (c) FFP intensity computed from the initial guess for normalized frequency $ka = 2.67$.

Here again, it shall be emphasized that since the level of noise is 20%, RR can not be under 20%. For 20% of noise level, the selected initial normalized frequency, as in all the other cases, is $ka = 2.67$. We observe the corresponding FFP measurements in Figure 5.1.8(b). During the first step, the shape regularization parameter is $\alpha_s = 1$, while for material parameters, it is $\alpha_m = 10^{-1}$. The convergence history of this step is depicted in Figure 5.1.10, and detailed at Table 5.1.6(a) together with the evolution of REM and RES. Then, we see that shape parameters have been successfully reconstructed, while material parameters seem to be stagnating far from the target. Figures 5.1.11(a) and (b) show that UVSdecays rapidly while UVMincreases a little after to get stagnated. Both behaviors are coherent with the fast reconstruction of shape parameters and the stagnation of material parameters reconstruction respectively.

As a step 2, we have tested several regularization parameters with lower values, but we have not obtained satisfactory results. As an example we have detailed the results corresponding to $\alpha_s = 1$ and $\alpha_m = 10^{-2}$ in Table 5.1.6(b). We observe that the relative residual continues decreasing slowly and shape parameters are reconstructed, but material parameters are not. This is why at the 11th iteration we propose to increase the frequency value. In Tables 5.1.7(a) - (b) we introduce two different experiments corresponding to the normalized frequency $ka = 5.33$, with different material regularization parameters, $\alpha_m = 10^{-1}$ and $\alpha_m = 10^{-2}$ respectively ($\alpha_s = 1$ is constant). It is observable that both reconstructions stop evolving at the 13th iteration, there is no improvement

♯ iter(n)	RR	REM	RES
0	106.93	50.99	50
1	51.01	50.05	15.56
2	22.32	48.56	2.82
3	21.17	47.84	1.12
4	20.38	47.51	0.85
5	20.14	47.39	0.75
6	20.05	47.33	0.71
7	20.01	47.34	0.65
8	19.96	47.39	0.6
9	19.93	47.45	0.58
10	19.92	47.53	0.57
11	19.91	47.62	0.5

(a) $\alpha_m = 10^{-1}$, $\alpha_s = 1$.

♯ iter(n)	RR	REM	RES
11	20.03	47.34	0.64
12	19.96	47.38	0.6
13	19.93	47.45	0.54
14	19.9	47.53	0.53
15	19.89	47.63	0.51
16	19.88	47.73	0.49

(b) $\alpha_m = 10^{-2}$, $\alpha_s = 1$.

Tab. 5.1.6: RR, REM and RES of a disk-shaped scatterer made of *steel*, $ka = 2.67$, noise level= 20%.

♯ iter(n)	RR	REM	RES
11	31.15	44.89	0.51
12	25.08	44.27	0.7
13	20.39	43.16	1.38
14	20.85	39.08	1.73
15	22.32	36.36	1.8

(a) $\alpha_m = 10^{-1}$, $\alpha_s = 1$.

♯ iter(n)	RR	REM	RES
11	31.15	41	0.44
12	24.6	44.57	0.87
13	20.32	42.61	1.52
14	21.15	29.56	1.55

(b) $\alpha_m = 10^{-2}$, $\alpha_s = 1$.

Tab. 5.1.7: RR, REM and RES of a disk-shaped scatterer made of *steel*, $ka = 5.33$, noise level= 20%.

on the recovery of material parameters. It is actually predictable once observing that the relative difference between the FFPs of the Target and of the initial guess $(\lambda^*, \lambda^*) = (50, 50)$GPa is about 10% at $ka = 5.33$. This suggests to increase the frequency again to make the difference between noisy FFP and updated FFP big enough. Ideally, we need to use a frequency that ensures the relative difference is at least around 20%. Figure 5.1.9(b) shows that $ka = 6$ is a good candidate since the relative difference is about 52%.

The history convergence corresponding to ka= 2.67 and 6 is illustrated in 5.1.10, and the evolution of RR, REM and RES corresponding to $ka = 6$, $\alpha_m = 10^{-4}$ and $\alpha_s = 1$, is depicted in Table 5.1.8. In this case, the relative residual stops decreasing at iteration 15, with a value of 19.82%, corresponding to 10.61% of relative error on material parameters and 1.8 10^{-2}% on shape parameters. If we check the evolution of $UVS$and UVMcorresponding to the normalized frequency $ka = 6$, we observe that $UVS$is almost constant due to the fact that the shape parameters have been already reconstructed and they do not move anymore while UVMdecays significantly, illustrating reconstruction of the material parameters.

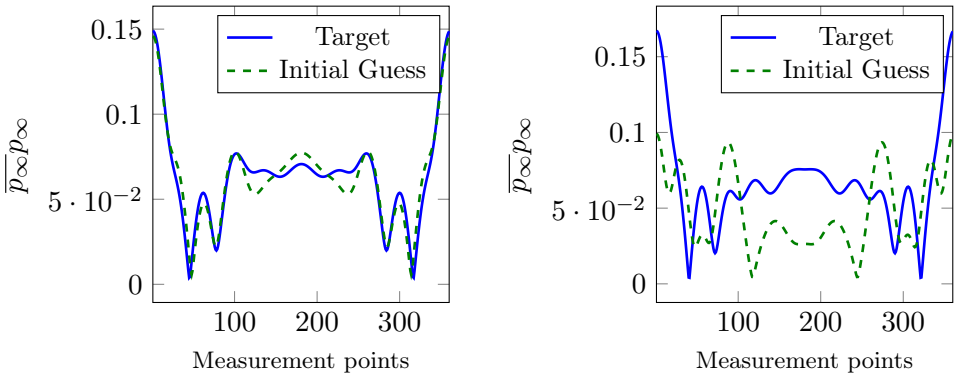

(a) $ka = 5.33$ (b) $ka = 6$

Fig. 5.1.9: The FFP intensity corresponding to the Target and material parameters $(\lambda^*, \mu^*) = (50, 50)$GPa for $k = 5.33, 6$ respectively.

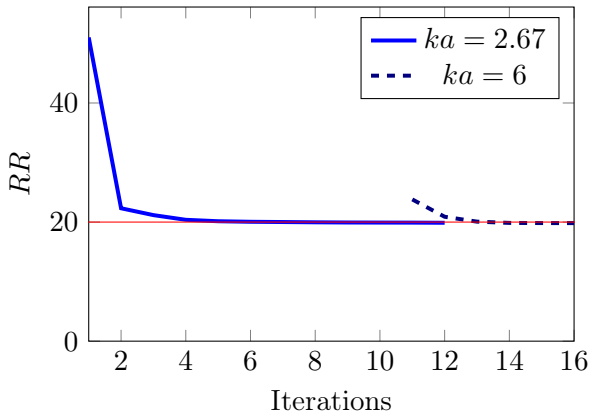

Fig. 5.1.10: Convergence history of a disk shaped scatterer made of *steel*, $ka = 2.67$ then 6, noise level= 20%.

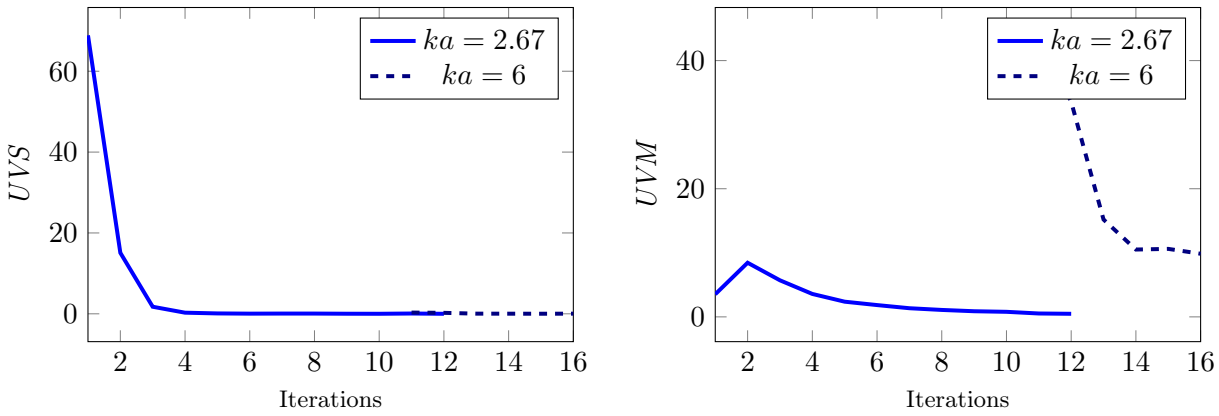

(a) Shape parameters (b) Material parameters

Fig. 5.1.11: $UVS$and $UVM$of a disk shaped scatterer made of *steel*, $ka = 2.67$ then 6, noise level= 20%.

♯ iter(n)	RR	REM	RES
11	23.81	43.94	0.31
12	20.89	33.57	0.24
13	20.07	15.19	$4.09 \cdot 10^{-2}$
14	19.86	10.51	$2.92 \cdot 10^{-2}$
15	19.83	10.61	$1.8 \cdot 10^{-2}$

Tab. 5.1.8: RR, REM and RES of a disk-shaped scatterer made of *steel*, $ka = 6$, noise level= 20%.

5.2 Determination of the Density, Shape and Location for Various Configurations

In this section, we introduce a multi-step procedure that retrieves the position of the obstacle together with other parameters. Our methodology is based on the strategy proposed by Ivanyshyn and Kress [63], which is based on first retrieving the shape using the intensity of the FFP ($\mid p_\infty^2 \mid = \overline{p}_\infty p_\infty$), and straightaway, retrieving the location. In our case, we will thus achieve the reconstruction of the solid including its shape and some constitutive parameters and we will next deliver its location with the far field pattern (p_∞). We thus introduce an additional parameter which is defined as a point in $\mathbb{R}^2$ called the reference point and denoted by (x_c, y_c). For illustrating that purpose, we consider for instance the following inverse problem:

(IP 3) Given one incident plane wave for a fixed wavenumber, from the access to full aperture data, find the density ρ_s, the reference point (x_c, y_c) and the shape parameters $s_1, ..., s_{N_\Gamma}$ such that

$$F\left(\rho_s, x_c, y_c, \Gamma\left(s_1, ..., s_{N_\Gamma}\right)\right)\left(\hat{x_j}\right) = \widetilde{p_\infty}\left(\hat{x_j}\right) \quad j = 1, ..., N_x \tag{5.2.1}$$

We have illustrated the reference point (x_c, y_c) in Figure 5.2.1, for a disk shaped scatterer. It can be added in the different parametrizations without any difficulty. For example, in the case of a disk shaped obstacle, the generalized parametrization can be introduced as:

$$\Gamma = \{(x_c, y_c) \quad + \quad s_1(\cos\theta, \sin\theta) \quad \theta \in [0, 2\pi]\}$$

In addition, we remind that the Fréchet derivative with respect to the position parameters can be computed as a solution to **(BVP 2)** with the corresponding directions:

$$h_1 = \frac{\partial \Gamma}{\partial x_c} = \overrightarrow{e_1}$$
$$h_2 = \frac{\partial \Gamma}{\partial y_c} = \overrightarrow{e_2}$$

(x_c, y_c) denoting the coordinates of the reference point of location.

First of all we have printed the influence of the density, as we have done for Lamé and shape parameters with $f_m(ka)$ and $f_s(ka)$ respectively in Chapter 4. We denote by ρ_0 the density parameter corresponding to the *steel* material ($\rho_0 = 7900\text{kg } m^{-3}$). We have then computed the corresponding FFP for different values of the frequency ka ranging from 1 to 20. We denote the corresponding function of ka by FFP_0. Then we propose to perturb the initial density parameter by considering 2ρ. Straightaway, we compute the corresponding FFP for frequencies ka ranging from 1 to 20 and we get the function of ka denoted by FFP. Then we introduce the function f_d defined by:

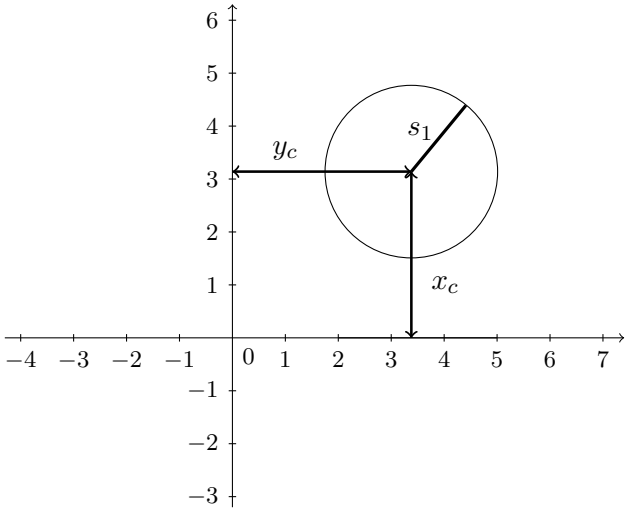

Fig. 5.2.1: The position parameters (x_c, y_c) illustrated for the disk shaped scatter of radius s_1.

$$f_d(ka) = \frac{\| FFP(ka) - FFP_0(ka) \|_2}{\| FFP_0(ka) \|_2} \times 100 \tag{5.2.2}$$

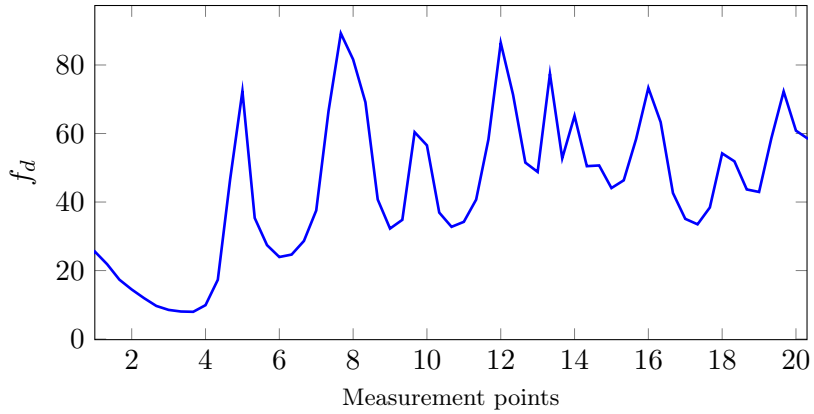

Fig. 5.2.2: The relative difference of FFP intensity for normalized frequency ka ranging from 1 to 20 and 100% of error on the density parameter.

We observe in Figure 5.2.2 that the impact of the density is at least of 9% reached for $ka = 3.5$. In order to measure the reconstruction of the density, we define the quality factor defined as the Relative Error on Density (RED) as follows:

$$RED(n) = \frac{| \rho - \rho^{(n)} |}{| \rho |} \times 100. \tag{5.2.3}$$

Another quantity of interest is the Relative Error on Location parameters (REL), defined as:

$$REL(n) = \frac{\left| \left(x_c - x_c^{(n)} \right)^2 + \left(y_c - y_c^{(n)} \right)^2 \right|^{1/2}}{| x_c^2 + y_c^2 |^{1/2}} \times 100. \tag{5.2.4}$$

Finally, we remind that the following experiments consist on two different stages. The first one corresponds to update the density and the shape parameters according to RR, while the second stage

corresponds to the reconstruction of the position parameters x_c and y_c using the FFP field. The Relative Residual corresponding to the FFP field, denoted by RR_2, is defined by:

$$RR_2(n) = \frac{\| \widetilde{p_\infty} - F(\mathcal{P}^n) \|_2}{\| \widetilde{p_\infty} \|_2} \times 100. \tag{5.2.5}$$

In what follows, we consider the two step reconstruction for three different cases. To this end, we consider three different parametrizations, and two different materials. For the normalized frequencies, ka is defined with $a = s_{min} = \min_{1 \le i \le N_\Gamma} s_i$.

5.2.1 Ellipse

The target is an ellipse made of *aluminium* with radii $s_1 = 1$cm and $s_2 = 0.5$cm and the initial guess is given by the pair of radii $s_1 = 0.75$cm and $s_2 = 0.75$cm, as illustrated in Figures 5.2.3(a) and (b) respectively. The external boundary is a circle with radius $b = 7.5$ cm and Lamé coefficients $\lambda = 51.09$GPa, $\mu = 26.32$GPa. The target of density is $\rho = 2700$ kg m^{-3}, while the initial guess is $\rho^{(0)} = 5200$ kg m^{-3}, with an initial relative error of 92%. The meshes corresponding to the target and initial guess are illustrated in Figure 5.2.4(a) and (b) respectively. Synthetic measurements are created numerically by employing the IPDG code introduced in Chapter 1. We compute the FFP with a fourth order finite element method applied on a mesh sized in such a way there are five points per wavelength. On the other hand, when we compute the numerical FFP, we use the same finite element method but with only three points per wavelength. In that way, we avoid making any inverse crime [28].

(a) Target (b) Initial Guess

Fig. 5.2.3: Ellipse-shaped domain for target vs. initial guess.

During the first stage, the initial relative residual for the selected normalized frequency $ka = 1.33$ is around 136%, as detailed in the first line of the Table 5.2.1(a). We observe that this quantity decreases swiftly (see curve of RR on the convergence history depicted in Figure 5.2.5) until below than 5% in four iterations for regularization parameters $\alpha_\rho = 10^{-11}$ and $\alpha_s = 10$. If we observe the columns RED and RES in Table 5.2.1(a), we deduce that the shape parameters have been quite successfully reconstructed (0.92% of error) while the density parameter is far away from being retrieved ($RED = 81.86\%$). This is, in fact, because the influence of shape parameters is bigger than the influence of the density. Previously we have seen that for $ka = 1.33$ the influence is clearly less than 20%, while for shape parameters it is bigger than 50%. After the stagnation at iteration 5, we have tested several regularization parameters. The best results correspond to the selection of $\alpha_\rho = 10^{-13}$ and $\alpha_s = 1$, and we observe that the relative residual decreases until 5.56 10^{-2}% in 5 iterations (see Table 5.2.1(b)). The final reconstruction is quite accurate as detailed in Table 5.2.2.

During the second stage, dealing with location retrieving, two different frequency values have been employed. The corresponding normalized frequencies are $ka = 0.33, 1.5$. During the first step, the regularization parameter has been $\alpha_{loc} = 0$, and we see that convergence history is quite slow. Bigger

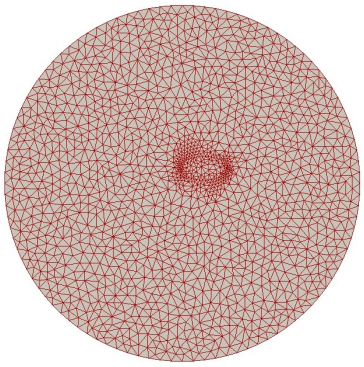

(a) Target: 5482 elements

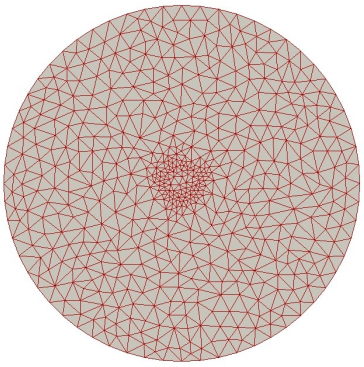

(b) Initial guess: 2884 elements

Fig. 5.2.4: Meshes for target vs. initial guess.

♯ iter(n)	RR	RED	RES
0	136.16	92.59	31.62
1	30.85	98.27	10.77
2	11.32	88.83	3.06
3	4.72	85.43	0.77
4	4.29	82.79	0.86
5	4.28	81.86	0.92

(a) $\alpha_\rho = 10^{-11}$, $\alpha_s = 10$.

♯ iter(n)	RR	RED	RES
6	4.14	78.6	0.99
7	2.28	11.92	0.7
8	0.49	0.48	0.12
9	0.15	$9.35 \cdot 10^{-2}$	$4.8 \cdot 10^{-2}$
10	$5.77 \cdot 10^{-2}$	$6.42 \cdot 10^{-2}$	$3.01 \cdot 10^{-2}$
11	$5.56 \cdot 10^{-2}$	$8.82 \cdot 10^{-2}$	$3.21 \cdot 10^{-2}$

(b) $\alpha_\rho = 10^{-13}$, $\alpha_s = 1$.

Tab. 5.2.1: Evolution of RR, RED and RES for *aluminium* ellipse shaped scatterer, $ka = 1.33$, noise level= 0%.

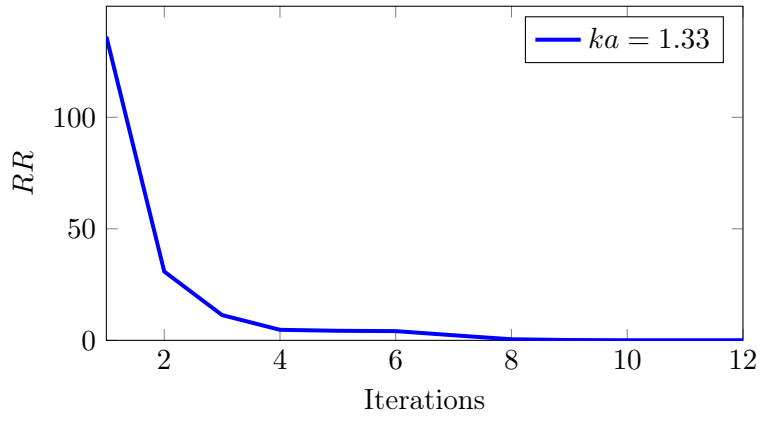

Fig. 5.2.5: Convergence history of an ellipse shaped scatterer made of *aluminium*, $ka = 1.33$, noise level= 0%.

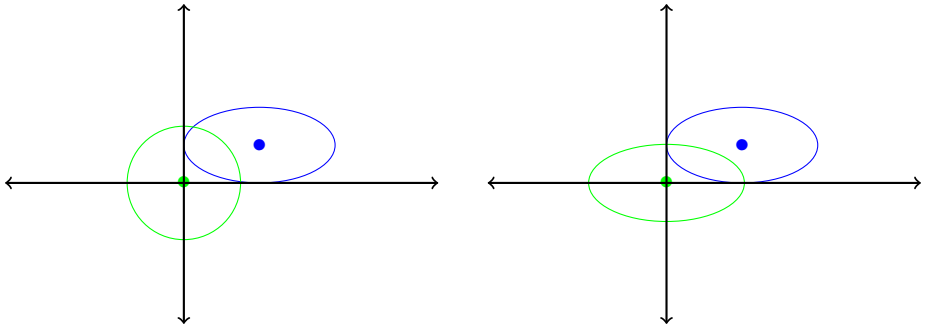

(*b*) Stage 1: Iteration 0.

(*b*) Stage 1: Iteration 5.

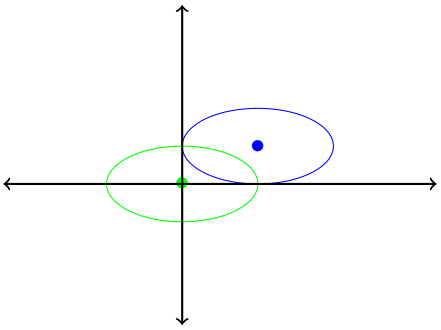

(*b*) Stage 1: Iteration 11.

Fig. 5.2.6: Shape and center point of an ellipse-shaped scatterer: target vs. computed parameters at different stagnations.

Parameter	**Target**	**Initial Guess**	**Computed**	**Relative error at convergence (%)**	
s_1	1	0.75	1.0003	$3.23\ 10^{-2}$	**RES**
s_2	0.5	0.75	0.5001	$2.77\ 10^{-2}$	$3.21\ 10^{-2}$
ρ	2700	5200	2702.38	$8.82\ 10^{-2}$	

Tab. 5.2.2: Target, initial guess and computed parameters corresponding to the *alluminium* ellipse shaped scatterer case, normalized frequency $ka = 1.33$, noise level= 0%.

frequency values have been tested in order to obtain faster reconstruction, but we have not found an efficient one. We have to mention that the tolerance (denoted by *tol* in the algorithms in Chapter 3) to define the stagnation has been eliminated, as the regularization parameter is $\alpha_{loc} = 0$ (so it is not possible to select a lower one), and increasing the frequency after the stagnation corresponding to tol= 0.1, was unfruitful.

The evolution of RR_2 corresponding to $ka = 0.33$ is detailed in Table 5.2.3(a) and illustrated in Figure 5.2.7 in the corresponding convergence history. Regarding REL, we observe that the reconstruction error of position parameters has decreased from 100% until 26%, and the corresponding position is illustrated in Figure 5.2.8(a). At iteration 16 RR_2 starts increasing, and consequently, the frequency is increased until $ka = 1.5$. It is observable in Table 5.2.3(b) that RR_2 decreases during two iterations and then starts increasing again. This behavior is illustrated in the convergence history of RR_2, in Figure 5.2.7. The final reconstruction of position parameters is 2.56% for the final quantity of $RR_2 = 8.2\%$, as depicted in Table 5.2.3(b). The final reconstruction of shape and position parameters is illustrated in Figure 5.2.8(b).

♯ iter(n)	RR	RR_2	REL
0	0.11	102.74	100
1	0.11	96.5	93.19
2	0.11	90.13	86.64
3	0.12	83.62	80.28
4	0.12	76.96	74.08
5	0.12	70.15	68
6	0.12	63.19	62.04
7	0.13	56.1	56.2
8	0.13	48.9	50.51
9	0.13	41.62	45.02
10	0.13	34.34	39.82
11	0.14	27.23	35.06
12	0.14	20.65	30.97
13	0.14	15.54	27.89
14	0.14	14.86	26.62
15	0.14	13.86	26.22

(a) $\alpha_{loc} = 0$.

♯ iter(n)	RR	RR_2	REL
16	$8.76 \cdot 10^{-2}$	65.4	26.25
17	$8.02 \cdot 10^{-2}$	8.2	2.56
18	$6.97 \cdot 10^{-2}$	38.06	13.31

(b) $\alpha_{loc} = 10^{-4}$.

Tab. 5.2.3: Evolution of RR, $RR2$ for an *aluminium* ellipse shaped scatterer, $ka = 0.33$, noise level= 0%.

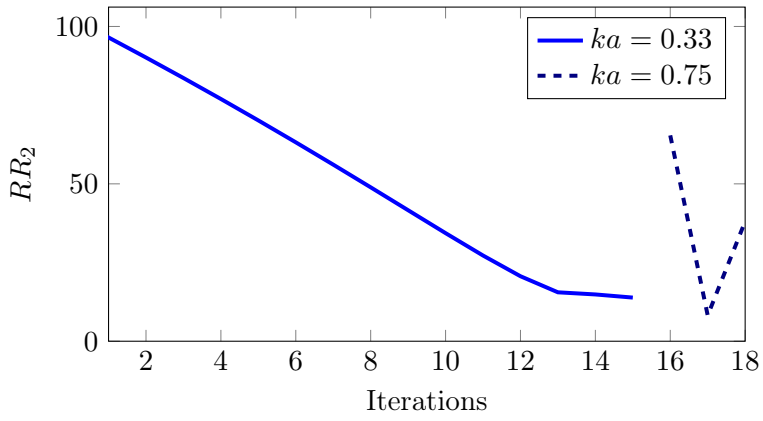

Fig. 5.2.7: Convergence history of an ellipse shaped scatterer made of *aluminium*, ka=0.33, 1.5, noise level= 0%.

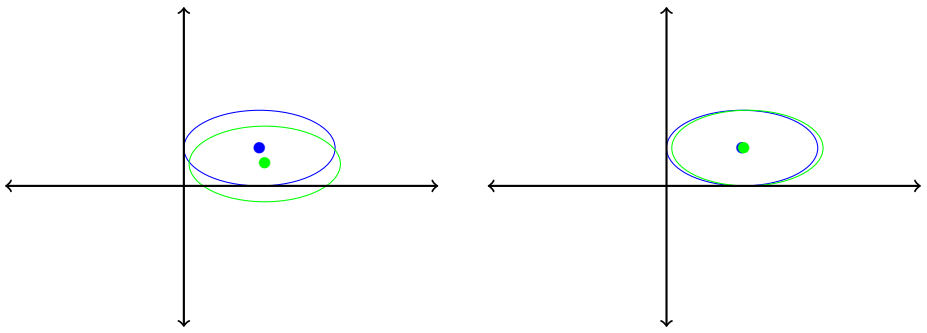

(*b*) Stage 2: Iteration 15. (*b*) Stage 2: Iteration 17.

Fig. 5.2.8: Shape and center point of an ellipse-shaped scatterer: target vs. computed parameters at different stagnations.

5.2.2 4-Point Star Domain

This is an example where the use of multifrequency data is necessary to obtain a full reconstruction. The target is a 4-point star domain illustrated in Figure 5.2.9(a), whose shape is defined with a polygonal parametrization involving shape parameters detailed in Table 5.2.4. The external boundary is a circle with radius $b = 7.5$ cm and Lamé coefficients $\lambda = 115.4$GPa, $\mu = 76.9$GPa. The targeted density is $\rho = 7900\text{kg m}^{-3}$, while the initial guess is $\rho^{(0)} = 3000\text{kg m}^{-3}$. The initial guess of the shape is a square illustrated in Figure 5.2.9(b) whose parametrization is detailed in Table 5.2.4. The meshes corresponding to the target and initial guess are depicted in Figure 5.2.10(a) and (b) respectively. We compute the FFP corresponding to the target with seven points per wavelength, while other computed FFPs, have been computed with 5 points per wavelength.

(a) Target (b) Initial Guess

Fig. 5.2.9: Polygonal-shaped domain for target vs. initial guess.

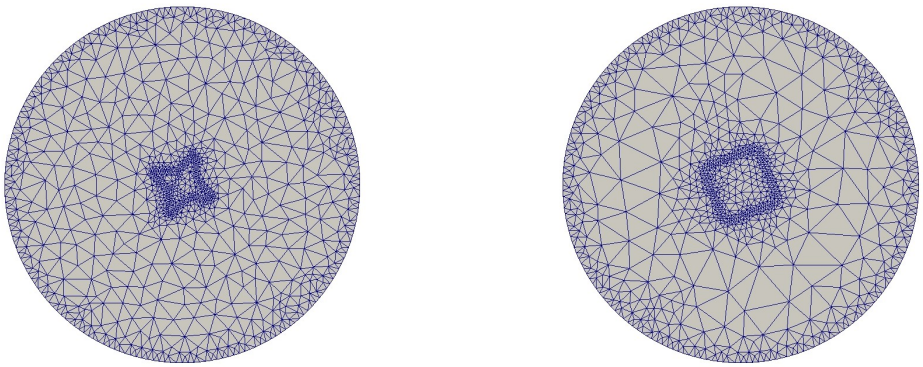

(a) Target: 1846 elements (b) Initial guess: 1774 elements

Fig. 5.2.10: Meshes for target vs. initial guess.

The first stage corresponding to the reconstruction of the density and shape parameters has been carried out first with the normalized frequency $ka = 0.4$. The relative residual starts around 64% and after five iterations using the regularization parameteres $\alpha_\rho = 10^{-5}$ and $\alpha_s = 50$ (as detailed in the evolution of RR in Table 5.2.5(a)), it decreases until 40.1%. This decay is observable in the convergence history illustrated in Figure 5.2.11. Regarding the column RES in Table 5.2.5(a), we observe that the reconstruction of shape parameters is quite slow (see Figure 5.2.12(b), the shape at stagnation at iteration 5), while the reconstruction of the density does not evolve (RED). As the influence of the shape parameters is bigger than the one of the density, we have decided to reduce the corresponding regularization parameter to $\alpha_s = 20$. In the following three iterations the reconstruction does not seem to be faster (see column RES in Table 5.2.5(b) and Figure 5.2.12(c)), but the relative

Parameter	Target	Initial Guess	Computed	Relative error at convergence (%)	
s_1	0.6	1.24	0.62	3.57	
s_2	1.5	1.75	1.45	3.24	
s_3	0.6	1.24	0.61	1.27	**RES**
s_4	1.5	1.75	1.51	0.89	
s_5	0.6	0.24	0.604	0.74	1.86
s_6	1.5	1.75	1.49	0.5	
s_7	0.6	0.24	0.58	3.08	
s_8	1.5	1.75	1.49	0.37	
ρ	7900	3000	7819.66	1.02	

Tab. 5.2.4: Target, initial guess and computed parameters corresponding to the 4-point star shaped scatterer case, 24 iterations, noise level= 0%.

residual decays until a level of 30%. After testing different regularization parameters, we have selected $\alpha_\rho = 5\ 10^{-12}$, $\alpha_s = 1$ to continue with the procedure. Results pertaining to this selection are detailed in Table 5.2.5(c), and we observe that the reconstruction of the density and the shape parameters is quite successful, as we achieve relative errors of 10% and 9% respectively (see Figure 5.2.12(d)). The reduction of the RR is also considerable, at it decreases from a level of 30% until 2%. After testing different regularization parameters, we observe that the accuracy of the reconstruction can be improved in only two iterations by using $\alpha_\rho = 10^{-12}$ and $\alpha_s = 10^{-1}$ as depicted in Table 5.2.5(d). Nevertheless, the relative errors reach values which are still high (see Figure 5.2.12(e)).

We have thus continued to test different values of regularization parameters and after not convincing results, we have decided to increase the frequency until $ka = 0.8$. The selected regularization parameters are $\alpha_\rho = 1,5\ 10^{-11}$, $\alpha_s = 5$, and we see in Figure 5.2.11 that the RR decays quickly, exactly from 7.52% until 0.33% in five iterations, as detailed in Table 5.2.6. The final relative errors on the density and shape parameters are respectively 1.02% and 1.86%, as summarized in Table 5.2.4.

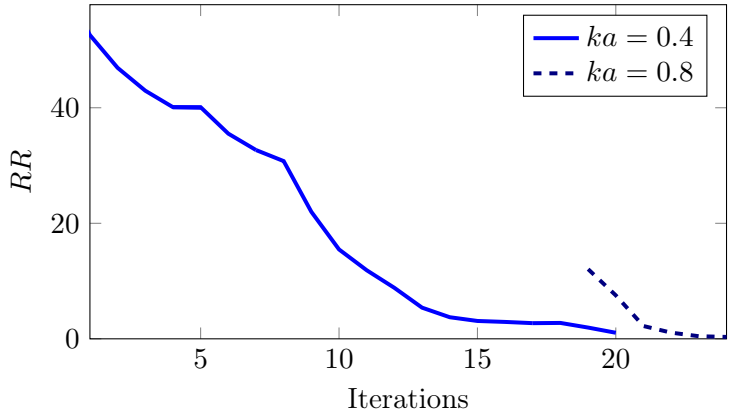

Fig. 5.2.11: Convergence history of a 4-point star shaped scatterer made of *steel*, ka=0.4, 0.8, noise level= 0%.

The reconstruction of the position parameters has been carried out with three different frequencies: $ka = 0.4, 1, 1.8$. The reconstruction corresponding to the first normalized frequency $ka = 0.4$ is detailed in Table 5.2.7(a), at column RR_2, and illustrated in the convergence history in Figure 5.2.13.

♯ iter(n)	RR	RED	RES
0	61.39	62.03	42.38
1	52.59	62.03	39.35
2	46.92	62.03	37.09
3	42.95	62.03	35.34
4	40.1	62.03	33.94
5	40.01	62.03	33.81

(a) $\alpha_\rho = 10^{-5}$, $\alpha_s = 50$.

♯ iter(n)	RR	RED	RES
6	35.52	62.03	31.61
7	32.68	62.03	30.13
8	30.77	62.03	29.21

(b) $\alpha_\rho = 10^{-5}$, $\alpha_s = 20$.

♯ iter(n)	RR	RED	RES
9	21.99	50.73	22.04
10	15.47	35.77	18.61
11	11.87	24.77	15.03
12	8.82	18.78	12.71
13	5.39	14	11.33
14	3.74	12	10.35
15	3.09	11.04	9.91
16	2.92	10.32	9.45
17	2.71	10.19	8.65

(c) $\alpha_\rho = 5\ 10^{-12}$, $\alpha_s = 1$.

♯ iter(n)	RR	RED	RES
18	2.75	8.98	6.39
19	1.95	8.58	6.2

(d) $\alpha_\rho = 10^{-12}$, $\alpha_s = 10^{-1}$.

Tab. 5.2.5: Evolution of RR, RED and RES for a *steel* 4-point star shaped scatterer, $ka = 0.4$, noise level= 0%.

♯ iter(n)	RR	RED	RES
20	7.52	4.83	3.18
21	2.21	2.01	1.74
22	1.07	1.19	1.89
23	0.45	1.06	1.88
24	0.33	1.02	1.86

(a) $\alpha_\rho = 1,5\ 10^{-11}$, $\alpha_s = 5$.

Tab. 5.2.6: Evolution of RR, RED and RES for a *steel* 4-point star shaped scatterer, $ka = 0.8$, noise level= 0%.

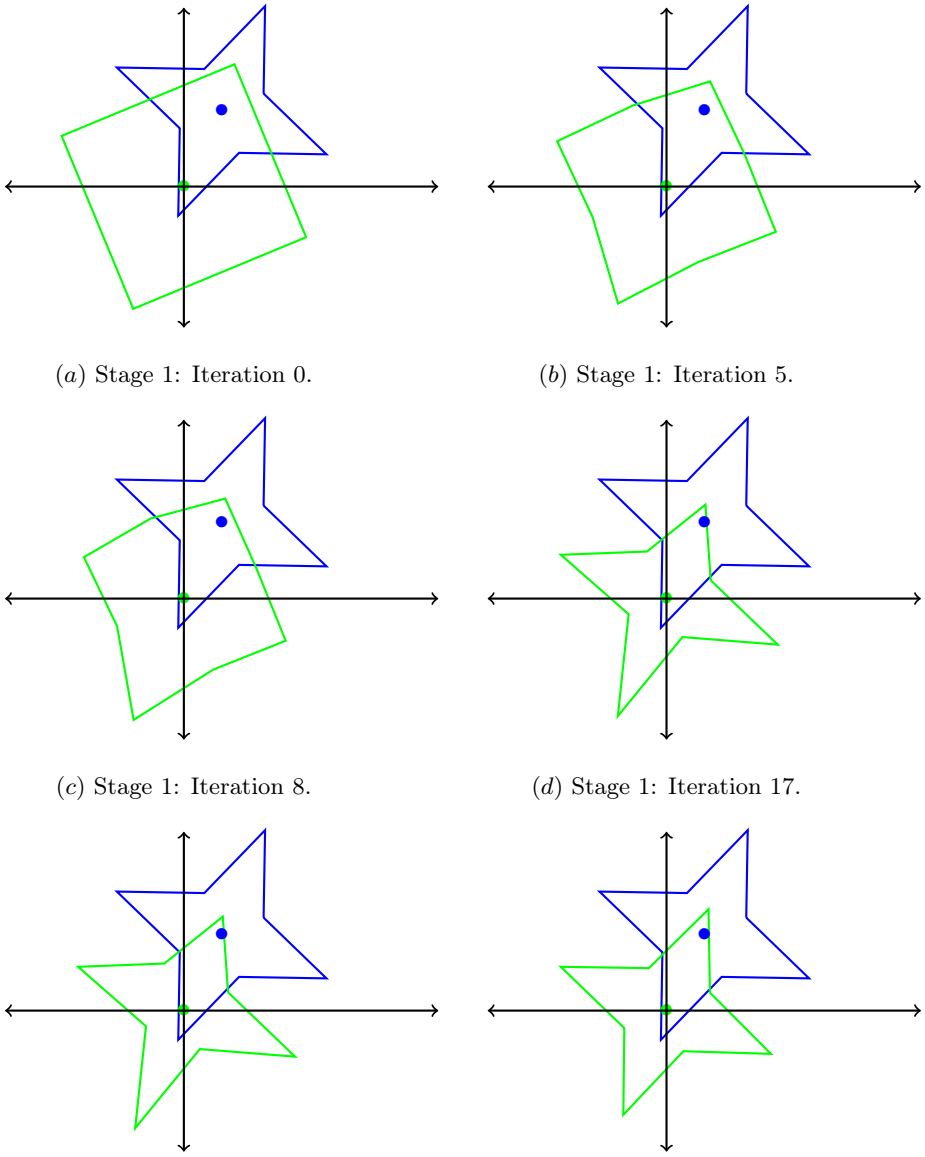

(a) Stage 1: Iteration 0.

(b) Stage 1: Iteration 5.

(c) Stage 1: Iteration 8.

(d) Stage 1: Iteration 17.

(e) Stage 1: Iteration 19.

(f) Stage 1: Iteration 24.

Fig. 5.2.12: Shape and center point of polygonal-shaped scatterer: target vs. computed parameters at different stagnations.

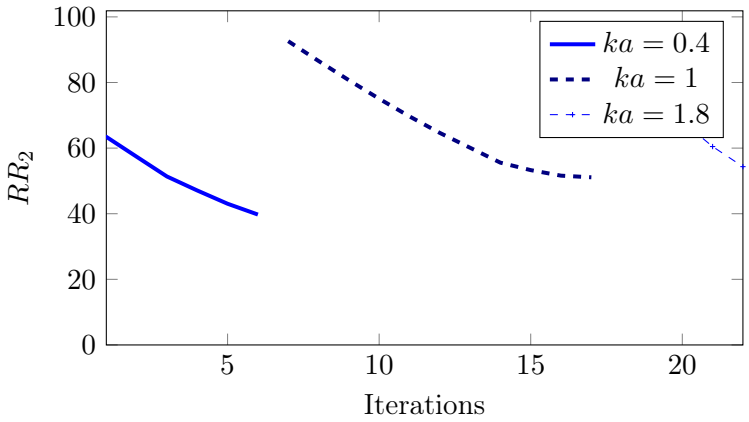

Fig. 5.2.13: Convergence history of RR_2 for a polygonal shaped scatterer made of *steel*, $ka = 0.4, 1, 1.8$, noise level= 0%.

We observe that the evolution of the residual of the FFP field decreases from a level of 63.43% to a level of 39.75%, together with the relative error on the position parameters from 100% until 39.7%. The regularization parameter employed is $\alpha_{loc} = 0$. The position at stagnation is illustrated in Figure 5.2.14(a).

As we can not decrease the regularization parameter after stagnation, we have increased the frequency until $ka = 1$. For $\alpha_{loc} = 0$, the RR_2 decreases from 92% until 51%, while the error on position parameters decreases from 39.26% until a level of 24.3% as we can observe in Table 5.2.7(b). The decay of RR_2 for this frequency is illustrated in the convergence history in Figure 5.2.13, and the updated position parameters at stagnation, in Figure 5.2.14(b).

After several tests considering lower regularization parameters and frequencies, we select $ka = 1.8$ and the regularization parameter $\alpha_{loc} = 10^5$. The relative residual decreases from a level of 86.21% until 54.35%, as illustrated in the convergence history in Figure 5.2.13, and detailed in Table 5.2.7(c) at column RR_2. We must admit the final relative residual of FFP field of 54.35% is not convincing at all, even the corresponding relative error on position parameters is around 17.72%, which is not that bad as we can observe in Figure 5.2.14(c). But it is the most accurate reconstruction that we have obtained.

♯ iter(n)	RR	RR_2	REL
0	0.91	65.1	100
1	0.9	63.43	88.33
2	0.88	57.37	76.91
3	0.88	51.35	68.29
4	0.87	47.08	58.46
5	0.87	43.04	48.87
6	0.87	39.75	39.71

(a) $\alpha_{loc} = 0$.

♯ iter(n)	RR	RR_2	REL
7	2.25	92.59	39.26
8	2.28	86.57	36.02
9	2.29	80.71	32.93
10	2.31	75.05	30.03
11	2.32	69.67	27.31
12	2.33	64.64	24.97
13	2.34	60.11	22.83
14	2.35	55.56	21.94
15	2.35	53.29	21.68
16	2.35	51.6	22.52
17	2.35	51.1	24.3

(b) $\alpha_{loc} = 10^5$.

♯ iter(n)	RR	RR_2	REL
18	8	86.21	22.11
19	8	76.78	20.38
20	8	68.12	19.09
21	8	60.48	18.26
22	7.99	54.35	17.72

(c) $\alpha_{loc} = 10^5$.

Tab. 5.2.7: Evolution of RR, $RR2$ for a *steel* polygonal shaped scatterer, $ka = 0.4, 1, 1.8$, noise level= 0%.

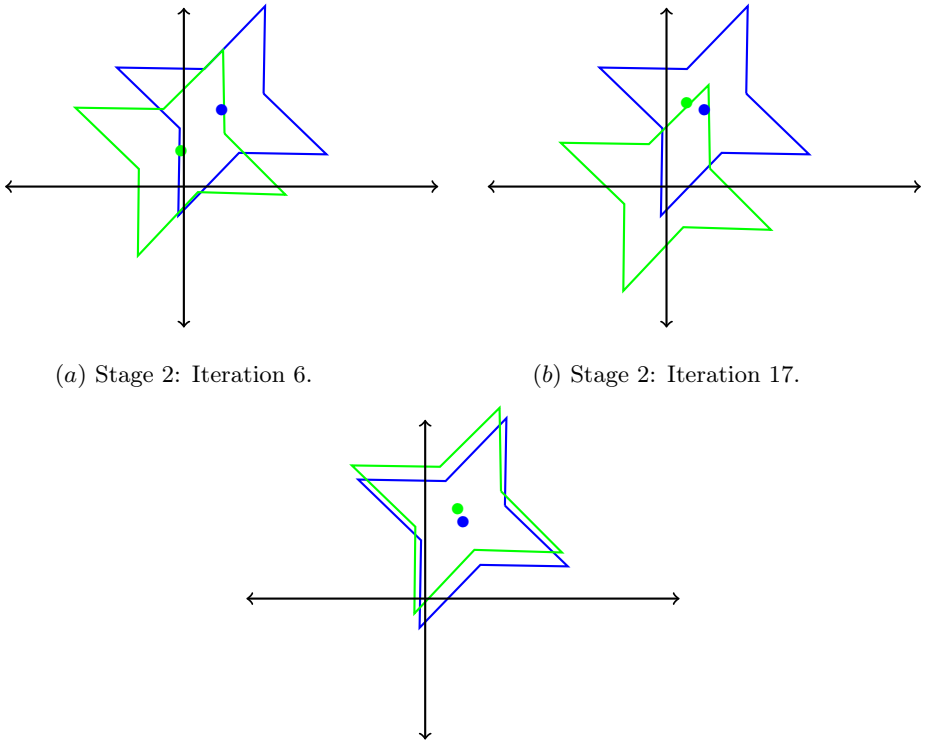

(a) Stage 2: Iteration 6.

(b) Stage 2: Iteration 17.

(c) Stage 2: Iteration 22.

Fig. 5.2.14: Shape and center point of polygonal-shaped scatterer: target vs. computed parameters at different stagnations.

5.2.3 Rounded Square Domain

The last selected experiment is a rounded square parametrized with B-splines (see target in Figure 5.2.15(a)), whose shape parameters are detailed in Table 5.2.8. The external boundary is a circle with radius $b = 7.5$ cm and Lamé coefficients $\lambda = 115.4$GPa, $\mu = 76.9$GPa. The target of the density is $\rho = 7900$kg m^{-3}, while the initial guess is $\rho^{(0)} = 3000$kg m^{-3}. The initial guess of the shape is a circle illustrated in Figure 5.2.15(b) and detailed in Table 5.2.8. The meshes corresponding to the target and initial guess are illustrated in Figure 5.2.16(a) and (b) respectively. We compute the FFP corresponding to the target with eight points per wavelength, while other computed FFPs have been produced with six points per wavelength.

(a) Target (b) Initial Guess

Fig. 5.2.15: B-spline shaped domain for target vs. initial guess.

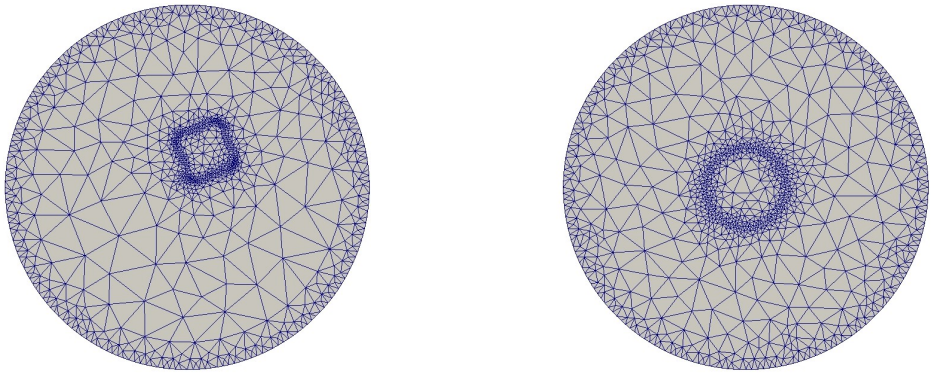

(a) Target: 1846 elements (b) Initial guess: 1774 elements

Fig. 5.2.16: Meshes for target vs. initial guess.

The first selected normalized frequency at stage 1 is $ka = 1$. We observe in Table 5.2.9(a) the fast evolution of RR for regularization parameters $\alpha_\rho = 10^{-8}$ and $\alpha_s = 50$. The fast decay of RR from a level of almost 98% until 20% in 7 iterations is remarkable in the convergence history illustrated in Figure 5.2.17. The reconstruction of the shape of the obstacle is also considerable, as detailed in the column RES in Table 5.2.9(a), and observable in Figure 5.2.18(b). We observe regarding the column RED in Table 5.2.9(a) that the density reconstruction is completely frozen.

Due to the bigger impact of shape parameters, we reduce the regularization parameter of shape parameters until $\alpha_s = 10$, and the corresponding impact on the evolution of the RR, RES and RED

Parameter	Target	Initial Guess	Computed	Relative error at convergence (%)	
s_1	1	1.75	0.97	2.81	
s_2	1.5	1.75	1.496	0.22	
s_3	1	1.75	0.002	0.22	**RES**
s_4	1.5	1.75	1.5003	0.02	
s_5	1	1.75	0.9997	0.03	0.67
s_6	1.5	1.75	1.509	0.6	
s_7	1	1.75	1.004	0.44	
s_8	1.5	1.75	1.507	0.53	
ρ	7900	3000	7835.56	0.8	

Tab. 5.2.8: Target, initial guess and computed parameters corresponding to the rounded-square shaped scatterer, 24 iterations, noise level= 0%.

is detailed in Table 5.2.9(b). The reconstruction of the density is still crippled regarding the column *RED*, while the shape has been updated until a relative error of 22.32% (see column *RES* and Figure 5.2.18(c)), and the relative residual decreases until a level of 14.7%. Straightaway, after testing several regularization parameters, we select $\alpha_\rho = 10^{-13}$, $\alpha_s = 10$ and we observe that the evolution of the reconstruction of all parameters is considerable (see columns *RED* and *RES* in Table 5.2.9(c)). The relative errors at stagnation are 11.53% and 13.48% for the density and shape parameters respectively, and the updated shape is illustrated in Figure 5.2.18(d).

After several experiments with different frequency values and regularization parameters, we select the normalized frequency $ka = 1.67$ and the pair of regularization parameters $\alpha_\rho = 2\ 10^{-11}$ and $\alpha_s = 10$. We observe at Table 5.2.10 that the relative residual drops from a level of 25% until 0.23% in 7 iterations, and we observe in Table 5.2.8 that the final relative errors of the density and the shape parameters are quite satisfactory, 0.8% and 0.67% respectively. The shape reconstruction is illustrated in Figure 5.2.18(e).

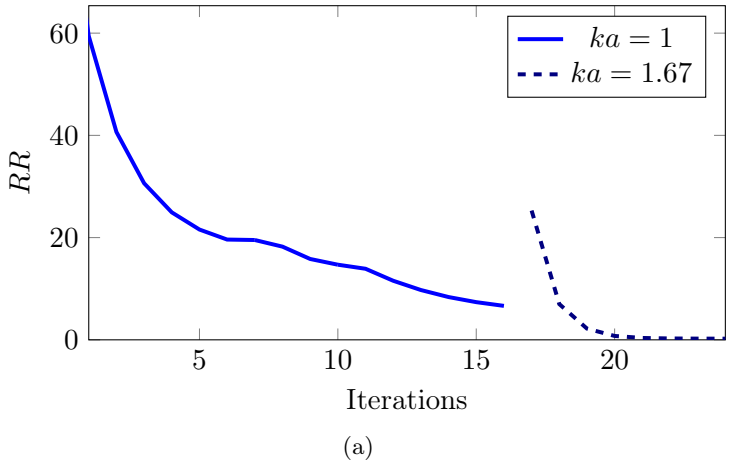

(a)

Fig. 5.2.17: Convergence history of a rounded square shaped scatterer made of *steel*, ka=1, 1.67, noise level= 0%.

The reconstruction of the position parameters that we study here is the most successful one that

♯ iter(n)	RR	RED	RES
0	97.76	62.03	43.85
1	59.42	61.82	35.36
2	40.66	61.68	31.07
3	30.63	61.57	28.76
4	24.94	61.48	27.42
5	21.58	61.41	26.56
6	19.62	61.36	26.12
7	19.53	61.34	25.95

(a) $\alpha_\rho = 10^{-8}$, $\alpha_s = 50$.

♯ iter(n)	RR	RED	RES
8	18.23	61.28	25.47
9	15.82	61.24	23.71
10	14.7	61.21	22.32

(b) $\alpha_\rho = 10^{-8}$, $\alpha_s = 10$.

♯ iter(n)	RR	RED	RES
11	13.9	61.18	21.14
12	11.56	52.41	18.89
13	9.74	42.53	17.06
14	8.37	31.73	15.62
15	7.37	21.06	14.46
16	6.64	11.53	13.48

(c) $\alpha_\rho = 10^{-13}$, $\alpha_s = 10$.

Tab. 5.2.9: Evolution of RR, RED and RES for a *steel* rounded square shaped scatterer, $ka = 1$, noise level= 0%.

♯ iter(n)	RR	RED	RES
17	25.29	3.81	12.62
18	7	1.63	4.64
19	2.2	0.93	1.71
20	0.76	0.77	0.95
21	0.37	0.75	0.79
22	0.27	0.76	0.73
23	0.24	0.78	0.7
24	0.23	0.8	0.67

(a) $\alpha_\rho = 2\ 10^{-11}$, $\alpha_s = 10$.

Tab. 5.2.10: Evolution of RR, RED and RES for a *steel* rounded square shaped scatterer, $ka = 1.67$, noise level= 0%.

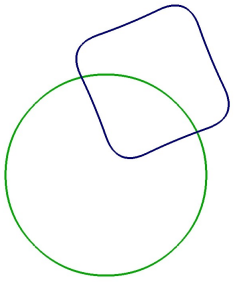

(a) Stage 1: Iteration 0.

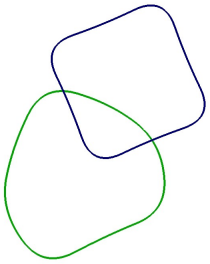

(b) Stage 1: Iteration 7.

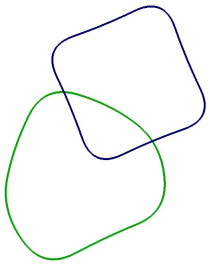

(c) Stage 1: Iteration 10.

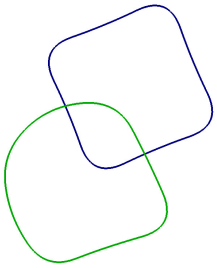

(d) Stage 1: Iteration 16.

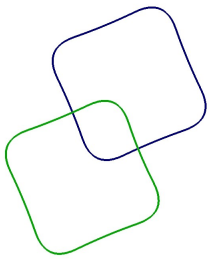

(e) Stage 1: Iteration 24.

Fig. 5.2.18: Shape and center point of a rounded square scatterer: target vs. computed parameters at different stagnations.

we have obtained in all experiments. As we can observe in Table 5.2.11, almost in two iterations the parameters have been reconstructed with a relative error around 2% (see the corresponding illustration in Figure 5.2.20(b)). We observe that RR_2 continues decreasing slowly until iteration 9 where it stagnates, as illustrated in Figure 5.2.19 and detailed in Table 5.2.11 (column RR_2). The final reconstruction of 0.38% is really accurate as observable in Figure 5.2.20(c).

♯ iter(n)	RR	RR_2	REL
0	0.43	93.51	100
1	0.35	8.5	5.15
2	0.37	4.25	2.14
3	0.36	2.16	1.6
4	0.37	1.1	0.44
5	0.36	0.59	0.67
6	0.37	0.35	0.27
7	0.36	0.25	0.43
8	0.36	0.24	0.38
9	0.36	0.22	0.38

(a) $\alpha_{loc} = 0$.

Tab. 5.2.11: Evolution of RR, $RR2$ for a *steel* rounded square shaped scatterer, $ka = 0.67$, noise level= 0%.

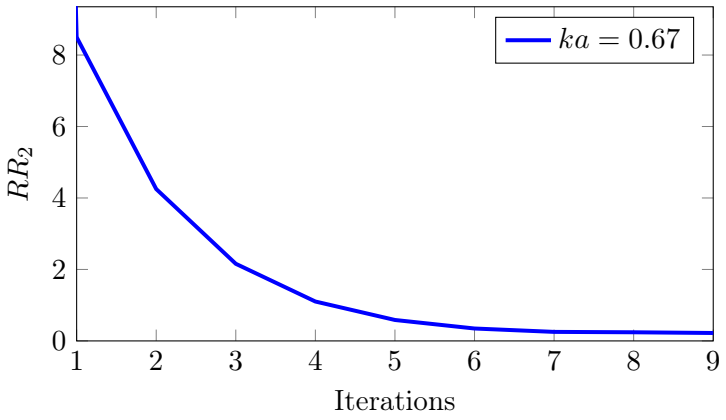

Fig. 5.2.19: Convergence history of a rounded square shaped scatterer made of *steel*, $ka = 0.67$, noise level= 0%.

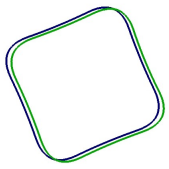

(a) Stage 2: Iteration 1.

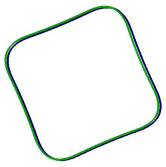

(b) Stage 2: Iteration 2.

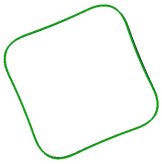

(c) Stage 2: Iteration 6.

Fig. 5.2.20: Shape and center point of a B-splines shaped scatterer: target vs. computed parameters at different stagnations.

5.3 Reconstruction from FFP Corresponding to Multiple Incident Phenomena with Limited-aperture Data

Until now in all the experiments we have considered full-aperture data while in most of the realistic cases, we have access to limited aperture ones (see Fig. 5.3.1(a)). In order to simulate more realistic tests, in this section we deal with back-scattering measurements.

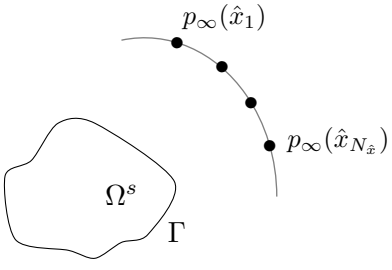

(a) Limited-aperture data.

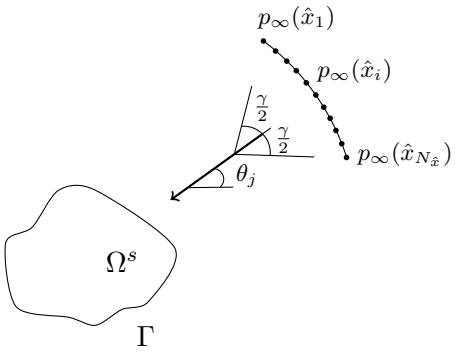

(b) Angles of the incident wave and the data-interval.

Fig. 5.3.1: Back-scattering measurements.

After discussions with physicists from I2M, we decided to mimic an experimental set up consisting of one source surrounded by $N_{\hat{x}}$ receivers equally placed along an aperture angle γ (see Fig. 5.3.1(b)).

The set up moves around the obstacle with an angle $\delta\theta$. The summarized algorithm can be described as follows:

- Stage 0, Parameters **Initialization**

  $\rho^{(0)}$, $\Gamma^{(0)}$, θ_0 and $\left[\theta_0 - \frac{\gamma}{2}, \theta_0 + \frac{\gamma}{2}\right]$

- Stage 1, Fix the frequency ω, and propose a pair of regularization parameters for shape and density parameters, (α_s, α_ρ).

  For $j = 1, ...N_\gamma$ being N_γ number of angles:

  - Apply regularized Newton algorithm to update shape and material parameters.
  - Update the angle of the incident wave $\theta_j = \theta_0 + j \cdot \delta\theta$
    and the corresponding data interval $\left[\theta_j - \frac{\gamma}{2}, \theta_j + \frac{\gamma}{2}\right]$.
  - Repeat Stage 1 until **convergence** or **stagnation**
  - If **stagnation**, go to Stage 2.

- Stage 2, **Switch** to a lower (α_s, α_ρ) or a higher frequency and repeat Stage 1.

For numerical experiments, we consider two different scatterers: (a) a disk shaped obstacle and (b) an elliptic scatterer (see Figure 5.3.2). Both scatterers are made of *aluminium*, and the corresponding material parameters are $\lambda = 51.09$GPa, $\mu = 26.32$GPa. The target for the density is $\rho = 2700$kg m^{-3}, while the initial guess for the density is $\rho^{(0)} = 5400$kg m^{-3} with an initial relative error of 100%, and the target and initial guesses for the shape parameters are detailed in Table 5.3.1, together with the density parameter. The inverse crime is avoided using five points per wavelength for computing the FFP corresponding to the target, while only three points per wavelength are used to compute the rest of the FFPs, and the employed frequency in all the cases is $f = 23.9$kHz, that corresponds to $ka = 1$ in the case of a circle and to $ka = 0.5$ in the case of the ellipse (we remind that $a = s_{min} = \min_{1 \le i \le N_\Gamma} s_i$). The fact that we use an unique frequency allows for comparing the effect of different angles such as θ_0 and γ.

(a) Disk shaped scatterer.

(b) Ellipse shaped scatterer.

Fig. 5.3.2: Considered obstacles

The scatterer selected for the next experiment is a elliptic shaped obstacle whose initial guesses and targeted shape and parameters are detailed in Table 5.3.1. We present in Table 5.3.2 the results corresponding to this experiment with the initial angle $\theta_0 = 0$, and the angle of the aperture $\gamma = \pi$. Regarding the evolution of the RR together with the decrease of the errors on the density and shape parameters (see RED and RES in Table 5.3.2), we conclude that the reconstruction is completely successful. As the aperture angle is quite big, we have retrieved all the parameters without changing

	Circle	Ellipse		Density
	a(cm)	s_1(cm)	s_2(cm)	ρ (kg m^{-3})
Target	1.00	1.00	0.50	2700
Initial guess	0.5	0.75	0.75	5400
Relative Error	50	25	50	100

Tab. 5.3.1: Target vs. initial guesses for the considered shape and density parameters.

#iter(n)	RR	RED	RES
0	80.81	92.59	31.62
1	64.29	74.07	42.65
2	53.6	53.88	56.72
3	46.94	23.33	56.76
4	21.01	27.27	42.32
5	7.64	21.94	31.66
6	8.26	9.39	14.26
7	5.63	3.19	5.62
8	2.04	1.22	2.12
9	0.8	0.49	0.82
10	0.31	0.2	0.32
11	0.12	$7.71 \cdot 10^{-2}$	0.13

Tab. 5.3.2: Evolution of RR, relative error on the density ρ and shape parameters in the ellipse case, noise level=0%.

the aperture angle. In this case, we have kept the incident angle $\theta_j = \theta_0$ for all $j = 1, ..., N_{iter}$, or equivalently, $\delta\theta = 0$.

Reducing the aperture angle to $\gamma = \frac{\pi}{4}$, we obtain quite good results as we can observe in the Table 5.3.3: the RR after one iteration is above 164% and decreases quickly in 4 iterations until 4.3%. The corresponding relative errors at this point are 7.52% and 2.97% for the density and shape parameters respectively. RR and the errors continue decreasing until stagnation at iteration 9. The final errors on density and shape parameters are 0.91% and 1.42% for $RR = 0.25$. In this case it was necessary to change the angle of the incident waves, and consequently the angle of aperture, in each iteration. The initial angle of the incident wave is $\theta_0 = 0$, and we increment it at each iteration with $\delta\theta = 0.025$.

#iter(n)	RR	RED	RES
0	570.84	92.59	31.62
1	163.37	66.01	17.48
2	38.39	39.09	8.8
3	10.98	18.48	4.75
4	4.3	7.52	2.97
5	1.49	2.93	2.09
6	0.75	0.82	1.74
7	0.42	0.23	1.58
8	0.28	0.72	1.49
9	0.25	0.91	1.42

Tab. 5.3.3: Evolution of RR, relative error on the density ρ and shape parameters in the ellipse case, initial angle of incident wave $\theta_0 = 0$, angle of aperture $\gamma = \frac{\pi}{4}$, angle difference $\delta\theta = 0.025$, noise level=0%.

#iter(n)	RR	RED	RES
0	164.02	92.59	31.62
1	142.81	51.71	28.52
2	33.08	19.95	24.06
3	18.41	2.44	20.51
4	5.79	10.05	19.54
5	2.66	11.93	19.16
6	2.95	12.54	18.74

Tab. 5.3.4: Evolution of RR, relative error on the density ρ and shape parameters in the ellipse case, initial angle of incident wave $\theta_0 = 0.15$, angle of aperture $\gamma = \frac{\pi}{4}$, noise level=0%.

In the case of the ellipse, we see that the recovery of the parameters seems to be very sensitive with respect to the angle of the incident waves. The selection of $\theta_0 = 0.15$ results in an unfruitful reconstruction as we can observe in Table 5.3.4: even if the RR achieves low values around 3%, we observe that the error on shape parameters is still around 18%.

We have repeated the experiments but in this case the scatterer is a disk shaped obstacle, whose initial guesses and target are depicted in Table 5.3.1. In what follows, we introduce two experiments with the common aperture angle $\gamma = \frac{\pi}{4}$ but different initial incident wave angles $\theta_0 = 0.25$ and $\theta_0 = 0$. The evolution of RR together with the behavior of RED and RES corresponding to these experiments

are depicted in Tables Tables 5.3.5-5.3.6, for $\theta_0 = 0.25$ and $\theta_0 = 0$ respectively. We observe that both experiments are successful as in 4 and 6 iterations all the parameters are reconstructed with really small final relative errors.

#iter(n)	RR	RED	RES
0	38.68	92.59	50
1	9.61	42.47	6.06
2	5.16	16.05	3.19
3	4.43	2.55	1.18
4	0.15	0.18	$5.38 \cdot 10^{-2}$

Tab. 5.3.5: Evolution of RR, relative error on the density ρ and shape parameters in the circle case, initial angle of incident wave $\theta_0 = 0.25$, angle of aperture $\gamma = \frac{\pi}{4}$, noise level=0%.

#iter(n)	RR	RED	RES
0	38.68	92.59	50
1	9.04	56.23	8.44
2	4.34	13.59	6.96
3	4.26	1	1.48
4	0.15	$1.08 \cdot 10^{-2}$	0.11
5	$4.52 \cdot 10^{-3}$	$1.34 \cdot 10^{-4}$	$5.74 \cdot 10^{-3}$
6	$1.87 \cdot 10^{-4}$	$1.14 \cdot 10^{-5}$	$2.25 \cdot 10^{-4}$

Tab. 5.3.6: Evolution of RR, relative error on the density ρ and shape parameters in the circle case, initial angle of incident wave $\theta_0 = 0$, angle of aperture $\gamma = \frac{\pi}{4}$, noise level=0%.

As a conclusion, we observe that when we consider a uniform shape as a circle, that different initial angles may not lead to different results. When we consider shapes as an ellipse, both the initial incident angle and angle of aperture may have important influence on the reconstruction of the shape. Future investigations should address the idea of finding an efficient strategy for selecting the different parameters like the incident angle, the increment angle and γ.

5.4 On the Full Reconstruction of the Solid

In this last section, we present numerical results to highlight the performance efficiency of the proposed computational procedure. To this end, we consider two scatterers: (a) a polygonal-shaped scatterer and (b) a mockup submarine, made of *steel* and *aluminum* respectively.

5.4.1 Case of a Polygonal-shaped Domain

The main goal here is to determine the characteristics of a non-convex-shaped domain Ω^s immersed in water Ω^f (see Figure 5.4.1(a)). More specifically, the objective is to recover the shape of the considered scatterer along with its material properties (the Lamé coefficients (λ, μ) and the density ρ_s, as well as its location (the center of the scatterer (x_c, y_c)). The sought-after scatterer Ω^s is made of *steel* whose material parameters are reported in Table 5.4.1. The wet surface Γ is represented by the polygonal parametrization (see Appendix C) where the shape parameters s_j together with the center of the scatterer (x_c, y_c) are given in Table 5.4.2. The density of the water is set to be $\rho_f = 1000kg \cdot m^{-3}$.

In all the performed numerical experiments, the initial guess $\Omega^{(0)}$ is an octogonal-shaped domain whose material parameters are reported in Table 5.4.1. Its shape parameters and its center are given in Table 5.4.2.

We consider synthetic measurements corresponding to a full aperture FFP i.e. the FFP is computed at 360 observation points. These measurements are computed with the DG solver [9] based upon the numerical method described in Chapter 1. As stated in Section 3, we employed fifth-order elements with a non structured mesh discretization involving seven elements per wavelength (see Figure 5.4.2(a) and Table 5.4.3). Note that, in order to avoid the inverse crime [28], we have solved the forward problems, arising in the iterative inversion procedure, with the same DG solver but employing a mesh discretization with five elements per wavelength (see Figure 5.4.2(b) and Table 5.4.3).

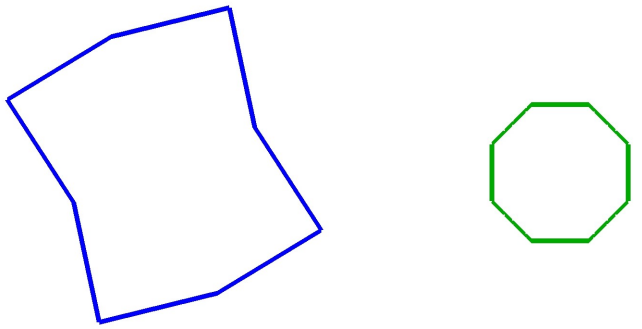

(a) Target (b) Initial Guess

Fig. 5.4.1: Polygonal-shaped domain for target vs. initial guess.

	λ(GPa)	μ(GPa)	$\rho_s(kg \cdot m^{-3})$
Target	115.40	76.90	7900
Initial guess	50.00	50.00	3000
Relative Error	56.67	34.98	62.03

Tab. 5.4.1: Material parameters: target vs. initial guess.

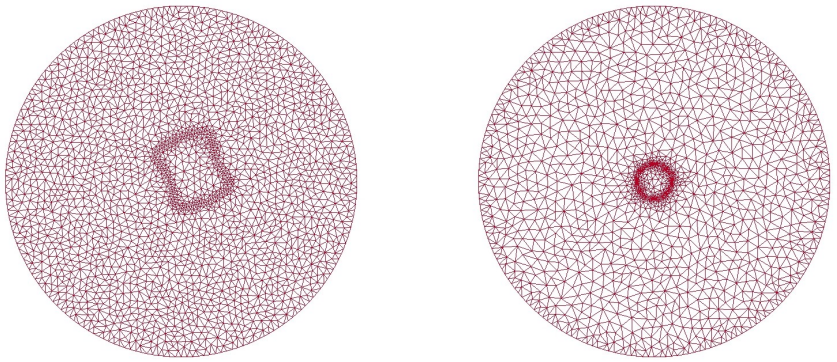

(a) Target: 4358 elements (b) Initial guess: 3088 elements

Fig. 5.4.2: Meshes for target vs. initial guess.

	s_1	s_2	s_3	s_4	s_5	s_6	s_7	s_8	x_c	y_c
Target	1.06	1.84	1.50	1.84	1.06	1.84	1.50	1.84	0.50	0.50
Initial guess	0.80	0.80	0.80	0.80	0.80	0.80	0.80	0.80	0.00	0.00
Relative Error	24.58	56.52	46.67	56.52	24.57	56.52	46.67	56.52	100	100

Tab. 5.4.2: Shape parameters: target vs. initial guess.

	# elements			
	Γ^s	Γ^f	Ω^s	Ω^f
Mesh 1	96	92	308	3862
Mesh 2	96	96	340	2556

Tab. 5.4.3: Distribution of the elements in the mesh depending the medium and the neighbourhood.

We investigate the convergence, accuracy and robustness to the noise of the reconstruction using FFP measurements corresponding to a *single* frequency. We then present results obtained with multiple frequencies measurements for illustration purpose. Recall that the determination of the sought-after parameters is acomplished into two stages. In stage 1, we use the intensity of the FFP field to retrieve the shape and the material parameters of Ω^s, whereas in stage 2, the location of the obstacle is determined using the FFP field.

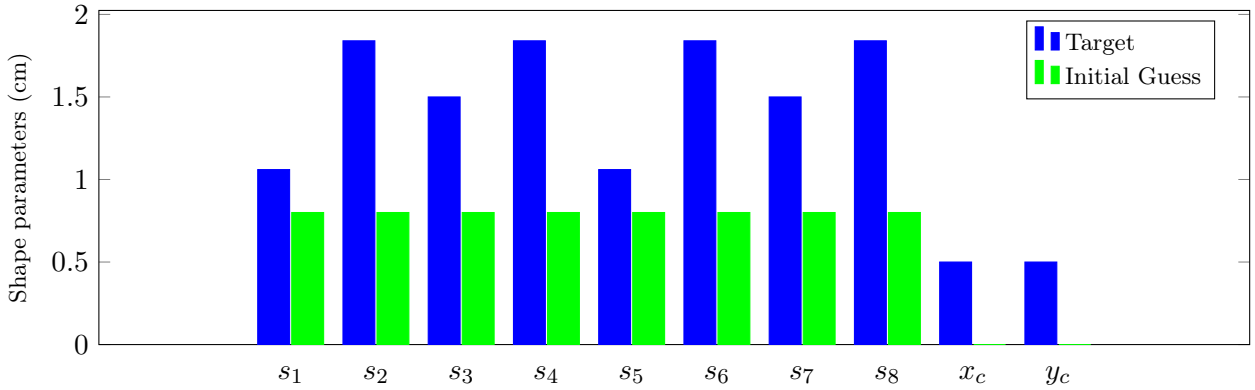

Fig. 5.4.3: Material parameters: target vs. initial guess.

Noise-free Mono-frequency Experiment

We set the normalized frequency to be $ka = 2.47$. The corresponding noise-free measurements for both the target and the initial guess are depicted at Figure 5.4.4. The obtained results are reported in Tables 5.4.4-5.4.5 and depicted in Figures 5.4.5-5.4.9. The following observations are worth noting:

- The initial guess for the parameters values (see Table 5.4.1-5.4.2) has been selected outside the preasymptotic region, ensuring that the algorithm is blind for the sought-after values of the parameters, as illustrated in Figure 5.4.8(a). Indeed, the initial relative errors in the shape parameters, Lamé coefficients, the density, and the location of the object, are 51.79%, 50.99%, 62.03%, 50%, respectively. These values lead to a computed initial FFP with a relative residual that exceeds 80% in the intensity (see Figure 5.4.4(c)) and 95% in the FFP field (see Figures 5.4.4(a)-(b)).

- Figure 5.4.5 indicates that the proposed methodology converges. More specifically, during the search for the shape and material parameters i.e. stage 1, the relative residual in the FFP intensity drops from above 80% to below 1% in 21 iterations. In stage 2 i.e. the determination of the location, the relative residual, the FFP field drops from above 115% to below 1% in 12 iterations.

- At the end (stagnation) of stage 1 the algorithm delivers the shape parameters, the Lamé coefficients and the density with relative errors of 0.08%, 2% and 0.5%, respectively (see Tables 5.4.4-5.4.5 and Figures 5.4.8(e) with the corresponding histogram in Figure 5.4.6 and the histogram corresponding to material parameters in Figure 5.4.9(e)). This is a highly accurate recovery of the parameters. One must point out that the regularization parameters values were changed each time the algorithm stagnated (see Figure 5.4.8(a)-(e) and Figure 5.4.9(a)-(e)). Moreover, the relative error on the FFP intensity is about 0.5% whereas the one on the FFP field is about 115%. The latter error is not surprising since the FFP field is not incorporated in stage 1 during the optimization process.

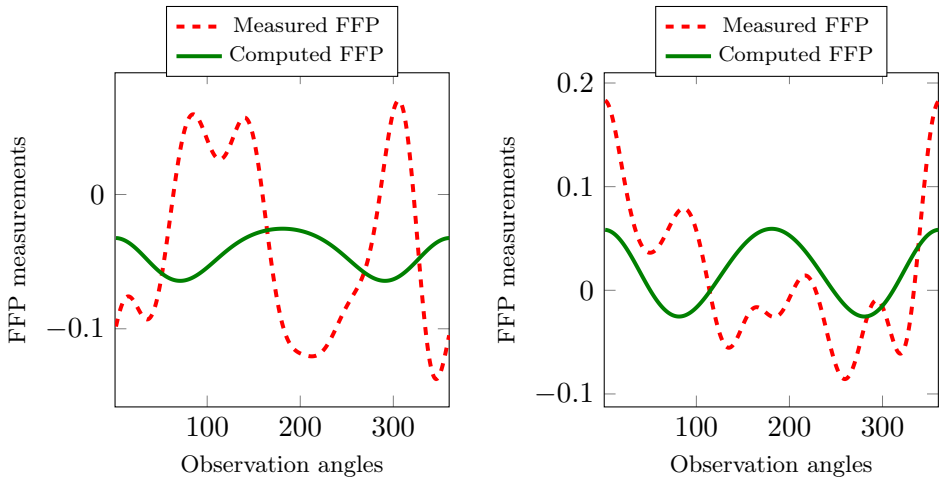

(a) Real part

(b) Imaginary part

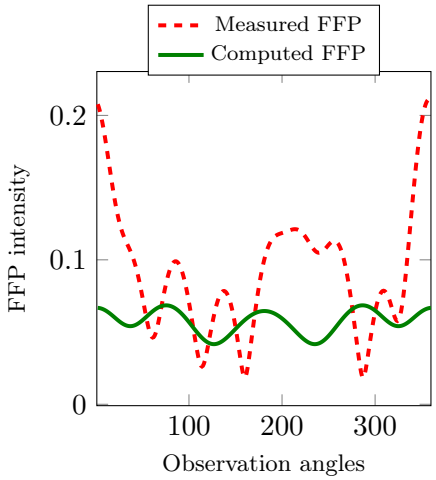

(c) Modulus

Fig. 5.4.4: Real and imaginary parts (top) and modulus (botton) of the FFP: Target vs. initial guess.

- At convergence i.e. at the end of stage 2, the location of the scatterer is retrieved with a relative error of about 1% while the computed values of the remaining parameters in stage 1 are frozen. As a consequence, the accuracy level on the FFP field improves significantly. Indeed, the relative error drops from 115% to about 1% (see Figure 5.4.8(f)-(g)).

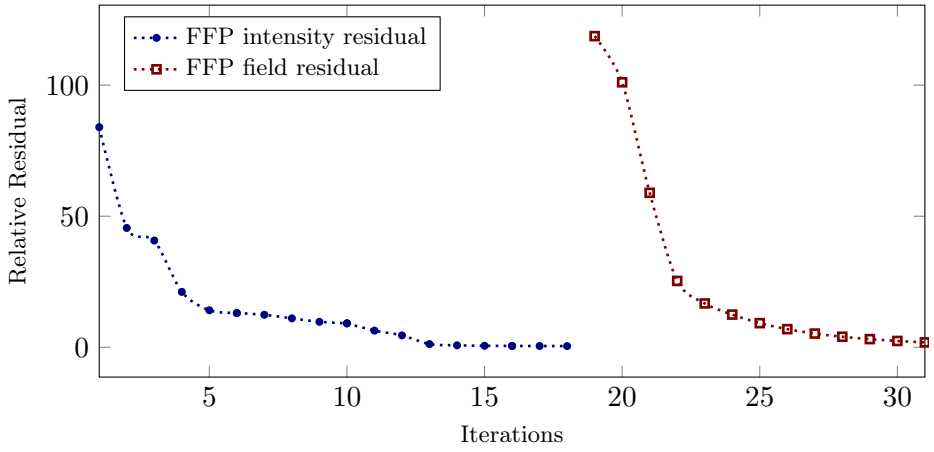

Fig. 5.4.5: Convergence history of the case of a polygonal-shape scatterer with material and shape parameters detailed in Tables 5.4.1-5.4.2 respectively, $ka = 2.47$ during the iterations of **SWA**, noise level= 0%.

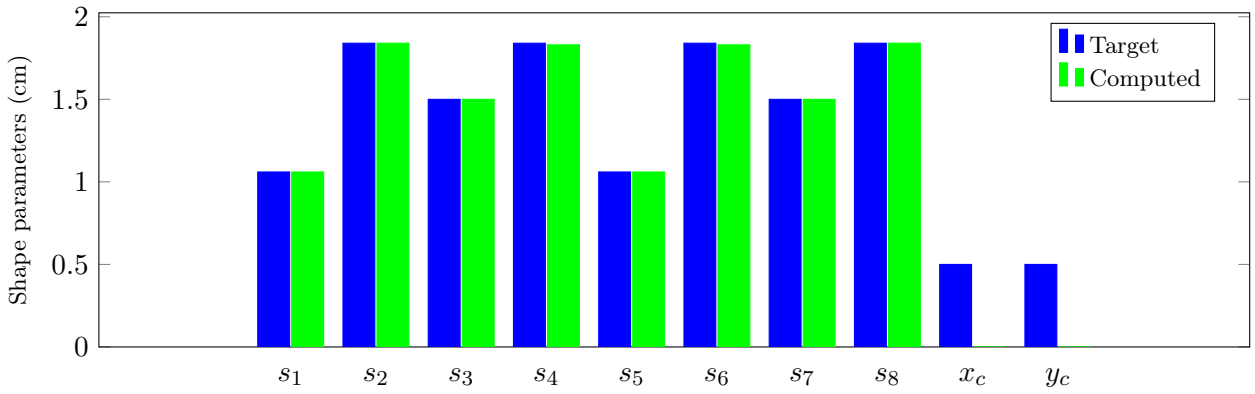

Fig. 5.4.6: Shape parameters: target vs. computed after the reconstruction with FFP intensity.

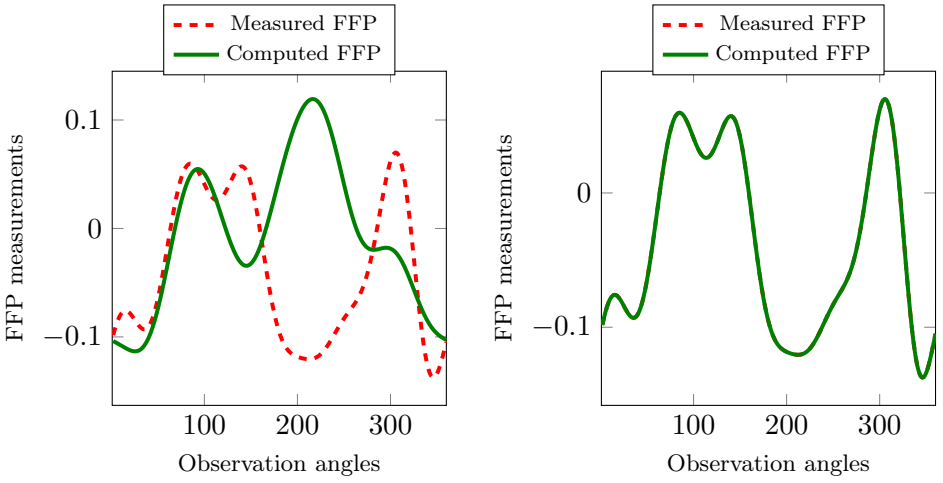

(a) Real part at stage 1

(b) Real part at stage 2

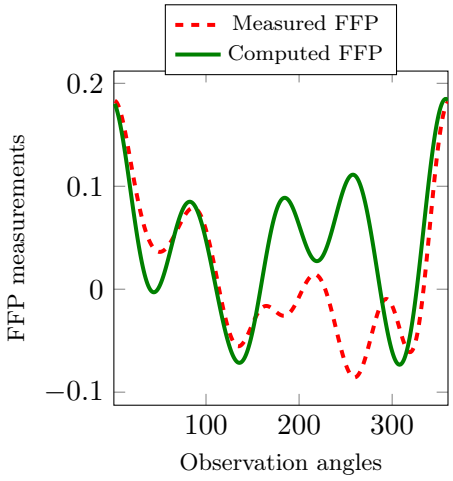

(c) Imaginary part at stage 1

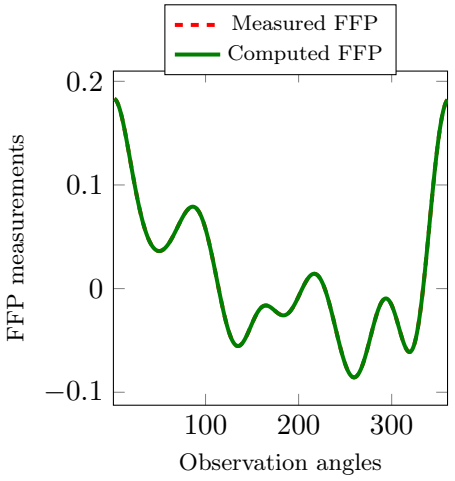

(d) Imaginary part at stage 2

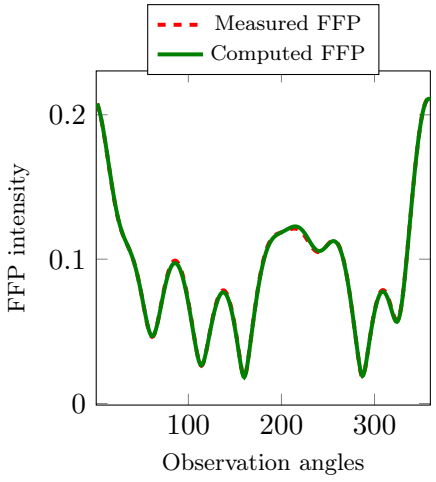

(e) Modulus at stage 1

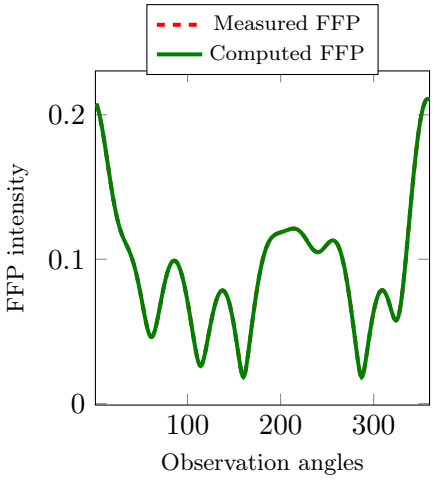

(f) Modulus at stage 2

Fig. 5.4.7: Real part, imaginary part and modulus of the FFP: measurements vs. computed at stage 1 and stage 2 .

	λ(GPa)	μ(GPa)	$\rho_s(kg \cdot m^{-3})$
Target	115.40	76.90	7900
Computed	111.78	76.23	7793.42
Relative Error	3.13	0.86	1.34

Tab. 5.4.4: Material parameters: target vs. computed parameters with $ka = 2.47$.

	s_1	s_2	s_3	s_4	s_5	s_6	s_7	s_8	x_c	y_c
Target	1.06	1.84	1.50	1.84	1.06	1.84	1.50	1.84	0.50	0.50
Computed	1.06	1.84	1.50	1.83	1.06	1.83	1.50	1.84	0.00	0.00
Relative Error	0.29	0.04	0.06	0.01	0.01	0.01	0.06	0.07	100	100

Tab. 5.4.5: Shape parameters: target vs. computed parameters with $ka = 2.47$.

Noise-free Multiple Frequency Experiment

The following example corresponds to the reconstruction using the normalized frequencies $ka = 2.47$ and $ka = 5.65$. This section illustrates that more accurate results can be obtained due to a multi-frequency strategy. The frequencies have been increased after the stagnation at stage 1, as we observe in the convergence history depicted in Figure 5.4.10. The final reconstruction of shape, material, density and position parameters correspond to an error of 0.4%, 0.1%,0.1%, and 1.7% respectively, as depicted in Tables 5.4.6 - 5.4.7.

	λ(GPa)	μ(GPa)	$\rho_s(kg \cdot m^{-3})$
Target	115.40	76.90	7900
Computed	115.38	77.04	7912.04
Relative Error	0.01	0.18	0.15

Tab. 5.4.6: Material parameters: target vs. computed parameters, for multi-frequency experiment.

	s_1	s_2	s_3	s_4	s_5	s_6	s_7	s_8	x_c	y_c
Target	1.06	1.84	1.50	1.84	1.06	1.84	1.50	1.84	0.50	0.50
Computed	1.06	1.84	1.49	1.84	1.06	1.84	1.50	1.84	0.50	0.49
Relative Error	0.31	0.09	0.09	0.15	0.16	0.12	0.06	0.04	0.35	2.18

Tab. 5.4.7: Shape parameters: target vs. computed parameters, for multi-frequency experiment.

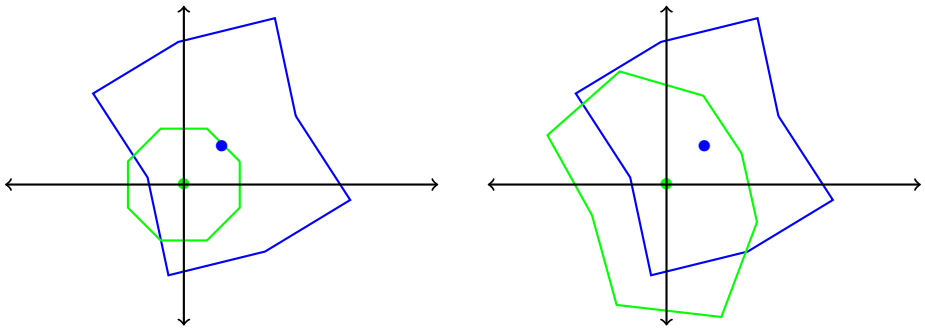

(a) Stage 1: Iteration 0.

(b) Stage 1: Iteration 6.

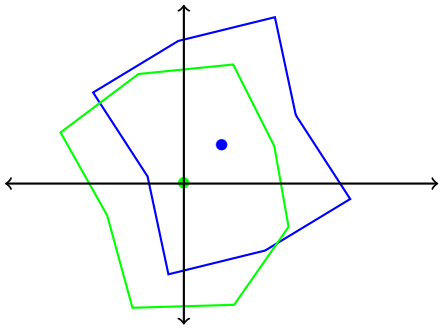

(c) Stage 1: Iteration 10.

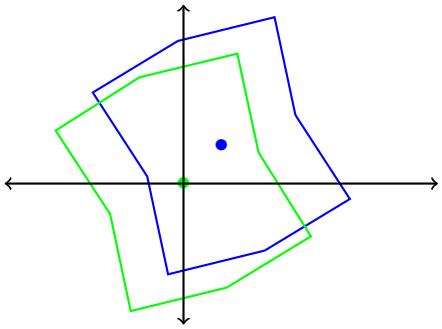

(d) Stage 1: Iteration 16.

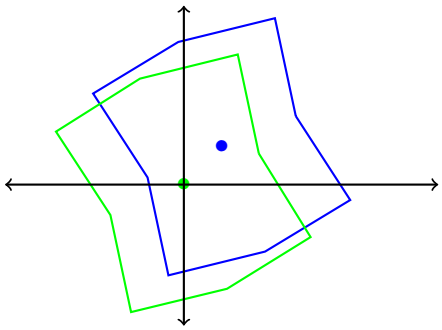

(e) Stage 1: Iteration 18.

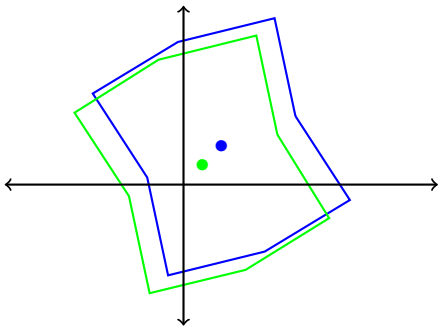

(f) Stage 2: Iteration 5.

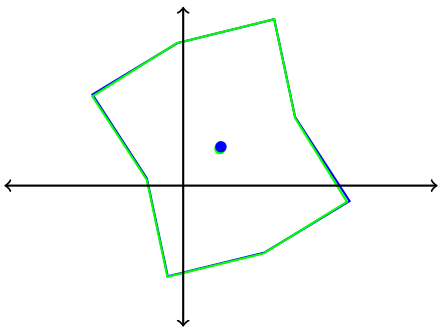

(g) Stage 2: Iteration 13.

Fig. 5.4.8: Shape and center point of polygonal-shaped scatterer: target vs. computed parameters at different stagnations, mono-frequency experiment.

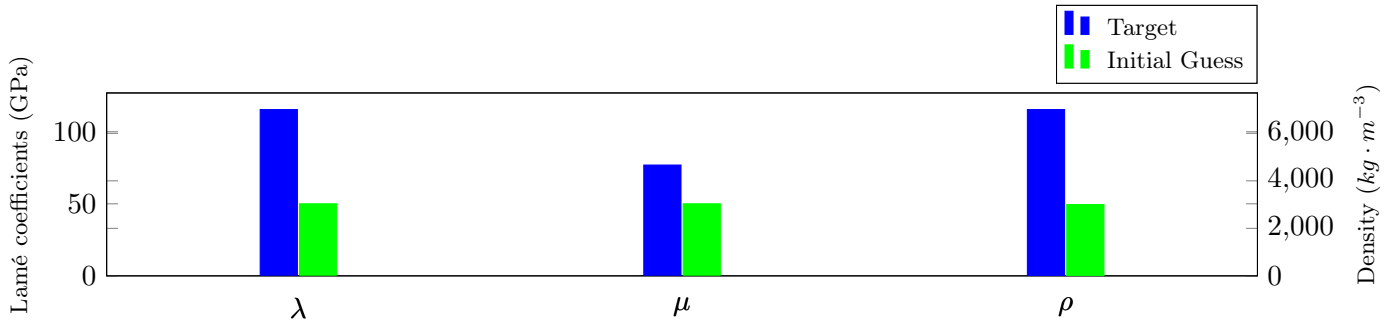

(a) Stage 1: Iteration 0.

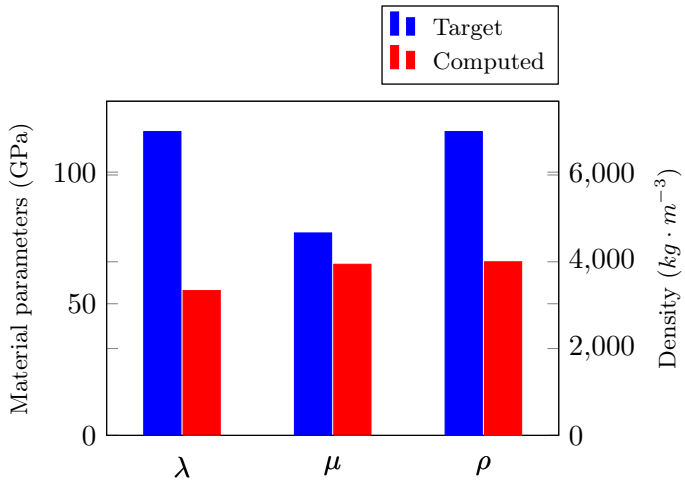

(b) Stage 1: Iteration 6.

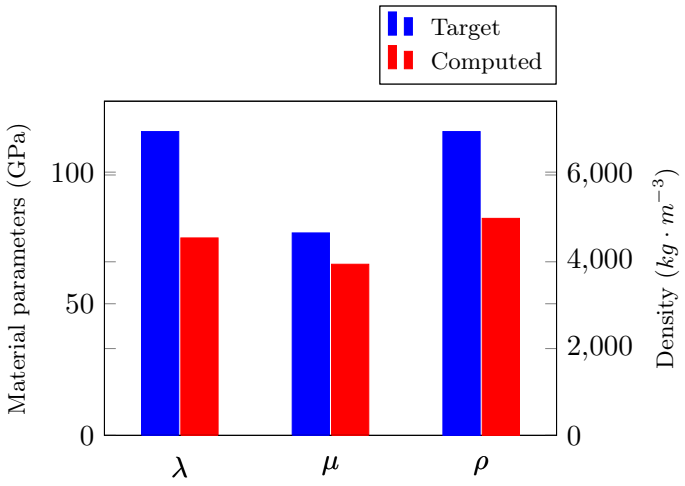

(c) Stage 1: Iteration 10.

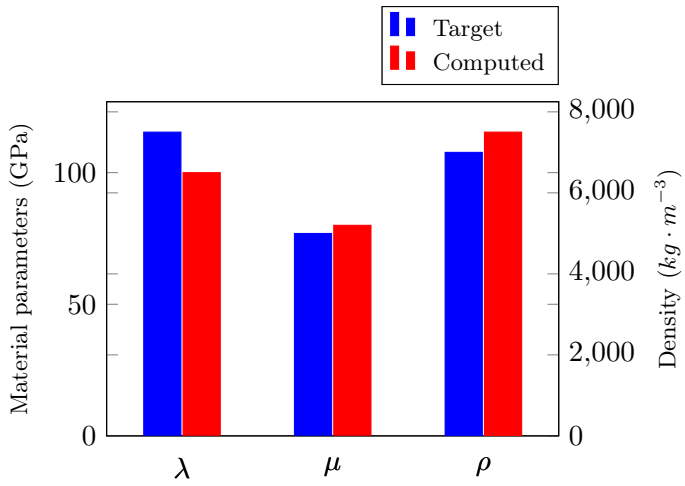

(d) Stage 1: Iteration 16.

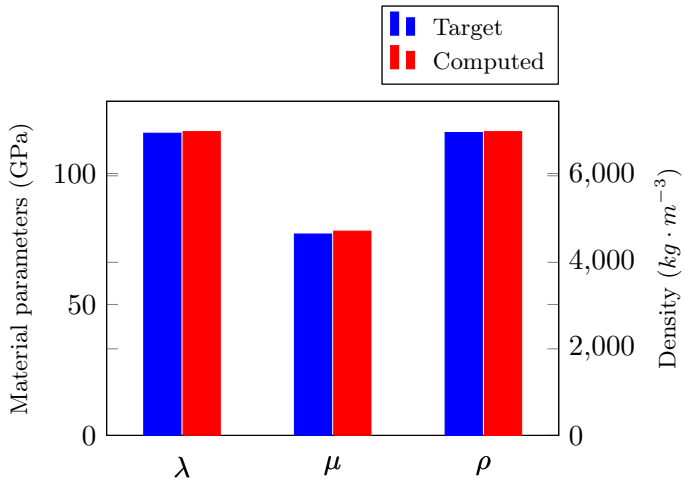

(e) Stage 1: Iteration 18.

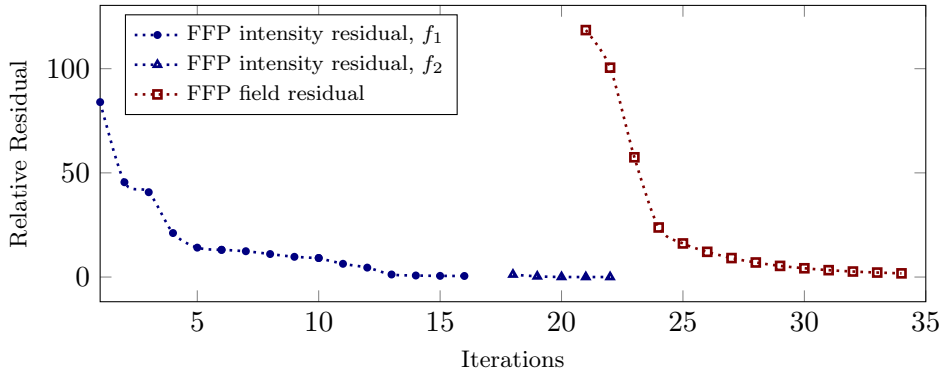

Fig. 5.4.10: Convergence history of the case of a polygonal-shape scatterer with material and shape parameters detailed in Tables 5.4.1-5.4.2 respectively, $ka = 2.47$ and 5.65 during the iterations of **SWA**, noise level= 0%.

Effect of Noise

In this section the influence of the noise on the reconstruction of shape and material parameters is analyzed. To this end, we consider four different cases depending on the noise level: $0\%, 5\%, 10\%, 15\%$. The corresponding results are depicted in Table 5.4.8. We observe that the final reconstructions are quite satisfactory: the final relative error on shape, Lamé and position parameters reconstruction is always below the noise level. For the density, for 10% and 15% noise levels the reconstruction error is a little bit higher than the noise level, 11.81% and 18.69% respectively. The convergence history corresponding to all these cases is depicted in Figure 5.4.11. In addition, the updated final shapes for different noisy cases are illustrated in Figure 5.4.12, while the updated final material parameters are detailed in Tables 5.4.13.

Noise level	Relative Residual		Relative Error			
	FFP Intensity	FFP Field	Shape parameters	Lamé coefficients	Density	Location
0%	1.02	1.88	1.02	2.61	0.47	1.53
5%	4.95	5.53	2.05	4.53	0.96	1.75
10%	10.98	12.77	4.64	9.14	11.58	3.87
15%	15.2	15.36	5.86	11.81	18.69	5.01

Tab. 5.4.8: Final Relative Residual and Relative error corresponding to different noise levels.

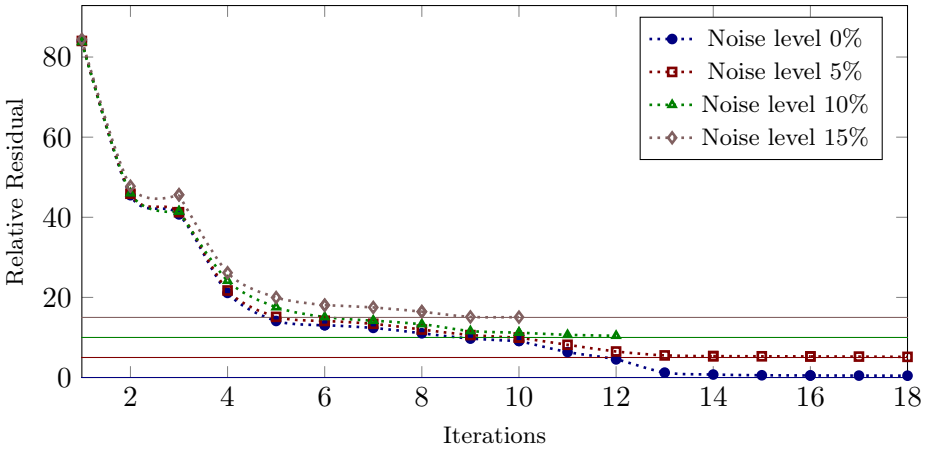

Fig. 5.4.11: Convergence history for different noise levels.

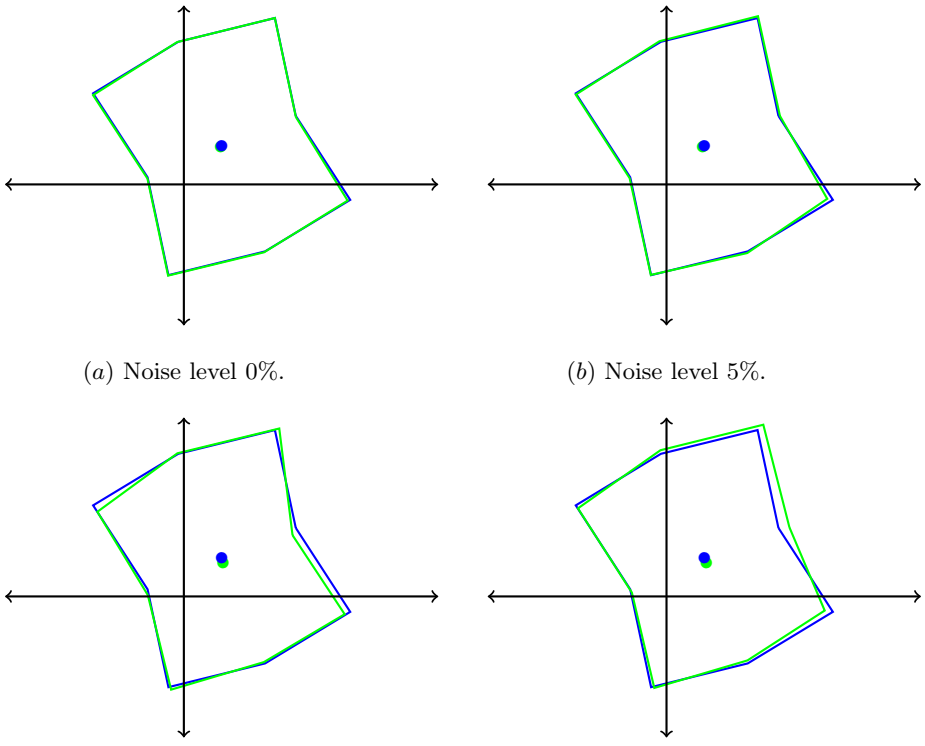

(*a*) Noise level 0%. (*b*) Noise level 5%.

(*c*) Noise level 10%. (*d*) Noise level 15%.

Fig. 5.4.12: The influence of the noise in the reconstruction of shape parameters and the center for the following noise levels: $0\% - 5\% - 10\% - 15\%$.

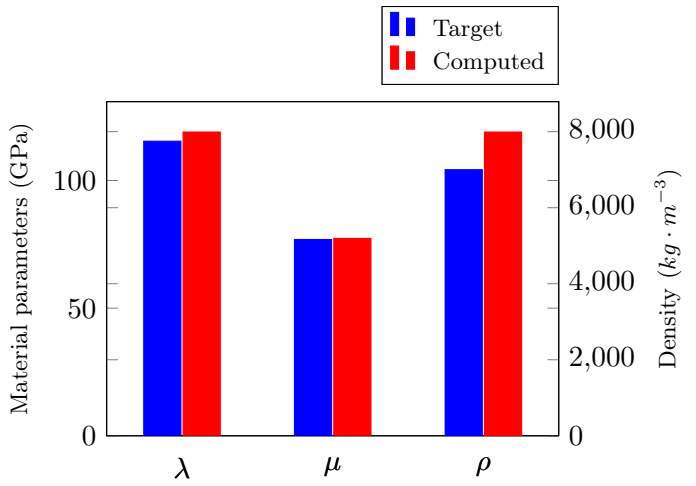

(a) Noise level 0%.

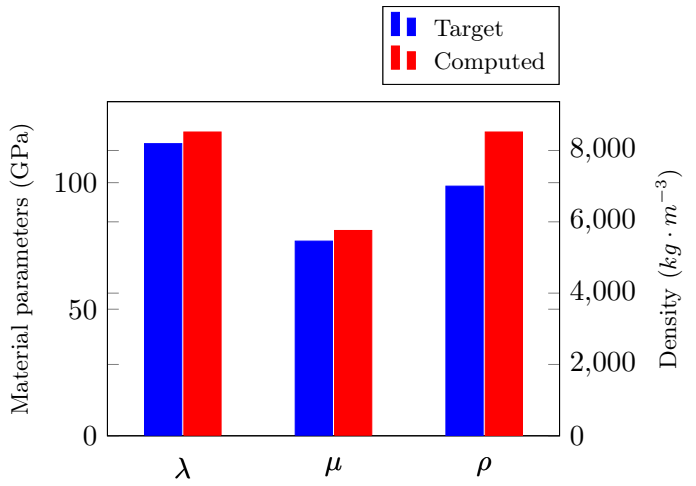

(b) Noise level 5%.

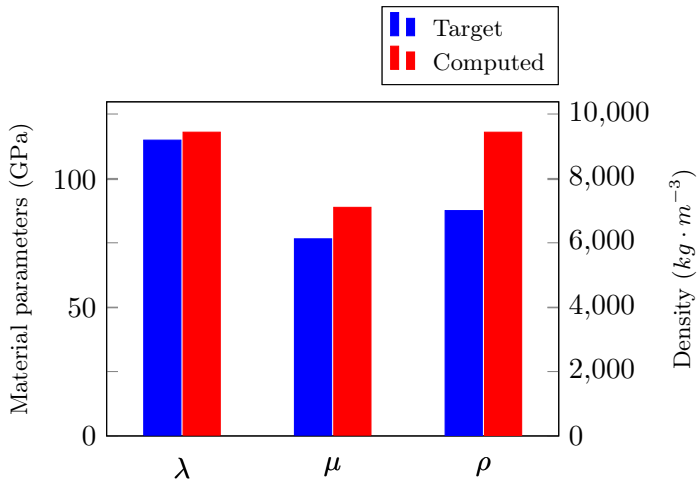

(c) Noise level 10%.

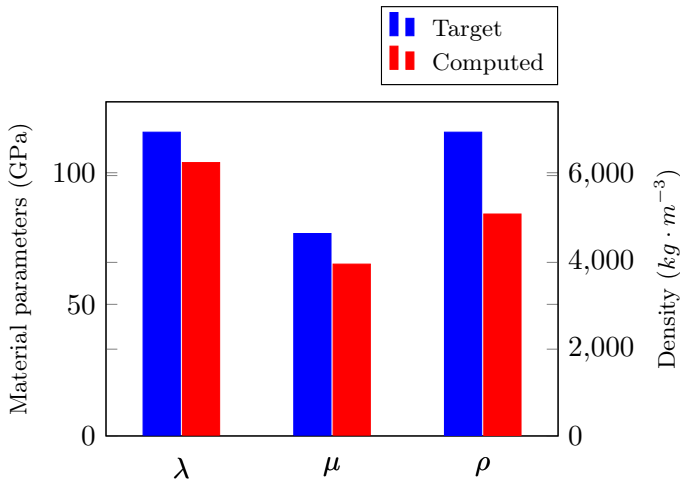

(d) Noise level 15%.

Fig. 5.4.13: The influence of the noise in the reconstruction of Lamé coefficients and the density for the following noise levels: $0\% - 5\% - 10\% - 15\%$.

5.4.2 Case of a Mockup Submarine

In this case, the sought-after scatterer Ω^s is made of *aluminum* whose material parameters are specified in Table (5.4.9). The surface Γ is described using the Fourier series parametrization (see Appendix C) with the shape parameters described in Table (5.4.10), and illustrated in Figure 5.4.15(a). In the following numerical experiments, the initial guess $\Omega^{(0)}$ is a circle depicted also in Table (5.4.10) and illustrated in Figure 5.4.15(b), while the initial guess of the material parameters is detailed in Table (5.4.9). The respective relative errors are 40.74%, 55.18% and 85.18% on shaper parameters, Lamé coefficients and on the density respectively.

The synthetic measurements correspond here also to a full aperture FFP with 360 observation points. The discretization involves fifth-order polynomials and we have eight elements per wavelength (Figure 5.4.14(a) and Table 5.4.11), while for computed measurements the mesh discretization uses six elements per wavelength (see Figure 5.4.14(b) and Table 5.4.11 for the mesh corresponding to the initial guess).

	$\lambda(\text{GPa})$	$\mu(\text{GPa})$	$\rho_s(kg \cdot m^{-3})$
Target	51.09	26.31	2700
Initial guess	30.00	50.00	5000
Relative Error	41.27	89.99	85.18

Tab. 5.4.9: Material parameters: target vs. initial guess.

	s_1	s_2	s_3	s_4	s_5	s_6	s_7	s_8	s_9
Target	1.50	0.50	0.05	0.60	0.01	0.20	0.10	0.20	0.30
Initial guess	1.75	0.60	0.00	0.10	0.00	0.00	0.00	0.00	0.00
Relative Error	16.67	20	100	83.33	100	100	100	100	100

Tab. 5.4.10: Shape parameters: target vs. initial guess.

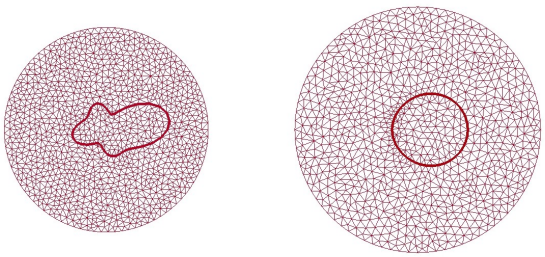

(a) Target: 2217 elements (b) Initial guess: 1792 elements

Fig. 5.4.14: Meshes for target vs. initial guess.

The radius of the external absorbing boundary condition has been selected as $b = 6$cm for the first experiments, which is not large enough to consider position parameters. In addition, the first noise-free and noisy experiments have been carried out using only the frequency $f = 55.7$kHz, while for the reconstruction of all parameters (material, shape and position parameters) with the radius

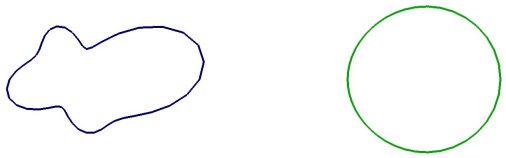

(a) Target (b) Initial guess

Fig. 5.4.15: Polygonal-shaped domain for target vs. initial guess.

	# elements			
	Γ^s	Γ^f	Ω^s	Ω^f
Mesh 1	46	46	196	1929
Mesh 2	42	42	156	1552

Tab. 5.4.11: Distribution of the elements in the mesh depending the medium and the neighbourhood.

of the external absorbing boundary condition $b = 7.5cm$ and two frequencies have been necessary, $f_1 = 55.7$kHz and $f_2 = 63.7$kHz (during these experiments as the quantity ka with $a = \min_{1\leq i\leq N_\Gamma} s_i$ can be confusing for Fourier parametrization, we describe the frequency in kHz).

Reconstruction with Noise-free FFP.

We set the frequency to be $f = 55.7$kHz. The reconstruction of the parameters at convergence is detailed in Tables 5.4.12)-(5.4.13, and illustrated in Figures 5.4.17-5.4.18. The following outcomes are note-worthy:

- The selected initial guess, outside the preasymptotic region, is depicted at Tables 5.4.9-5.4.10, certifying that the algorithm is blind for the sought-after values of the parameters, as depicted in Figure 5.4.17(a). Certainly, the initial relative errors in the shape parameters, Lamé coefficients and the density are 40.74%, 55.19% and 85.18% respectively.
- Figure 5.4.16 describes the decay of the relative residual intensity. More precisely, at stagnation, after reducing the regularization parameters, the relative residual increases a little (it is observable at iterations 10 and 14 in Figure 5.4.16 after the stagnations of iterations 9 and 13 resp.). The FFP intensity drops from 63.02% to 1.55%.
- At stagnation, the final reconstruction corresponds to the relative error of 2.19%, 1.02%, 2.73% on shape parameters, Lamé coefficients and density respectively (see Tables 5.4.12-5.4.13). The evolution of the reconstruction is observable at Figures 5.4.17-5.4.18 for different stagnations.

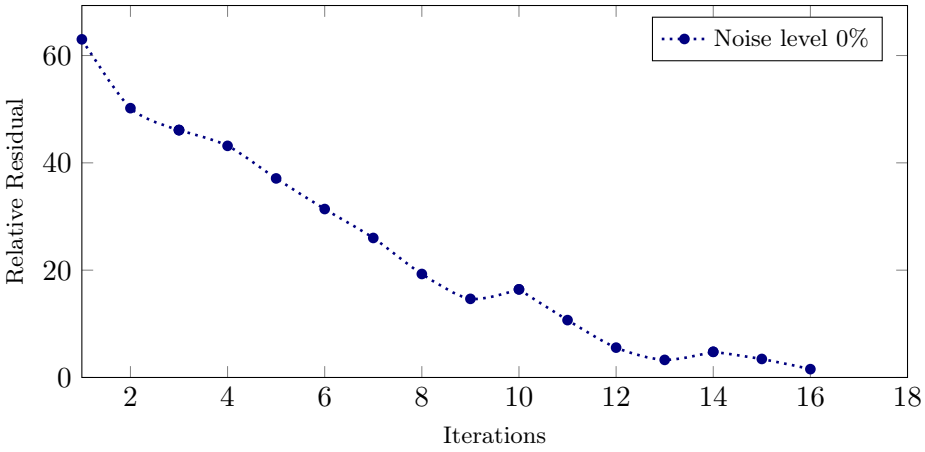

Fig. 5.4.16: Convergence history of the mockup submarine-shape scatterer, noise level= 0%.

	$\lambda(\text{GPa})$	$\mu(\text{GPa})$	$\rho_s(kg \cdot m^{-3})$
Target	51.09	26.31	2700
Computed	51.44	25.84	2476
Relative Error	0.71	1.77	2.73

Tab. 5.4.12: Material parameters: target vs. computed parameters with $f_1 = 55.7$kHz.

	s_1	s_2	s_3	s_4	s_5	s_6	s_7	s_8	s_9
Target	1.50	0.50	0.05	0.60	0.01	0.20	0.10	0.20	0.30
Computed	1.49	0.51	0.03	0.61	0.01	0.19	0.09	0.19	0.29
Relative Error	0.37	2.69	39.99	1.82	58.39	2.07	5.45	2.18	0.21

Tab. 5.4.13: Shape parameters: target vs. computed parameters with $f_1 = 55.7$kHz.

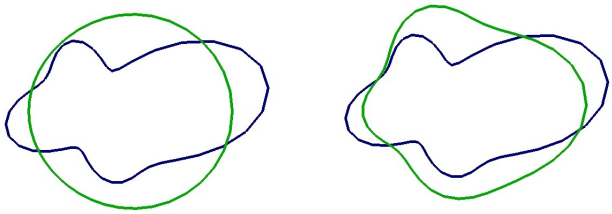

(a) Stage 1: Iteration 0.

(b) Stage 1: Iteration 3.

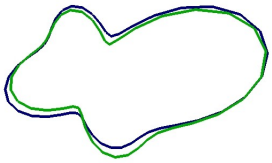

(c) Stage 1: Iteration 9.

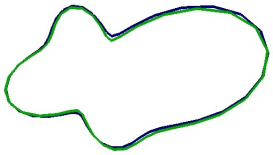

(d) Stage 1: Iteration 13.

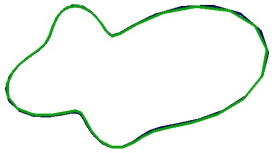

(e) Stage 1: Iteration 18.

Fig. 5.4.17: Shape of a mockup submarine-shaped scatterer: target vs. computed parameters at different stagnations, noise-free mono-frequency case.

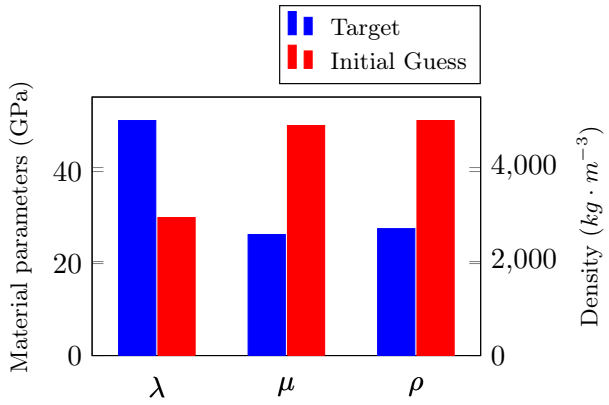

(a) Stage 1: Iteration 0.

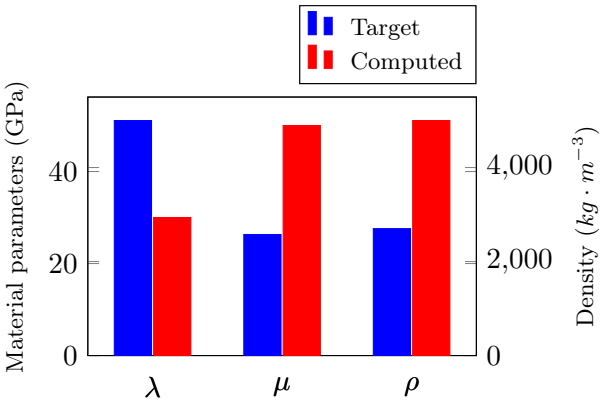

(b) Stage 1: Iteration 3.

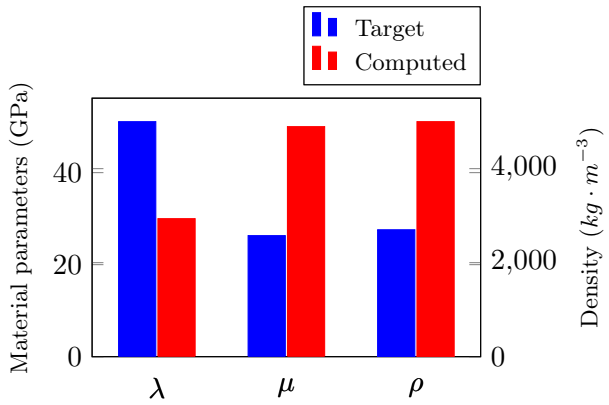

(c) Stage 1: Iteration 9.

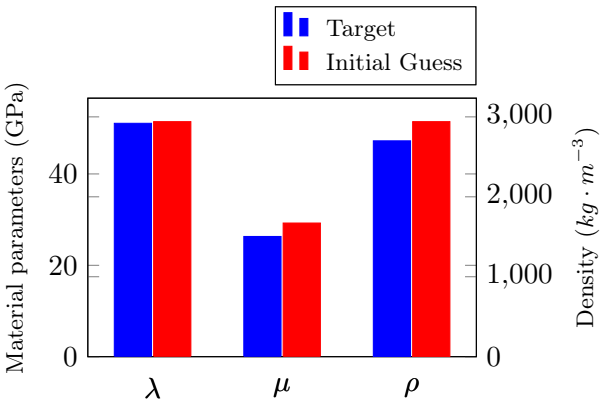

(d) Stage 1: Iteration 13.

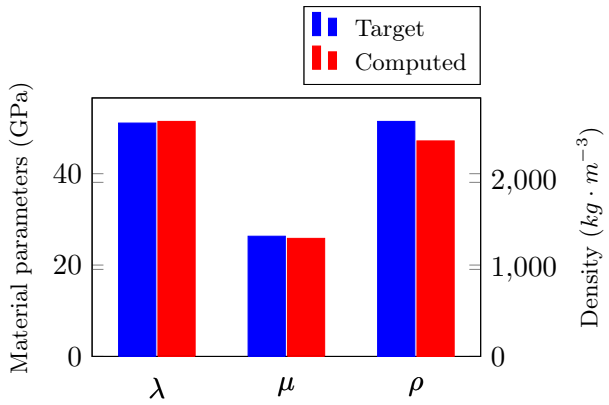

(e) Stage 1: Iteration 18.

Fig. 5.4.18: Histogram corresponding to the updated material parameters at different stagnations for mockup submarine reconstruction, noise-free mono-frequency case.

Effect of Noise

In this section the influence of the noise on the reconstruction of shape and material parameters is analyzed. To this end, we consider four different cases depending on the noise level: $0\%, 5\%, 10\%, 15\%$. The final results corresponding to these experiments are summarized in Table 5.4.14.

Regarding the convergence history illustrated for all these tests in Figure 5.4.19, we observe that for 15% of noise level the RR seems to increase a little at iteration 13. We must remind, that this kind of peaks usually correspond to the decrease of the regularization parameters introduced after a stagnation. They sometimes cause some increase of RR during the first iteration after stagnation.

In addition, we observe that RR achieves the noise level for 10% and 15% noisy cases, while for the other two experiments of $0\% - 5\%$ of noise level, the reconstruction is considered completed when RR achieves the minimum value of RR, that is 1.55% and 7.28% respectively.

Noise level	Relative Residual		Relative Error		
	FFP Intensity	FFP Field	Shape parameters	Lamé coefficients	Density
0%	1.55	7.01	2.19	1.03	2.73
5%	7.28	9.11	2.23	2.87	4.56
10%	9.99	12.97	2.79	2.33	2.76
15%	14.7	21.32	6.65	6.87	6.90

Tab. 5.4.14: Final Relative Residual and Relative error corresponding to different noise levels for mockup-submarine obstacle.

We observe that the final reconstruction of the shape for different noise levels is quite successful, as illustrated in Figure 5.4.20, and specified in Table 5.4.14. The final reconstruction of material parameters is illustrated in the histograms of Figure 5.4.21 and detailed in Table 5.4.14, which are also considerably accurate as they are lower than the noise level (expect the case 0%).

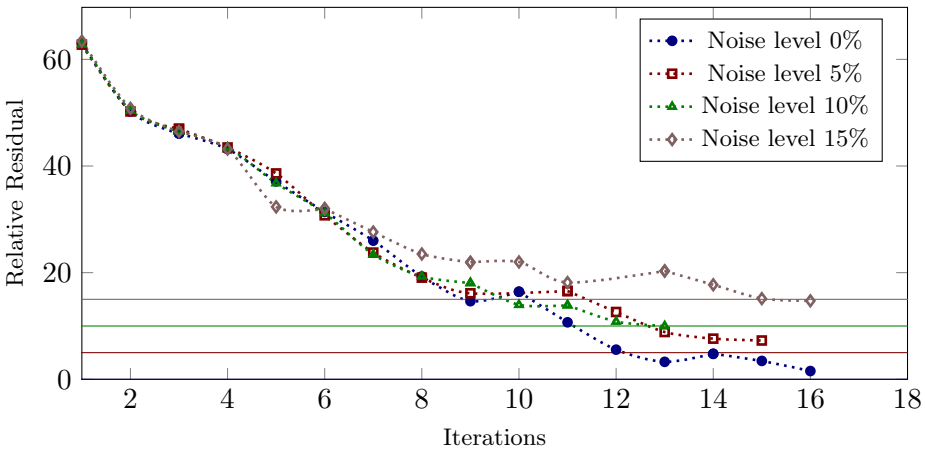

Fig. 5.4.19: Convergence history for different noise levels .

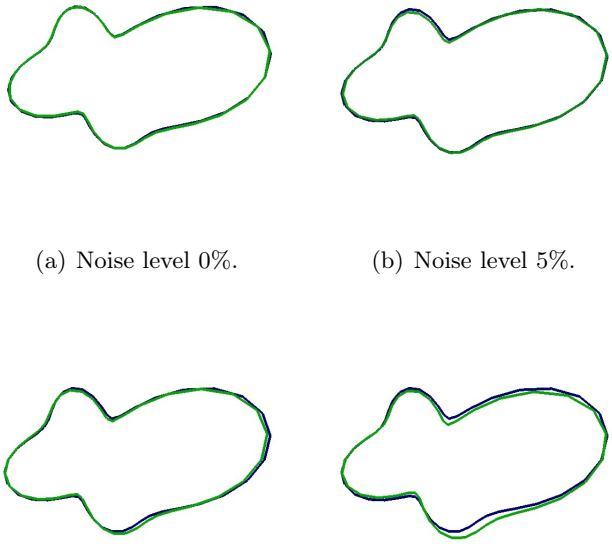

(a) Noise level 0%. (b) Noise level 5%.

(c) Noise level 10%. (d) Noise level 15%.

Fig. 5.4.20: Final reconstructed shape vs. target for different noise levels, mockup-submarine mono-frequency case.

Reconstruction of Location for Noisy Cases

In this last set of experiments, the external radius is $b = 7.5$cm. The target and initial guess corresponding to the shape and material parameters have been kept from previous tests, which are depicted in Tables 5.4.10 and 5.4.9 respectively. The target and initial guess of the position parameters are visible in Figure 5.4.22 and detailed in Table 5.4.15.

	x_c	y_c
Target	0.2	1.50
Initial guess	0.00	0.00
Relative Error	100	100

Tab. 5.4.15: Position parameters: target vs. initial guess.

We remind that we use the frequencies $f_1 = 55.7$kHz and $f_2 = 63.7$kHz during stage 1, corresponding to the reconstruction of the shape and material parameters. We have illustrated the convergence history of stage 1 and stage 2 in Figures 5.4.23 and 5.4.24 respectively. It is worth mentioning that during the stage 1, motivated with the non accurate reconstruction using the $f_1 = 55.7$kHz depicted in Table 5.4.16, we decide to increase the frequency to gain in accuracy as detailed in Table 5.4.17.

More precisely, the relative errors at stagnation corresponding to the frequency $f_1 = 55.7$kHz are detailed in Table 5.4.16. We observe that for the experiment corresponding to 15% it is sufficient to use only one frequency, as the reconstruction of all parameters is quite successful. On the contrary, in the case of 0% of noise level, the relative error at stagnation corresponding to Lamé coefficients is

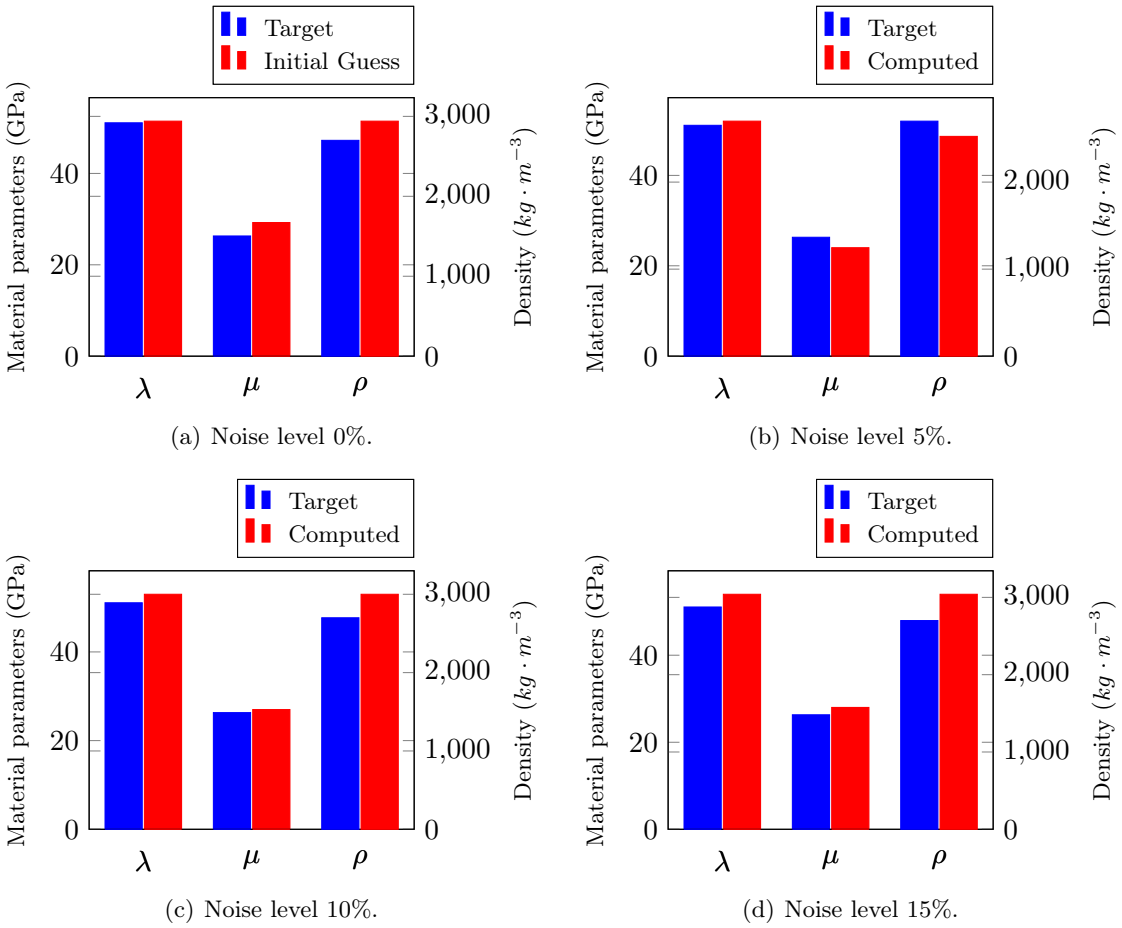

(a) Noise level 0%.

(b) Noise level 5%.

(c) Noise level 10%.

(d) Noise level 15%.

Fig. 5.4.21: Histogram corresponding to the final updated material parameters for different noise levels, mockup-submarine mono-frequency case.

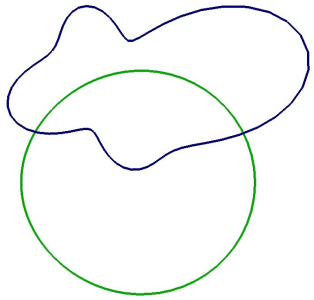

Fig. 5.4.22: Target vs. initial guess, represented by blue and green colors respectively.

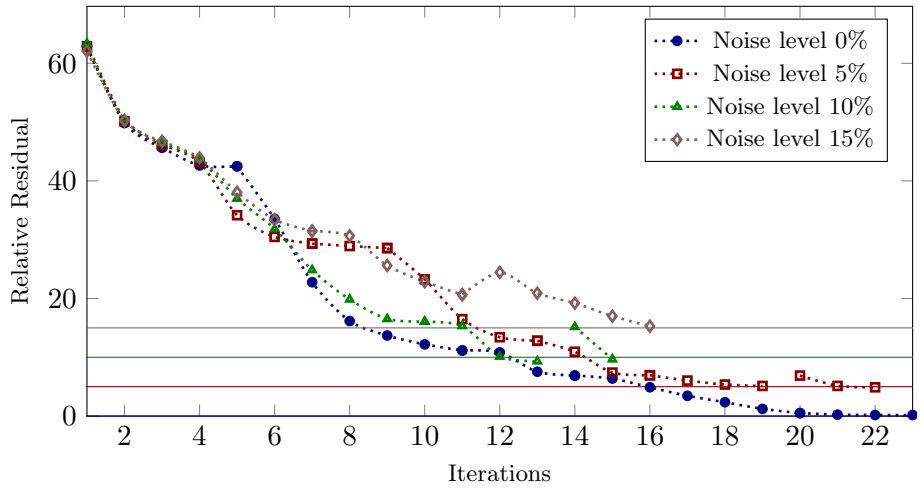

Fig. 5.4.23: Convergence history of RR corresponding to the reconstruction of shape and material parameters for different noise levels.

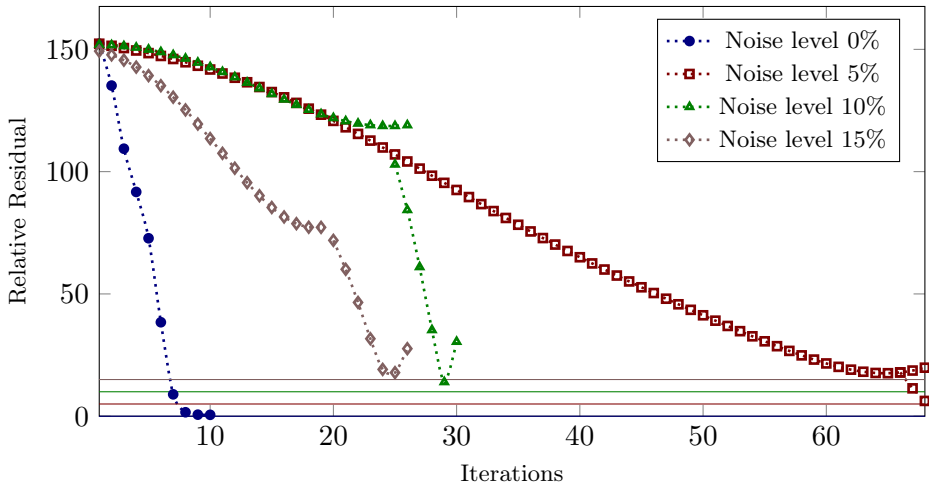

Fig. 5.4.24: Convergence history for the evolution of RR_2 corresponding to the reconstruction of position parameters for different noise levels.

Noise level	Relative Residual		Relative Error			
	FFP Intensity	FFP Field	Shape parameters	Lamé coefficients	Density	Location
0%	0.17	152.31	0.43	4.96	1.15	100
5%	5.12	152.49	1.60	17.55	4.95	100
10%	9.3	155.11	3.79	14.19	14.33	100
15%	15.29	150.03	2.34	17.15	11.36	100

Tab. 5.4.16: Final Relative Residual and Relative error corresponding to different noise levels using only the frequency $f_1 = 55.7$kHz.

around 5%. For 5% of noise level, even if we have achieved the level of 5.12% of RR, the relative error on Lamé coefficients is bigger than 17%. For 10% of noise level, we have a similar situation, with a relative error around 14% on all material parameters. This is why we proceed increasing the frequency. The final reconstruction for shape and material parameters (using only the frequency $f_1 = 55.7$kHz for 15% of noise case) are depicted in Table 5.4.17.

Noise level	Relative Residual		Relative Error			
	FFP Intensity	FFP Field	Shape parameters	Lamé coefficients	Density	Location
0%	0.42	163.43	0.67	0.613	0.01	100
5%	4.89	163.4	1.12	1.62	1.05	100
10%	9.65	162.87	1.17	0.75	0.19	100
15%	15.29	150.03	2.34	17.15	11.36	100

Tab. 5.4.17: Final Relative Residual and Relative error corresponding to different noise levels.

In addition, in order to observe the iterations corresponding to frequencies f_1 and f_2, the history convergence for the noise levels of $0\% - 5\% - 10\%$ has been illustrated independently in Figures 5.4.25, 5.4.26 and 5.4.27 respectively. We observe that in all cases RR achieves the noise level with the first frequency $f_1 = 55.3$kHz without obtaining an accurate reconstruction of material parameters as detailed in Table 5.4.16. Moreover, we remind that in practice we do not have access to the relative error, so we conclude from these experiments that in order to ensure a complete and successful reconstruction, it is a good idea to add some iterations with a higher frequency.

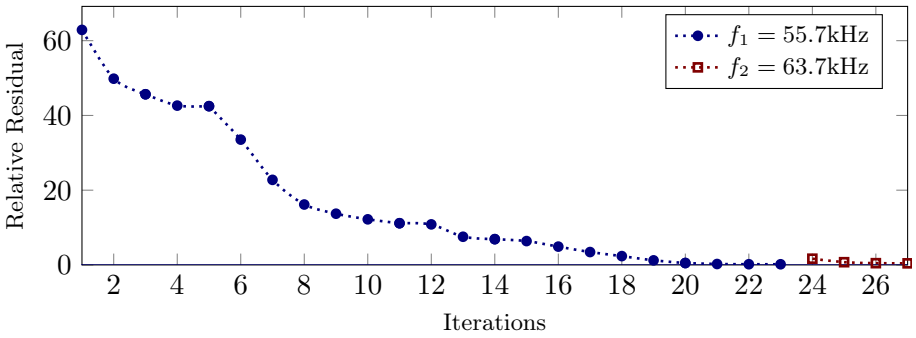

Fig. 5.4.25: Convergence history 0% noise level and frequencies $f_1 = 55.7$kHz and $f_2 = 63.7$kHz.

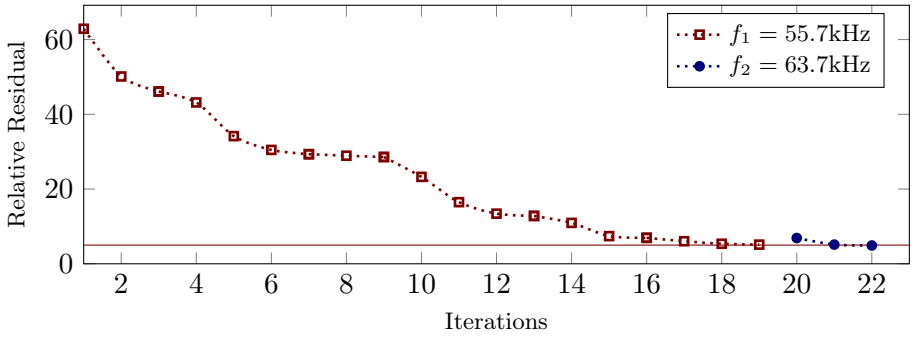

Fig. 5.4.26: Convergence history 5% noise level and frequencies $f_1 = 55.7$kHz and $f_2 = 63.7$kHz.

Finally, we address the reconstruction of position parameters. Here again we must precise that two different frequencies have been use, $f_1 = 55.7$kHz and $f_2 = 71.6$kHz, for the cases corresponding to

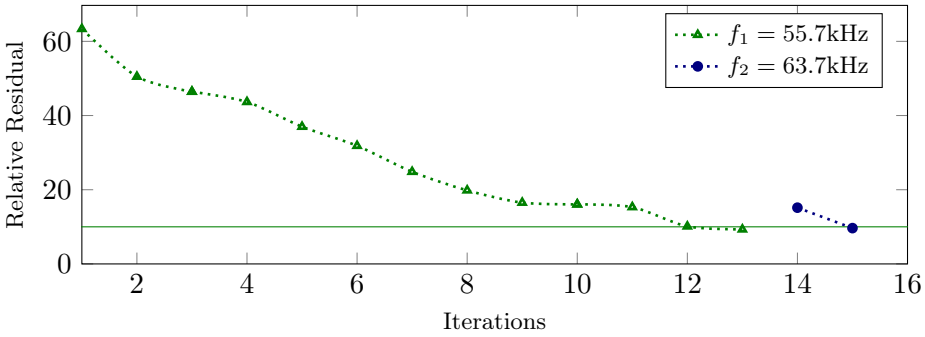

Fig. 5.4.27: Convergence history 10% noise level and frequencies $f_1 = 55.7$kHz and $f_2 = 63.7$kHz.

$10\% - 15\%$ of noise levels. The convergence history corresponding to RR_2, the relative residual of the FFP field, is depicted for all cases in Figure 5.4.24. The position parameters corresponding to $0\% - 5\%$ noise level have been successfully reconstructed using only $f_1 = 55.7$kHz, but the necessary number of iterations is completely different: 11 and 68 iterations respectively (see Figure 5.4.24). For 5% of noise level, different strategies have been tested as reducing the regularization parameters, increasing the frequency, even changing completely the frequency and the illustrated one has been the most accurate one.

The updated relative errors after using $f_1 = 55.7$kHz to retrieve the position parameters are depicted in Table 5.4.18. We observe that for $10\% - 15\%$ of noise level the relative error on position parameters is still 43.27% and 25.05% respectively (the updated shape parameters are illustrated in Figure 5.4.28 for all noisy cases). This is why we decide to increase the frequency for these cases with $f_2 = 71.6$kHz. The final reconstructions after increasing the frequency when necessary cases are depicted in Table 5.4.19. We observe that the relative residual of the FFP field does not achieve the noise level in the cases of $5\% - 10\% - 15\%$ (see column FFP field in Table 5.4.19), but the reconstructions corresponding to the minimum values on each case are good (see column Location).

Noise level	Relative Residual		Relative Error			
	FFP Intensity	FFP Field	Shape parameters	Lamé coefficients	Density	Location
0%	0.42	0.57	0.67	0.613	0.01	0.12
5%	4.92	6.29	1.12	1.62	1.05	1.77
10%	9.63	118.7	1.17	0.75	0.19	43.27
15%	14.96	77.22	2.34	17.15	11.36	25.05

Tab. 5.4.18: Relative Residuals and Relative errors corresponding to different noise levels at stagnation after using frequency $f_1 = 55.7$kHz.

The convergence history of the multi-frequency reconstruction of position parameters is illustrated independently, in order to observe better the different steps corresponding to distinct frequencies. The evolution of the relative residual of the FFP field for 10% of noise level is illustrated in Figure 5.4.29, while for 15% of noise level, in Figure 5.4.30. In both cases we observe that the RR_2 decreases smoothly until stagnation, while during the second step corresponding to the frequency $f_2 = 71.6$kHz the decrease is faster. In addition, the minimal value of RR_2 is visible in both cases. The final shape and position parameters in these cases are illustrated in Figure 5.4.31.

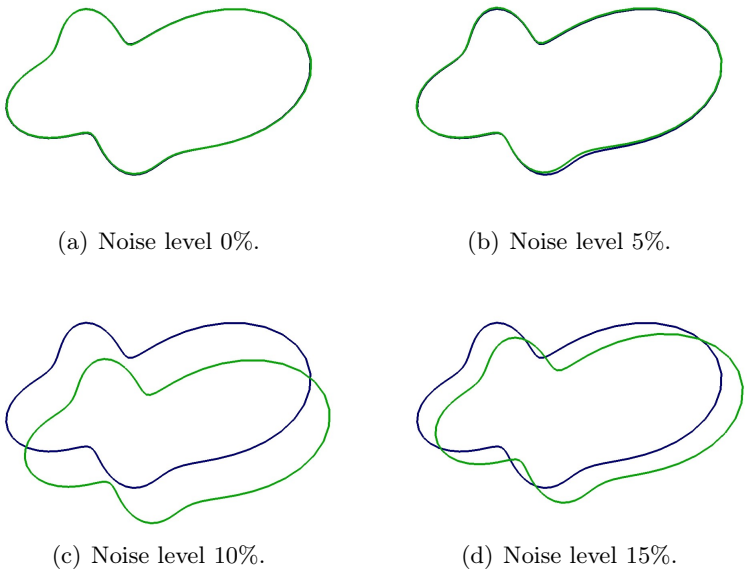

(a) Noise level 0%. (b) Noise level 5%.

(c) Noise level 10%. (d) Noise level 15%.

Fig. 5.4.28: Updated shape and position parameters after the reconstruction of position parameters with frequency $f_1 = 55.3$kHz.

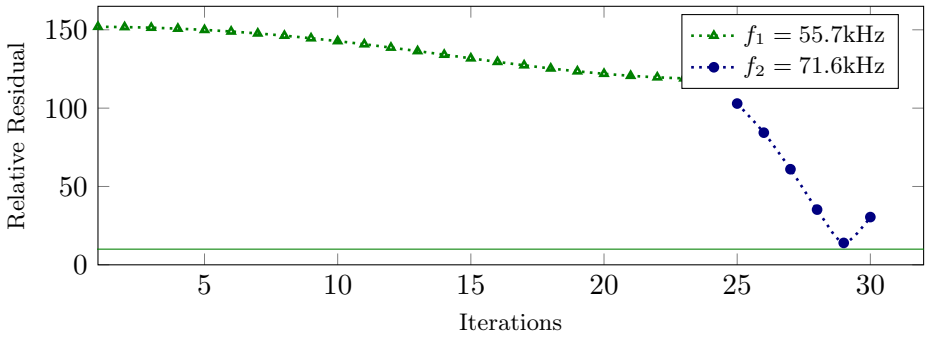

Fig. 5.4.29: Convergence history of RR_2 for 10% noise level and frequencies $f_1 = 55.7$kHz and $f_2 = 71.6$kHz.

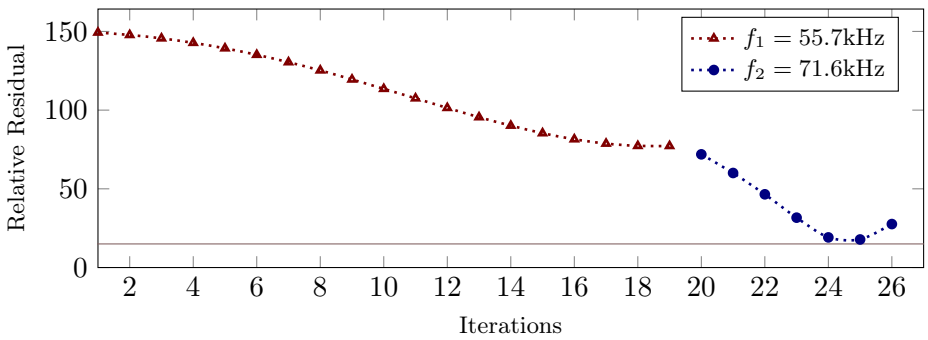

Fig. 5.4.30: Convergence history of RR_2 for 15% noise level and frequencies $f_1 = 55.7$kHz and $f_2 = 71.6$kHz.

Noise level	Relative Residual		Relative Error			
	FFP Intensity	FFP Field	Shape parameters	Lamé coefficients	Density	Location
0%	0.42	0.57	0.67	0.613	0.01	0.12
5%	4.92	6.29	1.12	1.62	1.05	1.77
10%	9.78	15.8	1.17	0.75	0.19	10.03
15%	15.46	17.82	2.34	17.15	11.36	4.75

Tab. 5.4.19: Final Relative Residual and Relative error corresponding to different noise levels.

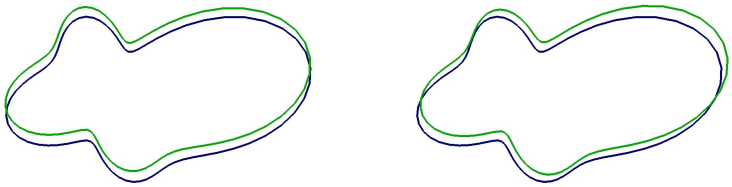

(a) Noise level 10%. (b) Noise level 15%.

Fig. 5.4.31: Updated shape and position parameters after the reconstruction of position parameters with frequency $f_2 = 71.6$kHz.

5.5 Conclusions and perspectives

In this chapter, we have tackled more practical problems. In particular, we have considered noisy data and limited aperture data. We have obtained very satisfactory results and we have demonstrated the interest of using a multi-frequency solution methodology. By this way, we clearly improve the convergence of the method. We have also achieved successful reconstructions when adding the location of the solid as a parameter of interest. In the future, we would like to address the case of heterogeneous obstacles. We could start from a solid whose elastic parameters can be represented by piecewise constant functions, assuming that the interfaces between the heterogenities are known. Then, we will address the problem of retrieving both the heterogenities and the interfaces.

Chapter 6

Application to Anisotropic Materials

Contents

In this chapter, we propose to apply our solution methodology to the case of anisotropic elastic obstacles. We first define the anisotropic media we consider (VTI media) and we analyze the impact of each anisotropic material parameter on the far field pattern. Then we assess the performance of our algorithm to recover these parameters first when the obstacle is a circle whose radius is assumed to be known (section 6.3), and second, when it is a convex obstacle whose shape is assumed to be known (section 6.4). Finally we consider the problem of recovering both material and shape parameters.

6.1 Problem Statement

In a geological layer, the speed of waves is in general non uniform in all the directions, and the distribution of wave fronts admits two orthogonal symmetry plans. This is the definition of orthotropy. The anisotropy of surface is considered orthotropic in one direction, which means that the wave front admits a symmetry with respect to one of the reference axes. This is the definition of Transverse Isotropy. In our case, we consider Vertical Transverse Isotropy (VTI) media. In that case, the matrix of elasticity can be described as follows:

$$C_{ortho} = \begin{pmatrix} c_{11} & c_{12} & 0 \\ c_{21} & c_{22} & 0 \\ 0 & 0 & c_{33} \end{pmatrix}$$

where the entries are defined by the material parameters which are the density ρ, the velocities V_p, V_s and the Thomsen parameters ϵ, δ in the following way:

- $c_{11} = \rho V_p^2(1 + 2\epsilon)$
- $c_{22} = \rho V_p^2$

- $c_{33} = \rho V_s^2$
- $c_{12} = c_{21} = \rho\sqrt{(V_p^2 - V_s^2)^2 + 2V_p^2\delta(^2_p - V_s^2)} - \rho V_s^2$

This set of parameters that describes the anisotropic media tensor is explained for instance in [100].

The objective of this section is to introduce some numerical results where these anisotropic material parameters are reconstructed together with the shape parameters. This motivates us to introduce the following inverse problem:

IP(4) Given one incident plane wave for a fixed wavenumber, from the access of full aperture data, find the anisotropic material parameters $\rho, V_p, V_s, \epsilon, \delta$ and the shape parameters $s_1, ..., s_{N_\Gamma}$ such that

$$F\left(\rho, V_p, V_s, \epsilon, \delta, \Gamma\left(s_1, ..., s_{N_\Gamma}\right)\right)\left(\hat{x_j}\right) = \tilde{p}_\infty\left(\hat{x_j}\right) \quad j = 1, ..., N_x, \tag{6.1.1}$$

We have seen in Chapter II that the Fréchet derivatives with respect to the Lamé parameters can be characterized as a solution to **(BVP 3-4)** defining properly the derivatives of the tensor C. Following the same strategy, we introduce the derivatives of the tensor with respect to the anisotropic material parameters in order to chacterize the corresponding Fréchet derivatives. In order to simplify the expression of the derivatives of the matrix, we continue adopting the generic notation ∂C to designate the derivative of C with respect to each parameter.

$$\partial C = \begin{pmatrix} \partial c_{11} & \partial c_{12} & 0 \\ \partial c_{21} & \partial c_{22} & 0 \\ 0 & 0 & \partial c_{33} \end{pmatrix} \tag{6.1.2}$$

The matrix corresponding to the derivative with respect to V_p, $\partial_{V_p} C$, is defined with the following entries:

- $\partial c_{11} = 2\rho V_p(1 + 2\epsilon)$
- $\partial c_{22} = 2\rho V_p$
- $\partial c_{12} = \partial c_{21} = \rho(4V_p(V_p^2 - V_s^2)(1 + \delta) + 4V_p^3\delta)/(2\sqrt{(V_p^2 - V_s^2)^2 + 2V_p^2\delta(V_p^2 - V_s^2)})$
- $\partial c_{13} = \partial c_{31} = \partial c_{23} = \partial c_{32} = \partial c_{33} = 0$

The matrix corresponding to the derivative with respect to V_s, $\partial_{V_s} C$, it is defined by:

- $\partial c_{33} = 2\rho V_s$
- $\partial c_{12} = \partial c_{21} = \rho(-4V_s(V_p^2 - V_s^2) - 4\delta V_p^2 V_s)/(2\sqrt{(V_p^2 - V_s^2)^2 + 2V_p^2\delta(V_p^2 - V_s^2)}) - 2\rho V_s$
- $\partial c_{11} = \partial c_{22} = \partial c_{13} = \partial c_{31} = \partial c_{23} = \partial c_{32} = 0$

The matrix corresponding to the derivative with respect to ϵ,$\partial_\epsilon C$, it is defined by:

- $\partial c_{11} = 2\rho V_p^2$

- $\partial c_{ij} = 0$ all others

The matrix corresponding to the derivative with respect to δ, $\partial_\delta C$, it is defined by:

- $\partial c_{13} = \partial c_{31} = \rho V_p^2 (V_p^2 - V_s^2) / \sqrt{(V_p^2 - V_s^2)^2 + 2V_p^2 \delta (V_p^2 - V_s^2)}$
- $\partial c_{ij} = 0$ all others

Finally, we introduce the quantities to measure the accuracy of the reconstruction of anitropic material parameters:

Relative Error on Density (RED):

$$RED(n) = \frac{\mid \rho - \rho^{(n)} \mid}{\mid \rho \mid} \times 100 \tag{6.1.3}$$

Relative Error on V_p (REV_p):

$$REV_p(n) = \frac{\mid V_p - V_p^{(n)} \mid}{\mid V_p \mid} \times 100 \tag{6.1.4}$$

Relative Error on V_s (REV_s):

$$REV_s(n) = \frac{\mid V_s - V_s^{(n)} \mid}{\mid V_s \mid} \times 100 \tag{6.1.5}$$

Relative Error on Thomsen parameter ϵ (RE_ϵ):

$$RE_\epsilon(n) = \frac{\mid \epsilon - \epsilon^{(n)} \mid}{\mid e \mid} \times 100 \tag{6.1.6}$$

Relative Error on Thomsen parameter δ (RE_δ):

$$RE_\delta(n) = \frac{\mid \delta - \delta^{(n)} \mid}{\mid \delta \mid} \times 100 \tag{6.1.7}$$

6.2 Influence of the Material Parameters on the Far Field Pattern

In the case of isotropic media (see Chapter III and IV) we have seen that some parameters have a stronger influence on the far field pattern than others. It turns out that the bigger the influence of the parameter is, the easier its reconstruction is. This is why we begin with a sensitivity test of the FFP with respect to the anisotropic material parameters.

In this section, we assume that the scatterer Ω^s is a circle of radius $a = 1$cm, with the external boundary is a circle with radius $b = 10$cm. To assess the influence of any parameter η, η standing for ρ, V_p, V_s, ϵ, δ, we compute the corresponding FFP for η and 2η denoted respectively by $p_{\infty,\eta}$ and $p_{\infty,2\eta}$. The different values of the parameters are summarized in Table 6.2.1. We then introduce some quantities of interest which are defined as follows:

$$f_\eta(ka) = \frac{\| p_{\infty,\eta}(ka) - p_{\infty,2\eta}(ka) \|_2}{\| p_{\infty,\eta}(ka) \|_2} \times 100$$

	ρ (Kg m^{-3})	V_p (m s^{-1})	V_s (m s^{-1})	ϵ	δ
Target	1	3000	2200	0.2	0.1
Initial guess	2	6000	4400	0.4	0.2
Relative Error	100	100	100	100	100

Tab. 6.2.1: Physical characteristics of VTI case-tests, [16].

$$f_\eta^*(ka) = \frac{\| p_{\infty,\eta}(ka)\overline{p_{\infty,\eta}(ka)} - p_{\infty,2\eta}(ka)\overline{p_{\infty,2\eta}(ka)} \|_2}{\| p_{\infty,\eta}(ka)\overline{p_{\infty,\eta}(ka)} \|_2} \times 100$$

$$f_\eta^{\mathcal{R}}(ka) = \frac{\| \mathcal{R}(p_{\infty,\eta}(ka)) - \mathcal{R}(p_{\infty,2\eta}(ka)) \|_2}{\| \mathcal{R}(p_{\infty,\eta}(ka)) \|_2} \times 100$$

$$f_\eta^{\mathcal{I}}(ka) = \frac{\| \mathcal{I}(p_{\infty,\eta}(ka)) - \mathcal{I}(p_{\infty,2\eta}(ka)) \|_2}{\| \mathcal{I}(p_{\infty,\eta}(ka)) \|_2} \times 100$$

We compute their values for frequencies ka in $[1, 7.5]$. We begin our analysis with the density. Figure 6.2.1 shows the variation of the previously defined quantities as functions of the frequency. We observe that their behavior is quite similar. Consequently, in order to ensure stability, the reconstruction of the density ρ will be carried out with the intensity of the FFP.

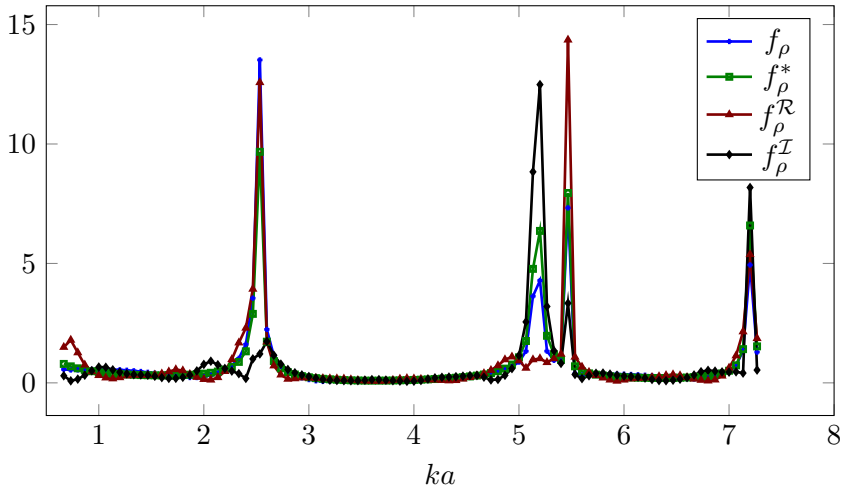

Fig. 6.2.1: Impact of the density ρ on the different quantities of the FFP.

According to Figure 6.2.2 (resp. 6.2.3, 6.2.4, 6.2.5), we have the same conclusion saying that each quantity gives the same feedback. We thus decide to use the intensity of the FFP for retrieving V_p (resp. V_s, ϵ and δ).

Now, in Figure 6.2.6, we have plotted the variations of $f_\rho^*, f_{V_p}^*$ and $f_{V_s}^*$ as functions of the frequency. We observe that they behave similarly for certain frequencies. For instance, there is a peak for $ka \in [2, 3]$ which shows that each of the parameters under interest have a strong influence simultaneously. Moreover, inside the interval $ka \in [0.5, 2.5]$ $f_{V_p}^*$ is bigger than f_ρ^* $f_{V_s}^*$, as we can observe in Figure 6.2.7(a), and f_ρ^* is slightly bigger than $f_{V_s}^*$. This may indicate that for $ka \in [0.5, 2.5]$ the material parameter V_p has more impact on the intensity of the FFP than the other material parameters, and consequently it should be easier to recover this parameter than the other ones for low

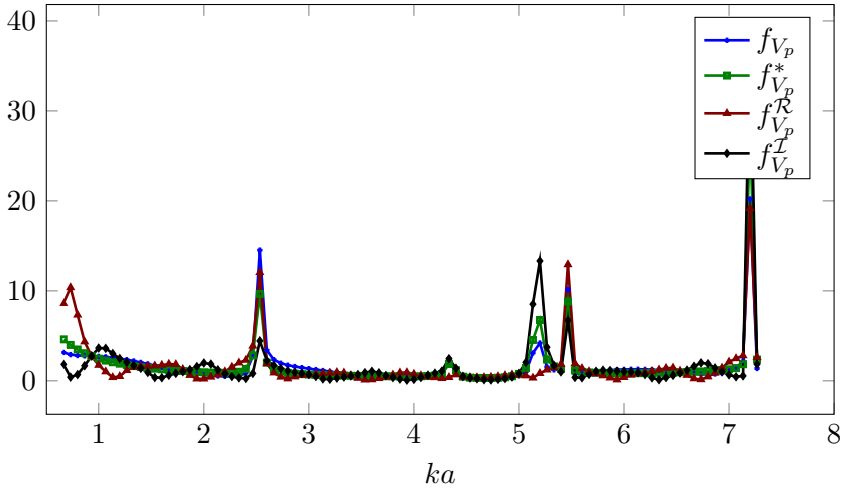

Fig. 6.2.2: Impact of the velocity V_p on the different quantities of the FFP.

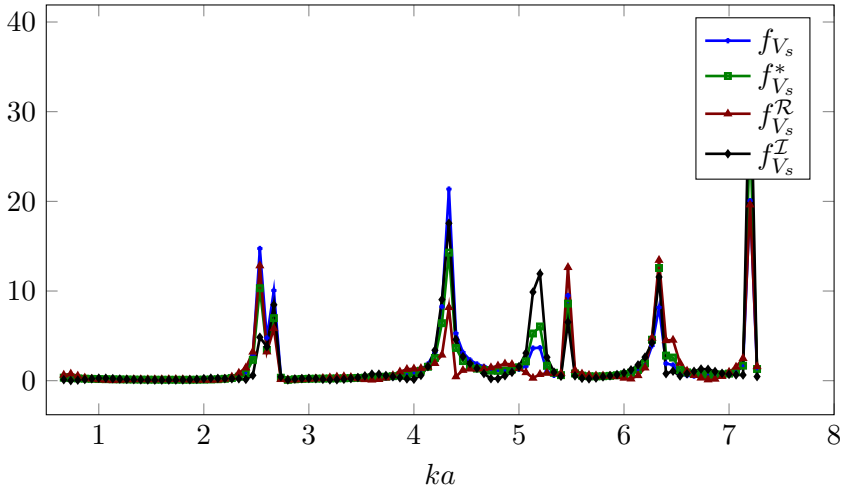

Fig. 6.2.3: Impact of the velocity V_s on the different quantities of the FFP.

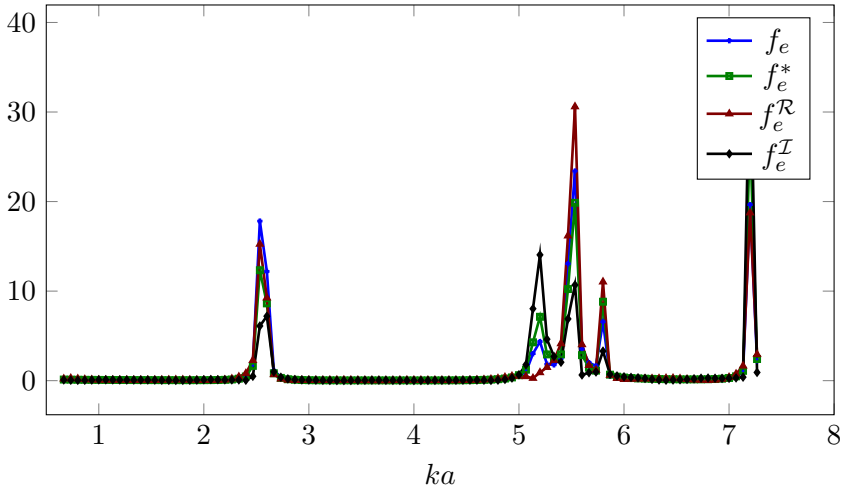

Fig. 6.2.4: Impact of the Thomsen parameter ϵ on the different quantities of the FFP.

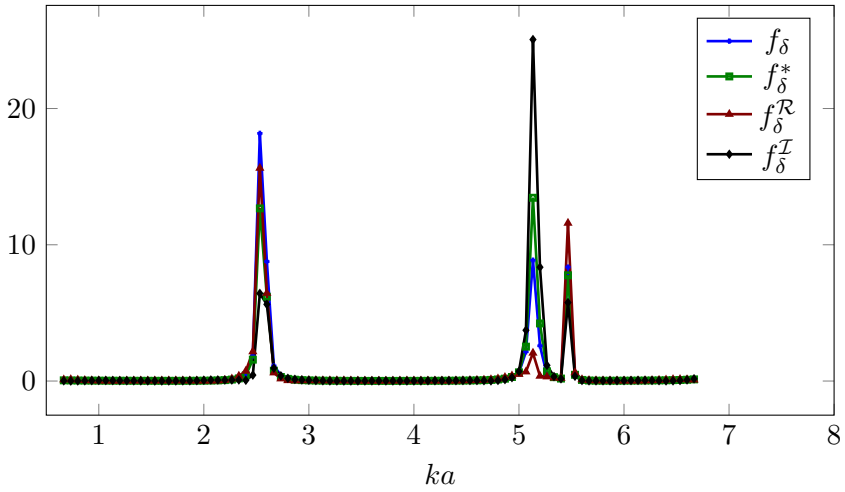

Fig. 6.2.5: Impact of the Thomsen parameter δ on the different quantities of the FFP.

frequencies. Nevertheless, the highest peaks correspond to $f^*_{V_s}$, so for higher frequencies we predict that V_s is the parameter with the higher influence at interval $ka \in [2.4, 2.8]$ as illustrated in Figure 6.2.7(b).

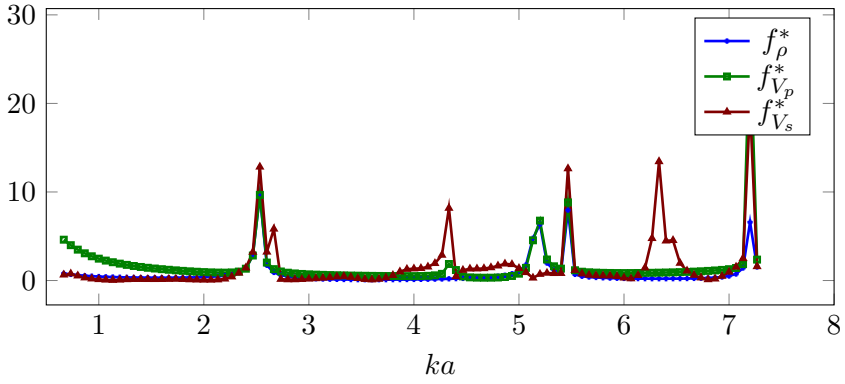

Fig. 6.2.6: Impact of the parameters ρ, V_p and V_s on the intensity of the FFP.

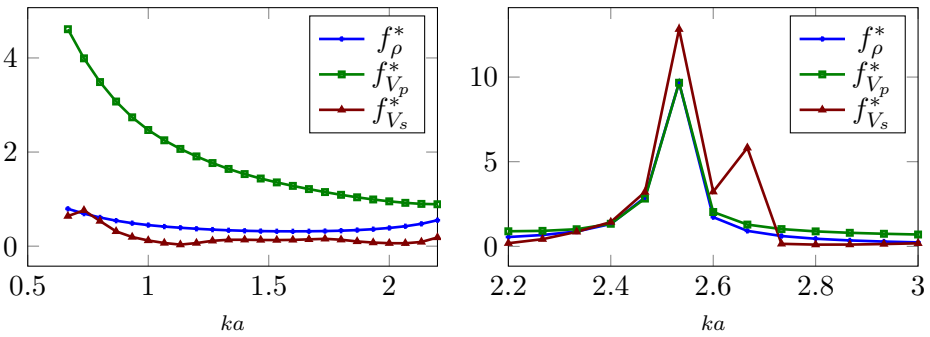

(a) $0.5 \leq ka \leq 2.5$ (b) $2.2 \leq ka \leq 3$

Fig. 6.2.7: Impact of the parameters ρ, V_p and V_s on the intensity of the FFP.

The same comparisons have been done for the Thomsen parameters keeping the velocity V_s in

Figure 6.2.8 as a reference. Apparently, there are not obvious differences between f^*_ϵ, f^*_δ and $f^*_{V_s}$ whereas if we zoom in the interval $ka \in [0.5, 2.2]$, the differences are more evident as illustrated in Figure 6.2.9(a): V_s seems to have the biggest impact, being the weakest one the Thomsen parameter δ. Nevertheless, in interval $ka \in [2.2, 3]$ they behave all similarly, as illustrated in Figure 6.2.9:

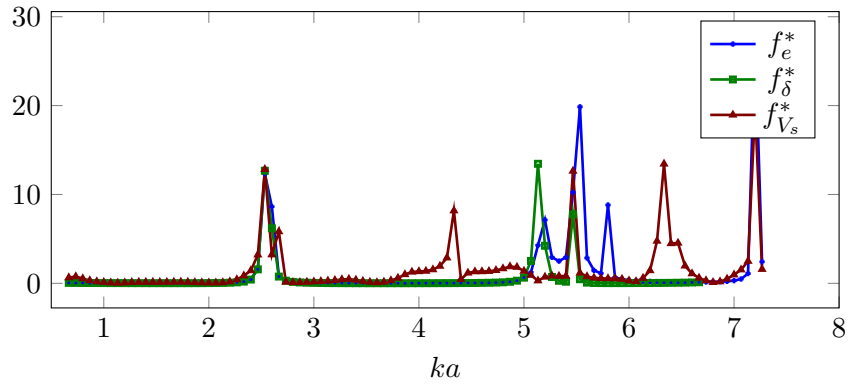

Fig. 6.2.8: Impact of the Thomsen parameters ϵ, δ and the velocity V_s on the intensity of the FFP.

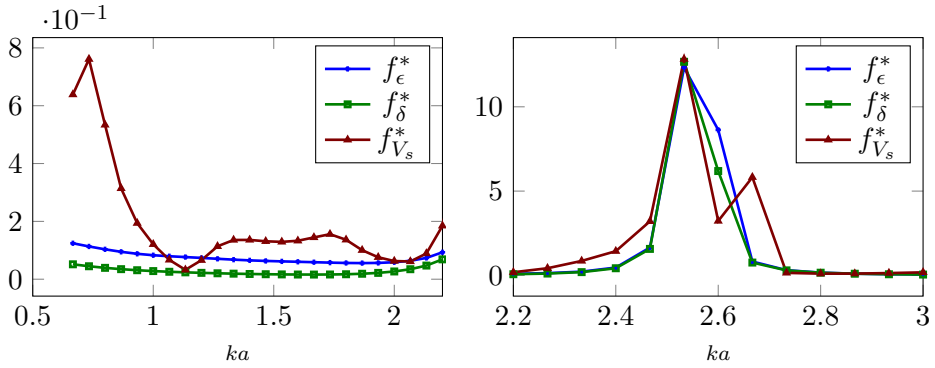

(a) $0.5 \leq ka \leq 2.5$ (b) $2.2 \leq ka \leq 3$

Fig. 6.2.9: Impact of the Thomsen parameters ϵ, δ and the velocity V_s on the intensity of the FFP.

The curves include some peaks which could indicate suitable frequencies for reconstruction since they show a strong impact of the parameter under interest. This is what we have done at first insight and unfortunately, we have been faced to stability issues. This is what happened with $ka = 2.53$. However, when slightly modifying the value of ka, we have obtained good results. This suggests us that $ka = 2.53$ is a Jones mode, explaining the instability we have observed. This justifies we have restricted our numerical study to low frequencies, avoiding then Jones modes.

The main conclusion then is that at low frequencies, the material parameter V_p has the strongest impact. Moreover, we can order the other parameters, starting with the highest influence, as follows: ρ, V_s, ϵ and δ.

6.3 Reconstruction of Material Parameters in the Case of a Circle

In what follows, we introduce the reconstruction of all anisotropic material parameters for a disk shaped scatterer (see Figure 6.3.1). We have seen that in Chapter 3, the reconstruction of the material parameters of isotropic media requires RR being at most $10^{-2}\%$. The weak impact on the FFP

intensity (around 0.1%) visualized in Fig. 6.2.9(a) for material parameters ϵ and δ motivates us to consider that in the case of a full reconstruction of an anisotropic medium involving ϵ and δ also, RR must lower than 10^{-3}%.

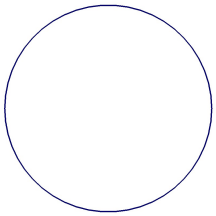

Fig. 6.3.1: Disk shaped scatterer.

The considered computational domain is an elastic circle Ω^s of radius $a = 1$cm surrounded by an acoustic domain Ω_b^f, whose external boundary is a circle of radius $b = 7.5$cm. The density of the fluid is $\rho_f = 1000$ kg m^{-3} (water), while the target and initial guess of the material parameters of the sought-after scatterer Ω^s are detailed in Table 6.2.1. In order to compute the FFP corresponding to the target, we employ the IPDG solver involving fourth-order elements with a mesh discretization defined by seven elements per wavelength, while for the rest of the FFPs we use five elements per wavelength. This reconstruction has been carried out using three normalized frequencies: $ka = 0.53, 1.33$ and 3.33.

The evolution of RR corresponding to $ka = 0.53$ is detailed in Tables 6.3.1(a) and (b). We observe that RR decreases from 7.84% until 0.34% in five iterations, while the error on V_p (resp. V_s) decreases from 100% until 31% (resp. 77%). As expected from the previous section, V_p is the easiest to reconstruct. On the other hand, even if we have tested several regularization parameters, the reconstruction of the density fails. After stagnation, we have decreased the regularization parameters, and the corresponding evolution of RR and the relative errors on the material parameters are depicted in Table 6.3.1(b). We observe that RR reaches a very low value (9.65 10^{-2}%) and we obtain a good reconstruction of V_p (around 3% of error) whereas the we do not reconstruct correctly the other parameters. We have tried several values of the regularization parameters without improving the reconstruction, and consequently we have increased the frequency.

$\#n$	RR	RED	REV_p	REV_s	RE_e	RE_δ
1	7.84	100	48.09	95.79	100	100
2	1.03	100	40.47	95.83	100	100
3	0.75	100	34.74	86.75	100	100
4	0.52	100	30.9	80.4	100	100
5	0.34	100	31.42	77.49	100	100

(a) $\alpha_\rho = 10^2$, $\alpha_{V_p} = 10^{-1}$, $\alpha_{V_s} = 10^1$, $\alpha_e = 10^3$, $\alpha_\delta = 10^4$.

$\#n$	RR	RED	REV_p	REV_s	RE_e	RE_δ
5	0.34	100	31.42	77.49	100	100
6	0.51	100	13.03	52.13	100	100
7	0.1	100	8.12	44.86	100	100
8	$9.65 \cdot 10^{-2}$	100	3.01	27.49	100	100

(b) $\alpha_\rho = 10^0$, $\alpha_{V_p} = 2.5\ 10^{-2}$, $\alpha_{V_s} = 10^{-3}$, $\alpha_e = 10^1$, $\alpha_\delta = 10^2$.

Tab. 6.3.1: Evolution of RR, relative error of all anisotropic material parameters for $ka = 0.53$, noise level=0%.

The second selected normalized frequency is $ka = 1.33$, and the related reconstruction of material parameters together with the evolution of RR are depicted in Table 6.3.2. After several tests, this is the best reconstruction that we have obtained: 1.17% of relative error on the density ρ, which has been quickly reconstructed in 4 iterations, 3% of error on the velocity V_p, which has not been improved, 0.57% of error on V_s, another successful reconstruction, 21.03% of error on the Thomsen parameter ϵ and finally, 100% of error on the Thomsen parameter δ, which is not surprising since it is

the weakest parameter. Here again, we have tried different values of the regularization parameters without any success, so that we have moved on another frequency.

$\#n$	RR	RED	REV_p	REV_s	RE_e	RE_δ
9	0.33	15.91	3.02	12.36	76.59	100.49
10	0.13	10.58	3	12.94	46.57	100.57
11	$4.95 \cdot 10^{-2}$	0.2	3	2.39	27.37	100.66
12	$1.34 \cdot 10^{-2}$	1.17	3	0.57	21.03	100.69

Tab. 6.3.2: Evolution of RR, relative error of all anisotropic material parameters for $ka = 1.33$, $\alpha_\rho = 10^{-8}$, $\alpha_{V_p} = 10^2$, $\alpha_{V_s} = 10^{-5}$, $\alpha_e = 10^{-7}$, $\alpha_\delta = 10^{-5}$, noise level=0%.

The last selected normalized frequency is $ka = 3.33$. We observe that in two iterations we have to stop as RR starts increasing, and the corresponding relative errors are really good except for the Thomsen parameter δ, with 100% of relative error as depicted in Table 6.3.3(a). After these iterations we decrease the regularization parameter corresponding to δ, and the final relative errors are really satisfactory as detailed in Table 6.3.3(b): 1.16% on the density, 0.23% and 0.45% on the velocities V_p and V_s, and finally 1.85% and 5.49% on Thomsen parameters ϵ and δ respectively.

$\#n$	RR	RED	REV_p	REV_s	RE_e	RE_δ
12	$1.34 \cdot 10^{-2}$	1.17	3	0.57	21.03	100.69
13	$8.21 \cdot 10^{-3}$	1.15	2.1	0.57	3.54	100.63
14	$5.59 \cdot 10^{-3}$	1.16	1.86	0.45	0.99	100.69
15	$6.07 \cdot 10^{-3}$	1.16	1.9	0.45	1.31	100.62

(a) $\alpha_\rho = 10^4$, $\alpha_{V_p} = 10^{-2}$, $\alpha_{V_s} = 10^4$, $\alpha_e = 10^{-8}$, $\alpha_\delta = 10^{-5}$.

$\#n$	RR	RED	REV_p	REV_s	RE_e	RE_δ
15	$6.08 \cdot 10^{-3}$	1.16	1.83	0.45	0.39	98.6
16	$5.56 \cdot 10^{-3}$	1.16	1.4	0.45	0.41	45.58
17	$4.65 \cdot 10^{-3}$	1.16	0.87	0.45	0.39	29.77
18	$3.06 \cdot 10^{-3}$	1.16	0.54	0.45	1.13	15.54
19	$2.93 \cdot 10^{-3}$	1.16	0.34	0.45	1.47	9.14
20	$1.47 \cdot 10^{-3}$	1.16	0.23	0.45	1.85	5.49

(b) $\alpha_\rho = 10^4$, $\alpha_{V_p} = 10^{-2}$, $\alpha_{V_s} = 10^4$, $\alpha_e = 10^{-8}$, $\alpha_\delta = 10^{-10}$.

Tab. 6.3.3: Evolution of RR, relative error of all anisotropic material parameters for $ka = 3.33$, noise level=0%.

6.4 Reconstruction of Material Parameters in the Case of a Convex Solid

It is necessary to mention during these experiments a different strategy has been applied to the reconstruction, which consists in increasing the frequency at each iteration. An initial normalized frequency k_1 is set for the first iteration, and for the rest of the iterations the frequency is updated adding a constant value. That is, the frequency for the second iteration is $k_2 = k_1 + \Delta k$. The following expression summarizes the selection of the frequency for the n-th iteration:

$$k_n = k_{n-1} + \Delta k = k_1 + (n-1)\Delta k \tag{6.4.1}$$

We remind that the value of a is defined as $a = s_{min} = \min_{1 \leq i \leq N_\Gamma} s_i$ for elliptic and B-splines parametrizations.

In what follows, we introduce some numerical experiments corresponding to two scatterers: (a) an ellipse and (b) a smooth symmetric solid (see Figures 6.3.1(a) and (b) respectively). The main goal in this subsection is the reconstruction of material parameters.

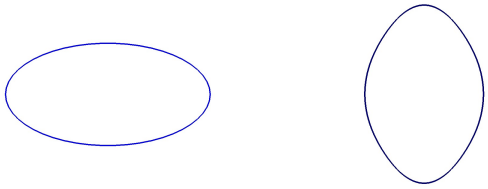

(a) Ellipse (b) Rugby ball

Fig. 6.4.1: Considered scatterers in the reconstruction of anisotropic materials.

6.4.1 Ellipse

The sought-after scatterer Ω^s is made of material parameters that are reported in Table 6.2.1. The wet surface Γ is represented by the following (6.4.2) parametrization:

$$\Gamma = \{(s_1 \cos\theta, s_2 \sin\theta) \quad \theta \in [0, 2\pi]\} \tag{6.4.2}$$

where the shape parameters of the Target are defined as $s_1 = 1$cm and $s_2$cm. The initial frequency is $k_1 a = 0.27$ while the constant difference to update the frequency is $\Delta k a = 0.16$. The radius of the external absorbing boundary is $b = 10$cm. The FFP corresponding to the Target is computed with a fourth-order finite element method with seven points per wavelength while the rest of the numerical FFPs are computed with five points per wavelength.

The fast decrease of the RR depicts the evolution of the relative residual in Table 6.4.1. We observe that accuracy errors decrease slower. At iteration 4 for example, we have errors of 37% on the density and 17% on the velocity V_s, but for V_p, the relative error is 3.78%. The regularization parameters have been kept constant during all iterations $\alpha_\rho = 10^{-7}, \alpha_{V_p} = 10^{-2}$ and $\alpha_{V_s} = 10^{-1}$. We observe that the reconstruction is quite successful. For 5.97 10^{-2} of RR we have final relative errors of 2.82%, 0.38% and 0.38% on the density and velocity parameters V_p and V_s respectively.

In addition, as we have formerly predicted, the material parameter V_p has been easily reconstructed.

#ITER(n)	ka	RR	RED	REV_p	REV_s
1	0.27	23.72	100.86	50.77	102.52
2	0.43	17.89	75.81	44.71	99.81
3	0.6	16.59	47.84	5.88	20.96
4	0.77	5.17	37.87	3.78	17.46
5	0.93	0.33	18.67	3.64	7.94
6	1.1	0.29	9.39	0.45	2.97
7	1.27	0.26	7.81	1.82	2.1
8	1.43	0.3	6.24	1.34	1.65
9	1.6	0.14	4.32	0.93	1.06
10	1.77	$5.97 \cdot 10^{-2}$	2.82	0.38	0.38

Tab. 6.4.1: Evolution of RR, relative error on ρ, V_p and V_s in the ellipse case, with constants values for $\epsilon = 0.2, \delta = 0.1$, noise level=0%.

6.4.2 Smooth-symmetric Solid

In this experiment we consider the B-splines parametrization involving four shape parameters. Even if the shape is similar to the ellipse, the nature is completely different. The computational domain is a smooth-symmetric solid shaped domain (see Figure 6.4.1(b)) parametrized with B-splines (see Appendix C) with the corresponding shape parameters detailed in Table 6.4.2. Target and initial guess corresponding to material parameters are summarized in Table 6.2.1. The radius of the external absorbing boundary is $b = 10$cm. Here also, the FFPs corresponding to the Target is computed with a fourth order finite element method with seven points per wavelength while the rest of the numerical FFP are computed with five points per wavelength.

	s_1	s_2	s_3	s_4
Target (cm)	1.00	1.50	1.00	1.50

Tab. 6.4.2: Shape parameters: target of smooth-symmetric solid scatterer.

We have not found the good frequencies and regularization parameters to stabilize the reconstruction of the material parameters ρ, V_p and V_s. Indeed, we have illustrated an example for $\Delta ka = 0.16$ and $k_1 a = 0.67$, in Table 6.4.3 with the corresponding evolution of RR and the errors on the material parameters ρ, V_p and V_s. The regularization parameters corresponding to the density parameter during these iterations have been $\alpha_\rho = 10^{-1}, 10^{-2}, 10^{-3}, 10^{-4}$ and 10^{-5} (starting from $\alpha_\rho = 10^{-1}$ it has been decreased each two iterations). The regularization parameters corresponding to the velocities V_p and V_s have been updated also each two iterations. These are the respective values: $\alpha_{V_p} = 10^{-2}, 10^{-3}, 10^{-4}, 10^{-5}, 10^{-6}$ and $\alpha_{V_s} = 1, 10^{-3}, 10^{-5}, 10^{7}, 10^{-9}$. We observe that the final relative errors on the material parameters ρ, V_p and V_s are 17.49%, 11.01% and 12.79% respectively, which means that it is not a successful case, but testing different frequencies and regularization parameters may improve the reconstruction.

In addition, we see that the error on V_p has generally lower values that the error of the other parameters.

On the contrary, the considering from the beginning the right values of Thomsen parameters and density, reconstruction of the material parameters V_p and V_s has been successfully carried out in 5 iterations. The decrease of the RR is really fast as depicted in Table 6.4.4, as the evolution of the

#ITER(n)	ka	RR	RED	REV_p	REV_s
1	0.67	14.47	99.02	47.68	79.96
2	0.83	8.49	87.1	80.81	157.14
3	1	2.5	79.9	11.23	41.41
4	1.17	1.14	52.6	38.25	33.39
5	1.33	0.6	30.12	37.75	28.84
6	1.5	0.29	62.29	38.06	38.7
7	1.67	0.46	41.61	27.9	25.39
8	1.83	0.44	28.35	16.66	11.61
9	2	0.41	22.38	6.85	10.17
10	2.17	0.35	17.49	11.01	12.79

Tab. 6.4.3: Evolution of RR, relative error on ρ, V_p and V_s in the smooth-symmetric solid case, with constants values for $\epsilon = 0.2, \delta = 0.1$, noise level=0%.

errors on both material parameters. The regularization parameters have been updated each iteration: $\alpha_{V_p} = 10^{-2}, 10^{-3}, 10^{-4}, 10^{-5}, 10^{-6}$ and $\alpha_{V_s} = 10^{-1}, 10^{-2}, 10^{-3}, 10^{-4}, 10^{-5}$. Final errors are really good: for RR with a value of 1.71 10^{-3}% we have the relative error of 2.33 10^{-4}% and 2.63 10^{-4}% on V_p and V_s respectively.

#iter(n)	ka	RR	REV_p	REV_s
1	0.67	1.92	52.1	84.08
2	0.83	$9.96 \cdot 10^{-2}$	36.37	64.54
3	1	$6.04 \cdot 10^{-2}$	0.43	4.54
4	1.17	$3.62 \cdot 10^{-2}$	0.23	0.36
5	1.33	$1.71 \cdot 10^{-3}$	$2.33 \cdot 10^{-4}$	$2.63 \cdot 10^{-4}$

Tab. 6.4.4: Evolution of RR, relative error on V_p and V_s in the smooth-symmetric solid case, with constant values for $\rho = 1, \epsilon = 0.2, \delta = 0.1$, noise level=0%.

6.5 Recovery of Shape and Material Parameters

The main goal of this section, is to introduce some experiments corresponding to the reconstruction of the shape parameters together with the material parameters ρ, V_p and V_s. Due to the different impact of the material parameters on the intensity of the FFP, we propose the following strategy: during the first stage, we retrieve first the shape parameters and the velocity V_p with the intensity of the far field pattern. Straightaway, we retrieve the material parameters ρ, V_p and V_s with the FFP field.

6.5.1 Ellipse

The computational domain Ω^s is an ellipse-shaped obstacle (see Figure 6.5.1(a)) whose shape parameters are detailed in Table 6.5.1 and material parameters in Table 6.2.1. The radius of the external absorbing boundary is $b = 10$cm, and the FFP corresponding to the Target is computed with a fourth order finite element method with seven points per wavelength while the rest of the numerical FFPs are computed with five points per wavelength.

The normalized frequency selected during Stage 1 is $ka = 0.27$. The evolution of the RR together with the errors corresponding to the shape parameters and material parameter V_p are depicted in Table 6.5.2. The relative residual decreases from a level of 34% until 1.01% in 11 iterations, while the shape error decreases from 31% (see initial guess depicted in Figure 6.5.1(b)) until 3.48 10^{-2}%. Indeed, the final errors of shape and the velocity V_p parameters are respectively 3.48 10^{-2} and 1.9% corresponding to the final value of 1.01% on RR, which is a good reconstruction. The regularization parameters used during this step are $\alpha_s = 1, 10^{-1}, 10^{-2}, 10^{-5}, 10^{-7}$ and $\alpha_{V_p} = 10^{-1}, 10^{-2}$.

In this case, as the reconstruction of shape parameters and the velocity V_p is quite successful, during Stage 2 we only search for the material parameters V_s and ρ. The same normalized frequency has been selected for the Stage 2, and the corresponding evolution of RR_2 together with the errors of V_s and ρ are depicted in Table 6.5.3. The final relative errors are 1.2% and 7.17% on the density ρ and the velocity V_s respectively. The regularization parameters used in this last step are: $\alpha_\rho = 10^{-1}, 10^{-2}, 10^{-3}, 10^{-4}$ and $\alpha_{V_s} = 1, 10^{-2}, 10^{-4}, 10^{-6}$, updated each three iterations.

	s_1	s_2
Target (cm)	1.00	0.50
Initial Guess (cm)	0.75	0.75
Relative Error (%)	25	50

Tab. 6.5.1: Shape parameters: target vs initial guess of ellipse scatterer.

(a) Target (b) Initial Guess

Fig. 6.5.1: Ellipse-shaped domain for target vs. initial guess.

#iter(n)	RR	REV_p	RES
1	34.07	100.1	26.62
2	21.21	76.68	21.92
3	14.06	31.31	17.37
4	11.63	20.16	12.07
5	7.97	18.29	10.45
6	1.73	17.53	7.69
7	1.65	14.17	5.86
8	1.57	7.73	1.31
9	1.01	4.34	0.29
10	1.01	2.58	0.22
11	1.01	1.9	$3.48 \cdot 10^{-2}$

Tab. 6.5.2: Evolution of RR, relative error on V_p and shape parameters in the ellipse case, with constant values for $\epsilon = 0.2, \delta = 0.1$, noise level=0%.

#ITER(n)	RR_2	RED	REV_s
1	0.83	89.87	91.81
2	0.68	68.86	73.45
3	0.22	50.16	68.49
4	0.18	49.48	51.35
5	0.14	42.26	46.54
6	0.11	39.85	38.45
7	$9.32 \cdot 10^{-2}$	38.42	34.06
8	$7.57 \cdot 10^{-2}$	26.42	27.46
9	$7.14 \cdot 10^{-2}$	14.69	26.85
10	$7.02 \cdot 10^{-2}$	5.4	16.5
11	$6.14 \cdot 10^{-2}$	1.2	7.17

Tab. 6.5.3: Evolution of RR_2, relative error on ρ and V_s in the ellipse case, with constant values for $\epsilon = 0.2, \delta = 0.1$, noise level=0%.

6.5.2 Smooth-symmetric Solid

We consider a rugby-ball shaped domain (see Figure 6.5.2(a)) parametrized with B-splines with shape parameters detailed in Table 6.5.4. The Initial Guess corresponding to the shape with a relative error of 43.85% is illustrated in Figure 6.5.2(b) and detailed in Table 6.5.4. The radius of the external absorbing boundary is $b = 10$cm, and the FFP corresponding to the Target is computed with a fourth order finite element method with seven points per wavelength while the numerical FFPs computed from initial guesses and updated parameters, are defined with five points per wavelength.

	s_1	s_2	s_3	s_4
Target (cm)	1.00	1.50	1.00	1.50
Initial Guess (cm)	1.75	1.75	1.75	1.75
Relative Error (%)	75	16.7	75	16.7

Tab. 6.5.4: Shape parameters: target vs initial guess of smooth-symmetric solid scatterer.

(a) Target (b) Initial Guess

Fig. 6.5.2: Smooth-symmetric domain: target vs. initial guess.

For the normalized frequency $ka = 0.67$ RR drops from an initial error around 30% until 0.15% in 12 iterations. This decrease of the errors of shape parameters and the velocity parameter V_p is depicted in Table 6.5.5, which is good: we observe that at iteration 12 the final errors corresponding to 0.15% of the RR are 6.67% and 0.59% on velocity parameter V_p and shape parameters respectively. The regularization parameters used during this procedure are: $\alpha_{V_p} = 10^{-1}, 10^{-2}, 10^{-3}$ while for shape parameters, $\alpha_s = 1, 10^{-1}, 10^{-2}, 10^{-3}, 10^{-4}, 10^{-5}$, updated each two iterations.

In this case we observe that the velocity parameter V_p can be improved, and this is why we proceed retrieving the material parameters ρ, V_s and V_p. In this case, the initial normalized frequency is $ka = 0.67$ and it has been added each iteration the quantity $\Delta k = 0.17$. We observe that the relative residual of the FFP field decreases from a level 0.52% until 8.45 10^{-2}%, and the corresponding final relative errors are 7.95%, 0.73% and 16.68% for the material parameters ρ, V_p and V_s respectively. The regularization parameters used in this last step are: $\alpha_\rho = 1, 10^{-1}, 10^{-2}, 10^{-3}$ and $\alpha_{V_s} = 1, 10^{-2}, 10^{-4}, 10^{-6}$, updated each two iterations, while $\alpha_{V_p} = 10^{-3}$ is constant. We conclude that the reconstruction is good but it can be improved.

6.6 Conclusion and Perspectives

One purpose for the future is to optimize these experiments exploiting all different strategies that we have developed with other experiments. The first goal is to reduce the number of frequencies.

#iter(n)	RR	REV_p	RES
1	30.62	101.14	40.18
2	6.22	103.65	19.95
3	1.76	103.17	14.14
4	1.53	101.54	15.88
5	1.23	93.97	13.35
6	1.06	81.28	11.43
7	0.68	24.37	9.42
8	0.43	24.14	0.22
9	0.36	23.19	0.58
10	0.27	21.73	1.01
11	0.18	9.55	1.57
12	0.15	6.62	0.59

Tab. 6.5.5: Evolution of RR, relative error on V_p and shape parameters in the smooth-symmetric solid case, with constant values for $\epsilon = 0.2, \delta = 0.1$, noise level=0%.

#ITER(n)	ka	RR_2	RED	REV_p	REV_s
1	0.67	0.51	89.74	7.82	62.08
2	0.83	0.48	66.84	6.76	44.2
3	1	0.35	57.87	2.37	31.39
4	1.17	0.27	47.66	1.47	13.93
5	1.33	0.18	31.34	0.99	20.34
6	1.5	0.14	15.08	0.82	17.66
7	1.67	0.11	9.03	0.94	11.72
8	1.83	$8.45 \cdot 10^{-2}$	7.95	0.73	16.68

Tab. 6.5.6: Evolution of RR_2, relative error on ρ, V_p and V_s in the smooth-symmetric solid case, with constant values for $\epsilon = 0.2, \delta = 0.1$, noise level=0%.

To this end, it is necessary to study and exploit as much as possible each frequency with different regularization parameters. This is an ongoing work.

General Conclusion

We have developed a procedure to reconstruct the shape and material parameters of an elastic obstacle immersed in a fluid medium from some external measurements given by the so called far-field pattern. Most of the experiments have been realized by using only one incident wave and by considering a solid composed of an isotropic medium. It is a nonlinear and ill-posed problem which is solved by applying a Newton-like iterative method involving the Fréchet derivatives of the scattered field. These derivatives express the sensitivity of the scattered field with respect to the parameters of interest. They are defined as the solution of boundary value problems which differ from the direct one only at the right-hand sides level. We have been able to establish the well-posedness of each problem in the case of a regular obstacle and it would be interesting in the near future to extend those results to the case of scatterers with polygonal boundaries. It requires to work with less regular Sobolev spaces for which the definition of traces is not obvious. We have also provided an analytical representation of the Fréchet derivatives in the case of a circle. This provide a way of validating the numerical experiments and it would be interesting to obtain their expression in the case of elliptical scatterers or spherical ones. It is worth mentioning that this work has been done only in the case of isotropic media and it would be interesting to extend it to anisotropic media as well. It requires to establish analytic representations of the scattered field in anisotropic media which is more difficult because it involves more parameters.

We have studied the response of the data to the different parameters. It turns out that the sensitivity of the far field pattern is very different regarding the shape or the material parameters. We have delivered a sensitivity analysis which has been essential for understanding that the reconstruction of the material parameters is conditioned by the recovering of the shape parameters. This makes the full reconstruction very difficult and sometimes unstable. In particular, in the case of a disk-shaped obstacle, when addressing the role of the frequency in the reconstruction, we have been faced to the issue of the existence of Jones modes which had been already observed by Elodie Estecahandy in her PhD thesis.

Next, we have introduced a series of numerical experiments that have been performed by applying two algorithms which propose two strategies of full reconstruction regarding the material parameters are retrieved simultaneously with the shape or not. It turns out that both work similarly delivering the same level of accuracy but the simultaneous reconstruction requires less iterations. We have thus opted for retrieving all the parameters simultaneously.

Since realistic configurations include noisy data, we have performed some simulations for the reconstruction of the shape along with the Lamé coefficients for different noise levels. Other interesting experiments have been carried out using a multistage procedure where the parameters of interest are the density of the solid interior, the shape of the obstacle and its position. We have considered the case of Limited Aperture Data in back-scattering configurations, using multiple incident plane waves, mimicing a physical disposal of non-destructive testing. This is an encouraging ongoing work which deserves to be completed by considering a wide range of examples including more general geometries of the scatterer. It should also be extended by dealing with limited aperture data using only one incident wave (which will probably require multiple frequency data).

Our solution methodology turns out to be very promising for isotropic media as illustrated by an example where we have been able to retrieve the Lamé coefficients, the density, the shape and location parameters from both noise-free and noisy data.

The last chapter provides some investigations on anisotropic media. This is a very challenging case which still deserves further works. We have obtained some results but since the impact of some of the anisotropic parameters on the FFP is even weaker than the Lamé coefficients, the reconstruction of these parameters together with the shape parameters requires several frequencies and carefully adapted regularization parameters. It is in particular difficult to retrieve the Thomsen parameters ϵ and δ because their reconstruction requires to have an accurate adjustment on the rest of material and shape parameters. The recovery process is thus computationally intensive and some efforts should be done in the near future to decrease the computational costs. We were able to recover all the anisotropic parameters when the shape were assumed to be known. However, when trying to recover both shape and material parameters, we could only recover the shape and some of the physical parameters (namely the three most important ones : the density and the two velocities V_p and V_s). We should now find a way to determine all the Thomsen parameters together with the shape. Then, we will have to deal with more complex media such as TTI media (this will add the angle of anisotropy as additional parameter). The last step will be to consider general anisotropy, which could be done by recovering each element of the elastic stiffness tensor. This is simple to implement, since the derivative of the stiffness tensor with respect to one of its component is easily computable (it is a tensor composed of zeroes and ones). However, the stability of the reconstruction is not guaranteed, since we will strongly increase the number of components to be retrieved.

Regarding what has been done in this thesis, there are some works that we would like to do in the near future. First, in the team, we have developed a numerical software package performing Full Waveform Inversion for geophysical applications and based on the adjoint method. We plan to make simulations to compare the performances of the approach. In particular, we would like to see how the FWI performs in the case where we had difficulties to regularize the method. Indeed, our approach delivers a high level of accuracy but it depends on regularization parameters that may be very tricky to choose. In that spirit a recent work by Grote, Kray and Nahum [47] kept our attention. The inverse Helmholtz problem is solved by using an inexact truncated Newton method and the parameter of interest is the propagation velocity. Unlike standard constant piecewise representation of the velocity, a particular eigenfunction basis is used and updated at each iteration. It brings regularity into the solution process and by this way there is no need of using Tikhonov regularization. We would like to explore that lead, the question being its feasibility when searching for several parameters.

A natural continuation of this work could be to address three dimensional problems. This is not that obvious due to the corresponding computational burden which should be very large in the 3D case. In particular, the necessity of remeshing the surface of the scatterer hampers significantly the reconstruction process. Using mesh deformation techniques could be helpful and is being explored in the team Magique-3D. Obviously, the solution of the direct problem is computationally intensive and any effort that could decrease the computational cost is welcome. A makeshift solution could be to replace the solid by an equivalent boundary condition depending on parameters containing information on the interior of the solid. We could then apply our solution methodology for retrieving both the shape and the impedance parameters.

Appendix A

Far-field Pattern

The characterization of the 2D analytic far-field pattern p_∞ for p pressure field solution to **BVP 0**, we can follow the methodology of [28]. The expression of the outgoing scattered pressure field in infinite domain is also depicted in [18, 40]. We first consider the pressure field solution to **BVP 0**:

$$p = \sum_{n=0}^{+\infty} A_n \, H_n^{(1)}(kr) cos(n\theta) \qquad a \leq r, \quad \theta \in [0, 2\pi), \tag{A.0.1}$$

where the coefficients A_n satisfy:

$$A_n \, H_n^{(1)}(kr) = \int_{C^1} p(r\hat{x}) \overline{cos(n\theta)} d\hat{x}. \tag{A.0.2}$$

In addition, for large radius, the Hankel functions have the following asymptotic behavior [28]:

$$H_n^{(1)}(kr) \backsim \sqrt{\frac{2}{k\pi r}} e^{i(kr - n\pi/2 - \pi/4)} \tag{A.0.3}$$

Nonetheless, due to the fact that the asymptotic behavior of Eq. A.0.3 does not hold uniformly in n, we can not take the limit for $r \to +\infty$ in order to compute the far-field pattern of the pressure field. Moreover, as the far-field pattern is an analytic function [28], the FFP p_∞ admits the following expression:

$$p_\infty(\hat{x}) = \sum_n \tilde{A}_n \, cos(n\theta), \tag{A.0.4}$$

where $\tilde{A}_n$ are coefficients given by:

$$\tilde{A}_n \, = \int_{C^1} p_\infty(\hat{x}) \overline{cos(n\theta)} d\hat{x}. \tag{A.0.5}$$

for $\hat{x} = \frac{x}{\|x\|_2}$. We recall the asymptotic behavior of the FFP [28]:

$$p(x) = \frac{e^{ikr}}{\sqrt{r}} \left(p_\infty \left(\frac{x}{r} \right) + \mathcal{O} \left(\frac{x}{r} \right) \right) \qquad , \qquad r = \|x\|_2 \longrightarrow +\infty \tag{A.0.6}$$

From Eq. A.0.6, the FFP has the following behavior:

$$p_\infty(\hat{x}) = \lim_{r \to +\infty} \sqrt{r} e^{-ikr} p(r\hat{x}). \tag{A.0.7}$$

As a consequence, replacing first Eq. A.0.7 and then Eq. A.0.2 in Eq. A.0.5, we get:

$$\begin{aligned}\tilde{A}_n &= \int_{C^1} \lim_{r\to+\infty} \sqrt{r} e^{-ikr} p(r\hat{x}) \overline{cos(n\theta)} d\hat{x} \\ &= \lim_{r\to+\infty} \sqrt{r} e^{-ikr} \int_{C^1} p(r\hat{x}) \overline{cos(n\theta)} d\hat{x} \\ &= \lim_{r\to+\infty} \sqrt{r} e^{-ikr} A_n \, H_n^{(1)}(kr).\end{aligned}$$

Consequently, we obtain that:

$$\tilde{A}_n = \sqrt{\frac{2}{k\pi}} \frac{e^{i\pi/4}}{i^{n+1}} A_n \tag{A.0.8}$$

Finally, we deduce that the analytical expression of the FFP Fréchet derivative can be formulated as follows:

$$p_\infty(\hat{x}) = \sum_n \sqrt{\frac{2}{k\pi}} \frac{e^{i\pi/4}}{i^{n+1}} A_n cos(n\theta) \tag{A.0.9}$$

where the coefficients A_n are given by Eq. A.0.1.

Appendix B

Fredholm Alternative Theorem

For completeness purpose, we introduce the abstract formulation of the Fredholm alternative, a standard result that can be found easily in functional analysis textbooks [95, 80].

Let T be a compact linear operator on $\mathbf{H}$. Then, we have the Fredholm alternative:

Theorem 3.

(a) *$ker(I-T)$ is a finite dimensional subspace of $\mathbf{H}$.*

(b) *$Im(I-T)$ is closed in $\mathbf{H}$ and $Im(I-T) = ker(I-T^*)^{\perp}$ where T^* denotes the adjoint of T in $\mathbf{H}$ and $\perp$ denotes the orthogonal in $\mathbf{H}$.*

(c) *$ker(I-T) = \{0\} \iff Im(I-T) = \mathbf{H}$.*

(d) *$dim\ ker(I-T) = dim\ ker(I-T^*)$* □

The Fredholm alternative says in particular that for any compact operator T, if $I-T$ is a one -to-one map, $I-T$ is a surjection and conversely. There exists another way for formulating the Fredholm alternative. It consists in working with the variational formulation of the problem [59].

Proposition 7. *Let $\mathbf{H}$ be a Hilbert space, and let a be a sesquilinear form. We consider the variational problem:*

$$\begin{cases} \text{Find } s \in \mathbf{H}, \text{ such that} \\ \\ a(s,t) = l(t), \qquad \text{for any } t \in \mathbf{H}, \end{cases} \tag{B.0.1}$$

Let W be a Hilbert space such that $\mathbf{H} \subset W$ with a compact embedding. If a satisfies the following Gårding's inequality

$$\begin{aligned} &\text{There exist } c > 0 \text{ and } \alpha > 0 \text{ such that} \\ &\Re\left[a(t,t)\right] + c \parallel t \parallel_W^2 \geq \alpha \parallel t \parallel_H^2 \qquad \forall t \in \mathbf{H} \end{aligned} \tag{B.0.2}$$

then a corresponds to a Fredholm operator.

According to the previous proposition, we thus have:

(a) either the variational problem admits a single solution in $\mathbf{H}$.

(b) or the corresponding equation with $l(t) = 0$ admits a finite number of solutions.

Appendix C

Parametrization of the Solid

The goal of this Appendix is to detail the different parametrizations that we have used to consider the reconstruction of distinct scatterers.

C.1 Parametrization of the Shape

We consider a flexible set of parameters as $s_1, ..., s_{N_\Gamma}$, N_Γ being the number of shape parameters. In what follows, we define different geometries of the obstacle : first a circle, then an ellipse, a polygon, and finally a smooth geometry parametrized by B-splines or Fourier series. In this section, we assume that the solid is centered at the origin.

In the following, we describe the various parametrizations we have considered.

C.1.1 Circular Object

When the scaterrer is a disk shaped obstacle, we parametrize its boundary thanks to it radius s_1:

$$\Gamma = \{s_1(\cos\theta, \sin\theta) \quad \theta \in [0, 2\pi]\}$$

C.1.2 Elliptic Object

In the case of the ellipse, the shape parameters correspond to two different radius denoted by s_1 and s_2:

$$\Gamma = \{(s_1\cos\theta, s_2\sin\theta) \quad \theta \in [0, 2\pi]\} \tag{C.1.1}$$

C.1.3 Polygonal Shaped Object

In the case of polygonal shaped object, we parametrize the shape Γ by means of N_Γ vertices $X_j = s_j \begin{pmatrix} \cos\theta_j \\ \sin\theta_j \end{pmatrix}$, $j = 1, ..., N_\Gamma$, uniformly distributed in the polar coordinate angle.

For each face S_j of the polygon, we use a linear interpolation as follows:

$$S_j(t) = (1-t)X_j + tX_{j+1} \quad t \in [0,1], \quad j = 1, ..., N_\Gamma \tag{C.1.2}$$

with $X_{N_\Gamma+1} = X_1$. This can be rewritten under the matricial form:

$$S_j(t) = (t \quad 1) \begin{pmatrix} -1 & 1 \\ 1 & 0 \end{pmatrix} \begin{pmatrix} X_j \\ X_{j+1} \end{pmatrix}. \tag{C.1.3}$$

Therefore, we have:

$$\Gamma = \{S_j(t), \quad t \in [0,1], j = 1, ..., N_\Gamma\} \tag{C.1.4}$$

The shape is entirely defined by the N_Γ parameters s_j, $j = 1, ..., N_\Gamma$, so that it can be written as follows:

$$\Gamma = \left\{ \sum_{j=1}^{N_\Gamma} s_j \phi_j(t) \begin{pmatrix} cos\theta_j \\ sin\theta_j \end{pmatrix}, \quad t \in [0, N_\Gamma] \right\}$$

For $j \neq 1$ we have

$$\phi_j(t) = \begin{cases} t - j + 1 & \text{if} \quad j - 2 \leq t \leq j - 1 \\ j - t & \text{if} \quad j - 1 \leq t \leq j \\ 0 & \text{otherwise} \end{cases}$$

$$\phi_1(t) = \begin{cases} t - N_\Gamma + 1 & \text{if} \quad N_\Gamma - 1 \leq t \leq N_\Gamma \\ 1 - t & \text{if} \quad 0 \leq t \leq 1 \\ 0 & \text{otherwise} \end{cases}$$

The negative point of selecting this parametrization is that requires *a priori* information about the number of shape parameters. We can not consider Initial Guess with null values representing a variable set of shape parameters.

C.1.4 B-spline Representation

In the case of curved scatterers, we consider two different parametrizations. The first one is based on the use of quadratic B-splines [92]. To that effect, we parametrize the shape Γ by means of N_Γ vertices $X_j = s_j \begin{pmatrix} cos\theta_j \\ sin\theta_j \end{pmatrix}$, $j = 1, ..., N_\Gamma$, uniformly distributed in the polar coordinate angle.

Then, the j^{th} B-spline of degree 2 denoted by S_j is the parametric curve defined as follows:

$$S_j(t) = \frac{1}{2}\left[(t^2 - 2t + 1)X_{j-1} + (-2t^2 + 2t + 1)X_j + t^2 X_{j+1}\right] \quad t \in [0, 1], j = 1, ..., N$$

with $X_{N+1} = X_1$ and $X_0 = X_{N_\Gamma}$. This can be rewritten under the matricial form:

$$S_j(t) = \frac{1}{2}\begin{pmatrix} t^2 & t & 1 \end{pmatrix} \begin{pmatrix} 1 & -2 & 1 \\ -2 & 2 & 0 \\ 1 & 1 & 0 \end{pmatrix} \begin{pmatrix} X_{j-1} \\ X_j \\ X_{j+1} \end{pmatrix}$$

Therefore, we have:

$$\Gamma = \{ S_j(t), \quad t \in [0, 1], j = 1, ..., _{N_\Gamma} \} \tag{C.1.5}$$

The shape is entirely defined by the N radii s_j, $j = 1, ..., _{N_\Gamma}$, so that it can be written as follows:

$$\Gamma = \left\{ \sum_{j=1}^{N} s_j \phi_j(t) \begin{pmatrix} cos\theta_j \\ sin\theta_j \end{pmatrix}, \quad s \in [0, N] \right\}$$

For $j \neq 1$ and $j \neq N_\Gamma$,

$$\phi_j(t) = \frac{1}{2} \begin{cases} t^2 + j^2 + 1 - 2tj + 2t & \text{if} \quad j - 2 \leq t \leq j - 1 \\ -2t^2 - 2j^2 + 4tj - 2t - 2j + 1 & \text{if} \quad j - 1 \leq t \leq j \\ t^2 + j^2 - 2tj + 2j & \text{if} \quad j \leq t \leq j + 1 \\ 0 & \text{otherwise} \end{cases}$$

while,

$$\phi_1(t) = \begin{cases} t^2+2 & \text{if} \quad N_\Gamma - 1 \le t \le N_\Gamma \\ -2t^2+2t+3 & \text{if} \quad 0 \le t \le 1 \\ t^2-2t+3 & \text{if} \quad 1 \le t \le 2 \\ 0 & \text{otherwise} \end{cases}$$

$$\phi_{N_\Gamma}(t) = \frac{1}{2} \begin{cases} t^2+N_\Gamma^2+1-2tN_\Gamma+2t & \text{if} \quad N_\Gamma - 2 \le t \le N_\Gamma - 1 \\ -2t^2-2j^2+4tj-2t-2j+1 & \text{if} \quad N_\Gamma - 1 \le t \le N_\Gamma \\ t^2+j^2-2tj+2j & \text{if} \quad 0 \le t \le 1 \\ 0 & \text{otherwise} \end{cases}$$

In this case too, the number of shape parameters is known before the reconstruction of the obstacle.

C.1.5 Fourier Series Representation

The second option we choose for parametrization of curved scatterers is the use of Fourier series. This class of domains belongs to the well-known star-like domains. Using polar coordinates, the shape can be parametrized as follows:

$$\Gamma = \{r(\theta) \begin{pmatrix} cos\theta \\ sin\theta \end{pmatrix}, \quad \theta \in [0, 2\pi)\} \tag{C.1.6}$$

where r represent the polar radius. We approximate r by its truncated Fourier series as follows:

$$r^M = a_0 + \sum_{k=1}^{M} b_k cos(k\theta) + c_k sin(k\theta) \tag{C.1.7}$$

In this case, the shape is entirely defined by the $N_\Gamma = 2M+1$ coefficients: a_0, $b_j \quad j = 1, ..., M$, and $c_j \quad j = 1, ..., M$,so that we have:

$$\Gamma = \{\sum_{k=1}^{M} s_j \phi_j(\theta) \begin{pmatrix} cos\theta \\ sin\theta \end{pmatrix}, \quad \theta \in [0, 2\pi)\} \tag{C.1.8}$$

where $s_1 = a_0, s_{2k} = b_k, s_{2k+1} = c_k$ for $k = 1, ..., M$ and

$$\begin{aligned} \phi_1(\theta) &= 1 \\ \phi_{2k}(\theta) &= cos(k\theta) \\ \phi_{2k+1}(\theta) &= sin(k\theta), \quad k = 1, ..., M \end{aligned}$$

C.2 Location Parameters

The pair of parameters denoted as (x_c, y_c) represents the reference point of the obstacle, as illustrated in Figure C.2.1, for a disk shaped scatterer. We define them as position parameters x_c, y_c, but it is worth mentioning that x_c, y_c can be considered as shape parameters, as they can be added

in the different parametrizations without any difficulty. For example, in the case of a disk shaped obstacle, the generalized parametrization can be introduced as:

$$\Gamma = \{(x_c, y_c) \quad + \quad s_1(\cos\theta, \sin\theta) \quad \theta \in [0, 2\pi]\}$$

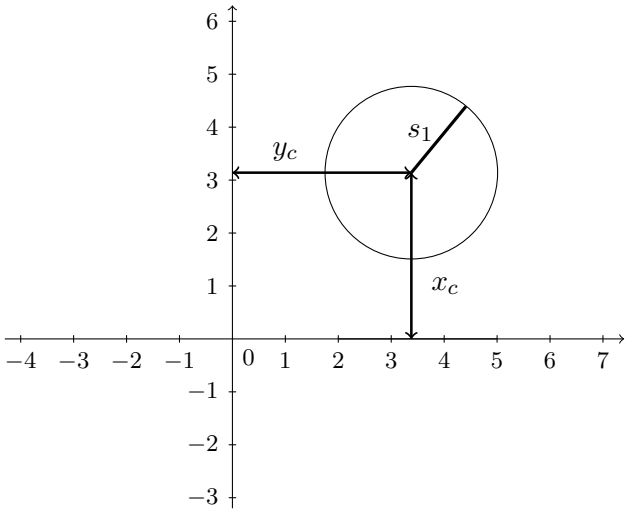

Fig. C.2.1: The position parameters (x_c, y_c) illustrated for the disk shaped scatter of radius s_1.

In addition, in order to characterize the Fréchet derivatives with respect to the location , we use **(BVP 2)** with the corresponding directions:

$$h_1 = \frac{\partial \Gamma}{\partial x_c} = \overrightarrow{e_1}$$
$$h_2 = \frac{\partial \Gamma}{\partial y_c} = \overrightarrow{e_2}$$

(x_c, y_c) denoting the coordinates of the reference point of location.

Ivanyshyn and Kress [63] have proposed a strategy which is based on first retrieving the shape using the intensity of the far field pattern $\|p_\infty\|^2 = \bar{p}_\infty p_\infty$, and straightaway, retrieving the location. We will use the the far field pattern p_∞ to retrieve the location of the immersed object.

C.3 Parametrization of the Material Properties

In what follows, we introduce different set of material parameters with the corresponding material properties.

C.3.1 Isotropic Material Parameters

We remind that when the scatterer is an isotropic medium, from [67], we know that the elastic-tensor can be defined by the Lamé coefficients λ and μ (see (1.1.2) in Chapter 1), corresponding to the Poisson coefficient and Young modulus respectively. These material parameters together with the density ρ_s can define the velocities V_p and V_s, as

$$V_p = \sqrt{\frac{\lambda + 2\mu}{\rho_s}} \qquad V_s = \sqrt{\frac{\lambda}{\rho_s}} \tag{C.3.1}$$

so that isotropic material scatteres can be reconstructed considering the pair of velocities. In this case, the matrix corresponding to the elastic tensor is usually defined as

$$C_{iso} = \begin{pmatrix} c_{11} & c_{11} - 2c_{66} & 0 \\ c_{11} - 2c_{66} & c_{11} & 0 \\ 0 & 0 & c_{66} \end{pmatrix},$$

where $c_{11} = \rho V_p^2$ and $c_{66} = \rho V_s^2$.

For the sake of simplicity, we consider λ, μ, ρ as a set of parameters concerning to isotropic materials.

We remind that The Fréchet derivative with respect to Lamé parameters can be characterized as a solution of **(BVP 3-4)** defining properly the derivative of the tensor C (see section 2 of Chapter II). For the sake of simplicity, we denote by ∂C the derivative of this tensor with respect to the different parameters. Indeed, in the case of λ, it would be defined as

$$\partial C = \partial_\lambda C = \begin{pmatrix} 1 & 1 & 0 \\ 1 & 1 & 0 \\ 0 & 0 & 0 \end{pmatrix}, \tag{C.3.2}$$

while, ∂C is defined as follows when deriving C with respect to μ:

$$\partial C = \partial_\mu C = \begin{pmatrix} 2 & 0 & 0 \\ 0 & 2 & 0 \\ 0 & 0 & 1 \end{pmatrix}. \tag{C.3.3}$$

C.3.2 Anisotropic Material Parameters

In a geological layer, the speed of waves is in general non uniform in all the directions, and the distribution of wave fronts admits two orthogonal symmetry plans. This is the definition of orthotropy. The anisotropy of surface is considered orthotropic in one direction, which means that the wave front admits a symmetry with respect to one of the reference axes. This is the definition of Transverse Isotropy. In our case, we consider Vertical Transverse Isotropy (VTI) media. In that case, the matrix of elasticity can be described as follows:

$$C_{VTI} = \begin{pmatrix} c_{11} & c_{12} & 0 \\ c_{21} & c_{22} & 0 \\ 0 & 0 & c_{33} \end{pmatrix},$$

where the entries are defined by the material parameters such as the density ρ, the velocities V_p, V_s and Thomsen parameters ϵ, δ in the following way:

- $c_{11} = \rho V_p^2(1 + 2\epsilon)$,
- $c_{22} = \rho V_p^2$,
- $c_{33} = \rho V_s^2$,
- $c_{12} = c_{21} = \rho\sqrt{(V_p^2 - V_s^2)^2 + 2V_p^2\delta(^2_p - V_s^2)} - \rho V_s^2$.

This set of parameters that describes the anisotropic media tensor is described in [100].

Following the same strategy as in previous subsection, we introduce the derivatives of the tensor with respect to the anisotropic material parameters. In order to simplify the expression of the derivatives of the matrix, we adopt the generic notation ∂C to designate the derivative of C with respect to

each parameter:

$$\partial C = \begin{pmatrix} \partial c_{11} & \partial c_{12} & 0 \\ \partial c_{21} & \partial c_{22} & 0 \\ 0 & 0 & \partial c_{33} \end{pmatrix}. \tag{C.3.4}$$

The matrix corresponding to the derivative with respect to V_p, is $\partial_{V_p} C$ with entries:

- $\partial c_{11} = 2\rho V_p(1 + 2\epsilon)$,
- $\partial c_{22} = 2\rho V_p$,
- $\partial c_{12} = \partial c_{21} = \rho(4V_p(V_p^2 - V_s^2)(1 + \delta) + 4V_p^3\delta)/(2\sqrt{(V_p^2 - V_s^2)^2 + 2V_p^2\delta(V_p^2 - V_s^2)})$,
- $\partial c_{13} = \partial c_{31} = \partial c_{23} = \partial c_{32} = \partial c_{33} = 0$.

The matrix corresponding to the derivative with respect to V_s is $\partial_{V_s} C$ and is defined by:

- $\partial c_{33} = 2\rho V_s$,
- $\partial c_{12} = \partial c_{21} = \rho(-4V_s(V_p^2 - V_s^2) - 4\delta V_p^2 V_s)/(2\sqrt{(V_p^2 - V_s^2)^2 + 2V_p^2\delta(V_p^2 - V_s^2)}) - 2\rho V_s$,
- $\partial c_{11} = \partial c_{22} = \partial c_{13} = \partial c_{31} = \partial c_{23} = \partial c_{32} = 0$.

The matrix corresponding to the derivative with respect to ϵ, is $\partial_\epsilon C$:

- $\partial c_{11} = 2\rho V_p^2$,
- $\partial c_{ij} = 0$ all others.

The matrix corresponding to the derivative with respect to δ, is $\partial_\delta C$:

- $\partial c_{13} = \partial c_{31} = \rho V_p^2(V_p^2 - V_s^2)/\sqrt{(V_p^2 - V_s^2)^2 + 2V_p^2\delta(V_p^2 - V_s^2)}$,
- $\partial c_{ij} = 0$ all others.

Appendix D

Invariance of FFP intensity with respect to the location

The main goal of this section is to remind the prove of that the intensity of the FFP is invariant with respect to the location of the scatterer, as demonstrated in [28]. Now we consider a shifted scatterer denoted by $\Omega_z^s = \{x = z + y : y \in \Omega^s\}$, translated with the vector $z \in \mathbb{R}^2$, and its boundary $\Gamma_z = \{x = z + y : y \in \Gamma\}$. From *Lemma* 1 we know that the surface solutions $p_{z+\Gamma}$ and $\frac{\partial p_{z+\Gamma}}{\partial \nu}$ satisfy the following equalities:

$$p_{z+\Gamma} = e^{ikz\cdot d} p, \qquad \frac{\partial p_{z+\Gamma}}{\partial \nu} = e^{ikz\cdot d} \frac{\partial p}{\partial \nu} \tag{D.0.1}$$

From Eq. 3.1.2, we have that far field patter of the scatterer Ω^s is given by:

$$p_\infty(\hat{x}) = \frac{e^{i\pi/4}}{\sqrt{8\pi k}} \int_\Gamma e^{-ik\hat{x}\cdot y} \left(\frac{\partial p}{\partial \nu}(y) + ik\hat{x} \cdot \nu p(y) \right) d\Gamma \tag{D.0.2}$$

Therefore, using D.0.1, the far field patterns of Ω_z^s is given by:

$$p_{\infty, z+\Gamma}(\hat{x}) = \frac{e^{i\pi/4}}{\sqrt{8\pi k}} \int_{z+\Gamma} e^{-ik\hat{x}\cdot q} \left(\frac{\partial p_{z+\Gamma}}{\partial \nu}(q) + ik\hat{x} \cdot \nu p_{z+\Gamma}(q) \right) d\Gamma \tag{D.0.3}$$

$$= \frac{e^{i\pi/4}}{\sqrt{8\pi k}} e^{ikz\cdot d} \int_\Gamma e^{-ik\hat{x}\cdot y} \left(\frac{\partial p}{\partial \nu}(y) + ik\hat{x} \cdot \nu p(y) \right) d\Gamma = e^{ikz\cdot d} p_\infty(\hat{x}) \tag{D.0.4}$$

for $y = q - z$. Consequently, we have that $\mid p_{\infty, z+\Gamma}(\hat{x}) \mid = \mid e^{ikz\cdot d} p_\infty(\hat{x}) \mid = \mid p_\infty(\hat{x}) \mid$, i.e. the FFP intensity is invariant under translation of the scatterer.

Lemma 1. *Let (p, u) be solution to **BVP 1**. If we denote by (p_T, u_T) the solution to **BVP**$_T$ defined as*

$$\boldsymbol{BVP}_T \quad \begin{cases} \nabla \cdot \sigma(u) + \omega^2 \rho_s u = 0 & \text{in } z + \Omega^s \quad \text{(a)} \\ \Delta p + k^2 p = 0 & \text{in } z + \Omega_b^f \quad \text{(b)} \\ \tau(u) = -p\nu - p^{inc}\nu & \text{on } z + \Gamma \quad \text{(c)} \\ \omega^2 \rho_f u \cdot \nu = \frac{\partial p}{\partial \nu} + \frac{\partial p^{inc}}{\partial \nu} & \text{on } z + \Gamma \quad \text{(d)} \\ \frac{\partial p}{\partial \nu} = Bp & \text{on } z + \Sigma \quad \text{(e)} \end{cases}$$

we then have the following equality:

$$p_T(z + y) = e^{ikz\cdot d} p(y) \quad \forall y \in \Omega_b^f \quad \text{and} \quad u_T(z + y) = e^{ikz\cdot d} u(y) \quad \forall y \in \Omega^s. \tag{6.0.5}$$

Proof: We first apply the change of variable $y = x - z$ to $\boldsymbol{BVP}_T$:

$$\boldsymbol{BVP}_T \quad \begin{cases} \nabla \cdot \sigma(u) + \omega^2 \rho_s u = 0 & \text{in } \Omega^s \quad \text{(a)} \\ \Delta p + k^2 p = 0 & \text{in } \Omega_b^f \quad \text{(b)} \\ \tau(u) = -p\nu - e^{ikz\cdot d} e^{iky\cdot d}\nu & \text{on } \Gamma \quad \text{(c)} \\ \omega^2 \rho_f u \cdot \nu = \frac{\partial p}{\partial \nu} + e^{ikz\cdot d}\frac{\partial}{\partial \nu}[e^{iky\cdot d}] & \text{on } \Gamma \quad \text{(d)} \\ \frac{\partial p}{\partial \nu} = Bp & \text{on } \Sigma \quad \text{(e)} \end{cases}$$

*as $p^{inc} = e^{ikx\cdot d} = e^{ikz\cdot d}e^{iky\cdot d}$ and $\frac{\partial p^{inc}}{\partial \nu} = e^{ikz\cdot d}\frac{\partial}{\partial \nu}[e^{iky\cdot d}]$. Now, for (p,u) solution to **BVP 1**, we denote the solution pair $(e^{ikz\cdot d}p, e^{ikz\cdot d}u)$ by $(\mathfrak{z}p, \mathfrak{z}u)$. We want to see that $(\mathfrak{z}p, \mathfrak{z}u)$ is solution to $\boldsymbol{BVP}_T$.*

As $\mathfrak{z}$ is a constant, $\nabla(\mathfrak{z}u) = \mathfrak{z}\nabla u \Rightarrow \varepsilon(\mathfrak{z}u) = \mathfrak{z}\varepsilon(u) \Rightarrow \sigma(\mathfrak{z}u) = \mathfrak{z}\sigma(u) \Rightarrow \nabla\cdot\sigma(\mathfrak{z}u) = \mathfrak{z}\nabla\cdot\sigma(u)$. Consequently,

$$\nabla \cdot \sigma(\mathfrak{z}u) + \omega^2 \rho_s \mathfrak{z}u = \mathfrak{z}(\nabla \cdot \sigma(u) + \omega^2 \rho_s u) = 0 \tag{6.0.6}$$

*as u is a solution component to **BVP 1**. We proceed similarly with $\mathfrak{z}p$ to see that satisfy Eqs. $\boldsymbol{BVP}_T$(b) and (e). Straightaway, we prove that $(\mathfrak{z}p, \mathfrak{z}u)$ satisfies the transmission condition $\boldsymbol{BVP}_T$(c). We have that*

$$\tau(\mathfrak{z}u) = \mathfrak{z}\tau(u) = -\mathfrak{z}p\nu - e^{ikz\cdot d}e^{iky\cdot d}\nu \Rightarrow \mathfrak{z}\tau(u) = \mathfrak{z}(-p\nu - e^{iky\cdot d}\nu) \tag{6.0.7}$$

*which is true, as $p^{inc} = e^{iky\cdot d}$ and (p,u) is solution to **BVP 1**. We proceed similarly to prove that $(\mathfrak{z}p, \mathfrak{z}u)$ satisfies the transmission condition $\boldsymbol{BVP}_T$(d).*
Finally, due to the uniqueness modulo Jones frequencies of the pressure field as consequence of Corollary 1, we have that

$$p_T(z+y) = e^{ikz\cdot d}p(y) \quad \forall y \in \Omega_b^f \quad \text{and} \quad u_T(z+y) = e^{ikz\cdot d}u(y) \quad \forall y \in \Omega^s. \qquad \square \tag{6.0.8}$$

Bibliography

[1] M. Abramowitz and I. A. Stegun. Handbook of mathematical functions: with formulas, graphs, and mathematical tables*, volume 55. Courier Corporation, 1964.*

[2] R. A. Adams and J. J. Fournier. Sobolev spaces*, volume 140. Academic press, 2003.*

[3] P. Amestoy, A. Buttari, A. Guermouche, J.-Y. L'Excellent, and B. Ucar. Mumps: a multifrontal massively parallel sparse direct solver, 2013.

[4] X. Antoine. Conditions de Radiation sur le Bord*. PhD thesis, Pau, 1997.*

[5] X. Antoine, H. Barucq, and A. Bendali. Bayliss–turkel-like radiation conditions on surfaces of arbitrary shape. Journal of Mathematical Analysis and Applications*, 229(1):184–211, 1999.*

[6] D. N. Arnold. An interior penalty finite element method with discontinuous elements. SIAM journal on numerical analysis*, 19(4):742–760, 1982.*

[7] D. N. Arnold, F. Brezzi, B. Cockburn, and L. D. Marini. Unified analysis of discontinuous Galerkin methods for elliptic problems. SIAM journal on numerical analysis*, 39(5):1749–1779, 2002.*

[8] H. Barucq, R. Djellouli, and E. Estecahandy. Characterization of the Fréchet derivative of the elasto-acoustic field with respect to Lipschitz domains. Journal of Inverse and Ill-Posed Problems*, 22(1):1–8, 2014.*

[9] H. Barucq, R. Djellouli, and E. Estecahandy. Efficient DG-like formulation equipped with curved boundary edges for solving elasto-acoustic scattering problems. International Journal for Numerical Methods in Engineering*, 98(10):747–780, 2014.*

[10] H. Barucq, R. Djellouli, and E. Estecahandy. On the existence and the uniqueness of the solution of a fluid–structure interaction scattering problem. Journal of Mathematical Analysis and applications*, 412(2):571–588, 2014.*

[11] H. Barucq, R. Djellouli, E. Estecahandy, and M. Moussaoui. Mathematical Determination of the Fréchet Derivative with Respect to the Domain for a Fluid-Structure Scattering Problem. Case of Polygonal-Shaped Domains. SIAM, Journal of Mathematical Analysis*, pages 1–29, 2017.*

[12] H. Barucq, R. Djellouli, and A.-G. Saint-Guirons. Two-dimensional approximate local dtn boundary conditions for elliptical-shaped boundaries. In International Conference on Theoretical and Computational Acoustics*, 2007.*

[13] D. Behmardi and E. Nayeri. Introduction of fréchet and gâteaux derivative. Applied Mathematical Sciences*, 2(20):975–980, 2008.*

[14] C. Bellis, M. Bonnet, and F. Cakoni. Acoustic inverse scattering using topological derivative of far-field measurements-based l2 cost functionals. Inverse Problems*, 29(7):075012, 2013.*

[15] *C. Bellis, M. Bonnet, and B. B. Guzina. Apposition of the topological sensitivity and linear sampling approaches to inverse scattering.* Wave Motion, *50(5):891–908, 2013.*

[16] *L. Boillot.* Contributions à la modélisation mathématique et à l'algorithmique parallèle pour l'optimisation d'un propagateur d'ondes élastiques en milieu anisotrope. *PhD thesis, Pau, 2014.*

[17] *L. Bourgeois, N. Chaulet, and H. Haddar. On simultaneous identification of the shape and generalized impedance boundary condition in obstacle scattering.* SIAM Journal on Scientific Computing, *34(3):A1824–A1848, 2012.*

[18] *J. J. Bowman, T. B. Senior, and P. L. Uslenghi. Electromagnetic and acoustic scattering by simple shapes. Technical report, Michigan Univ. Ann Arbor Radiation Lab., 1970.*

[19] *H. Brezis, P. G. Ciarlet, and J. L. Lions.* Analyse fonctionnelle: théorie et applications, *volume 91. Dunod Paris, 1999.*

[20] *J. Brigham, W. Aquino, F. Mitri, J. Greenleaf, and M. Fatemi. Inverse estimation of viscoelastic material properties for solids immersed in fluids using vibroacoustic techniques.* Journal of applied physics, *101(2):023509, 2007.*

[21] *J. C. Brigham and W. Aquino. Inverse viscoelastic material characterization using pod reduced-order modeling in acoustic–structure interaction.* Computer Methods in Applied Mechanics and Engineering, *198(9):893–903, 2009.*

[22] *R. Brossier, S. Operto, and J. Virieux. 2d elastic frequency-domain full-waveform inversion for imaging complex onshore structures. In* 71st EAGE Conference and Exhibition incorporating SPE EUROPEC 2009, *2009.*

[23] *A. Buffa. Trace theorems on non-smooth boundaries for functional spaces related to Maxwell equations: an overview.* Lecture notes in computational science and engineering, *28:23–34, 2003.*

[24] *F. Cakoni and D. Colton.* Qualitative methods in inverse scattering theory: An introduction. *Springer Science & Business Media, 2005.*

[25] *P. G. Ciarlet.* The finite element method for elliptic problems. *SIAM, 2002.*

[26] *D. Colton, J. Coyle, and P. Monk. Recent developments in inverse acoustic scattering theory.* Siam Review, *42(3):369–414, 2000.*

[27] *D. Colton and A. Kirsch. A simple method for solving inverse scattering problems in the resonance region.* Inverse problems, *12(4):383, 1996.*

[28] *D. Colton and R. Kress.* Inverse acoustic and electromagnetic scattering theory, *volume 93. Springer Science & Business Media, 2012.*

[29] *D. Colton, M. Piana, and R. Potthast. A simple method using Morozov's discrepancy principle for solving inverse scattering problems.* Inverse Problems, *13(6):1477, 1997.*

[30] *M. Costabel. Boundary integral operators on Lipschitz domains: elementary results.* SIAM Journal on Mathematical Analysis, *19(3):613–626, 1988.*

[31] *M. Costabel and F. Le Louër. Shape derivatives of boundary integral operators in electromagnetic scattering. part I: Shape differentiability of pseudo-homogeneous boundary integral operators.* Integral Equations and Operator Theory, *72(4):509–535, 2012.*

[32] *B. E. Dahlberg, C. E. Kenig, and G. C. Verchota. Boundary value problems for the systems of elastostatics in Lipschitz domains.* Duke Math. J*, 57(3):795–818, 1988.*

[33] *R. Dautray and J.-L. Lions.* Mathematical Analysis and Numerical Methods for Science and Technology: Volume 1 Physical Origins and Classical Methods*. Springer Science & Business Media, 2012.*

[34] *R. Djellouli and C. Farhat. On the characterization of the Fréchet derivative with respect to a Lipschitz domain of the acoustic scattered field.* Journal of mathematical analysis and applications*, 238(1):259–276, 1999.*

[35] *R. Djellouli, C. Farhat, A. Macedo, and R. Tezaur. Finite element solution of two-dimensional acoustic scattering problems using arbitrarily shaped convex artificial boundaries.* Journal of Computational Acoustics*, 8(01):81–99, 2000.*

[36] *R. Djellouli, C. Farhat, J. Mandel, and P. Vanek. Continuous Fréchet differentiability with respect to a Lipschitz domain and a stability estimate for direct acoustic scattering problems.* IMA journal of applied mathematics*, 63(1):51–69, 1999.*

[37] *N. Dominguez, V. Gibiat, and Y. Esquerre. Time domain topological gradient and time reversal analogy: an inverse method for ultrasonic target detection.* Wave motion*, 42(1):31–52, 2005.*

[38] *G. Duvaut and J. L. Lions.* Les inéquations en mécanique et en physique*. Dunod, 1972.*

[39] *A. Edalat. A continuous derivative for real-valued functions. In* New Computational Paradigms*, pages 493–519. Springer, 2008.*

[40] *E. Estecahandy.* Contribution à l'analyse mathématique et à la résolution numérique d'un problème inverse de scattering élasto-acoustique*. PhD thesis, Pau, 2013.*

[41] *C. Farhat, R. Tezaur, and R. Djellouli. On the solution of three-dimensional inverse obstacle acoustic scattering problems by a regularized Newton method.* Inverse problems*, 18(5):1229, 2002.*

[42] *F. Faucher.* Contributions to Seismic Full Waveform Inversion for Time Harmonic Wave Equations: Stability Estimates, Convergence Analysis, Numerical Experiments involving Large Scale Optimization Algorithms*. PhD thesis, Université de Pau et des Pays de l'Adour, 2017.*

[43] *X. Feng and H. Wu. Discontinuous galerkin methods for the helmholtz equation with large wave number.* SIAM Journal on Numerical Analysis*, 47(4):2872–2896, 2009.*

[44] *V. Girault and B. Rivière. Dg approximation of coupled navier–stokes and darcy equations by beaver–joseph–saffman interface condition.* SIAM Journal on Numerical Analysis*, 47(3):2052–2089, 2009.*

[45] *D. Givoli. Non-reflecting boundary conditions.* Journal of computational physics*, 94(1):1–29, 1991.*

[46] *M. J. Grote and J. B. Keller. On nonreflecting boundary conditions.* Journal of Computational Physics*, 122(2):231–243, 1995.*

[47] *M. J. Grote, M. Kray, and U. Nahum. Adaptive eigenspace method for inverse scattering problems in the frequency domain.* Inverse Problems*, 33(2):025006, 2017.*

[48] *Z. Guo, S. You, X. Wan, and N. Bićanić. A FEM-based direct method for material reconstruction inverse problem in soft tissue elastography.* Computers & structures*, 88(23):1459–1468, 2010.*

[49] W. Hackbush. Elliptic differential equations. Theory and Numerical Treatment*, 1992.*

[50] J. Hadamard. Lectures on Cauchy's problem in linear partial differential equations*. Courier Corporation, 2014.*

[51] H. Haddar and R. Kress. On the Fréchet derivative for obstacle scattering with an impedance boundary condition. SIAM Journal on Applied Mathematics*, 65(1):194–208, 2004.*

[52] P. C. Hansen and D. P. O'Leary. The use of the L-curve in the regularization of discrete ill-posed problems. SIAM Journal on Scientific Computing*, 14(6):1487–1503, 1993.*

[53] T. Hargé. Valeurs propres d'un corps élastique. Comptes rendus de l'Académie des sciences. Série 1, Mathématique*, 311(13):857–859, 1990.*

[54] R. Hartmann and P. Houston. Symmetric interior penalty dg methods for the compressible navier-stokes equations i: Method formulation. 2005.

[55] R. Hartmann and P. Houston. Symmetric interior penalty dg methods for the compressible navier-stokes equations ii: Goal–oriented a posteriori error estimation. 2005.

[56] F. Hettlich. Fréchet derivatives in inverse obstacle scattering. Inverse problems*, 11(2):371, 1995.*

[57] T. Hohage. Iterative methods in inverse obstacle scattering: regularization theory of linear and nonlinear exponentially ill-posed problems*. PhD thesis, Johannes-Kepler-Universitat Linz, 1999.*

[58] G. C. Hsiao, R. E. Kleinman, and G. F. Roach. Weak solutions of fluid–solid interaction problems. Mathematische Nachrichten*, 218(1):139–163, 2000.*

[59] G. C. Hsiao and W. L. Wendland. Boundary integral equations*, volume 164. Springer, 2008.*

[60] T. Huttunen, J. Kaipio, and P. Monk. An ultra-weak method for acoustic fluid–solid interaction. Journal of Computational and Applied Mathematics*, 213(1):166–185, 2008.*

[61] F. Ihlenburg. Finite element analysis of acoustic scattering*, volume 132. Springer Science & Business Media, 2006.*

[62] O. Ivanyshyn. Shape reconstruction of acoustic obstacles from the modulus of the far field pattern. Inverse Problems and Imaging*, 1(4):609, 2007.*

[63] O. Ivanyshyn and R. Kress. Identification of sound-soft 3D obstacles from phaseless data. Inverse Problems and Imaging*, 4(1):131–149, 2010.*

[64] O. Ivanyshyn and R. Kress. Inverse scattering for surface impedance from phase-less far field data. Journal of Computational Physics*, 230(9):3443–3452, 2011.*

[65] D. S. Jerison and C. E. Kenig. The Neumann problem on Lipschitz domains. Bulletin of the American Mathematical Society*, 4(2):203–207, 1981.*

[66] D. Jones. Low-frequency scattering by a body in lubricated contact. The Quarterly Journal of Mechanics and Applied Mathematics*, 36(1):111–138, 1983.*

[67] M. C. Junger and D. Feit. Sound, structures, and their interaction*, volume 225. MIT press Cambridge, MA, 1986.*

[68] M. Kern. Numerical Methods for Inverse Problems*. John Wiley & Sons, 2016.*

[69] A. Kirsch. The domain derivative and two applications in inverse scattering theory. Inverse problems*, 9(1):81, 1993.*

[70] A. Kirsch. Characterization of the shape of a scattering obstacle using the spectral data of the far field operator. Inverse problems*, 14(6):1489, 1998.*

[71] A. Kirsch. Factorization of the far-field operator for the inhomogeneous medium case and an application in inverse scattering theory. Inverse Problems*, 15(2):413, 1999.*

[72] A. Kirsch. An introduction to the mathematical theory of inverse problems*, volume 120. Springer Science & Business Media, 2011.*

[73] R. Kress and W. Rundell. A quasi-Newton method in inverse obstacle scattering. Inverse Problems*, 10(5):1145, 1994.*

[74] R. Kress and W. Rundell. Inverse obstacle scattering with modulus of the far field pattern as data. Inverse problems in medical imaging and nondestructive testing*, pages 75–92, 1997.*

[75] P. Lailly. The seismic inverse problem as a sequence of before stack migrations. In Conference on Inverse Scattering–Theory and Application*, pages 206–220. SIAM, 1983.*

[76] P. D. Lax and R. S. Phillips. Scattering theory*, volume 26. Academic press, 1990.*

[77] F. Le Louër. Optimisation de forme d'antennes lentilles intégrées aux ondes millimétriques*. PhD thesis, Université Européenne de Bretagne, 2009.*

[78] C. Luke and P. A. Martin. Fluid–solid interaction: acoustic scattering by a smooth elastic obstacle. SIAM Journal on Applied Mathematics*, 55(4):904–922, 1995.*

[79] M. M. Mehrabadi and S. C. Cowin. Eigentensors of linear anisotropic elastic materials. The Quarterly Journal of Mechanics and Applied Mathematics*, 43(1):15–41, 1990.*

[80] R. Meise and D. Vogt. Introduction to functional analysis*. Clarendon Press, 1997.*

[81] L. Mönch. A Newton method for solving the inverse scattering problem for a sound-hard obstacle. Inverse Problems*, 12(3):309, 1996.*

[82] P. Monk and E. Süli. The adaptive computation of far-field patterns by a posteriori error estimation of linear functionals. SIAM Journal on Numerical Analysis*, 36(1):251–274, 1998.*

[83] C.-C. Mow and Y.-H. Pao. Diffraction of elastic waves and dynamic stress concentrations*. RAND, 1971.*

[84] F. Nataf. Absorbing boundary conditions and perfectly matched layers in wave propagation problems, 2013.

[85] J.-C. Nédélec. Acoustic and electromagnetic equations: integral representations for harmonic problems*, volume 144. Springer Science & Business Media, 2001.*

[86] O. A. Oleinik, A. Shamaev, and G. Yosifian. Mathematical problems in elasticity and homogenization*, volume 26. Elsevier, 1992.*

[87] R.-É. Plessix. Three-dimensional frequency-domain full-waveform inversion with an iterative solver. Geophysics*, 2009.*

[88] R.-E. Plessix and C. Perkins. Thematic set: Full waveform inversion of a deep water ocean bottom seismometer dataset. First Break*, 28(4):71–78, 2010.*

[89] *R. Potthast. Fréchet differentiability of boundary integral operators in inverse acoustic scattering.* Inverse Problems, *10(2):431, 1994.*

[90] *R. Potthast. Domain derivatives in electromagnetic scattering.* Mathematical Methods in the Applied sciences, *19(15):1157–1175, 1996.*

[91] *R. Potthast. Fréchet differentiability of the solution to the acoustic Neumann scattering problem with respect to the domain.* Journal of Inverse and Ill-Posed Problems, *4(1):67–84, 1996.*

[92] *H. Prautzsch, W. Boehm, and M. Paluszny.* Bézier and B-spline techniques. *Springer Science & Business Media, 2013.*

[93] *S. Rosenbaum-Raz. On scatterer reconstruction from far-field data.* IEEE Transactions on Antennas and Propagation, *24(1):66–70, 1976.*

[94] *S. A. Sauter and C. Schwab. Boundary element methods. In* Boundary Element Methods, *pages 183–287. Springer, 2010.*

[95] *M. Schechter.* Principles of functional analysis, *volume 2. Academic press New York, 1971.*

[96] *O. Scherzer. The use of Morozov's discrepancy principle for Tikhonov regularization for solving nonlinear ill-posed problems.* Computing, *51(1):45–60, 1993.*

[97] *S. H. Schot. Eighty years of Sommerfeld's radiation condition.* Historia mathematica, *19(4):385–401, 1992.*

[98] *A. Sommerfeld. Die Greensche Funktion der Schwingungslgleichung.* Jahresbericht der Deutschen Mathematiker-Vereinigung, *21:309–352, 1912.*

[99] *A. Tarantola. Inversion of seismic reflection data in the acoustic approximation.* Geophysics, *49(8):1259–1266, 1984.*

[100] *L. Thomsen. Weak elastic anisotropy.* Geophysics, *51(10):1954–1966, 1986.*

[101] *A. N. Tikhonov, V. I. Arsenin, and F. John.* Solutions of ill-posed problems, *volume 14. Winston Washington, DC, 1977.*

[102] *S. Tordeux.* Méthodes asymptotiques pour la propagation des ondes dans les milieux comportant des fentes. *PhD thesis, Université de Versailles-Saint Quentin en Yvelines, 2004.*

[103] *J. E. Warner, M. I. Diaz, W. Aquino, and M. Bonnet. Inverse material identification in coupled acoustic-structure interaction using a modified error in constitutive equation functional.* Computational mechanics, *54(3):645–659, 2014.*

[104] *C. H. Wilcox.* Scattering theory for the d'Alembert equation in exterior domains, *volume 442. Springer, 2006.*

[105] *K. L. Williams. Acoustical scattering from an elastic sphere in water: Surface wave glory, resonances, and the Sommerfeld-Watson transformation for amplitudes. Technical report, Washington State Univ. Pullman of Physics, 1985.*

[106] *S. Yamamuro.* Differential calculus in topological linear spaces, *volume 374. Springer, 2006.*